THE UNIVERSITY *of* EDINBURGH

Ultrafast Photophysics of High-Spin Metal Complexes

THE UNIVERSITY *of* EDINBURGH

Florian Liedy

Degree of Doctor Philosophy

The University of Edinburgh

2020

Abstract

Transition metal complexes (TMCs) show unusual optical, magnetic and chemical properties in comparison to purely organic molecules. These properties make them suitable for several applications. Organic light emitting diodes (OLEDs), catalysis, anti-cancer drugs, molecular switches and new magnetic materials are all areas where TMCs are in current use or within the scope of future applications. It is important to study their photophysical properties since they are of great importance in all these applications.
To study the photophysical dynamics of TMCs, an ultrafast broadband transient absorption (TA) spectrometer was set up. For that, two spectrometers were build using charge coupled device(CCD) cameras as detector. Further, a white light continuum was required in order to measure broadband spectra. White light generation was induced in CaF_2, which needs continuous movement in order to avoid damage on the crystalline CaF_2 disk itself.
In this thesis, the photophysics of three groups of TMCs were studied by several optical techniques including ultrafast TA spectroscopy. First, three manganese complexes - two of them showing single molecule magnet (SMM) behaviour - were studied. Manganese complexes are known to have fascinating magnetic and catalytic properties. Their usage as SMMs and catalytic centre in chlorophyll makes them an important class of TMCs. To study the photophysical properties of Mn SMMs, a comparison of Mn complexes with one, three and six Mn ions in one molecule was performed.
Two out of the three samples were Mn(III)-based SMMs, which are $[Mn(III)_3O(Et-sao)_3(\beta-pic)_3(ClO_4)]$ or Mn_3 and $[Mn(III)_6O_2(Et-sao)_6(O_2CPh(Me)_2)_2(EtOH)_6]$ or Mn_6. The third one was the $Mn(acac)_3$ (acac $\equiv$ acetylacetonate anion) complex. As a result from the ultrafast TA, it was found that a vibrational wave packet is formed upon photoexcitation of all three complexes. The results show new possibilities for

non-thermal control of the magnetisation in SMMs and open up new molecular design challenges to control the wave packet motion in the excited state.

Iron complexes, especially iron in oxidation state +2 with six electrons in the d-orbitals, are well-studied due to a spin-crossover phenomenon that can be triggered by optical stimulation. In this thesis, the focus is on the complex $[Fe_3O(Ac)_6(H_2O)_3]$ (Fe_3) with three iron ions in mixed oxidation states. One ion is in oxidation state +2 while the other two are in oxidation state +3 (Fe(III)Fe(III)Fe(II)). This molecule is of interest due to possible long-lived charge transfer states and spin dynamics due to the mixed oxidation states. Ultrafast transient absorption spectroscopy was performed of the Fe complex in solution at room-temperature exciting either at 400 nm or 520 nm and a long-lived excited-state absorption (ESA) signal was observed. The broad ESA band is comprised of several un-resolved bands, showing shoulders at 405 nm, 440 nm and 530 nm. From the transient absorption results, three decay constants of $\tau_1 = 360 \pm 30$ fs, $\tau_2 = 5.3 \pm 0.6$ ps, $\tau_3 = 65 \pm 5$ ps and a long-lived state ($\tau_4 > 500$ ps) were extracted by a global multi-exponential fit over the full wavelength range (340 nm to 690 nm). The comparison of the TA results with two pump wavelengths indicates that the lowest excited state is populated on a sub 120 fs time scale. Calculations on the coupled cluster level of theory, performed by collaborators, showed that this state has a mixture of both charge-transfer and ligand-field/d-orbital character.

Third, the ultrafast photophysics of a terbium phthalocyanine double-decker complex ($TbPc_2$) were investigated. The interaction of the ligands via the terbium linker and the luminescence properties are studied. Static UV/Vis absorption and luminescence spectroscopy were performed. The typical Q- and B-bands associated with excitations in the first and second excited singlet states of the phthalocyanine ligands were found. In the luminescence spectrum after excitation in the UV, signatures of the typical emission for a Tb(III) ion in the green part of the spectrum were found, overlapped with emission from the ligands. The ultrafast TA difference spectra are dominated by ground state bleach bands, which overlap with ESA. The dynamics show a long-lived state, which is important for the luminescence of the Tb^{3+} ion. The energy transfer pathway was tentatively assigned to a direct excitation of the emissive Tb^{3+} via the B-band levels of the radical phthalocyanine.

Lay Summary

Metal coordination complexes are molecules consisting of a central metal atom or ion and bound organic or inorganic molecules or atoms which are called ligands. The most common metal coordination complexes have six or four ligands surrounding the metal in an octahedral or tetrahedral geometry. Some complexes are strongly coloured. E.g. the deep purple potassium manganate ($K[MnO_4]$) or the blue hexaaquacopper complex ($[Cu(H_2O)_6]^{2+}$). In nature metal coordination complexes are extremely important for photosynthesis (Chlorophyll), oxygen transport in the blood (Heme complex), red blood cell and nerve cell health (Vitamin B12) and much more.

In science and industry metal coordination complexes are also in use for homogeneous catalysis and in medicine metal coordination complexes are highly effective anti-cancer drugs. Another application is to study the unique magnetic properties of some complexes for future data storage applications. These molecules behave like bar magnets, but their size is on the nanometer scale. The usage of molecular sized magnetic particles would be a huge increase in storage density for data storage media. The field of data storage on a molecular level is currently on the research level. The first metal coordination complexes showing such magnetic properties were found in the beginning 1990s. So the field of what is now called single molecule magnets is new.

Another field of science deals with processes in molecules and atoms on very short time scales. The time range this part of science is dealing with is in the range of 10^{-15} to 10^{-12} seconds (s) (1×10^{-15} s = 1 femtosecond (fs)). The term "ultrafast" is used to describe processes on the femtosecond time scale. The only tool that can produce signals on that time scale is a laser. The scientific field of light matter interaction is called spectroscopy. Femtosecond transient absorption spectroscopy which uses femtosecond laser pulses to measure processes in molecules on the ultrafast time scale is used for

several experiments in this work.

In this thesis an apparatus was build to perform the femtosecond transient absorption spectroscopy. This apparatus was then used to measure the ultrafast processes in three groups of metal coordination complexes. The first group are manganese coordination complexes which show single-molecule magnet properties. To understand the ultrafast processes happening in this kind of complexes is helpful for the development of new single-molecule magnets.

The second metal coordination complex is based on iron. Iron complexes are of interest for industrial purposes, because iron is earth abundant. One example where iron complexes could be helpful are organic light emitting diodes (OLEDs). OLEDs are widely used as light sources for displays and TVs. At the moment OLED materials are largely base on palladium and iridium complexes, due to their extraordinary luminescent properties. New science is going towards copper complexes as emitting materials for OLEDs. Iron complexes would be great for OLED applications, if they would posses the right properties. So we performed experiments on one iron complex which is known to show interesting photophysics. It was found that a long living (in relation to the femtosecond scale) state is populated.

The third metal complex is based on terbium and also shows single-molecule magnet properties. Terbium is a rare earth metal which is known for being luminescent. The structure of the complex, a so-called sandwich complex, makes it interesting to look at the ultrafast photophysics and the luminescent properties, to find out how the two sandwich halves interact and if luminescence can be detected. Luminescence was found and a model was developed how this is possible in the unusual sandwich structure.

Acknowledgements

I would like to thank Dr Olof Johansson for the supervision of my Phd project, for the help in the laser lab and for the successful work over the past three years. His passion for science was an inspiration during my PhD project.

I want to acknowledge Prof Euan Brechin for his work as my second supervisor and for the good collaboration on the Mn SMM and Fe_3 projects, which both led to publications.

I want to thank my collaborators Dr Julien Eng and Dr Thomas Penfold from Newcastle University for their work on the Mn SMM project. Without their great work, the publication in Nature Chemistry would not have been possible.

Thanks to Rui Shi, Prof Georgios Lefkidis and Prof Wolfgang Hübner from the University of Kaiserslautern for the calculations on the Fe_3 molecule and the good collaboration on publishing the results.

I would like to thank Dr Luke Hedley, Minas Stefanou, Hal Lewis, Dr Debi Pattnaik and Jake Sutcliffe for the great working environment in our office. It was a pleasure working alongside you all.

Thanks to Dr Andrei Gromov for the help in the chemistry lab and with the Raman microscope. It was always fun working with you.

At this point, I would like to thank my family, my mum Ilona, my father Günther

and my brother Oliver. They supported me throughout my studies, all those years.

Finally I would like to thank Xiaomin for her love and her support in so many ways throughout the last three years. I am, and always will be happy having you around me.

Contents

Chapter 1

Introduction and Aims

This thesis is about ultrafast photophysics of open shell, high spin metal coordination complexes. The open shell, high spin electronic structure leads e.g. to JT distortion, mixed valence states and magnetic anisotropy.

The thesis consists of a methods chapter, describing the work that was done building the broadband UV/Vis ultrafast TA spectrometer and three experimental result chapters.

Ultrafast means that laser pulses in the fs range are used to measure photophysical properties. Metal coordination complexes are metals, mostly in an oxidized form, which are surrounded by non-metal bound molecules and ions (ligands). The founder of modern coordination chemistry is the Swiss Nobel prize winner (1913) Alfred Werner who invented the concept of coordination on basis of oxidation state and coordination number of metal atoms/ions. The photophysics of metal coordination complexes were always of great interest, due to their sometimes strongly coloured appearance. Today metal coordination compounds can be found in industry as catalyst and as pigments. In nature, metal coordination compounds are important for many catalytic functions. E.g. Chlorophyll, the green natural pigment, allows plants to perform photosynthesis and therefore produce oxygen and carbohydrates. The heme group in hemoglobin is responsible that the oxygen can be transported through the lungs in to the muscles via the blood stream.

For modern science the application in nature is a motivation to develop drugs with unmatched properties. E.g. for cancer treatment, where the Cisplatin complex was one of the first drugs found to be effective. Current state science is dealing with photoact-

ive therapy, combining the anti-cancerogenous and light absorbing properties of metal coordination compounds(e.g. [1–4]). A huge impact of metal coordination compounds lies in the field of organic light emitting devices (OLEDs), where highly emissive metal complexes are used to produce light from electricity (e.g. [5–9]). One group of highly emissive metal complexes is using an approach called thermally activated delayed fluorescence (TADF). A group of Cu(I) complexes showing TADF were studied extensively by ultrafast spectroscopic methods [10–13]. These studies are a great example of how the understanding of the photophysics of transition metal complexes can accelerate the material development. This is the reason why the results of the studies on the Cu(I) complexes is discussed in more details in this chapter.

Another field of science where metal coordination compounds are of great interest is the field of data storage applications. Modern hard disks equipped with Heat-Assisted Magnetic Recording (HAMR) developed by Seagate can store approximately up to 100 TB by 2025 with an areal density of up to 2 TB/sq. inch. But the development for more dense and faster electronic data storage devices will not stop. In search for smaller magnetic particles, several kinds of molecules are under debate. Two of the most promising ones are spin crossover (SCO) systems and SMMs. SCO is the process of changing the spin state between low and high spin state. SCO can be used to achieve a bistable system in a molecule. This is the so called spin state trapping, where a metal coordination complex is trapped in an electronic excited state which shows a strong geometry change in relation to the ground state. So the energy barrier for relaxation to the ground state is large. Fe complexes with the Fe in oxidation state II are mostly used in this field. The Fe(II) complexes have a total spin S = 0 (low spin) ground state and the first excited state is the S = 2 (high spin) state. To excite molecules into the high spin state several ways like pressure, temperature and light are possible. The low spin to high spin switching using light, especially laser light, became the most promising way. The whole process of trapping the metal coordination compound in a high spin state using light is called light induced excited spin state trapping (LIESST) [14]. This process is a promising way of using molecules with two stable spin states as medium for data storage and spin switches. The limitation for the usage of SCO complexes is that the energy barrier height is limited and so the temperature range for long living high spin states is in the liquid helium region. Another problem might be that the

SCO complexes do not work as classic magnets. This could be a problem for the read and write process. Another obstacle is the volume change of the SCO complex from low spin to high spin which could be a mechanical strain problem for applications. The photophysics of the light induced SCO process are very well studied and are a example of the huge differences in ultrafast photophysics of metal complexes in relation to organic molecules. Since the ultrafast photophysics are a well studied example for metal coordination complexes and the ultrafast transient absorption (TA) experiment of the $[Fe(II)(bpy)_3]^{2+}$ complex (bpy≡ bipyridine) in ethanol solution is shown as example for the performance of the TA set-up in Chapter 2, the ultrafast photophysics are discussed in this chapter.

SMMs are transition metal complexes with two stable magnetic ground states. In contrast to macroscopic magnetic materials, the magnetism in SMMs has a purely molecular origin and does not depend on long range co-operative effects. The reason for this behaviour is a combination of unpaired spins and anisotropy. The uniaxial anisotropy in the molecule defines a preferred projection axis for the total spin vector in an Ising-type fashion (easy-axis). Easy-axis describes the energetically favourable axis for magnetization.

This behaviour is also known as super-paramagnetic. Super-paramagnetic means that the magnetization relaxation time is getting large in relation to the measurement time below a specific blocking temperature T_B. In a simple manner , the relaxation time τ_M can be expressed in an Arrhenius type equation

$$\tau_M = \tau_0 \times e^{(U_{eff}/k_bT)}, \tag{1.1}$$

with U_{eff} the effective energy barrier and, τ_0 the characteristic relaxation time of the system. The aim for usage in e.g. storage devices is an almost infinite relaxation time at temperatures as high as possible. For this purpose the energy barrier, which can be expressed by

$$U_{eff} = |D|S^2 \tag{1.2}$$

for integer spin system, has to be as large as possible. D is the zero-field splitting parameter. For a high energy barrier for spin reversal, D should be negative and as large as possible.

Another measure of the performance of a SMM is the blocking temperature (T_B), where several definitions exist. In the following T_B is defined as the highest temperature where a magnetic hysteresis loop is observed in an external magnetic field vs. magnetization plot, because this behaviour is the closest to classic bulk magnets. Comparison between different SMMs using T_B is difficult, since T_B strongly depends on the sweep rate of the experiment [15].

The advantage of SMMs over SCO systems is that the anisotropy and the total spin are tunable. It was shown by Guo et al. [16] that an approach of a linear coordination of a dysprosium ion leads to a record blocking temperature of 80 K. The disadvantage of the linear coordination is clearly the chemical instability.

Beside the synthesis of SMMs with higher blocking temperatures, the research is searching for new and faster ways to control the magnetization in magnetic materials. For metals it was shown that by using circularly polarized, femtosecond light pulses, the magnetization can be controlled [17–19]. Stupakiewicz et al. [20, 21] showed that in an cobalt-substituted yttrium iron garnet it is possible to control the magnetization using linear polarized fs laser light. The mechanism for switching the direction of magnetization was found to work via excitation of dd transitions on the Co ions. For metals the proposed mechanism is via direct interaction of the magnetic field of the light with the field of the metal.

1.1 Coordination chemistry and Jahn-Teller distortion

Metal coordination complexes are molecules consisting of a central metal atom or ion and several negatively charged or neutral molecules or ions which are called ligands. The interaction between the metal centre and the ligands are determined by both electrostatic and orbital interactions. Depending on the metal and the ligands this leads to a large variety of coordination numbers and geometries. Metal complexes tend to have a sum of 18 electrons, counting the d-electrons on the metal together with the donor electrons of the ligands. This behaviour is due to the stability of filled shells. For transition metals, e.g. 3d metals the outer shell consists of the 4s, 4p and 3d shells where a total of 18 electrons can be placed.

JT distortion arises through a molecules aim to minimize it's energy by lifting the de-

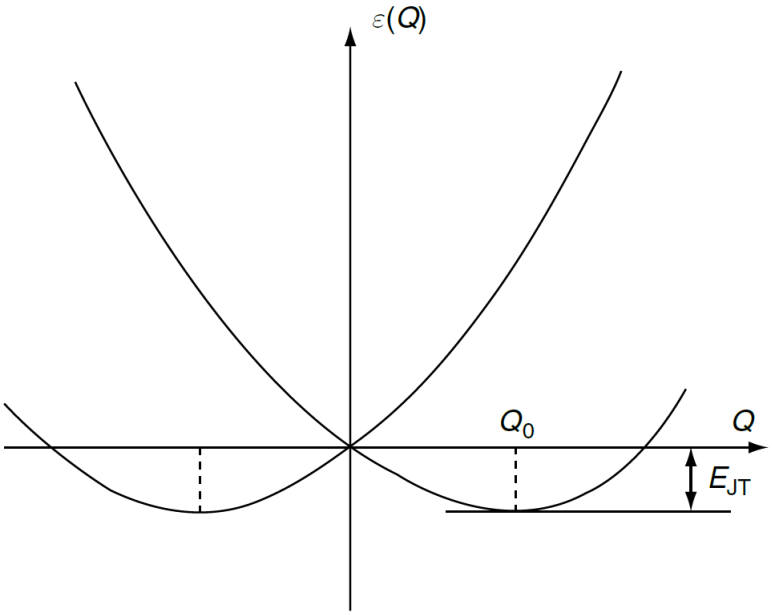

Figure 1.1: *Scheme of a adiabatic potential energy curve for a molecular system with a twofold orbitally degenerate electronic state. The scheme shows that there are two minima for a distortion along the Q coordinate with E_{JT} is the JT stabilization energy. The figure is taken from [22].*

generacy of orbitals. The basic condition for this process to be effective is that one of the initially degenerate orbitals is not fully occupied. In the scope of this thesis, the focus is on octahedral metal complexes, but JT can be found in any molecule with degenerate orbitals.

JT distortion in octahedral metal complexes can be found for d^1, d^2, d^4 high spin(HS) and low spin (LS), d^5 (LS), d^6 (HS), d^7 (HS and LS) and d^9 configuration. The amount of distortion depends on the involved orbitals. If the d-orbitals are non-bonding, the effect of lifting the degeneracy is small. If bonding or anti-bonding d-orbitals are involved, as for d^4 (HS) and d^9 configurations, the distortion effect is large. For these two octahedral complexes (both double degenerate (E-state) in a fully symmetric octahedral environment), the JT distortion can manifest itself in two ways. First, an elongation of the bond lengths along the z-axis (tetragonal elongation) and a compression along the x,y-axes. This is equal to a energy lowering of the d_{z^2} orbital and an increase of energy of the $d_{x^2-y^2}$ orbital. Second, a compression along the z-axis (tetragonal compression) and a elongation along the x,y-axes. This relates to a energy lowering of the $d_{x^2-y^2}$ orbital and an increase of the d_{z^2} orbital. This behaviour is shown in Figure 1.2 on hand of the d^4 (HS) configuration. The other three d-orbitals also adjust their

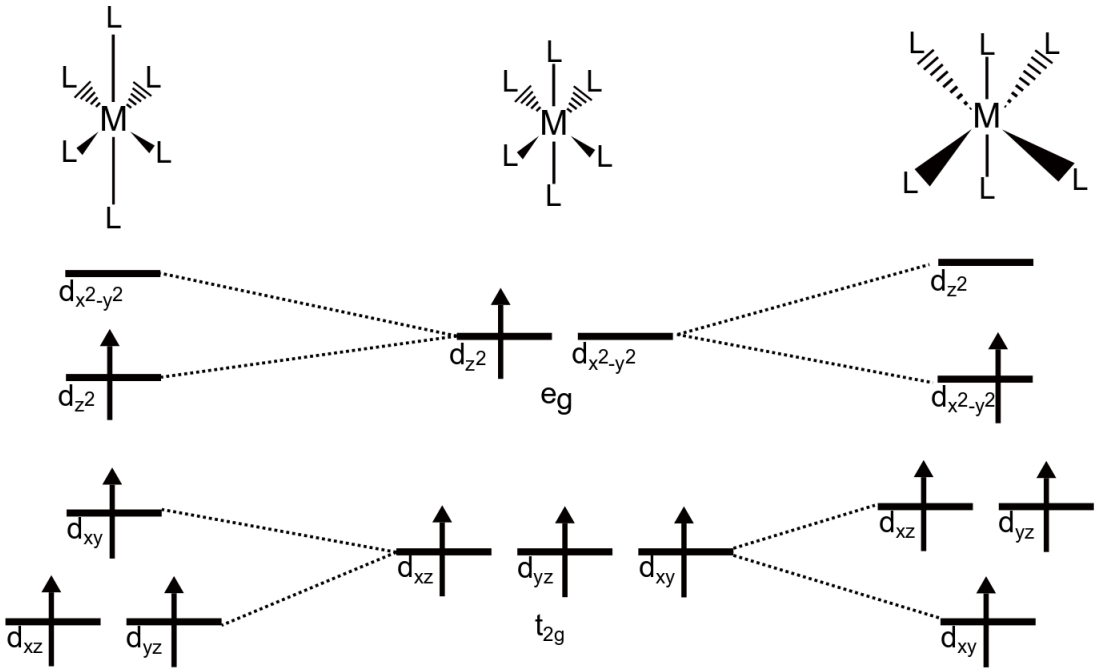

Figure 1.2: *Scheme of d-orbital splitting for a d^4 (HS) system, due to the JT effect. For an E state two possible tetragonal distortions are possible. Tetragonal elongation on the left side and tetragonal compression on the right. The compression will destabilize orbitals with components along the z-axis while elongation will stabilize them.*

energetic position depending on the distortion, but no net energy gain can be achieved since these orbitals are symmetrically occupied. The two possible distortion geometries are typically very close in energy [22] and the energy potential landscape could be described in a simple fashion as a double well potential as it is shown in Figure 1.1. In Figure 1.1 the energy of the system is plotted as a function of a bond length Q. JT distortion can be described as a crossing of two potential energy surfaces belonging to the two possible geometries described before. The crossing point is the octahedral geometry without distortion. The minima on both sides at Q_0 are E_{JT}, the JT stabilization energy below the maximum. For some metal complexes the energy barrier and energy difference is so low, that especially in solution, an equilibrium between the two geometries was found. This is called dynamic JT effect. For larger energy barriers and energy differences and also in crystals, where the geometry is limited by the lattice, one or the other JT distortion geometry is found.

The JT-distortion has a large impact on the spectroscopic properties of the metal complexes. By lifting the degeneracy of the d-orbitals, new dd- and charge transfer (CT) -transitions can be observed. For example an octahedral d^4 (HS) system without

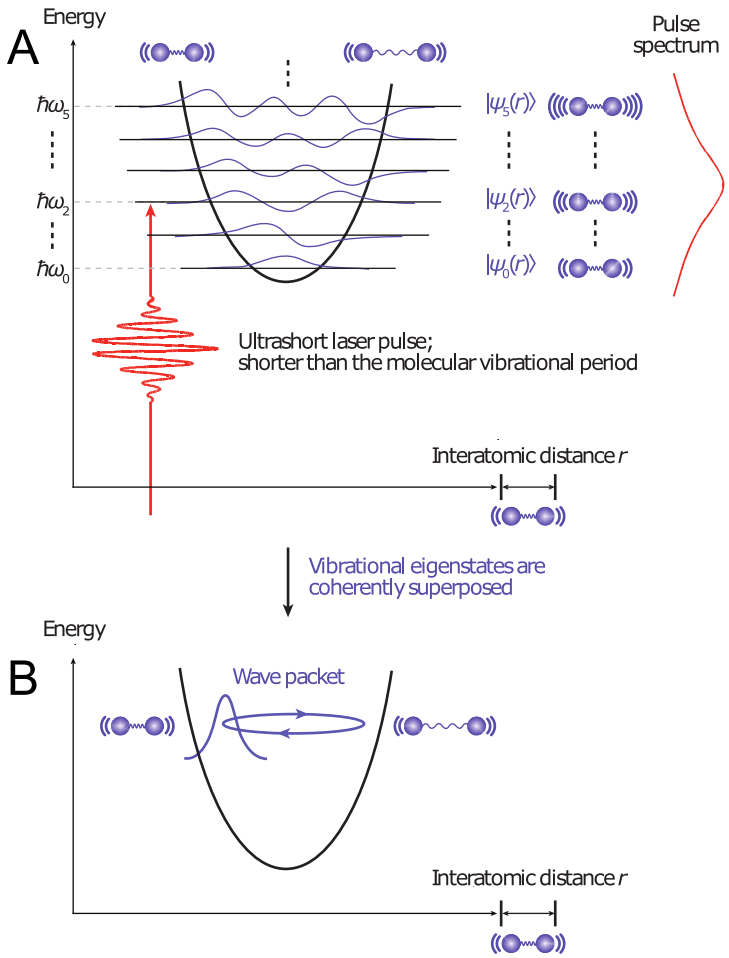

Figure 1.3: ***A*** *Scheme of the excitation of a vibrational wave packet in an electronic excited state of a diatomic molecule by a laser pulse shorter than the molecular vibrational period.* ***B*** *Scheme showing the oscillatory movement of the wave packet in the potential. Figure was taken from Kenji Ohmori [23].*

JT distortion, has one spin allowed transition from the t_{2g} orbitals into the e_g orbitals. With JT distortion there are three spin allowed dd transitions. The splitting of the t_{2g} and e_g orbitals also splits metal-to-ligand charge transfer (MLCT) and ligand-to-metal charge transfer (LMCT) transitions.

1.2 Vibrational wave packets in molecules

A wave packet is a coherent superposition of eigenstates of a system. These can be rotational, vibrational or electronic states. In this section, the focus is on vibrational wave packets. For reasons of simplicity the description of a vibrational wave packet

is limited to a diatomic molecule. The section is roughly ordered in the creation of a wave packet using a fs laser pulse in resonance with a rovibronic transition, it's temporal evolution in the potential energy surface and it's dephasing due to anharmonic coupling and energy loss to the surrounding.

A vibrational wave packet is formed by by an ultrashort laser pulse exciting the ground state population into an excited state. The need for an ultrashort laser pulse lies in the definition of a wave packet. A superposition of vibrational eigenstates needs to be formed. Assuming an harmonic potential, the spacing between the ground vibrational state ω_0 and all excited states is equal. This is shown in Figure 1.3 **A** for a diatomic molecule. For a low frequency vibrational mode the energy spacing is on the order of hundreds of wavenumbers. To create a superposition of at least two vibrational levels, the laser pulses energy spectrum needs to be as broad as the spacing of the vibrational levels. The width of the energy spectrum (ΔE) is directly related to the pulse duration (Δt) by the time-bandwidth product. For Gaussian pulses the product limit is $\Delta E \times \Delta t \geq 0.441$. So for a larger ΔE the pulse duration Δt has to decrease. So this is the reason why femtosecond laser pulses are needed to excite a vibrational wave packet.

In Figure 1.3 **B** it is shown that after excitation, the wave packet will move in the energy potential with a period of a classic particle in the according potential. This is due to the Heisenberg uncertainty principle. A wave packet is localized in space but broad in energy which is equivalent to the laser pulse which excited the wave packet in the first place. In a harmonic potential a wave packet will get broader if it is narrower than the wave function of the vibrational ground state and narrower if it is broader than the vibrational ground state [24].

For energy surfaces which are not harmonic and therefore more realistic, e.g. a Lennard-Jones potential, the energy spacing between the energy levels will decrease for higher energy levels. Therefore longer laser pulses would be sufficient to excite a vibrational wave packet, if the Frank-Condon region lies in the upper part of the Lennard-Jones potential. Another effect of a slightly anharmonic potential is that a reformation of the wave packet, after a dephasing is observed. This can be explained by the finite number of vibrational states forming a superposition [24]. A reformation of the wave packet can be only observed if the energy is not getting distributed over

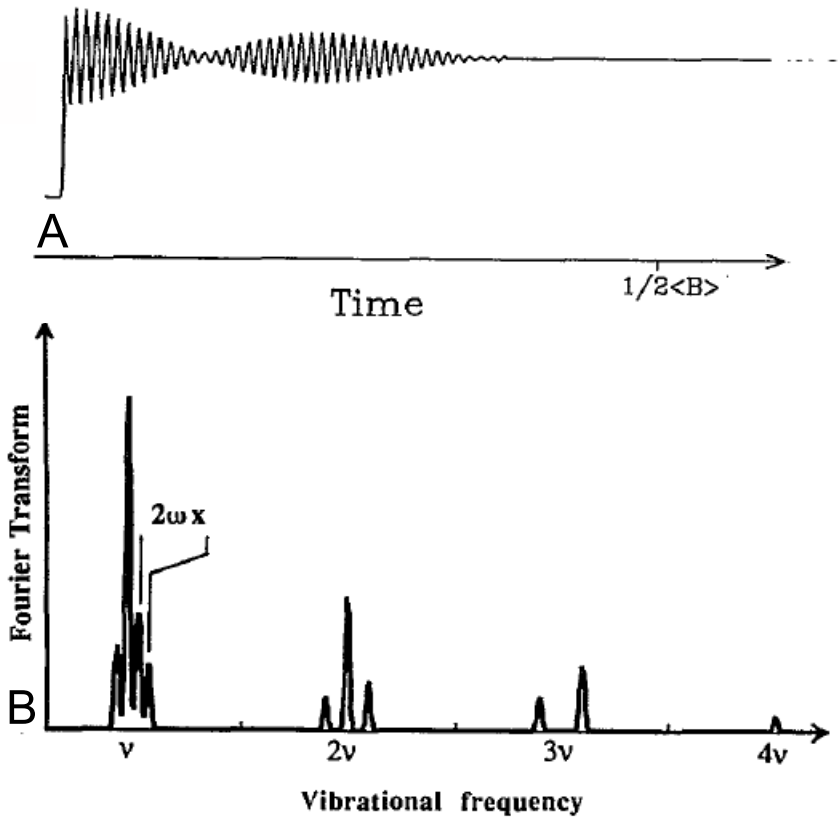

Figure 1.4: ***A*** *Simulated wave packet evolution of several superimposed vibrational modes.* ***B*** *Fourier transform of the trace in* ***A*** *showing and ν the initially excited vibrational modes and subsequent as 2ν and so on the higher order frequencies. The figure was taken from M. Gruebele and A. H. Zewail [25].*

time to other modes or to the surrounding. This is why this phenomenon can be only observed in gas phase for molecules which potential is close to harmonic, as it was shown on Na_2, using multiphoton pump-probe ionization spectroscopy [26].
Figure 1.4 shows in **A** an example of a transient wave packet formed after ultrafast photoexciation. It is comprised of several vibrational modes. To analyse the frequencies of a vibrational wave packet a fast Fourier transformation (FFT) can be used. Figure 1.4 **B** shows the FFT of the transient in **A**. It can be seen, that the frequencies of the different involved modes repeat in equal intervals for ν, 2ν etc.. The intensity of the peaks decrease for higher order vibrational levels.
In ultrafast transient absorption spectroscopy, using a broadband probe pulse, oscillations can not only be observed in transients, but also in spectra. This can be seen well in Figures 1.6 **C** and 1.7 **a**, where the wavelength can be seen oscillating in time. The oscillations of the wavelength is explained by the movement of the wave packet in the potential. Assuming two potentials at different energies, where the position of the potential minimum is at the same position. The wave packet is formed in the lower energy potential and the probe pulse will measure the absorption into the higher lying potential. If the wave packet is at one of the turning points the energy required to reach the upper potential is higher than when the wave packet is in the middle between the turning points. As explanation for the intensity change of the transition: The wave packet moves in the excited state energy potential, the Frank-Condon overlap to higher lying states changes and the intensity of the absorption is modulated by the frequency of the wave packet.

1.3 Ultrafast photophysics of $[Fe(II)(bpy)_3]^{2+}$

It was shown by McCusker et al. [29] in 1993 that the $[Fe(II)(tpen)](ClO_4)_2$ and other Fe(II) complexes (also $[Fe(II)(bpy)_3](ClO_4)_2$) do not follow the until then accepted theory of internal vibrational redistribution (IVR)/vibrational cooling as the fastest process after photoexciation. The understanding at that time was that the IVR process is followed by internal conversion and intersystem crossing (ISC). ISC was until then considered the slowest process, due to the forbidden change in spin state. McCusker et al. [29] found in 1993 that after excitation ($^1A_1 \rightarrow {}^1$LMCT), the ^{1}LMCT decays

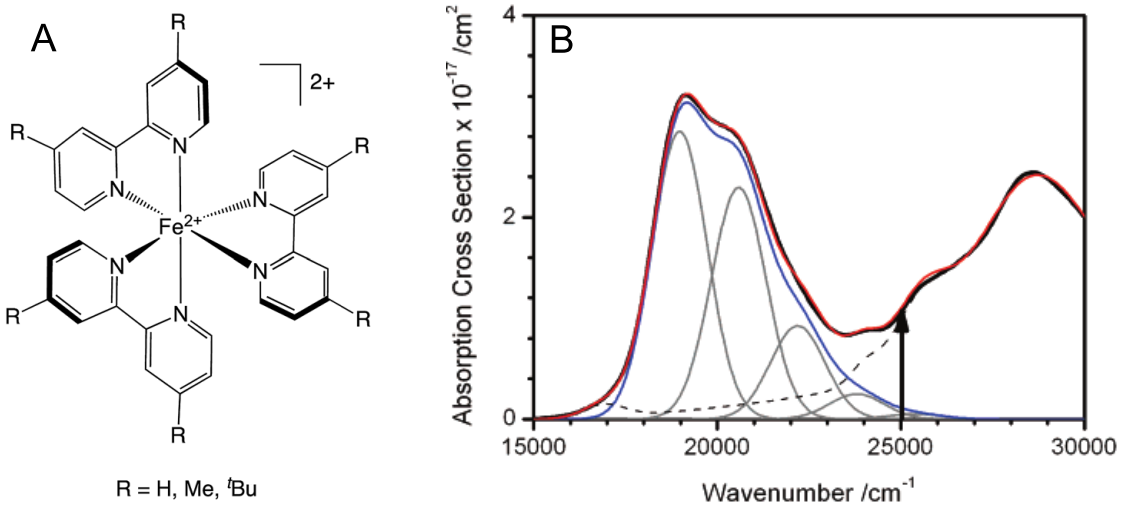

Figure 1.5: ***A*** *Structure of $[Fe(II)(bpy)_3]^{2+}$ (for R = H) taken from Carey et al. [27]. The bpy ligand is a bidentate ligand. The coordination geometry is octahedral.* ***B*** *UV/Vis absorption spectrum (black solid line) of the $[Fe(II)(bpy)_3]^{2+}$ complex in aqueous solution taken from Gawelda et al. [28]. The black, experimental spectrum was fitted by a sum of Gaussian curves (red line). The peak around 20,000 cm^{-1} is assigned as $^1A_1 \rightarrow {}^1$LMCT (LMCT = ligand-to-metal charge transfer) transition. The arrow at 25,000 cm^{-1} marks the excitation energy of the pump in the TA experiments.*

in sub 700 fs into the $^5T_2$ high spin state. This is one of the first examples where it was shown that metal complexes do not follow the photophysical rules for organic molecules. The ISC can be much faster than IVR in transition metals because of the enhanced spin-orbit coupling (SOC) and the higher density of states. The molecular structure and the UV/Vis absorption spectrum of $[Fe(II)(bpy)_3]^{2+}$are shown in Figure 1.5.

In 2000, Monat and McCusker [33] showed for $[Fe(tren(py)_3)]_2^+$ that the ISC is with 80 ± 20 fs even faster in Fe(II) complexes than they previously assumed. In the meanwhile it was also shown in $[Ru(bpy)_3]_2^+$ that ISC can be on the scale of around 100 fs [34]. It was clear at that point that ISC on a sub 100 fs scale is not an exemption, but the rule for transition metal complexes. Later it was actually shown that ISC in $[Ru(bpy)_3]_2^+$ is $\leq$ 20 fs [35]. The final assignment of the SCO time of $[Fe(II)(bpy)_3]^{2+}$ was done in 2015 from Auböck and Chergui [30] and it was assigned as <50 fs. Beside the discussion about the SCO time, the pathway into the high spin state was also not clear for some time. Monat and McCusker [33] interpreted their data as that the ^{1}LMCT directly decays into the $^5T_2$ state. This statement was challenged by Gawelda

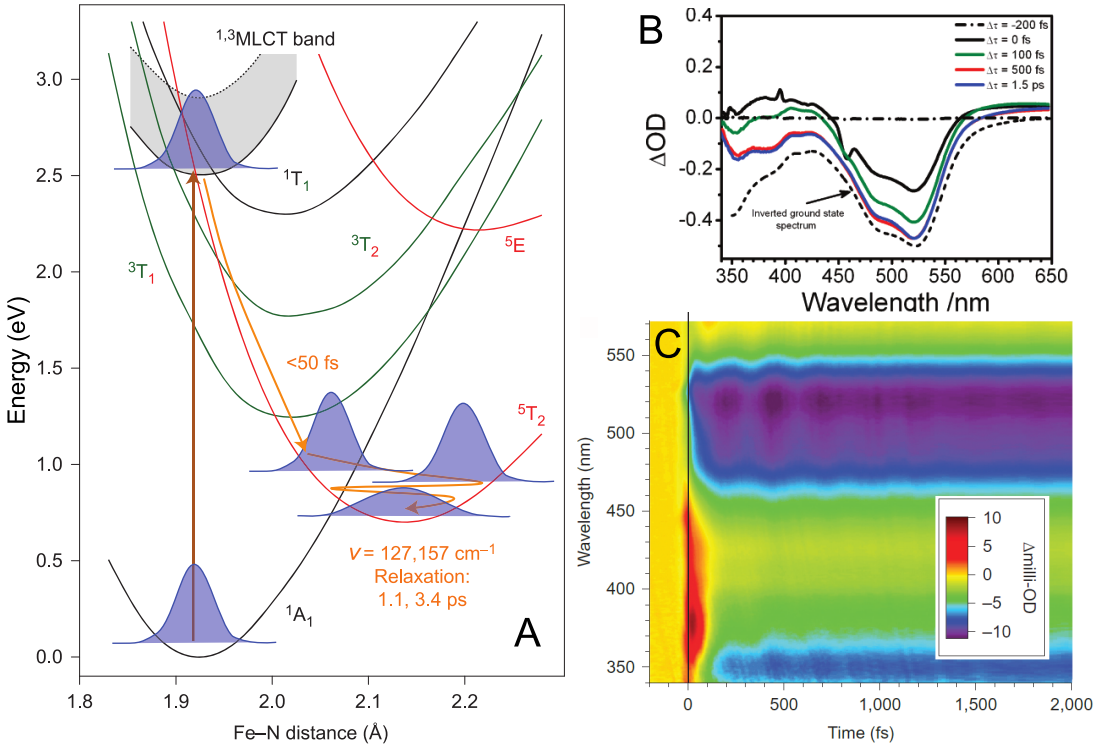

Figure 1.6: ***A*** *Scheme of the photoinduced SCO in* $[Fe(bpy)_3]^{2+}$ *after photoexcitation into the MLCT band. The ISC time from the MLCT manifold to the* $^5T_2$ *state is* < 50 *fs. Two wave packets were found with frequencies of 127 cm* $^{-1}$ *and 157 cm* $^{-1}$*. The frequencies are assigned to non-totally-symmetric Fe-N stretching and bending modes. Additionally, cooling of the molecule on time scales of 1.1 ps and 3.4 ps is observed.* ***B*** *Difference spectra of* $[Fe(II)(bpy)_3]^{2+}$ *(9 mM in water) for selected pump-probe delays up to 1.5 ps. The peak around 400 nm at* $t = 0$ *is scattered pump light. The inverted ground-state spectrum is shown as dashed line.* ***C*** *Visible-range TA results of aqueous* $[Fe(bpy)_3]^{2+}$ *on excitation at 550 nm, recorded with a time resolution of* ≤ 40 *fs.* ***A*** *and* ***C*** *were taken from Auböck and Chergui [30] and* ***B*** *from Gawelda et al. [28].*

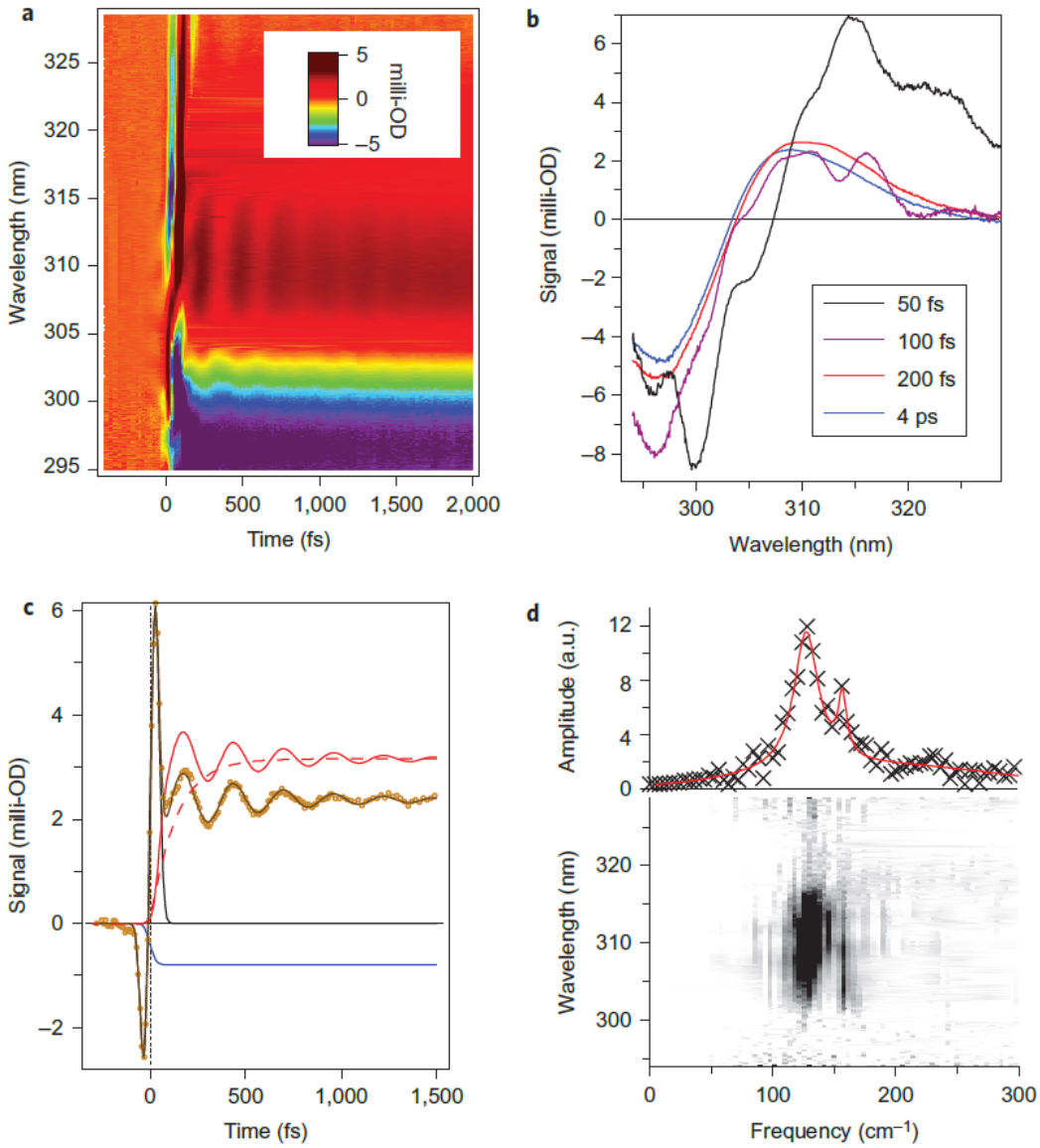

Figure 1.7: *Ultraviolet TA results of aqueous $[Fe(bpy)_3]^{2+}$ on excitation at 580 nm, recorded with a time resolution of ≤60 fs.* ***a*** *Time–wavelength plot of the ultraviolet TA. The ESA from the high spin quintet state dominates between 303 nm and 315 nm, whereas the strong negative signal below 303 nm results from the ground state bleach (GSB) of the intense ligand-centred absorption of $[Fe(bpy)_3]^{2+}$. In the region of the high spin ESA, pronounced coherent oscillations are observed, which are nearly absent in the regions where GSB is dominant.* ***b****, Transient ultraviolet spectra at different time delays after excitation.* ***c****, A typical time trace (brown for 311 nm probe wavelength) with its fit (black) and the decomposition of the latter into ground state bleach (blue), excited state absorption (red) and cross-phase modulation (black) contributions. The red dashed line is the kinetic trace expected for a rise time of 120–130 fs, previously reported [31, 32].* ***d****, Fourier transform of the data shown in* ***a****. The Figure and the caption were taken from Auböck and Chergui [30].*

et al. [28] who found emission of the ^{3}LMCT in fluorescence up-conversion experiments and therefore claimed that a ^{3}LMCT state and further metal centred triplet states had to be included. Bressler et al. [31] used a femtosecond optical pump and x-ray probe technique based on x-ray absorption near-edge structure (XANES) to settle this discussion. The results showed that the ^{3}LMCT is populated via ISC on a 20 fs time scale and the $^5T_2$ high spin state is populated with a 120 fs time-constant. With further development of the time resolution of ultrafast TA in the UV and visible spectral range Auböck and Chergui [30] showed 2015, that ESA of the $^5T_2$ state is already observed at pump-probe delays of around 50 fs. So they concluded that, if there are other metal centred states involved, they would need to be looked at on a < 20 fs time scale. The summarized photophysical cycle is shown in Figure 1.6 **A**. In Figure 1.6 **B** and **C** spectrally resolved ultrafast TA data is shown. Figure 1.6 **B** shows the difference spectra for selected pump-probe delays from Gawelda et al. [28]. For a pump-probe delay of 0 fs, ESA below 450 nm can be seen. This feature was assigned as decay of the LMCT state. This ESA can be also seen in the contour plot in Figure 1.6 **C** where the excitation wavelength was 550 nm. Beside the fast population of the $^5T_2$, also slower dynamics of 1.1 ps and 3.4 ps were found and assigned as vibrational cooling in the $^5T_2$ state.
Beside the fascinatingly fast SCO properties, the $[Fe(bpy)_3]^{2+}$ complex also shows coherent oscillations after photoexcitation. The wave packet is launched because of the population of anti-bonding e_g orbitals in the $^5T_2$ state and the following rapid expansion of the Fe-N bonds. The wave packet can be observed in the contour plot of the ultrafast TA data in Figure 1.7 **a**. This ultrafast TA experiment was performed by Auböck and Chergui [30] using a pump wavelength of 580 nm and a broadband UV probe. Strong oscillations can be observed between 305 nm and 315 nm in the ESA signal. Below 305 nm ground state bleach (GSB) is observed and no oscillations are found. A kinetic trace at 311 nm is plotted in Figure 1.7 **c** as brown circles. The trace was fitted using a model containing three contributions of GSB (blue), ESA (red) and cross phase modulation (XPM). The oscillations were assigned to the excited state, so the ESA part of the fit contains the damped cosine contribution. The red dashed line is a kinetic trace expected for a rise time of 120-130 fs, which was reported earlier on [31, 32]. It is visible that the rise time has to be faster than this, which means that the $^5T_2$ is already populated for very short pump-probe delay times. The Fourier

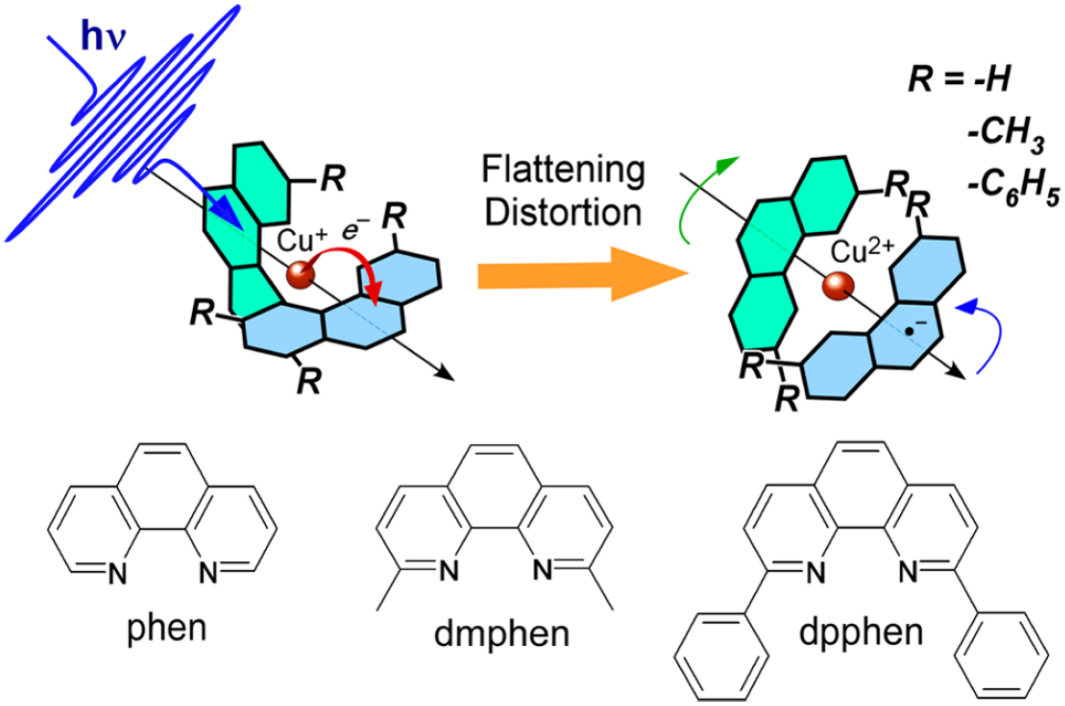

Figure 1.8: *Photoinduced structural change of bis-diimine Cu(I) complexes. The ligands of the three Cu(I) complexes to be discussed are also shown. phen ≡ phenanthroline; dmphen ≡ 2,9-dimethyl-1,10-phenanthroline; dpphen ≡ 2,9-diphenyl-1,10-phenanthroline. The figure and caption were taken from Iwamura et al. [13].*

transform data of the oscillatory part of the dynamics is plotted in Figure 1.7 **d**. Two peaks at 127 and 157 cm $^{-1}$ can be seen, implying that two wave packets are launched. The found frequencies are tentatively assigned as Fe-N bending mode at 127 cm $^{-1}$ and as bending modes at 157 cm $^{-1}$.

This section, covering the initial photophysics of $[Fe(II)(bpy)_3]^{2+}$, shows that the ultrafast TA technique in the UV and visible is a powerful technique for elucidating the dynamics of transition metal complexes. This section also shows the difficulties of interpreting and assigning TA data, even for such a small transition metal complex. This point is further underlined by knowing that 2017 Lemke et al. [36] used fs-XANES and found a SCO time of around 120 fs. The two main points from all the mentioned studies is that ISC can be remarkably fast and that a vibrational wave packet can be launched in the excited state due to electronic changes (in this case ISC) on the metal, followed by impulsive geometrical changes (Fe-N bond lengthening).

1.4 Ultrafast photophysics of Cu(I) complexes

The $[Fe(II)(bpy)_3]^{2+}$ system is one of the most famous metal complexes where vibrational coherences were found. But there are several other transition metal complexes showing vibrational coherences. In this section a group of Cu(I) complexes with 1,10-phenanthroline (phen) based ligands are presented. These complexes are interesting because of their emission from the ^{3}MLCT and ^{1}MLCT state. Depending on the substitution of the phen ligand, high quantum yields are reached for the fluorescence via TADF [37]. TADF is a process where the triplet state is close in energy to the singlet state so that back-ISC takes place by thermal excitation. The TADF process is of great interest for the use in highly emissive OLED devices. More interesting in the scope of this thesis are the vibrational coherences together with a change of dihedral angle between the two phen ligands after photoexcitation into a metal-to-ligand charge transfer (MLCT) state. The intermediate formal Cu(II) is degenerate in an tetrahedral ligand field and the following change of dihedral angle is tentatively assigned as Jahn-Teller (JT) distortion effect [13].

The ultrafast photophysics of a group of $[Cu(phen)_2]^+$ complexes were studied by the group of Tahei Tahara using ultrafast optical spectroscopy. As mentioned earlier these complexes are of interest due to their luminescence. The absorbance and emission spectra of three molecules, $[Cu(phen)_2]^+$, $[Cu(dmphen)_2]^+$ and $[Cu(dpphen)_2]^+$, are plotted in Figure 1.9. The structure of the ligands is shown in Figure 1.8. Figure 1.8 also shows a scheme for the basic idea of the distortion of the ligands after photon absorption. The absorbance spectra in blue show two transitions, $S_0 \rightarrow S_1$ and $S_0 \rightarrow S_2$ in the visible for all three molecules. Both transitions are assigned as MLCT transitions. The intensity ratio between the two transitions is changing depending on how bulky the ligands are. In phen and dmphen the dihedral angle between the ligand planes is 90°. For dpphen this angle gets smaller and so the for phen dipole forbidden $S_0 \rightarrow S_1$ transition becomes allowed for dpphen.

The emission spectra are plotted in orange in Figure 1.9. Again, a big difference between the unsubstituted phen complex and the dmphen and dpphen is visible. The phen complex shows no emission while the other two complexes emit light in the range of 700-800 nm. The emission is assigned as phosphorescence from the lowest ^{3}MLCT

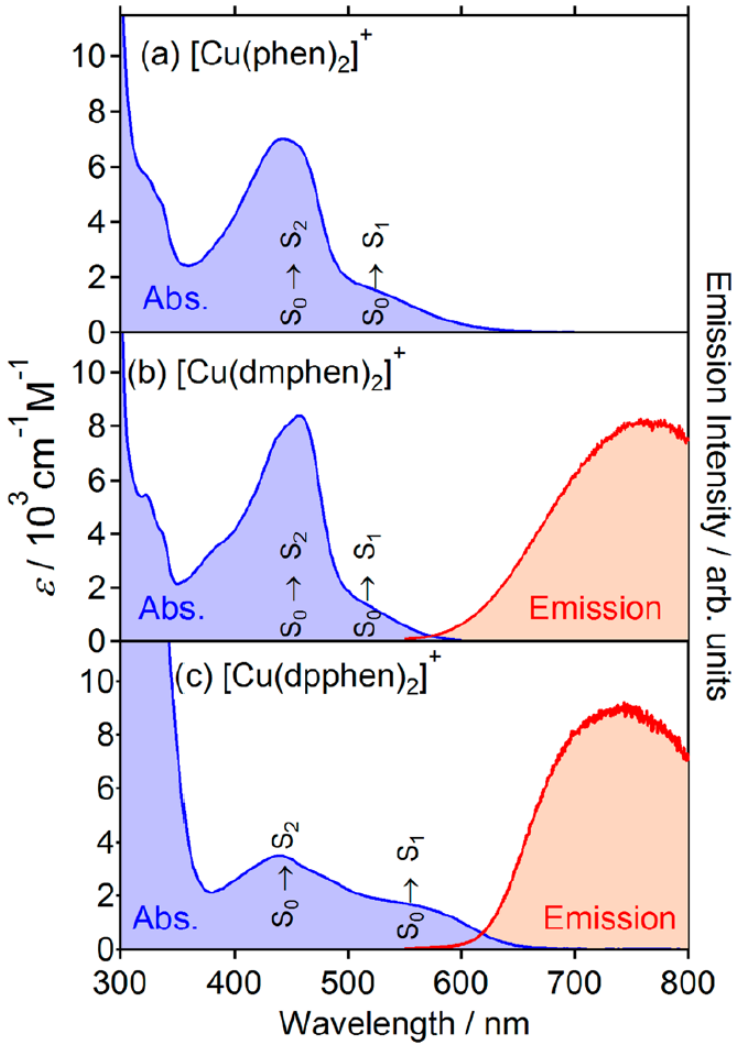

Figure 1.9: ***a-c*** *Steady-state absorption and emission spectra of* $[Cu(phen)_2]^+$, $[Cu(dmphen)_2]^+$ *and* $[Cu(dpphen)_2]^+$ *in dichloromethane. The figure and caption were taken from Iwamura et al. [13].*

state and emission from the lowest ^{1}MLCT state via TADF. The large Stokes shift is explained by a large geometric change in the excited state. The reason for the lack of luminescence for the phen complex also lies in the large geometric change after photoexcitation. The more bulky ligands (dmphen and dpphen) sterically restrict the change, while the phen ligands have no limitation, which makes IC to the ground state the dominating deactivation process [38, 39].

The structural change of the Cu(I) complexes can be explained by JT distortion of the formal Cu(II) in the excited MLCT state. The Cu(II) has nine d-electrons and in the tetrahedral geometry of the ground state, the d-orbital electronic structure on the

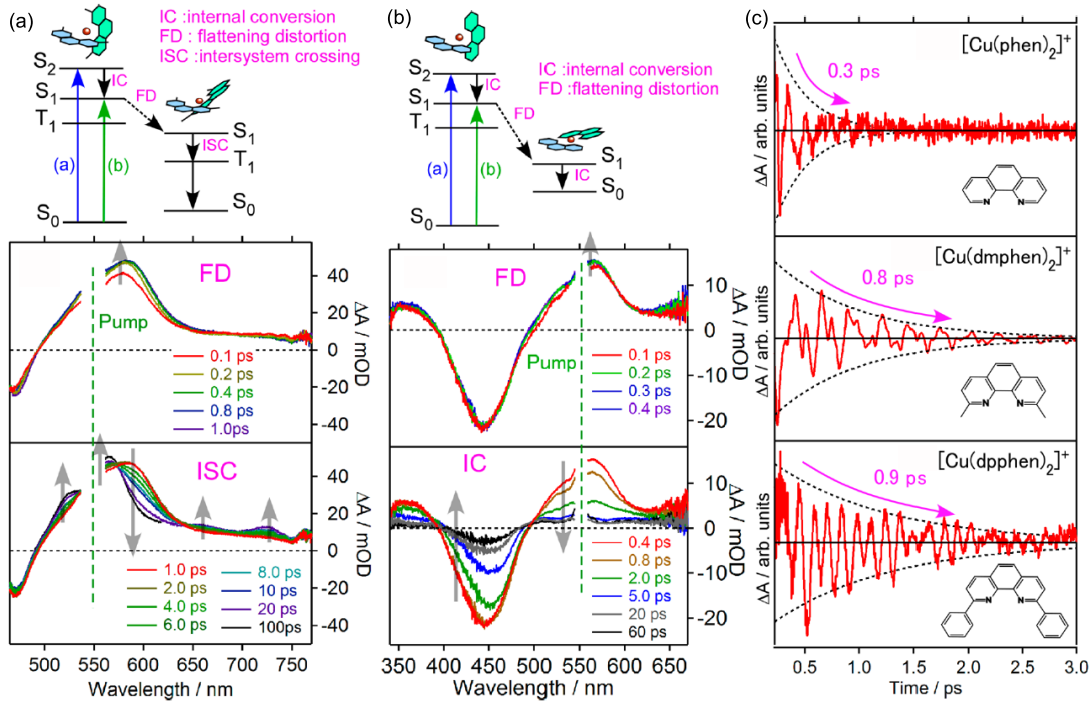

Figure 1.10: *Femtosecond time-resolved TA spectra of $[Cu(dmphen)_2]^+$ (**a**) and $[Cu(phen)_2]^+$ (**b**) measured with 200 fs time resolution in dichloromethane. Excitation wavelength was set to 550 nm. On top of both TA difference spectra are the Jablonski diagrams for each complex. **c** The oscillatory component of the S_1 time-resolved absorption signal of $[Cu(phen)_2]^+$, $[Cu(dmphen)_2]^+$ and $[Cu(dpphen)_2]^+$. The Figures were taken from [12] and [11]*

Cu(II) is degenerate. This leads to JT-distortion which leads to a different d-orbital splitting than in the ground state (Cu(I), d^{10}, tetrahedral) and a geometry close to square planar. This easy explanation is based on the degeneracy of the Cu(II) in a tetrahedral geometry, but the overall electronic state of the molecule in the excited state is non-degenerate. Cunningham et al. [39] used a second-order JT effect (pseudo-JT effect) to explain the flattening of the dihedral angle between the ligands.

Figure 1.10 **a** shows the difference spectra from the ultrafast TA experiments of $[Cu(dmphen)_2]^+$ in dichloromethane [11,12]. The excitation was set to 550 nm, so that the S_1 state is populated. For early time delays the growth of a ESA feature at 580 nm can be seen. The ESA band is assigned as absorption of the S_1 state. The growth of the ESA band is assigned to the structural change of the ligands. This was assigned by fluorescence up-conversion experiments by Iwamura et al. [10], where a fast wavelength shift is observed on the same time scale as the growth. In this case the fluorescence up-conversion technique is more sensitive to structural changes than the TA. For longer

time delays up to 100 ps several changes in the difference spectra can be observed. This is assigned as ISC from the S_1 state of the flattened structure into the T_1 state of the flattened structure. This is also in agreement with the fluorescence up-conversion results from Iwamura et al. [10], where the formation of the phosphorescence is found on the same time scale.

The difference spectra from the ultrafast TA experiments of the $[Cu(phen)_2]^+$ complex are shown in Figure 1.10 **b**. The difference spectra for early time delays show the same feature as for the $[Cu(dmphen)_2]^+$ complex of a growing band at 560 nm. This is also assigned to the structural change of the ligands. While for early pump-probe delays the difference spectra are similar to $[Cu(dmphen)_2]^+$, for longer pump-probe delays the $[Cu(phen)_2]^+$ complex shows different bands and dynamics. After the flattening distortion on the S_1 potential into the new geometry, internal conversion (IC) into the ground state is the dominating decay channel [13]. This explains why there is no phosphorescence in the emission spectrum.

Beside the broadband probe TA experiments on the Cu(I) complexes with a time resolution of 200 fs, the group of Tahei Tahara also performed ultrafast TA experiments using a narrow bandwidth probe in Iwamura et al. [11] and Hua et al. [12]. This has the advantage of a time resolution of around 35 fs. The pump pulse had a pulse duration of 18 fs at a central wavelength of 550 nm and the probe pulse had a pulse duration of 19 fs at a central wavelength of 1000 nm. The main results of the experiments in form of the oscillatory residuals from the kinetic traces are shown in Figure 1.10 **c**. For all three Cu(I) complexes oscillations were found. Partially these oscillations are due to stimulated Raman excitation of the dichloromethane solvent as it is shown in Hua et al. [12]. A Fourier transform spectrum showed several frequencies and most of them belong to the Cu(I) complexes showing the complex reaction pathway towards the flattened geometry [11–13]. The indicated dephasing times in Figure 1.10 **c** of the vibrational wave packets of the three Cu(I) complexes show a strong correlation to the bulkiness of the ligand. The more bulky the ligand is, the longer is the dephasing time. Also are the dephasing times closely related to the time scale of the flattening motion of the according complex. Together with the results from the broadband TA and the fluorescence up-conversion, this shows that the flattened geometry is not instantaneously populated after photoexciation and the perpendicular S_1 state has a

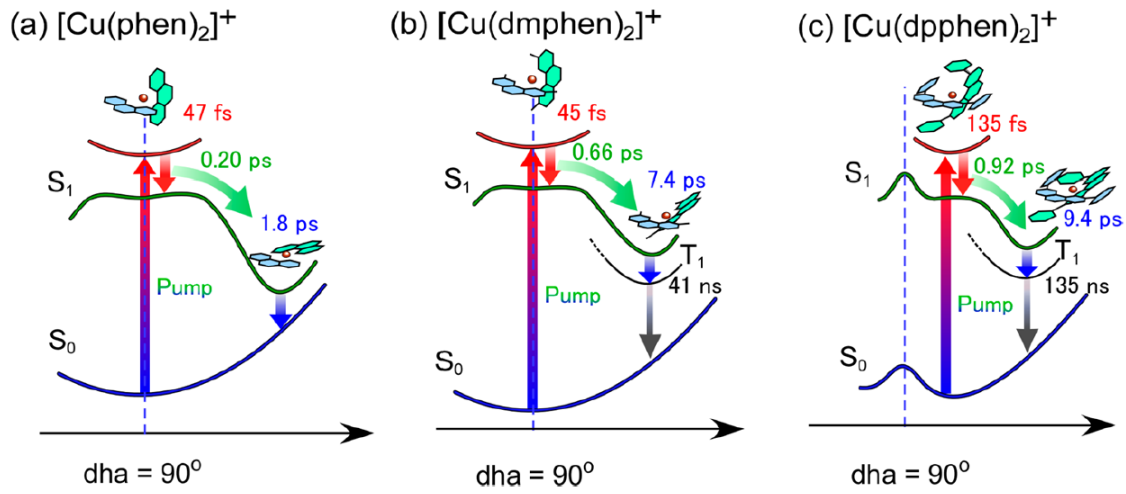

Figure 1.11: ***a-c*** *Schematic potential curves and ultrafast relaxation processes of $[Cu(phen)_2]^+$, $[Cu(dmphen)_2]^+$ and $[Cu(dpphen)_2]^+$ in dichloromethane at room temperature (r.t.). The figure and caption were taken from Iwamura et al. [13].*

finite lifetime.

The summarized results are shown in Figure 1.11. The main results from the optical studies on the Cu(I) complexes are that the properties of the metal complex can be strongly tuned by modifying ligands. These studies are really important in the development of TADF emitters. The wave packet is launched, as for the $[Fe(bpy)_3]^{2+}$, after a change in charge distribution in the metal d-orbitals and the resulting coherent movement of the ligands towards the new potential energy minimum. For the Cu(I) complexes this movement is complex, including several modes. The modes were assigned by Katayama et al. [40] who identified the main reaction coordinates of the $[Cu(dmphen)_2]^+$ wave packet using fs-XANES in combination with theoretical simulations. They wrote that identifying the electronic changes and nuclear motions is playing a key role in an ultrafast chemical reaction [40]. Also the studies show the importance of (pseudo-) JT distortion for the photophysics of transition metal complexes. As for the $[Fe(bpy)_3]^{2+}$ complex, the progress in free electrons lasers (FEL) allows for further insides into the structural and electronic dynamics after photoexcitation.

1.5 Ultrafast photophysics of platinum complexes

Coordination compounds of Pt(II) are of great interest due to their high luminescence quantum yield which is an important factor for the performance as OLED material.

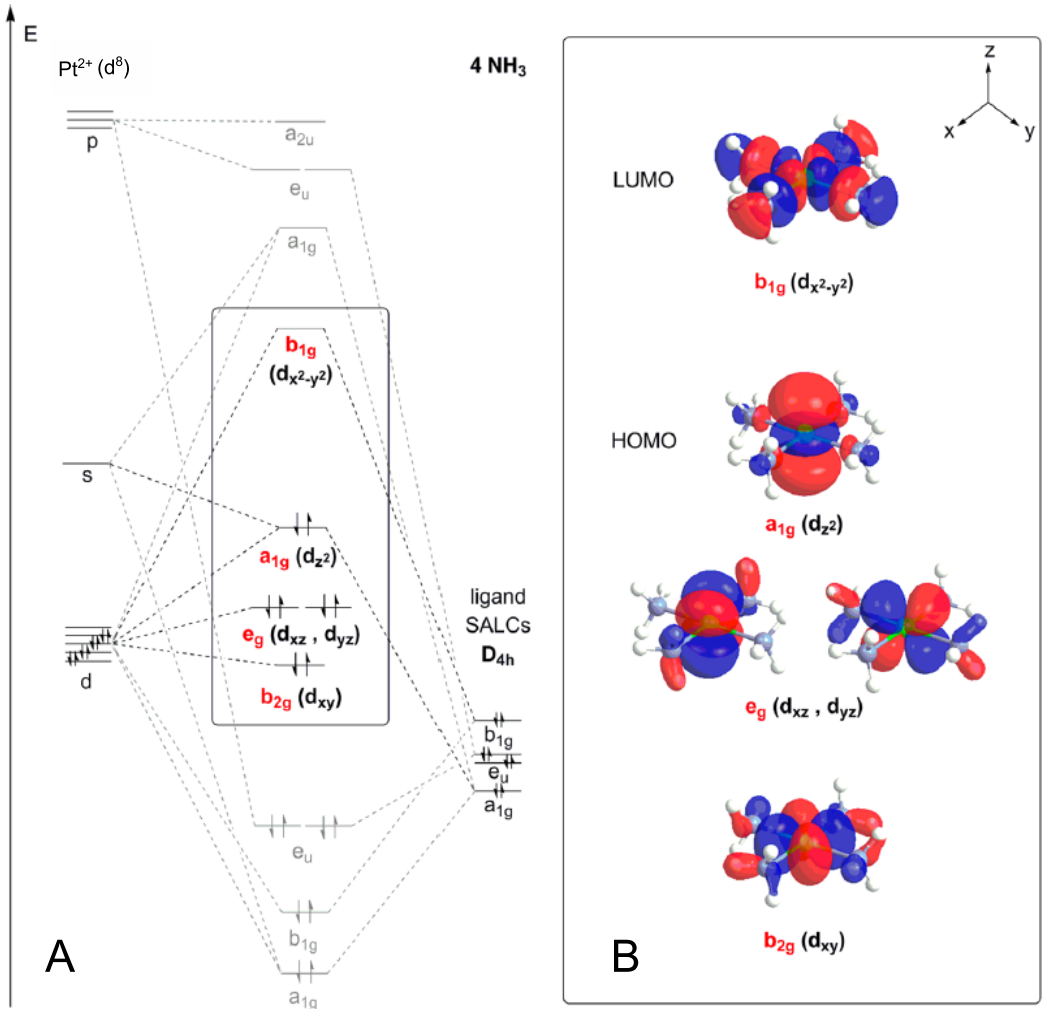

Figure 1.12: *Splitting of the d-orbitals on a Pt(II) ion in an square planar ligand field.* ***A*** *Qualitative molecular orbital diagram for the* d^8 $[Pt(II)(NH_3)_4]^{2+}$ *complex. The molecular orbitals with d-orbital character are highlighted in red. Ligand orbitals are shown as symmetry adapted linear combinations (SALCs) of the point group* D_{4h}*.* ***B*** *Molecular orbitals with d-orbital character. The figure was taken from Boergel et al. [41].*

The high quantum yield of these complexes is based on several properties of the Pt(II) complexes. Pt, as a 5d transition metal, shows a high SOC [42] which is crucial for the phosphorescence efficiency. The square planar geometry makes Pt(II) complexes not as good as emitter as e.g. octahedral Ir(III) complexes. This is related to the splitting of the d-orbitals, where for square planar complexes the splitting between the lower lying four d-orbitals is large in comparison to the three t_{2g} orbitals of an octahedral coordination. The small splitting of the t_{2g} orbitals allows for a larger SOC between the lowest ^{3}MLCT and the ^{1}MLCT as well as other ^{3}MLCT states and therefore results in a faster inter-system crossing (ISC) and a fast and efficient phosphorescence [43]. Since Pt(II) complexes are generally square planar geometry, the d-orbital splitting of the four lowest orbitals and therefore the luminescence properties strongly depend on the ligands. The d-orbital splitting of the Pt(II) (d^8) is shown in Figure 1.12.
The square planar coordination geometry is also responsible for the tendency of Pt(II) complexes to form aggregates (e.g. dimers) via stacking. This can either lead to quenching of the luminescence [43] or it can be used to develop emission wavelength tunable Pt complexes [44] by utilizing bridging ligands to form di-platinum complexes with variable Pt-Pt distance. These di-platinum complexes show a Pt-Pt interaction which is antibonding in the ground state. Photoexcitation from the $^1A_{1g}$ (d_{z^2} like orbital) ground state into the $^1A_{2u}$ (p_z like orbital) excited state leads to a shortening of the Pt-Pt bond due to the bonding interaction formed by the two p_z like orbitals on the two Pt ions. Also a lengthening of the Pt-ligand bonds is observed, which is also explained by the Pt-Pt bond formation [45].

One of these di-platinum complexes was studied with ultrafast transient absoprtion and fluorescence up-conversion spectroscopy by van der Veen et al. [47]. The Pt complex is the $[Pt^{2+}(P_2O_5H_2)_4]^{4-}$ or Pt(POP) complex which is a well studied di-platinum complex [46], where four pyrophosphito ligands coordinate the two Pt(II) ions, so that each of them has a square planar coordination. The chemical structure is shown in Figure 1.13 **B**. The absorption spectrum is shown in Figure 1.13 **A** where a prominent peak at 370 nm is visible. This peak is assigned as $^1A_{1g}$ (d_{z^2} like orbital)to $^1A_{2u}$ (p_z like orbital) transition. The lower lying $^3A_{2u}$ state, as it is shown in Figure 1.13 **B**, is populated via ISC. The resulting phosphorescence from this state back to the ground state is seen in the emission spectrum in Figure 1.13 **A**, where the peak at around

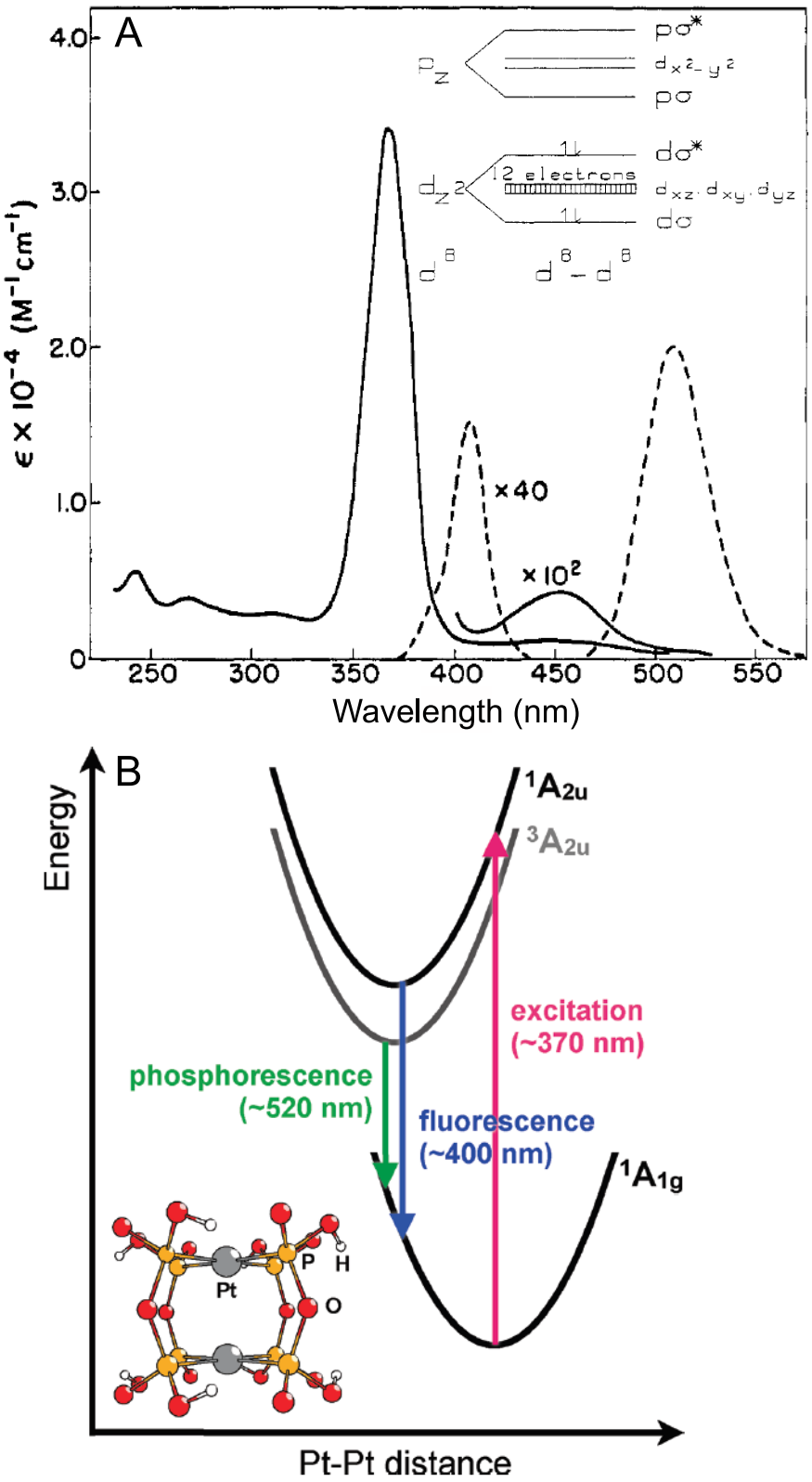

Figure 1.13: ***A*** *Absorbance (solid line) and emission spectra (dotted line) for the* $[Pt^{2-}(P_2O_5H_2)_4]^{4-}$ *complex in aqueous solution at r.t.. Simplified picture for the splitting of the orbitals for an interaction of two square planar* d^8 *systems along the metal-metal axis. The Figures were taken from M. Roundhill, H. Gray and C.-H. Che [46].* ***B*** *Simplified energy scheme for the absorbance and emission of the* $[Pt^{2-}(P_2O_5H_2)_4]^{4-}$ *complex. Chemical structure of the complex is shown in the lower left corner. The Figure was taken from van der Veen et al. [47]*

520 nm is assigned to this transition. The emission peak at around 410 nm is assigned as fluorescence. The absorption peak at 450 nm is assigned as direct excitation of the triplet state. The energy scheme in Figure 1.13 **B** indicates that the Pt-Pt bond distance shortens in the excited singlet and triplet state.

Fluorescence up-conversion spectroscopy showed that the $^1A_{1g}$ decays with at least two decay components which were determined around 1.5 ps and 15 ps for an aqueous solution at r.t. [47]. Beside the exponential decay also oscillations were found superimposed on the TA signal. The oscillation period was determined as 224 ± 1 fs (or 149 cm^{-1}) [47] which is in good agreement with the Pt-Pt stretch vibration in the excited $^1A_{1u}$ state [48, 49]. Ultrafast TA spectroscopy in the UV and visible of the Pt(POP) in solution was also performed by van der Veen et al. [47].

This measurement showed two ESA features after 370 nm excitation. One ESA band at 320 nm to 350 nm and the second one at 430 nm to 490 nm. GSB is observed around the excitation wavelength and stimulated emission (SE) is observed in good agreement with the observed fluorescence at around 400 nm. A contour plot of the TA data of Pt(POP) is shown in Figure 1.14 **A**. The dip in the GSB signal is due to pump scatter. The inset shows the data up to a maximum pump-probe delay of 10 ps. The oscillations are clearly visible up to almost 10 ps. Also visible is the initial blue shift of the SE within the first 2 ps after excitation. The blue shift is explained by vibrational cooling in the $^1A_{1u}$ state. Figure 1.14 **B** shows two difference spectra at 11 ps and 100 ps with the described features of ESA, GSB and SE. The SE band clearly decayed after 100 ps. Figure 1.14 **C** shows three kinetic traces at 340 nm, 410 nm and 460 nm. The kinetic traces at 340 nm and 460 nm belong to ESA and both show a fast change in the first 5 ps, followed by slower kinetic component. The 410 nm trace belongs to the SE band and shows stronger modulations than the ESA traces. Panel **D** of Figure 1.14 shows more kinetic traces and their fits up to a pump-probe delay of 5 ps. A global fit using a sum of exponential decay functions plus an exponentially damped cosine function was used to fit the TA data. To determine the decay constants, a singular value decomposition and a global exponential fit of the kinetic amplitude vectors was used, and for water three exponential decay components were extracted. The values found for the TA data of Pt(POP) in water are $\tau_1 = 210 \pm 40$ fs, $\tau_2 = 1.31 \pm 0.04$ ps and $\tau_3 = 13.7 \pm 0.2$ ps. The first and second decay constants are

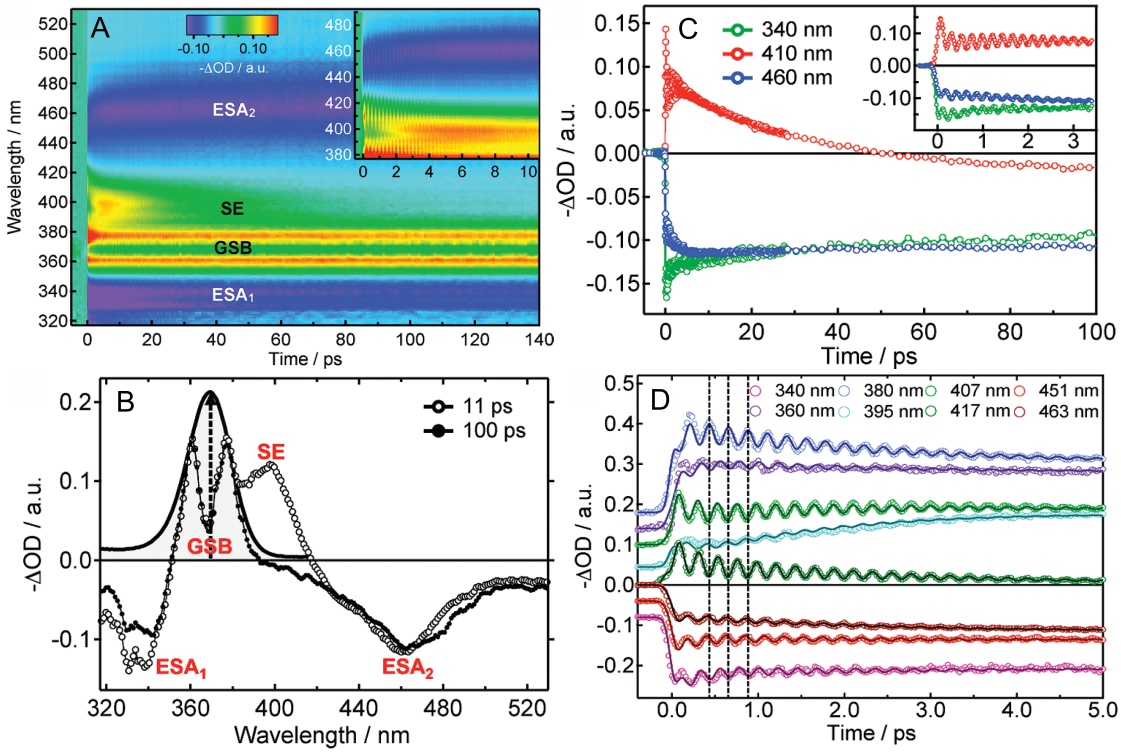

Figure 1.14: ***A*** *Contour plot of the TA data for the Pt(POP) dissolved in ethylene glycol. A 100 fs laser pulse at 370 nm was used for excitation. The probe pulse was a white light pulse, produced by focusing the 800 nm fundamental laser beam into a* CaF_2 *crystal. The pump-probe delay is plotted on the x-axis while the wavelength is plotted on the y-axis. The colour code represents the absorbance change.* ***B*** *Representative transient spectra showing the absorbance change at 11 ps and 100 ps. The solid line spectrum shows the ground state absorption.* ***C*** *Kinetic traces for 340 nm, 410 nm and 460 nm. The inset shows the kinetic traces up to a pump-probe delay of 3.5 ps.* ***D*** *Kinetic traces and fits up to a pump-probe delay of 5 ps showing the phase shift of* π *between the high energy and low energy side of the stimulated emission band. The Figures were taken from van der Veen et. al. [47]*

assigned as vibrational cooling in the $^1A_{1u}$ state, where $\tau_1 = 210 \pm 40$ fs is labelled as impulsive process [47]. The ISC to the $^3A_{1u}$ state is assigned to the slowest, third time constant. The kinetic amplitude vectors containing the oscillatory part were fitted with a sum of two exponentially damped cosine functions. The resulting oscillation periods found are $T_1 = 224 \pm 0.1$ fs and $T_2 = 281 \pm 1$ fs, with T_1 fitting excellent to the period found in the ultrafast fluorescence up-conversion experiment of 224 fs. As mentioned earlier, van der Veen et al. [47] assigned this period to the Pt-Pt stretch vibration in the excited state. The longer period is assigned to a wave packet in the ground state which is excited by a Raman process.

The vertical lines in Figure 1.14 **D** show that there is a phase shift of around π between the red and blue side of the SE which is typical for a wave packet between classic turning points of the potential [47].

The ESA bands were assigned by van der Veen et al. as transitions from the singlet and triplet A_{2u} states to the $^1A_{1g}$ state (ESA at 335 nm) and to the singlet and triplet E_g states (ESA around 460 nm). The interpretation of the ISC time as the slowest time constant is counter-intuitive, but van der Veen et al. [47] give three reasons for their assignment. First is the large energy gap of more than 5000 cm^{-1} between the singlet and triplet A_{1u} states and there isolated position to other higher lying states. Second, the two potential curves of singlet and triplet states are parallel which leads to a small Frank-Condon overlap between the ν_0 vibrational ground state of the $^1A_{1u}$ potential with the resonant vibrational levels of the $^3A_{1u}$ potential. Third, the SOC is symmetry forbidden for the singlet and triplet A_{1u} states.

The lifetime of the vibrational wave packet of the Pt(POP) with a exponential dephasing time constant of 2 ps is remarkable in relation to the time constants of the vibrational cooling [47]. The $^1A_{1u}$ potential is described by van der Veen et al. [47] as exceptional harmonic. This is due to their results of different excitation energies which have no or very limited effect on the period of the wave packet. The slow dephasing is explained by the cage like structure of the complex, just leaving the free coordination sites on the two Pt ions for solvent interaction. Also is the Pt-Pt stretch vibration the lowest energy vibrational mode and therefore no IVR was found.

1.6 Aims

The scientific studies reported in this thesis have four main aims. The first aim is to build an ultrafast broadband UV/Vis TA experiment. This is shown in chapter 2, together with results from two well studied samples to show the performance of the new set-up.

The second aim is to study the ultrafast photophysics of exchange coupled manganese SMMs in respect to possible dynamics of the strong axial JT distortion. The observation of dynamics in the JT distortion directly relates to the magnetic anisotropy of the SMMs. Metal complexes could also provide a microscopic model of these processes because molecules can be studied using a high level of quantum chemistry, as it is shown in chapter 3.

The third aim is to explore the delocalization of electronic states via a μ_3-oxo bridge in a highly correlated tri-nuclear iron complex. Ultrafast TA spectroscopy together with high level quantum mechanical calculations is shown in chapter 4.

The fourth aim is to study the ultrafast photophysics and the luminescence properties of a terbium SMM. Lanthanide SMMs are known for their high blocking temperatures and the magnetic properties are well studied. Here, ultrafast TA, luminescence and static UV/Vis absorption are used to investigate the photocycle after excitation.

Chapter 2

Methods

This chapter gives insight into the experimental methods that were used to measure the data in the following chapters. The first part in this chapter deals with the ultrafast TA set-up to measure absorbance as a function of time after photoexcitation. The second part describes the set-up for measuring Faraday rotation (FR) and Faraday ellipticity (FE). The third section in this chapter describes the commercial UV/VIS/NIR absorption and Fourier Transform Infrared (FTIR) spectrometers as well as the Raman microscope. After the description of the experimental set-up three well studied samples are measured to ensure the functionality and accuracy of the constructed apparatus. These measurements are an ultrafast TA experiment in pure ethanol using two different pump wavelengths, an ultrafast TA experiment of a laser dye and a ultrafast TA experiment of the $Fe(bpy)_3^{2+}$.

2.1 Ultrafast UV/Vis transient absorption setup

This section shows the ultrafast TA set-up with all major parts. The main parts are the Ti:sapphire femtosecond laser, a commercial NOPA (TOPAS from Light Conversion), a translation stage for the white-light generation station, a second harmonic generation (SHG) part and two prism spectrometers. The main aim of performing ultrafast TA experiments is to measure the dynamics after photoexciation and absorbance bands of the excited state(s).

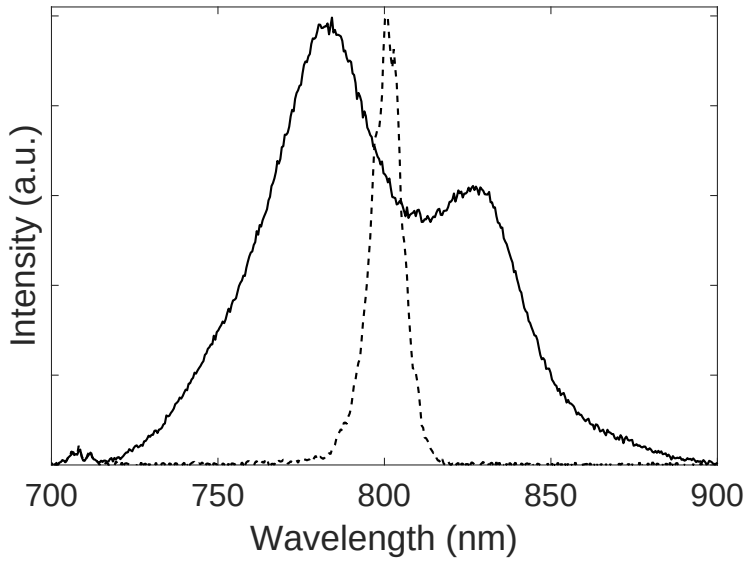

Figure 2.1: *Spectra for the laser output of the mode-locked Mantis oscillator (continuous line) and the Legend amplifier (dashed line). The Legend amplifier spectrum is centred at 800.8 nm and has a full width at half maximum (FWHM) of 11 nm (173 cm^{-1}). The Mantis spectrum is centred around 800 nm and has roughly a FWHM of 80 nm (1253 cm^{-1}).*

2.1.1 Ti:sapphire femtosecond laser

The Ti:sapphire femtosecond laser is a commercial Coherent Legend elite system producing 120 fs laser pulses at a repetition rate of 1 kHz and a power of around 3.5 mJ per pulse. The laser system consists of two major parts. An oscillator (Coherent Mantis) and an amplifier. The amplifier uses chirped pulse amplification (CPA) where the oscillator laser pulses are used as seed.

2.1.1.1 Mantis Oscillator

The Mantis oscillator is pumped by a continuous wave (cw), optically pumped semiconductor laser at 532 nm with 5 W output power. The active laser medium is Ti:sapphire. The Mantis laser can operate in a cw and a pulsed mode which is called mode-locked. The mode-locking is achieved by rapidly changing the cavity length, which induces strong intensity fluctuations. These fluctuations form a Kerr lens in the active medium. A Kerr lens focuses the more intense modes more effective than weaker modes. The intense modes overlap better with well focused pump beam and experience a more

efficient amplification. This process totally discriminates the weaker modes. This produces laser pulses with around 20 fs at a repetition rate of 80 MHz. The broad mode-locked spectrum is shown in Figure 2.1 with a full width at half maximum (FWHM) of around 80 nm. The centre of the spectrum is around 800 nm.

2.1.1.2 Legend elite regenerative amplifier

The Legend elite amplifier is pumped by a frequency doubled Nd:YLF laser (Coherent Evolution, Nd = Neodymium, YLF = Yttrium-Lithium fluoride) at 527 nm with a pump power of around 17 W and a repetition rate of 1 KHz. The amplifier is based on a method called chirped pulse amplification (CPA) [50]. CPA is a method where a fs seed pulse is stretched in time, gets amplified and is finally compressed again. This method is necessary since a direct amplification of a fs laser pulse produces too high pulse intensities in the resonator which would damage the optics. The method is an elegant way to get high intensity fs laser pulses. The active medium in the amplifier is a Ti:Sapphire crystal which is cooled via a thermo-electric element to -10 °C to avoid damage by the high intensity pump beam. The seed pulse is introduced into the cavity by a Pockels cell. Each time the seed passes through the active medium it gets amplified. This will go on until a maximum gain is reached and the pulse is coupled out of the cavity by a second Pockels cell. For the laser in our lab describe here, roughly 11 round trips are needed in the amplification process. After that the laser pulse will pass through the compressor. The pulses after the compressor are 120 fs long at a central wavelength of around 801 nm and have a energy of around 3.5 mJ. The power per pulse is around 2.92 GW. The spectrum of the Legend output can be found in Figure 2.1.

2.2 The TOPAS light conversion unit

The TOPAS light conversion unit is a commercial NOPA which is used to produce 30-50 fs laser pulses in the range of 490 nm to 1000 nm (Figure 2.2). Due to the wavelength tunability, the TOPAS is an excellent tool for spectroscopy of molecules with narrow absorption bands in relation to solid state materials like e.g. metals and semi-conductors. Here the practical application in the TOPAS light conversion unit is introduced.

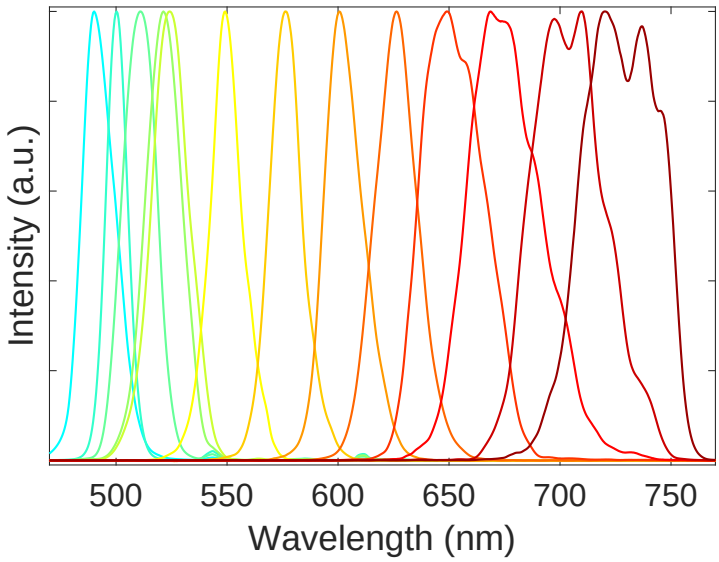

Figure 2.2: *Spectra for the laser output for several wavelengths of the commercial non-collinear parametric amplifier (NOPA) (TOPAS from Light Conversion).*

The TOPAS is pumped by about 0.8 mJ of the Legend output. The 800 nm fundamental is split into two parts as it enters the TOPAS. The major part ($> 99\%$) is frequency doubled to 400 nm while a small part is focused in a sapphire disk to produce a white light continuum which is later used as seed for the first amplification stage. The white light beam is collimated and passed through a beam shaper. The 400 nm pump beam passes through a beam splitter, to get separate pump beams for the first (about 20 %) and second (about 80%) amplification stage. After the beam shaper, the white light seed gets focused into a β-barium borate (BBO) crystal where it is spatially and temporally overlapped with the first 400 nm pump pulse. The wavelength which should be amplified has to be selected by changing the temporal overlap, due to the chirp of the white light seed and with the crystal angle in relation to the beam propagation direction, due to the phase matching condition. The phase matching condition together with the law of conservation of energy determines that one 400 nm photon is split in two, so that the energy of both photons is equal to the pump photon. The two beams are called signal and idler. The signal beam is used for further amplification here and the idler is stopped by a beam dump. The amplified beam gets collimated and again focused into the same BBO crystal, where it is overlapped (spatially and temporally) with the second pump pulse. Again the wavelength which should be amplified has to be selected

by changing the temporal overlap, due to the chirp of the fist stage amplified pulse. To satisfy the phase matching condition of the 1st and 2nd amplification, the two beams have to be parallel. Both pump beams get blocked by a beam dump. The now amplified pulse is collimated and compressed in time by two fused silica wedges. The laser pulse before the compressor has a negative chirp. Fused silica wedges introduce positive chirp so that the beam is compressed when exiting the TOPAS. The path length through the prisms can be adjusted to achieve optimum compression.

2.3 Laser pulse duration measured by autocorrelation

To measure the pulse duration on the scale of around 120 fs a commercial autocorrelator (APE Pulsecheck) is used. The 800 nm output of the Legend elite were measured with a FWHM autocorrelation of 169 $\pm$ 10 fs which gives a pulse duration of around 120 fs. The TOPAS output at 535 nm was measured with 50 $\pm$ 5 fs FWHM autocorrelation which is equal to a pulse duration of 35 fs.

2.4 Broadband UV/Vis ultrafast transient absorption setup

In this section the ultrafast TA set-up (see Figure 2.3) is shown and the technical solutions are discussed. For the broad band ultrafast transient absorption spectroscopy, a pump and a probe beam is needed. In the set-up, the pump beam can be either the fundamental 800 nm, the SHG at 400 nm,the TOPAS output (490 nm to 1000 nm) or the SHG of the TOPAS output. A CaF_2 white light is used as probe light (315 nm to 720 nm). For the detection of the probe light a home build prism spectrometer is used. In the following paragraphs these parts of the set-up and the overall optical layout are described.

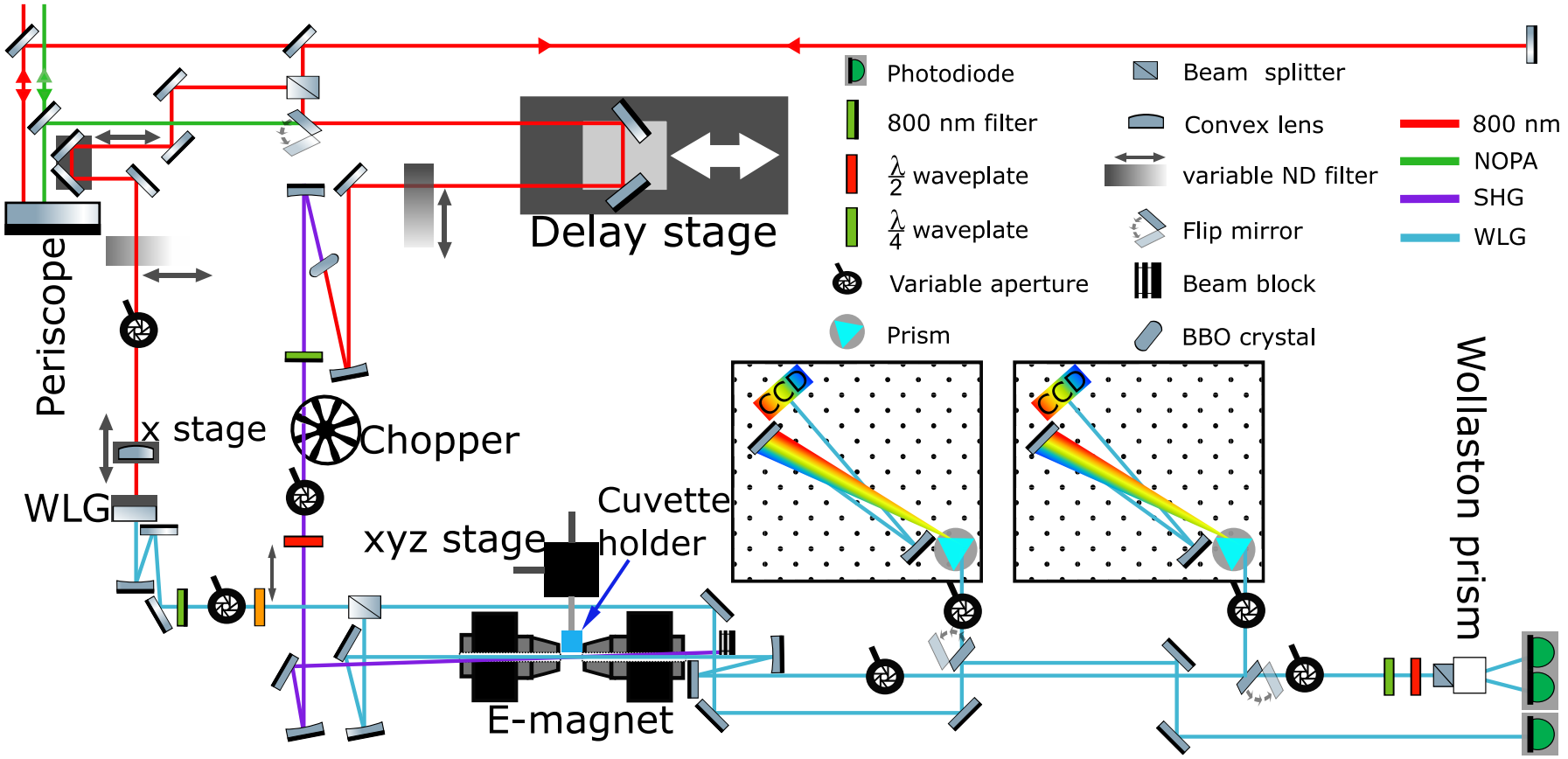

Figure 2.3: *Optical setup scheme. The legend is in the figure. The main parts are labelled in the figure. In the upper left corner the 800 nm and TOPAS beam arrive at the laser table from the neighbouring table.*

In Figure 2.3 the schematic of the optical layout is shown. The set-up itself is located on a Melles-Griot laser table. The Coherent Legend elite laser as well as the TOPAS (Light conversion) are located on a separate laser table. Both beams are directed onto the TA set-up table and brought to the right hight by a periscope. The 800 nm beam is horizontally polarized in relation to the laser table surface while entering the periscope and horizontally polarized while leaving. This is due to the parallelity of incoming and outgoing beam. The TOPAS beam is vertically polarized.
First the beam path in case of a usage of the TOPAS beam as pump laser pulse is described. The 800 nm beam therefore needs to go along a delay part to arrive at the same time as the TOPAS pump pulse at the sample. The 800 nm beam is split in two parts at the first beam splitter. Around 10 % is being reflected for the white light generation part. The beam is passing a small delay stage which can be moved if small temporal pump-probe overlap adjustments are needed. Before focusing the beam into a CaF_2 disk the laser power can be adjusted by a variable ND filter.

White light continuum in CaF_2

For the white light generation around 1.37 ± 0.1 nJ of the 800 nm laser output are focussed with a 10 cm focal length fused silica lens into a 5 mm thick, 25 mm diameter CaF_2 disk from Layertec. The disk is moved in two dimensions perpendicular to the laser direction to avoid laser induced damage. A DC electric motor is used to move the stage via a rubber o-ring. The applied voltage is 5 V which moves the stage with a frequency of around 1 Hz. The stage was designed and built by the group of Prof. Dr. Eberhard Riedle at the Ludwig-Maximilians-University (LMU) in Munich. The spectrum should span from 280 nm to around 1500 nm. Due to a 310-700 nm high transmission (795 nm to 835 nm high reflectance) mirror (Eksma Optics) to stop the 800 nm fundamental light, the NIR part and wavelengths below 310 nm can not be used for experiments. The spectrum of the white light measured by a commercial Ocean Optics 2000+ spectrometer is shown in Figure 2.5. The interference pattern in the spectrum originates from the filter/mirror. The spectrum also shows the residue of the 800 nm fundamental and parts of the NIR which is mostly cut out by the dielectric mirror. The spectrum of the white light continuum on the home build spectrometers can be seen in panel **A** in Figure 2.6. The standard deviation over 100 spectra is plotted in

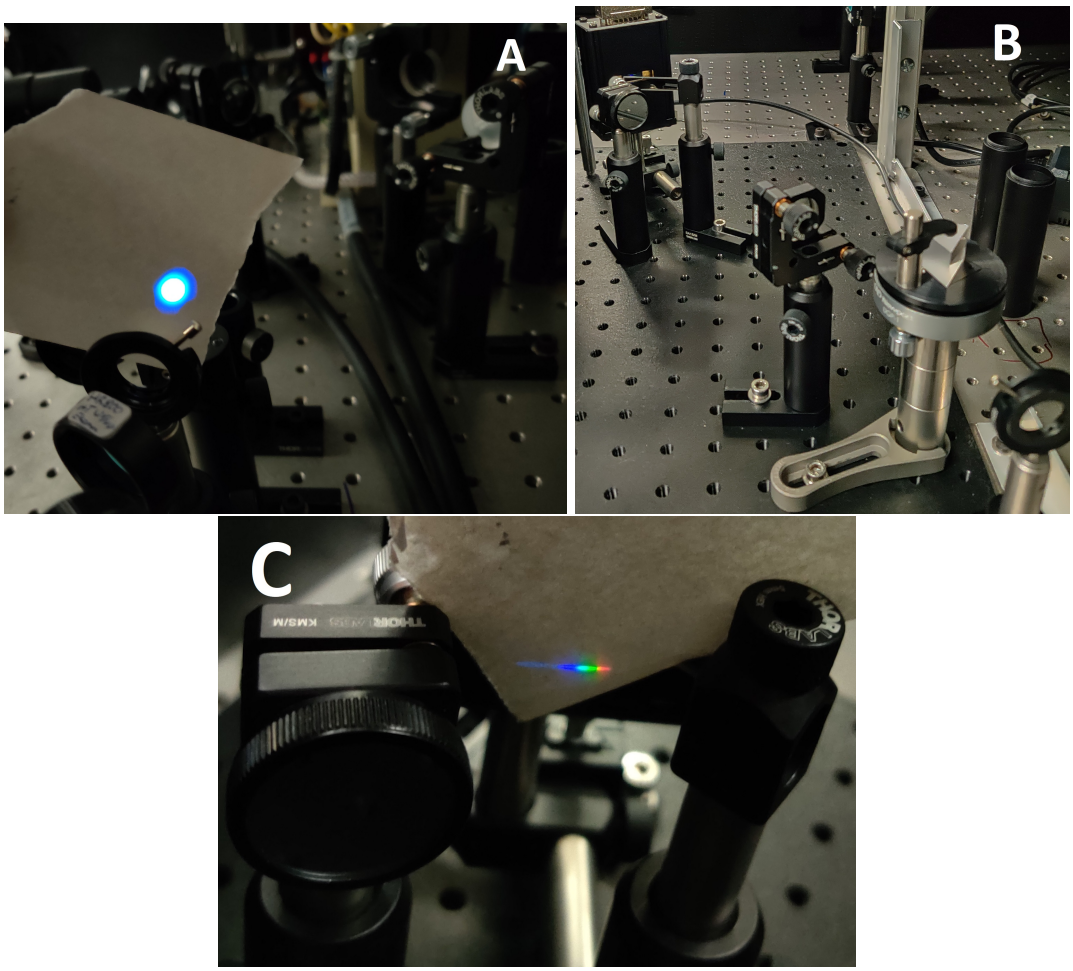

Figure 2.4: ***A*** *Picture of the white light beam shortly after the 800 nm high reflective mirror.* ***B*** *Picture of the spectrometer. Showing the aperture, the prism, one flat mirror, one concave mirror and the CCD camera* ***C*** *Picture of the dispersed white light beam in front of the CCD camera.*

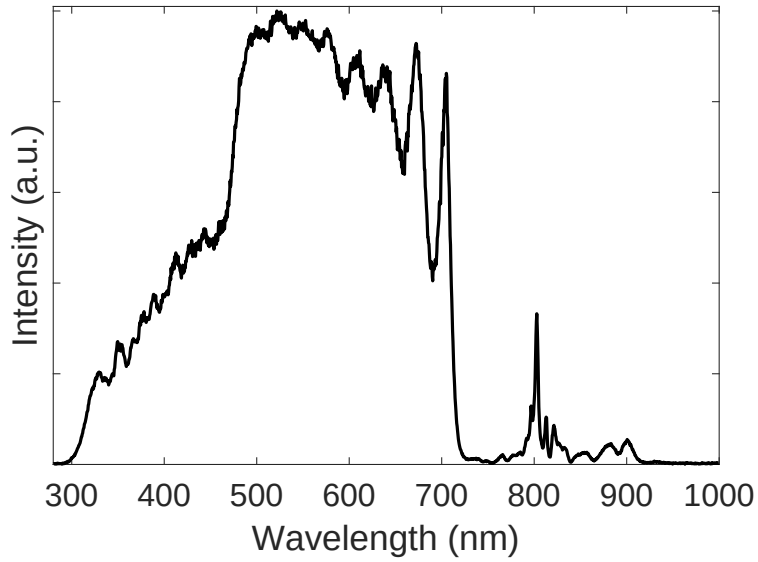

Figure 2.5: *Spectrum of the white light after passing the 310-700 nm high transmission (795 nm to 835 nm high reflectance) mirror from Eksma Optics. The interference pattern also originates from the mirror. The spectrum was measured with a commercial Ocean Optics 2000+ spectrometer.*

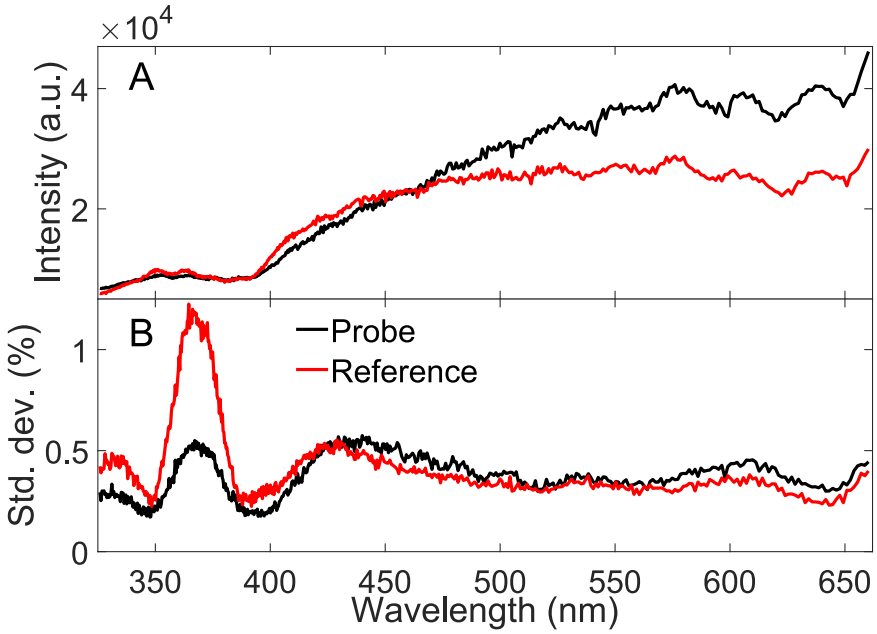

Figure 2.6: ***A*** *White light spectrum (average over 100 spectra) on the home build spectrometer.* ***B*** *Standard deviation of the white light spectrum is shown.*

panel **B**. The standard deviation for most of the spectrum is below 0.5 %. The spectra of the white light using the ocean optics spectrometer in Figure 2.5 looks different to the spectrum in Figure 2.6 since there are several reflections and different ND filters in use. Also the CCD chips in the Ocean optics and the home build spectrometers surely have a different sensitivity.

The white light is collimated by a 10 cm focal length concave mirror and the 800 nm non-converted fundamental beam is largely reflected of the 310-700 nm high transmission (795 nm to 835 nm high reflectance) mirror. In Figure 2.4 **A** the white light beam on a paper card is shown. After the 800 nm part is removed from the white light, it is split in two parts by a metallic reflective ND filter (1 OD / from Newport). Around 85 % is reflected of the metallic surface and used as the probe beam. The approximately 10 % which are transmitted are used as a reference beam and pass by the sample, directly into the left of the two spectrometers in Figure 2.3. The probe beam is getting focused into the sample by a 50 cm focal length concave mirror. After it passed through the sample, the probe beam is collimated again by another 50 cm focal length concave mirror and is then transferred into the second spectrometer.

Prism based spectrometer

Two prism based spectrometers were built to detect the white light. As a model system the spectrometers from Prof. Dr. Eberhard Riedle's group were chosen [51]. The optical geometry is equal for probe and reference spectrometers. After the light enters the spectrometer, which is built on an optical breadboard, a UV fused silica Brewster angle prism (Eksma Optics) disperses the white light. A one inch aluminium mirror reflects the light towards a 25 cm focal length concave aluminium mirror (both from Eksma Optics) which focuses the dispersed beam on a line scan camera system CCD 2000 with a 512x56 pixel Hamamatsu S7030 CCD chip (from Entwicklungsbüro G. Stresing in Berlin). The spectrometer is shown in Figure 2.4 **B**. In Figure 2.4 **C** the dispersed white light continuum is shown directly in front of the CCD camera. The different dispersion of the red and blue part of the spectrum can be seen clearly.
The vertical pixels are summed up which is called binning. This improves the signal to

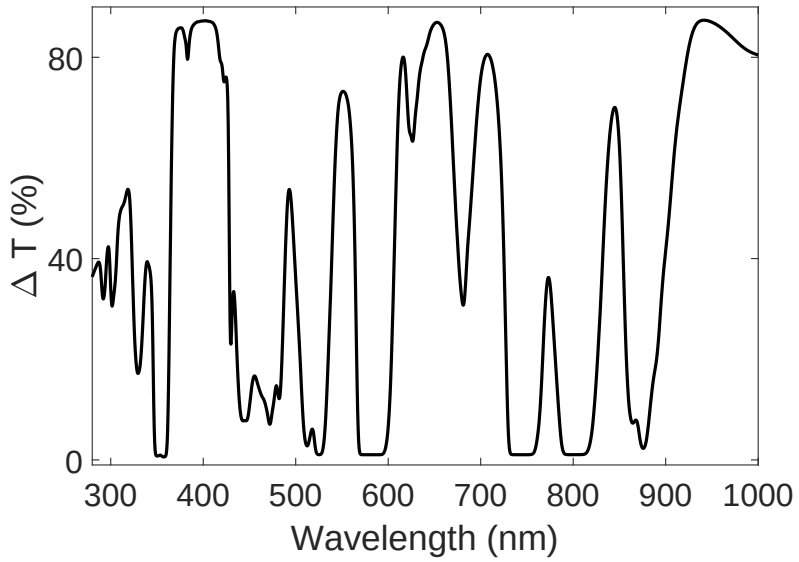

Figure 2.7: *Spectrum of the BG36 multiband filter from Schott glass. The spectrum was measured with a commercial UV/Vis/NIR spectrometer.*

noise since due to spherical aberration the beam shape is vertical elongated to form an elliptical beam shape. A variable continuous metallic ND filter in front of the camera is used to attenuate the light. The least attenuating part of the ND filter is used for the UV and blue part of the spectrum. This has the advantage of adjusting the intensities of the spectrum in a way that they are more equal across all wavelengths. The camera read-out speed is equal to the Legend laser repetition rate of one kHz, which allows to have a shot-to-shot statistic.

The pump beam in this version of the ultrafast transient absorption experiment is the output of the above described TOPAS. After the periscope the TOPAS beam passes through a broadband hollow retroreflector (Newport UBBR2.5-1S) mounted on a motorized delay stage (Newport M-ILS100BPP). The delay stage can be controlled by a computer and has a maximum travel range of 100 mm and a minimum step size of 1 μm. Therefore a maximum time delay between pump and probe laser pulse of around 666 ps can be used. After the delay stage the laser power can be adjusted by a variable ND filter. The polarization direction of the TOPAS is vertical in relation to the laser

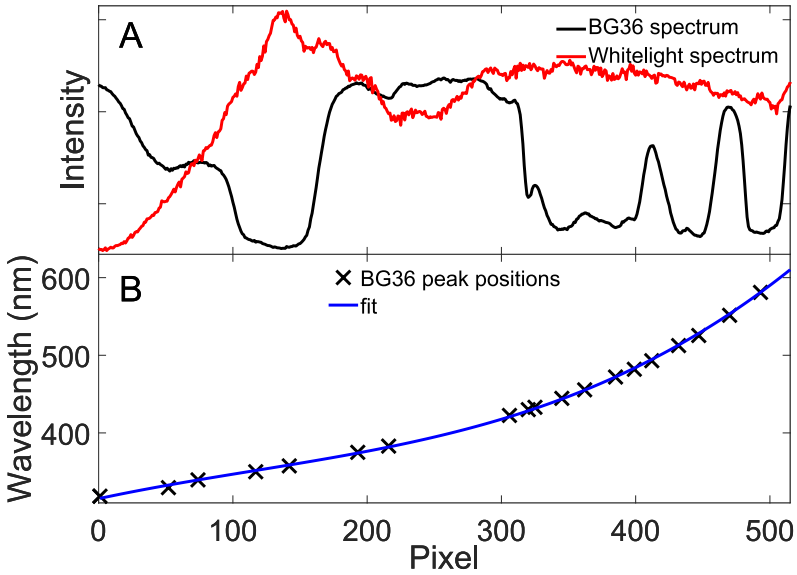

Figure 2.8: ***A*** *Spectrum of the white light continuum and the BG36 multiband filter from Schott glass plotted as a function of pixel.* ***B*** *Peak positions of the BG36 filter taken from Figure 2.7 as a function of pixel (black ×). A third order polynomial fit is used to fit the peak positions in order to assign each pixel a wavelength.*

table plane. A $\lambda/2$ waveplate can be used to adjust the polarization angle. An optical chopper (Thorlabs MC2000B-EC) is used to reduce the repetition rate of the pump to half of the Legend laser repetition rate (1 KHz). The TOPAS pump beam is focused into the sample by a 50 cm focal length concave mirror. The sample is positioned behind the focus of the pump beam so that the pump beam diameter is larger then the probe beam diameter. The TOPAS pump beam has a small angle in relation to the probe beam which allows to block it after the sample.

Another possible source for the pump pulse is the SHG of the 800 nm fundamental. Therefore the flip mirror behind the first beam splitter has to be flipped up, the BBO crystal has to be put into the post holder and a filter to block the residual 800 nm light has to be put into the post holder as well. The tilting angle of the BBO crystal has to be optimized by checking the SHG efficiency by monitoring the power using a power meter.

2.4.1 Calibration of the spectrometers

For calibrating the cameras a Schott BG36 filter with several absorption bands in the UV, visible and NIR region is used. The absorption spectrum of the BG36 filter is

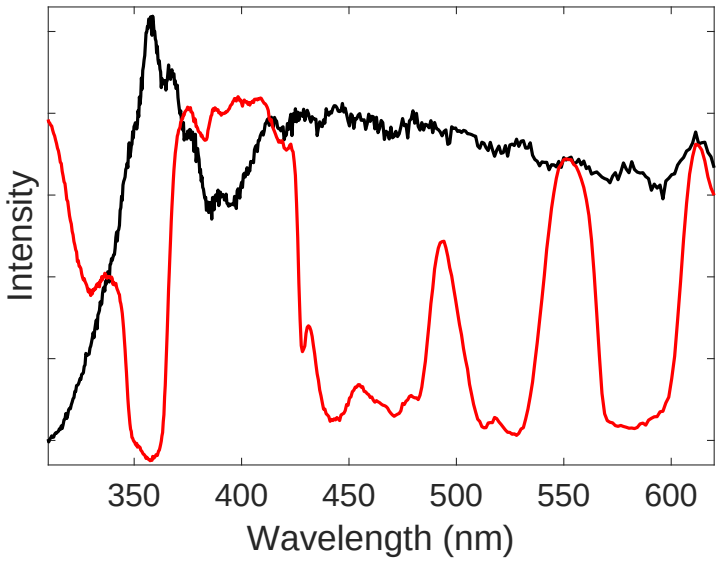

Figure 2.9: *Spectrum of the white light continuum and the BG36 multiband filter from Schott glass plotted as a function of wavelength.*

plotted in Figure 2.7. Figure 2.8 illustrates the fitting procedure. In Figure 2.8 **A** the spectrum of the white light continuum is plotted together with the spectrum of the BG36 filter as a function of pixel. Due to dispersion, the part of the spectrum at small pixel numbers, which represents the UV and blue part of the spectrum is stretched in relation to the red part of the spectrum at large pixel numbers. When the peak positions in wavelength are now plotted as a function of pixel, as it is in Panel **B**, a third order polynomial fit can be used to assign to each pixel a wavelength value. The resulting spectrum is plotted in Figure 2.9 where the same spectra are plotted as in panel **A** of Figure 2.8 but now as a function of wavelength.

2.4.2 Beam diameter of probe and pump pulses / Energy per area

The beam diameter were measured with a CMOS camera (Basler acA1920-25um). This camera has the advantage of a small pixel size of 2.2 $\times$ 2.2 μm. This allows to get a smooth beam profile. The procedure for measuring the beam profile in the sample plane is the following. The spatial pump-probe overlap is optimized by monitoring the TA signal of a known sample (e.g. a laser dye in methanol). After the optimization a mirror is inserted in front of the electromagnet which reflects the pump and probe

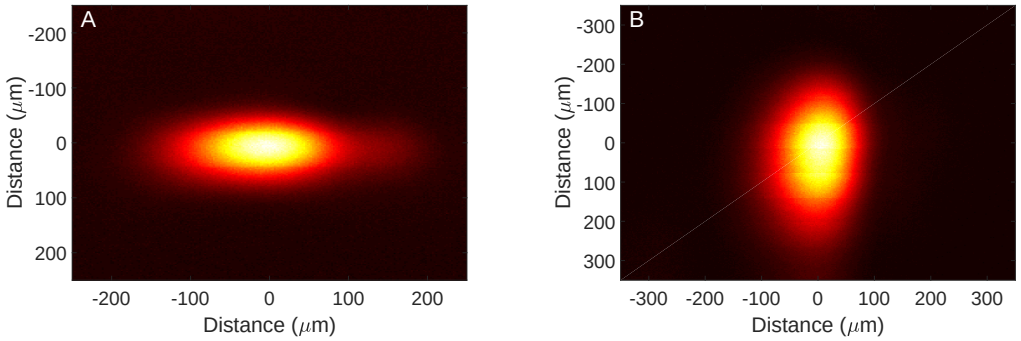

Figure 2.10: *Beam profiles of the 400 nm SHG beam (**A**) and the 535 nm TOPAS beam (**B**) in the sample plane, measured with a CMOS camera (Basler acA1920-25um). Assuming a Gaussian beam profile, the $1/e^2$ beam diameter for the 400 nm beam (**A**) is 163 ± 4 microns, while for the 535 nm TOPAS beam the $1/e^2$ beam diameter is 332 ± 9 microns.*

beam onto the camera. The live camera mode was then used to find the maximum overlap of pump and probe beam, which is assumed as the sample plane. The camera is therefore moved along the beam propagation axis in order to find the focal plane. No further adjustments on mirrors are made. ND filter with an optical density of at least three have to be inserted before the camera is exposed to the laser beam.

The live camera mode is also effective for optimizing the focus conditions of the probe beam by using the linear stage of the collimation mirror. Since the focal diameter is wavelength dependent, a bandpass filter can be inserted in the white light beam to purely look at the focus of a small wavelength range. With the linear stage of the collimation mirror the focus can then be adjusted.

For determining the laser fluence of the pump pulse the area of the beam focus has to be determined. A good approximation of the beam intensity profile is a Gaussian shaped intensity profile. In this thesis the $1/e^2$ diameter of the intensity is used to calculate the area. The fluence is then calculated by dividing the measured pump power by the $1/e^2$ area. In Figure 2.10 two example beam profiles for the 400 nm SHG pump in panel **A** and for the 535 nm TOPAS pump in panel **B** are shown. The $1/e^2$ diameters are calculated by a MatLab program which uses perpendicular cuts through the maximum intensity. The cuts are fitted by a Gaussian curve and the $1/e^2$ values are determined. Since the beam profiles are not always round, an approximation has to be made at this point. The $1/e^2$ values for the two cuts are averaged to calculate the area.

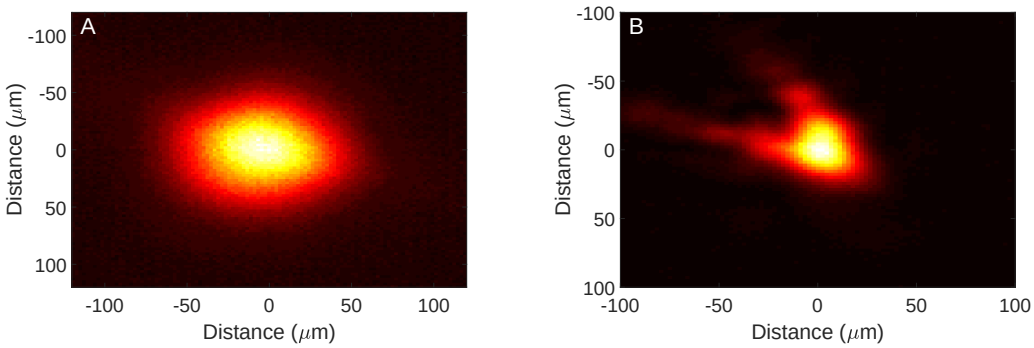

Figure 2.11: *Beam profiles of the white light continuum beam (**A**) and the 355 nm part of the white light continuum beam (**B**) in the sample plane, measured with a CMOS camera (Basler acA1920-25um). The $1/e^2$ beam diameter for the white light continuum (**A**) is 121 microns, while for the 355 nm part the $1/e^2$ beam diameter is 63 microns. The discrepancy arises due to optimization of the focussing conditions for the UV part.*

For the beam profile of the 400 nm SHG pump a $1/e^2$ diameter of 163 $\pm$ 4 micron and a $1/e^2$ area of $2.1 \pm 0.1 \times 10^{-4}$ cm^2 was found. For the beam profile of the 535 nm TOPAS pump a $1/e^2$ diameter of 332 $\pm$ 9 micron and a $1/e^2$ area of $8.7 \pm 0.5 \times 10^{-4}$ cm^2 was found.

The beam profile in the sample plane of the white light continuum is shown in Figure 2.11 panel **A**. The beam $1/e^2$ diameter is with 121 micron around 26 % smaller then the 400 nm SHG pump beam. This is advantageous for the signal to noise because just the excited sample volume is probed which should give the maximum absorbance change signal. In panel **B** of Figure 2.11 the beam profile of the white light continuum with inserted 355 nm (FWHM=10 nm) bandpass filter (Thorlabs FL355-10) is shown. First observation is that the beam shape is less round then the beam profile of the whole white light continuum. The second observation is that the beam diameter is with 63 microns smaller then the beam profile of the whole white light continuum. Due to the chromatic aberration it is not possible to collimate the whole white light spectrum equally well. The quality of the collimation of the UV light is given priority above the rest of the spectrum since the intensity is low and the losses of the UV part along the pathway into the spectrometers are higher then for the visible part of the spectrum.

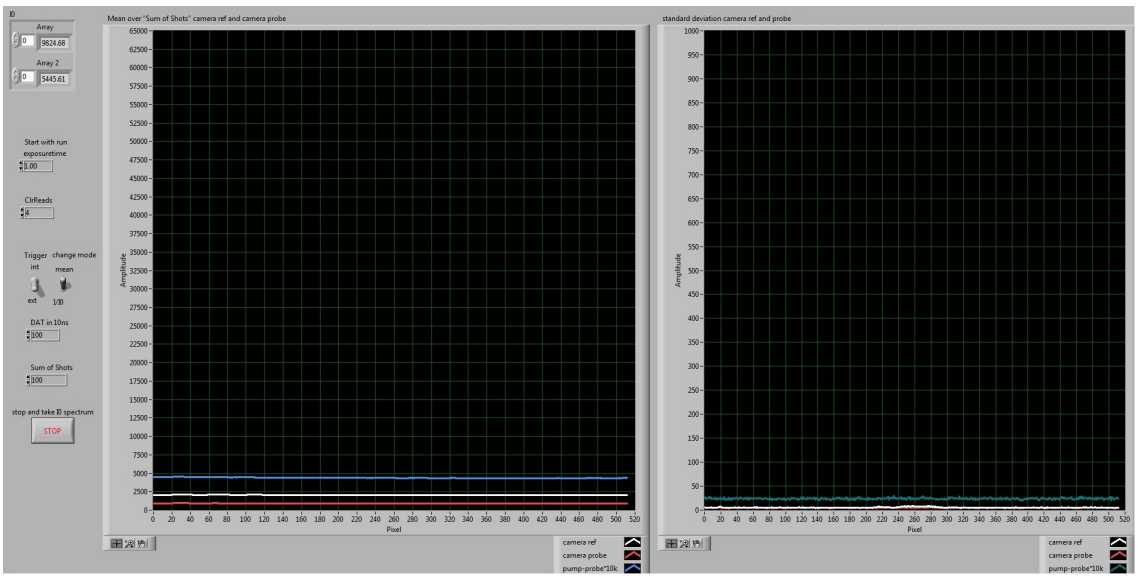

Figure 2.12: *LabView program which plots the spectrum on the spectrometers against the pixel number, which is shown in the left panel of the program. The right panel shows the standard deviation over 100 spectra.*

2.5 LabView programs

LabView (Laboratory Virtual Instrument Engineering Workbench / National Instruments)is a program which uses a visual programming language. Mostly all lab equipment can be controlled via LabView which makes writing a program and running an experiment easier then using other programming languages (e.g. C,C++, Python). Labview programs were written for running a TA experiment. Therefore the spectrometers, the delay stage and the chopper need to be controlled and/or data has to be read. Before starting a TA experiment three programs will help to set up the experiment. One program (whitelightstability(ffm)) measures the spectral intensity and plots it against the pixel number of the CCD cameras in the spectrometers. The GUI is shown in Figure 2.12. The left window shows the intensity plotted against the pixel number and the right window shows the standard deviation. A second program is used for calibration. It is an half automated way to calibrate the spectrometers according to the procedure described in section 2.4.1. It is still necessary to assign the peaks of the BG36 glass filter spectrum by hand, but the program will then fit the calibration curve (see Figure 2.8) and save a file which can be used by other programs. A third program (Livespectrum) uses the calibration file and plots the spectrum intensity against the

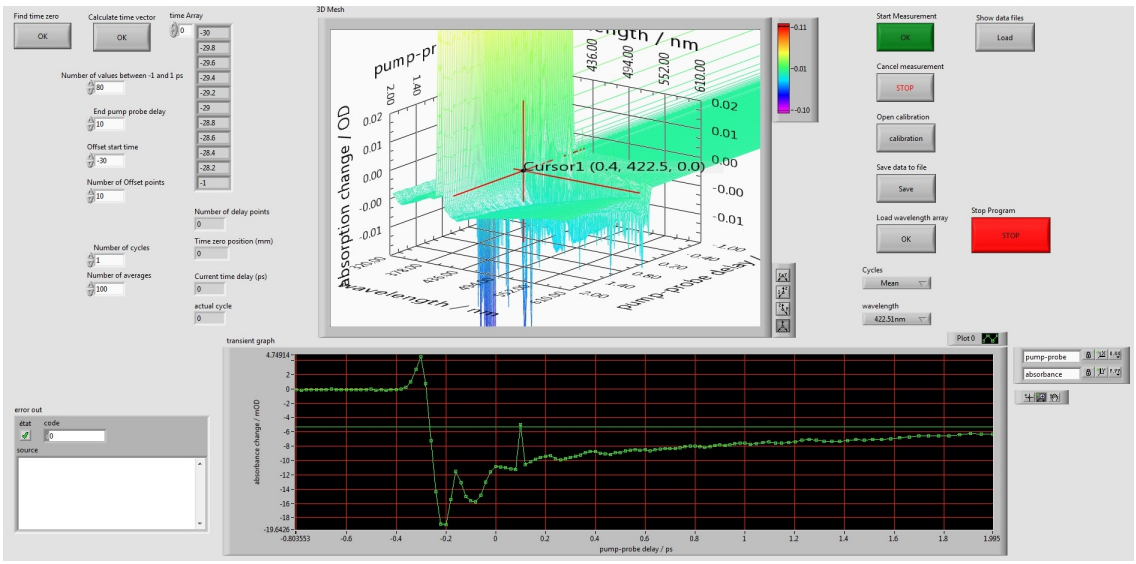

Figure 2.13: *LabView program for measuring TA experiments. The lower graph plots the kinetic traces for a specific wavelength. The upper 3D plot shows the total data set. The wavelength and pump-probe delay is plotted against the absorbance change.*

wavelength. By inserting the BG36 filter and compare the peak positions with the actual spectrum, this program is useful to check if the calibration is correct. This program also can be used to measure a static UV/Vis absorption spectrum by utilizing the white light continuum as broad band light source. The TA program (PumpProbeMeasurement) GUI, shown in Figure 2.13, has several functions. In the upper left corner are the "Find time zero" and the "Calculate time vector" buttons. The "Find time zero" button opens a program which shows the TA signal plotted against pixel number. The pump-probe delay can be set in the sub-program so it can be used to find the temporal and spatial overlap of pump and probe pulse in the sample. The "Calculate time vector" button produces an array with pump-probe delay positions according to the user input. There are several input fields below the "Calculate time vector" button. The upper four are for producing the delay time array. The delay times are calculated with a formalism from Megerle et al. [52]. First the number of steps between -1 ps and +1 ps have to be set. E.g. 100 steps between -1 ps and 1 ps means a step size of 20 fs. Second the maximum pump-probe delay has to be chosen. Here the number in ps can not be larger then the length of the delay stage. This also depends on the temporal overlap of pump and probe pulse. The maximum possible pump-probe delay can be found using the "Find time zero" program. The third and forth input panel are to set

the start time for the offset and the number of offset points. The offset here means the probe pulse arrives at the sample earlier then the pump pulse. This is defined as negative pump-probe delay and it allows to remove signals which are purely based on scattered light. The program calculates pump-probe delay steps from -1 ps up to the maximum delay with an linearly increasing step size on the base of:

$$\Delta t(i) = \begin{cases} -1 + \frac{2i}{N} & \text{for} \quad i = 0...N-1 \\ 10^{-1+i/N} & \text{for} \quad i = N...M \end{cases}$$

With N being the number of steps between -1 ps and 1 ps. M is given by the maximum delay Δt_{max} with $M = N(1 + log\Delta t_{max})$. This procedure for the delay array avoids huge amounts of unnecessary data. There are two input panels to set the number of repetitive TA measurements and the number of averaged spectra for one time delay, which are positioned right under the time delay input panels. To the right of the input panels are some output panels giving several information. The two middle windows show the plotted data. In the lower window the absorbance change (for a specific wavelength) is plotted against the pump-probe delay. The upper window shows the whole data set as 3D plot. On the right side of the GUI (Figure 2.13) are several buttons to control the program. The "Save data to file " button saves the measured data as text files. It also saves the wavelength and delay array as separate files. The " Show data files" button loads an old data set and shows it in the two middle graphs. The "wavelength" menu can be used to show a kinetic trace for a specific wavelength in the loaded data set.

2.6 Faraday rotation and Faraday ellipticity spectroscopy

In this section the experimental instrumentation for the Faraday rotation (FR) and Faraday ellipticity (FE) spectroscopy is explained. There are two types of experiments which can be performed on the set-up. First a static FR or FE measurement can be performed using a continuous wave (cw) laser diode or a helium-neon laser. The second experiment is a time resolved FR or FE measurement using the fs laser.

The commercial electromagnet (GMW 3470) is set to a pole-to-pole distance of around 26 mm, which allows to place the head of the commercial cryostat (Oxford Microstat

HE2 Rectangular Tail) in the centre between the poles. The poles have holes with a diameter of 10 mm to allow both pump and probe beam to pass throught the electromagnet. The diameter of the holes are limited by the geometry of the pump and probe beam, since the probe beam passes through the electromagnet perpendicular to the pole surface and the pump beam at an small angle. The magnetic field strength was determined by using a calibrated Hall sensor (HGCA-3020). The highest field at 6 A is equal to 450 mT. This current can be just applied for around one minute due to heating of the coils. The maximum constant current which is feasible is 5 A or 375 mT. The cryostat used for cryogenic temperature measurements has optical windows which allows to do optical experiments and is small enough to fit into the electromagnet. The windows itself show static FR and FE which is shown in Figure 2.23. The cryostat can be cooled to cryogenic temperatures by using either liquid helium or liquid nitrogen. With liquid helium the temperature range is < 4 K to 500 K. With liquid nitrogen, 77 K is the lowest stable temperature.

2.6.1 Ultrafast magneto-optical measurements

For the ultrafast FR and FE pump-probe measurement, the CaF_2 white light continuum is used as probe and the 400 nm SHG is used a pump. Bandpass filters after the sample are used for probing at different wavelengths. Another change in the set-up is the extra wire grid polarizer (Thorlabs WP25M-VIS) after the 800 nm high reflective mirror (see Figure 2.3) in the white light continuum beam path. The polarizer is set so that horizontally polarized light is passing through. For the detection of FR and FE signals a $\lambda/2$ wave plate (Thorlabs AHWP05M-600), a $\lambda/4$ wave plate (Thorlabs AQWP05M-600) and a Wollaston prism (Thorlabs WP10) were used to analyse the light and the result is detected by a balanced photodiode (Thorlabs PDB210A). The signal output of the photodiodes is fed into a lock-in amplifier (Zurich Instruments MFLI) which is connected to the lab computer.

The Wollaston prism splits incoming unpolarized light into two orthogonal polarized beams. For linear polarized light the splitting ratio depends on the angle of the light polarization to the crystal axis. For a polarization angle of 45 deg in relation to the prisms vertical axis the splitting ratio is 50:50. For any deviation of the angle the splitting ratio will change.

For the FR rotation experiment just the $\lambda/2$ wave plate is used. The angle of linear polarized light rotates when passing through a magnetized medium. For the experiment, this means that the balanced photodiodes are balanced by rotating the $\lambda/2$ wave plate without external magnetic field. With applied field the polarization angle will change and therefore the splitting ratio and a FR signal is observed. The conversion from the measured voltage signal of the balanced photo diodes to rotation angle is performed according to

$$\Theta = \frac{\Delta V}{2V} rad = \frac{\Delta V}{V} \times 14.25°. \tag{2.1}$$

Where ΔV is the measured lock-in amplifier signal and V is the static voltage value for one diode on the detector. For the FE measurement a $\lambda/4$ wave plate is added into the beam path in front of the $\lambda/2$ wave plate. A FE signal arises due to a energy shift in peak position of right hand circular polarized (RCP) and left hand circular polarized (LCP) light by passing through a magnetized medium. Since the medium has to absorb at the energy/ wavelength, the FE signal is also wavelength dependent. The linear polarized light can be mathematically expressed as a superposition of LCP and RCP light. This explains why elliptical polarized light is observed in the experiment. For the experiment the $\lambda/2$ wave plate is used to balance the photodiodes without magnetic field. After that the $\lambda/4$ wave plate s inserted and also used to balance the photodiode signal. The $\lambda/4$ wave plate makes circular polarized light. The same as circular polarized light can be expressed as a superposition of LCP and RCP light, circular polarized light also can be expressed by a orthogonal set of two equal intense linear polarized light beams. The following $\lambda/2$ wave plate will rotate the two equal intense linear polarized parts. So the main point here is that the $\lambda/4$ wave plate converts ellipticity into a rotation signal which can be analysed by the Wollaston prism. Since the polarization angles are perpendicular to each other, both polarized beams are passing the Wollaston prism at an angle of 45° in relation to the prisms vertical axis. Both beams get split by the prism in a set of two linear orthogonal polarized beams of equal intensity. With applied magnetic field elliptical polarized light will pass through the $\lambda/4$ wave plate. After the $\lambda/4$ wave plate it is still elliptical polarized but the two orthogonal linear polarized components are rotated. The $\lambda/2$ wave plate will rotate them further and the light polarisation will not be at 45° in relation to the Wollaston prisms vertical axis. This produces a static signal. Time resolved measurements are performed by measuring the

changes of the FR/FE signal as a function of pump-probe delay.

2.6.2 Static single wavelength magneto-optical measurements

For the static magneto-optical (MOP) measurement at single wavelengths a HeNe laser at 633 nm as well as two diode lasers at 532 nm (Thorlabs CPS532) and 450 nm (Thorlabs CPS450) can be used. The two lasers are positioned on the laser table so that two extra mirrors are sufficient to align the laser beam so that it follows the same beam path as the probe beam of the fs experiment.

2.7 UV/Vis, Luminescence, IR and Raman spectroscopy

Static UV/Vis/NIR, luminescence and Raman spectroscopy was performed on commercial spectrometers. For the UV/Vis/NIR spectroscopy (Shimadzu UV-1800) a pair of one cm pathlength quartz cuvettes (Hellma) were used. Before the measurements a background spectrum was recorded. One cuvette filled with solvent was placed in the reference beam path of the spectrometer. The other cuvette was then filled with the dissolved sample. In general the settings that were used were a medium scan speed and a 0.5 nm step size.

For the luminescence spectroscopy (Horiba Jobin-Yvon Fluoromax 3 spectrometer) a one cm pathlength quartz cuvette (Hellma) with four polished sides was used. The settings for the slits, integration time and averaged scans depends on the measurement and will be mentioned for each shown spectrum.

FT-IR spectroscopy was performed on a Perkin-Elmer Spectrum Two spectrometer using a attenuated total reflection (ATR) attachment. With the ATR attachment a spectrum of a powder or crystalline sample can be measured without using potassium bromide or mineral oil to disperse the sample.

Raman spectroscopy was performed on a Renshaw Raman microscope using crystalline samples. For all the Raman measurements shown in this thesis, a 785 nm laser was used as excitation source.

2.8 Sample preparation

For the ultrafast TA measurement two kind of samples were used. For r.t. measurements the samples were dissolved in spectroscopy grade solvents. For some measurements the solvent was degassed using a stream of nitrogen. For dissolving a sample, an ultrasonic bath was used if necessary. For low temperature ultrafast TA or MOP measurements, a Poly(methyl methacrylate)(PMMA) film was used. In the following sections the sample preparation for the two kinds of samples is explained.

2.8.1 PMMA films for cryogenic temperature measurements

PMMA films were made differently depending on the sample. For the Mn SMMs 2 g PMMA beads (350 000 g/mol) were dissolved in 27 mL ethyl acetate. To dissolve the PMMA completely, the solution was stirred for 5 days at r.t.. The solution was checked for small PMMA particles using a light microscope. For the Mn_6 film, 0.7 mg of the Mn_6 complex were dissolved in 2 ml of the PMMA in ethyl acetate solution. The solution was poured in a 60 mm diameter extra flat glass petri dish (Schott Duroplan) where a copper ring was placed as a mould and support for the PMMA film. After drying the film underneath a large glass bowl to avoid any air turbulences influence the drying process, the film was carefully removed by gentle heating of the glass petri dish. For the Mn_3 sample the same procedure was used. Just instead of 0.7 mg of sample, 0.4 mg were dissolved in 2 ml PMMA in ethyl acetate solution.

For the Fe_3 sample 0.52 g of PMMA (350,000 g/mol) were dissolved in 6 ml tetrahydrofuran (THF). THF is used in this case since the Fe_3 sample does not dissolve in ethyl acetate. 0.9 mg of Fe_3 sample (627.88 g/mol) were then dissolved under stirring in 3 ml PMMA/ THF solution. The solution of PMMA and Fe_3 sample in THF was then poured into the copper ring positioned in a the glass petri dish for drying. The rest of the procedure is equivalent to the Mn samples.

The PMMA film for the $Tb(Pc)_2$ complex was made using the PMMA in ethylacetate solution prepared for the Mn samples. 0.7 mg of $Tb(Pc)_2$ were dissolved in 2 ml of the PMMA/ethylacetate solution. The rest of the procedure is equivalent to the Mn samples.

All the resulting thin films had a thickness of around 200-500 μm. This means that

for spectroscopic experiments no problems with internal reflection or interference are expected. In none of the experiments thermal oscillations in the films were observed.

2.8.2 Solution measurements

For the ultrafast TA measurement of solutions at r.t., the dissolved sample was either placed in a one mm pathlength quartz cuvette or a flow cuvette was used. The cuvette is placed in a cuvette holder in the centre of the electromagnet. The cuvette holder is mounted on a xyz translation stage. The cuvette holder are made by a 3D printer. This allowed to make special holders for the two cuvette types.

Flow cuvette system

The Starna flow cuvette (45/UTWA) with 200 μm pathlength and 200 μm thick windows is used for samples which dissolve well so that a high enough absorbance (> 0.3 O.D.) at the excitation wavelength is reachable with the short pathlength. For an easier handling, just a round cut-out with a diameter of 5 mm in the centre of the cuvette is 200 micron thin. The rest of the windows are 1 mm thick. A syringe pump was used to pump the solution through the cuvette using a flow rate between 5 and 10 $\mu L/min$. To calculate how many times per second the illuminated volume is exchanged the pump beam diameter is needed. Figure 2.10 gives for the 400 nm pump 163 μm. From that the volume can be calculated with $4.17 \times 10^{-3}\ mm^3$ ($mm^3 \triangleq \mu L$). With a minimum flow rate of 5 $\mu L/min$, an exchange frequency of around 20 Hz is found. This means that after every 25 pump pulses the sample volume is totally exchanged.

2.9 Test measurements

In this section the performance of the ultrafast TA setup is demonstrated by measuring two samples which are well studied in literature. The first test sample is trans-4-dicyanomethylene-2-methyl-6-p-dimethylaminostyryl-4H-pyran (DCM) ,which is a laser dye. The DCM laser dye can be easily dissolved in methanol and it shows strong TA signals. The second sample is the $Fe(bpy)_3^{2+}$ complex. This complex also dissolves easily in water or ethanol and it is strongly red coloured due to a strong LMCT transition in the green part of the electromagnetic spectrum. Further this metal complex has

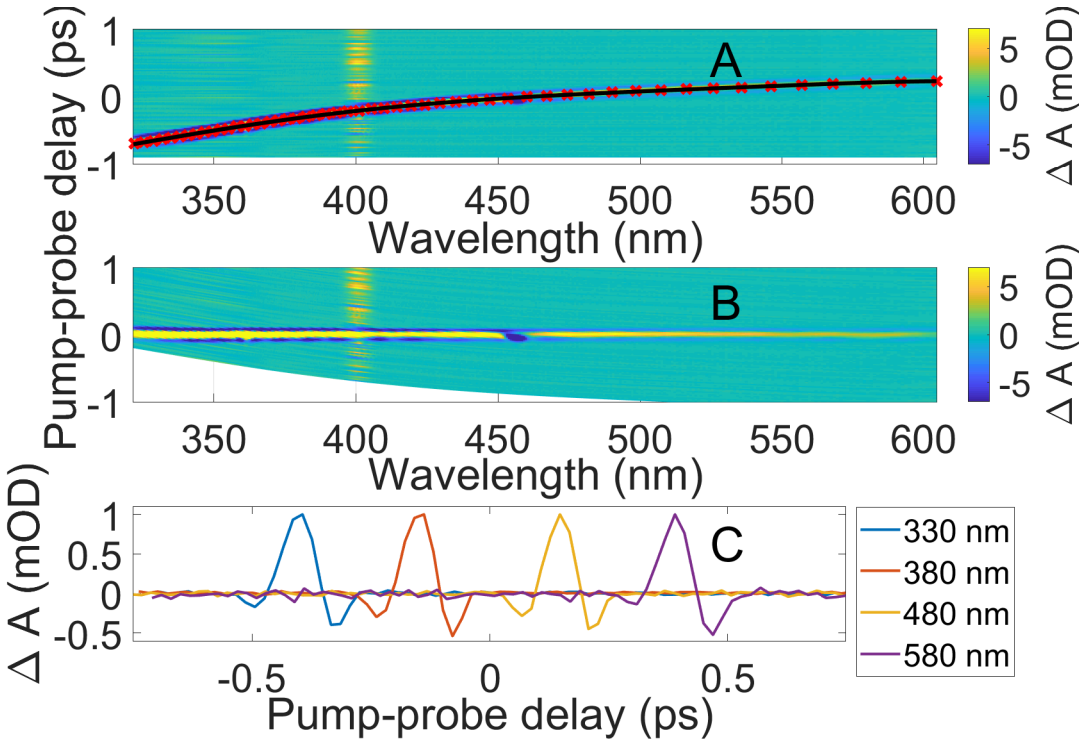

Figure 2.14: ***A*** *Contour plot for the ultrafast TA measurement of pure ethanol showing the white light chirp overlaid with a third order polynomial fit of chosen XPM maxima.* ***B*** *In the chirp corrected contour plot the data points are shifted according to the polynomial fit.* ***C*** *The XPM is plotted as a function of time for four wavelengths. The data was taken from the time corrected data set and shifted so that the XPM signals do not overlap. A 0.2 mm cuvette was used. At 400 nm scattered pump light is interfering with the TA signal.*

been studied extensively (see the Introduction 1 for more detailed information).

First in this section ultrafast TA spectra of pure solvents are shown. From this measurements the time resolution can be extracted and possible signals (e.g. XPM) which do not belong to the actual sample can be detected and removed if necessary. The XPM signal can be used to determine the time of pump probe overlap in the sample and therefore a correction for all wavelengths to the same arbitrary time zero can be performed.

2.9.1 Ultrafast transient absorption spectroscopy of ethanol

XPM in a pure solvent is a well known effect and can be used to determine the chirp of the probe pulse in an ultrafast TA experiment. In this section ultrafast TA experiments

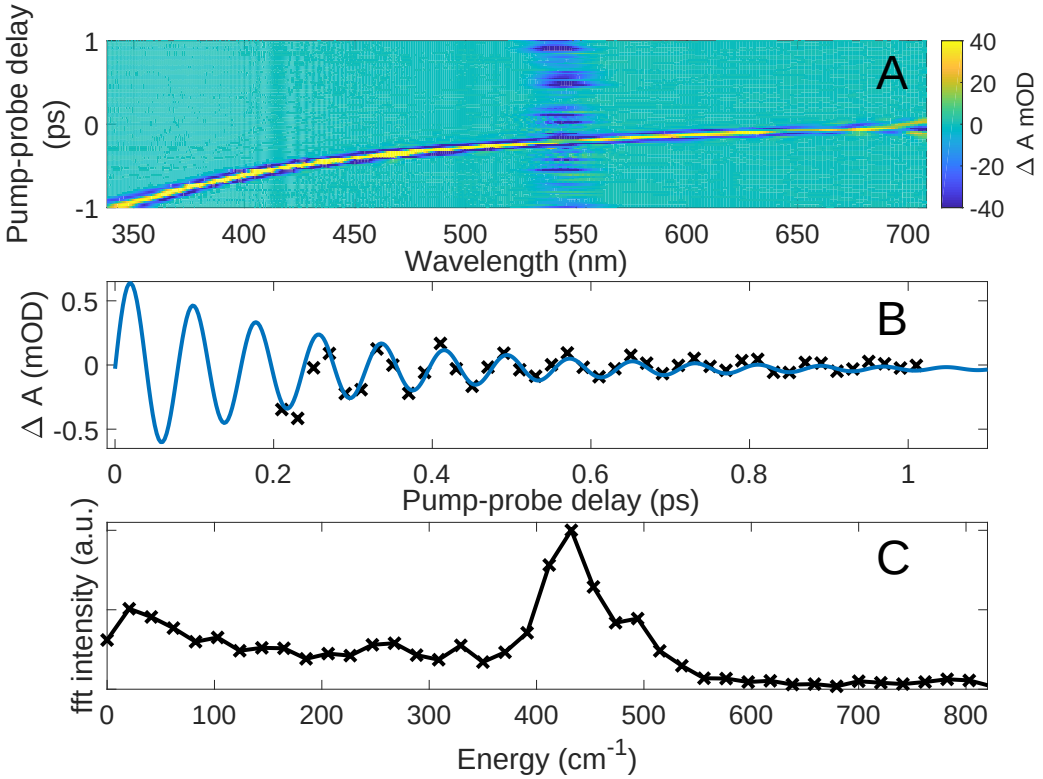

Figure 2.15: ***A*** *Contour plot for the ultrafast TA measurement of pure ethanol showing the white light chirp.* ***B*** *The kinetic traces (120 average traces from 377 nm to 422 nm) show a oscillatory pattern which is fitted by a exponentially damped sine fit. The oscillations are very weak in relation to the XPM, so that averaging was necessary.* ***C*** *The Fourier transformation of the trace in* ***B*** *shows a single peak at 427 cm^{-1} which is typical for ethanol. A 0.2 mm cuvette was used. The pump wavelength is 535 nm.*

in spectroscopy grade ethanol are shown. Two experiments were performed using the 200 μm flow cuvette and excitation wavelengths of $\lambda_{pump} = 400$ nm (3.3 mJ/cm^2) and $\lambda_{pump} = 535$ nm (2.88 mJ/cm^2).

The XPM central positive signal for the $\lambda_{pump} = 400$ nm measurement in Figure 2.14 **A** is fitted using a third order polynomial function. By adjusting every wavelength channel by the polynomial, the data set can be corrected for the chirp so that time zero for all wavelengths is at the same arbitrary time zero. This is shown in panel **B** in Figure 2.14. The time resolution of a pump-probe experiment can be estimated by the cross-correlation time of the pump and probe pulse. The XPM signal is a good measure for the cross-correlation time. So by plotting the induced absorbance change by XPM as a function of time (panel **C** in Figure 2.14), the typical shape of the XPM signal is visible. The distance between the two minima is a good approximation for the cross correlation time of the experiment [53]. The cross correlation depends on the probe wavelength and increases with distance to the pump wavelength [52]. For the four chosen probe wavelengths this effect is also visible. For the XPM at 330 nm the cross correlation is around 180±20 fs, for 380 nm it is decreasing to 160±20 fs. For longer wavelengths than the pump wavelength, the cross correlation time is increasing as can be seen from the 480 nm cross correlation time of 140±20 fs in relation to the 159±20 fs at 580 nm.

When a laser pulse is shorter than the period of a vibrational mode in a solvent and the solvent does not absorb at the wavelength of the laser pulse, it is possible to excite a coherent vibrational wave packet of the electronic ground state of the solvent by a stimulated Raman process. This behaviour of ethanol can be seen in Figure 2.15 where the ultrafast TA experiment in ethanol using $\lambda_{pump} = 535$ nm is shown. In panel **A** the contour plot with the chirp is shown. In panel **B** a kinetic trace from 0.2 ps to 1 ps is plotted together with a damped sine fit for the oscillations. The sine fit has a period of 79 ± 1 fs and a damping constant of 260 ± 117 fs. The period converted into energy is 422 cm^{-1}. This is in good agreement with the Fourier transform spectrum in panel **C** of Figure 2.15 where a peak at 427 cm^{-1} is found. This vibrational mode is assigned in literature as C-C-O in-plane bending mode [54] and is usually found in Raman spectra of samples containing ethanol [55, 56].

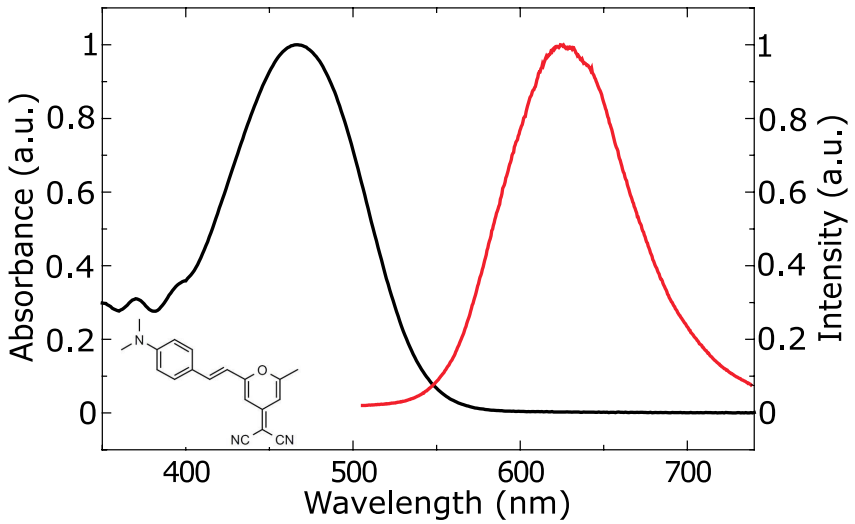

Figure 2.16: *Absorbance spectrum of the DCM laser dye in methanol (black line). Emission spectrum of the DCM laser dye in methanol (red line). The spectra were taken from Maciejewski et al. [57]. In the lower left corner is the chemical structure of the DCM molecule.*

2.9.2 DCM laser dye ultrafast transient absorption

The DCM laser dye ground state absorption spectrum shows a strong absorption band at 470 nm and some smaller absorption bands in the UV (see Figure 2.16). The emission at 630 nm in methanol is strong (quantum yield = 0.59 in n-propanol [58]) and lives for over 2 ns [59]. This is due to the stabilization of the excited CT state, where the dimethylamino group is the donor and the pyran ring with the two cyano groups is the acceptor [58]. Another well know behaviour is the red shift of the DCM emission peak with a larger dipole moment of the solvent [59, 60]. This behaviour was also found in time resolved experiments in polar solvents [57, 61]. The red shift can be seen well in the measurements performed on our set-up shown in Figure 2.17 **F**. A shift from 590 nm (Pump-probe delay = 0.5 ps) to 640 nm (Pump-probe delay = 32 ps) is observed (ΔE =1324 cm^{-1}). This is in excellent agreement to earlier ultrafast TA experiment [57, 62] and to a fluorescence up-conversion experiment [60].

The kinetics after photoexcitation of DCM are complex and depend on the excitation wavelength. The isosbestic point at 545 nm in Figure 2.17 **B** is shifted in relation to the 572 nm found in Kovalenko et al. [61]. Also the TA spectra at early time delays ($<$ 500 fs) from Kovalenko et al. [61] show GSB around 490 nm which is not seen in the ex-

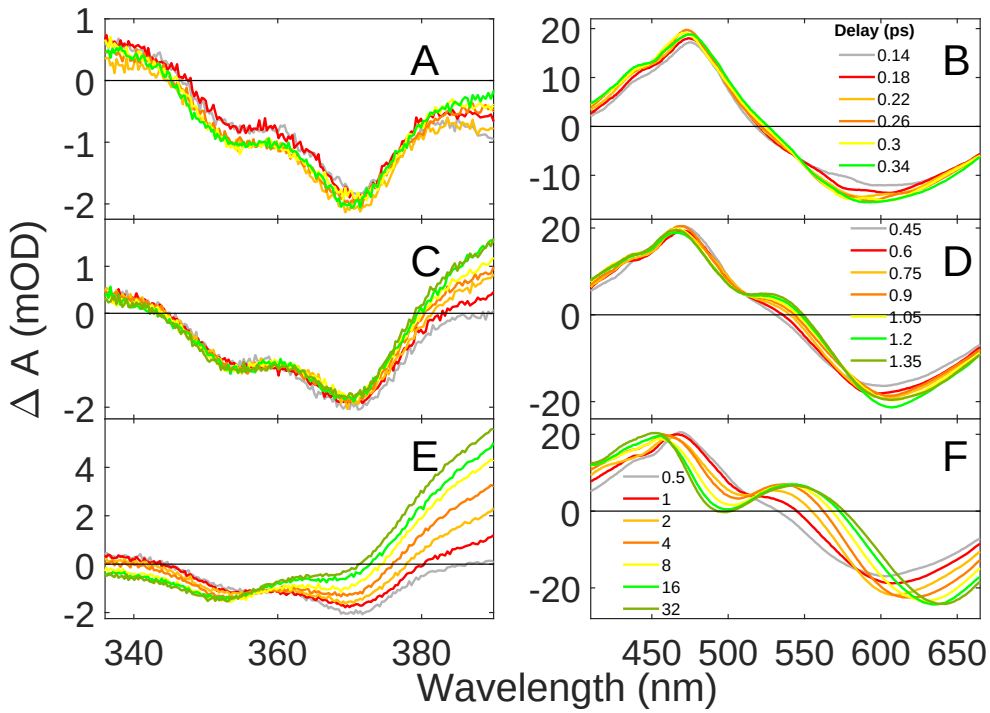

Figure 2.17: ***A*** *and* ***B*** *Difference spectra from the TA measurement of DCM in methanol. The figure is split in six sub panels. The upper row shows the difference spectra for early delay times from 0.14 ps to 0.4 ps.* ***C*** *and* ***D*** *The middle row shows the difference spectra for intermediate delay times from 0.45 ps to 1.35 ps.* ***E*** *and* ***F*** *The lower row shows the difference spectra for later delay times from 0.5 ps to 32 ps. In the left panel the wavelength range from 336 nm to 390 nm and in the right panel the wavelength range from 410 nm to 664 nm is plotted, because the regions show a very different absorbance change.*

periment here. Both observations are explained by the different excitation wavelengths from the shown experiment here and the literature (400 nm and 530 nm). The 400 nm excitation leads to a large amount of excess vibrational energy in the experiment shown here. The time resolution of Kovalenko et al. [61] is better then the time resolution for the presented measurement, so they can show TA spectra for earlier pump-probe delays. By comparing difference spectra from Kovalenko et al. [61] with the earliest pump-probe delay TA spectra in 2.17 **B**, it can be seen that the peak structures for 0.14 ps and 0.18 ps pump-probe delay in 2.17 **B** are in good agreement with Kovalenko et al. [61]. The loss of the structure is interpreted by Kovalenko et al. [61] as a change of the initial excited state to the earlier mentioned CT state by isomerization around a single bond in the DCM molecule. To distinguish the isomerization process from IVR processes Kovalenko et al. [61] excited at 530 nm, which is at the red side of the absorbance peak at 470 nm. Since the excitation wavelength for the measurement here is 400 nm, it is not possible to distinguish between IVR and isomerization to the CT state. Pommmeret et al. [62] and Maciejewski et al. [57] excite at 400 nm and they observe the same ESA band for early time delays (Figure 2.17 **B**).

While the time resolution in our TA experiment is not as good as in Kovalenko et al. [61], the probed spectral range is much larger and reaches 330 nm in the UV. As a result of that, Figure 2.17 **A**, **C** and **E** show the UV part from 330 nm to 400 nm. No TA measurement in literature was found covering this spectral area.

Figure 2.17 **A** shows the early time delays from 0.14 ps to 0.34 ps in steps of 40 fs. From 336 nm to around 370 nm the observed GSB is increasing. The shape of the GSB bleach signal fits perfectly to the ground state absorbance spectrum in Figure 2.16. From 370 nm to 390 nm the GSB signal decreases. So the ESA increases in this wavelength region.

By using the Glotaran software package (from Introduction 1), a global fit was produced. A sequential exponential decay model with four components according to

$$\Delta A(\lambda, t) = \sum_{i}^{n} a_i(\lambda) \times e^{-\frac{t}{\tau_i}} \tag{2.2}$$

was used to fit the data. n is the number of exponential components and the amplitude $a_i(\lambda)$ is the pre-exponential factor which can be plotted for all λ as the decay-associated

spectrum (DAS). τ_i is the exponential decay constant. The results are plotted in Figure 2.19. Figure 2.19 **A** shows the kinetic traces for three wavelength values and the according fits. In Figure 2.19 **B**, the DAS for the four decay components are plotted. The first two time constants of τ_1=360 ± 80 fs and τ_2=2.3 ± 0.2 ps fit well to the time constant of 2.1 ps which was found in Pommeret et al. [62] and the time constants of 0.23 ps and 3.27 ps found in Maciejewski et al. [57]. No equivalent time scale for τ_3=11 ± 2 ps was found in literature. This can be explained by knowing that the cited TA experiments just run up to a maximum pump-probe delay of 14 ps. So a decay constant of 11 ps would have been very difficult to extract from the data. The fourth decay constant of τ_4 = 143 ns can be seen as an offset on the time scale of the measurement. Since the fluorescence lifetime of DCM is over 2 ns in methanol, this decay can not be fitted correctly on a time scale of 50 ps.

Overall the ultrafast TA measurements of the DCM laser dye are in good agreement to the literature. Because of the spectrally broad probe pulse, new GSB features in the UV part of the difference spectra are shown which are currently not published. The conclusion from this section is that the set-up is reliable even for small pump-probe delays and that the calibration of the spectrometers is accurate.

2.9.3 $Fe(bpy)_3^{2+}$ ultrafast transient absorption

The literature of the $Fe(bpy)_3^{2+}$ molecule (see Figure 2.18 **A**) is discussed in terms of the SCO and LIESST effects and there potential usage in storage devices in Chapter 1. In this section the ultrafast TA measurements of $Fe(bpy)_3^{2+}$ in ethanol is shown and compared with the literature. This is done to show that the set-up can reproduce data from the literature and to show that the data measured in the UV is reliable. Further is expected that a vibrational wave packet in the UV part of the spectrum (< 330 nm) can be observed. This is a well documented phenomenon in literature [30, 32, 64, 65] and will help to evaluate the sensitivity of the ultrafast TA set-up.

Synthesis of $[Fe^{II}(bpy)_3]^{2+}[(BF_4)_2]^{2-}$

The $Fe(bpy)_3^{2+}$ was synthesized using 0.8 mg of bpy and 0.2 mg of $FeCl_2$. The bpy was dissolved in some ethanol, while the $FeCl_2$ was dissolved in water. The bpy and $FeCl_2$ solutions were mixed under stirring and a solution of 0.4 mg of $NaBF_4$ dissolved in

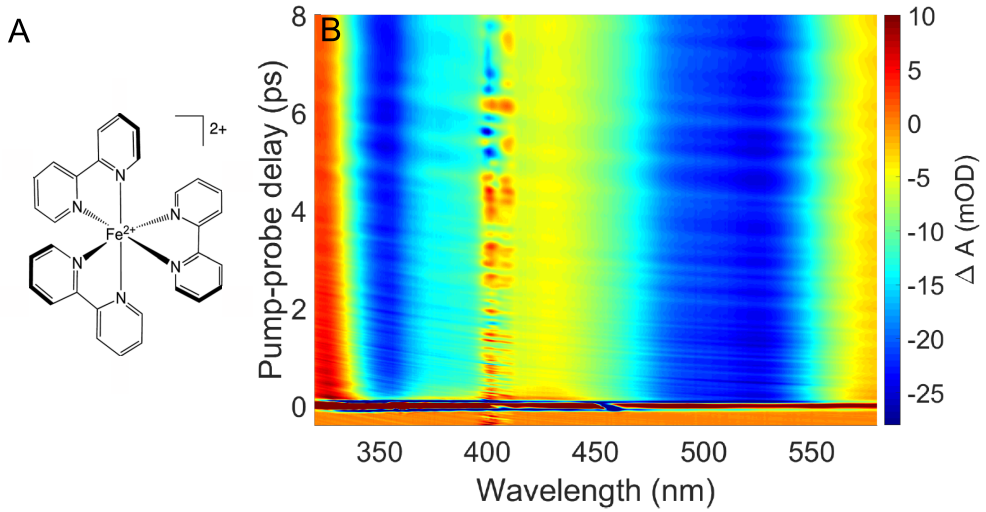

Figure 2.18: ***A*** *Chemical structure of the* $[Fe^{II}(bpy)_3]^{2+}$ *ion.* ***B*** *Ultrafast TA data of* $[Fe^{II}(bpy)_3]^{2+}[(BF_4)_2]^{2-}$ *dissolved in ethanol plotted as a contour plot. The pump-probe delay is plotted against the wavelength. The colour code is used to describe the absorbance change. Orange to blue colour represents a negative absorbance change while red represents positive absorbance change. Around 400 nm scattered pump light is visible. For wavelengths below 330 nm and pump-probe delays up to 1 ps oscillations are visible.*

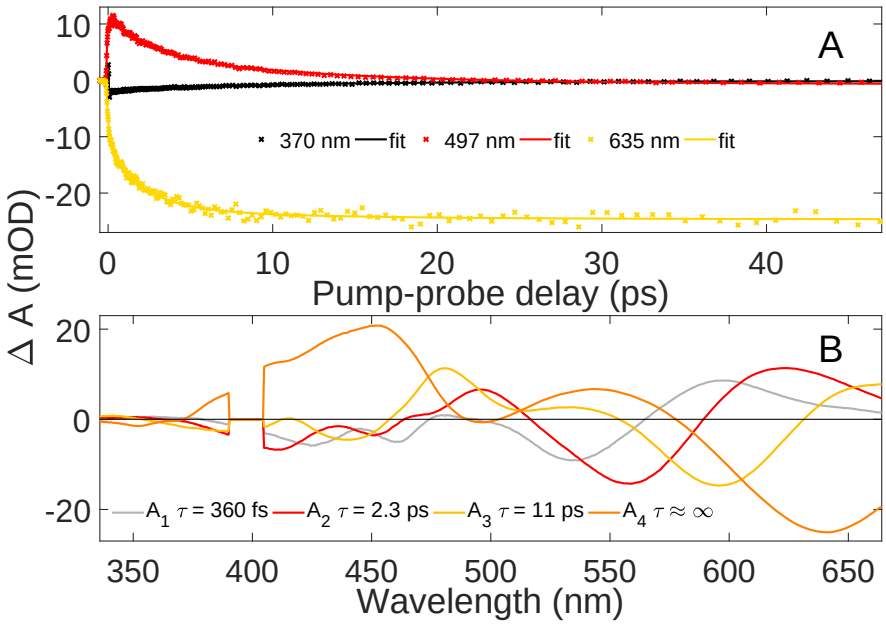

Figure 2.19: *Kinetic traces(**A**) and DAS (**B**) of the ultrafast TA measurement of DCM laser dye in methanol. The global analysis program Glotaran was used to fit the data to a sequential model [63].*

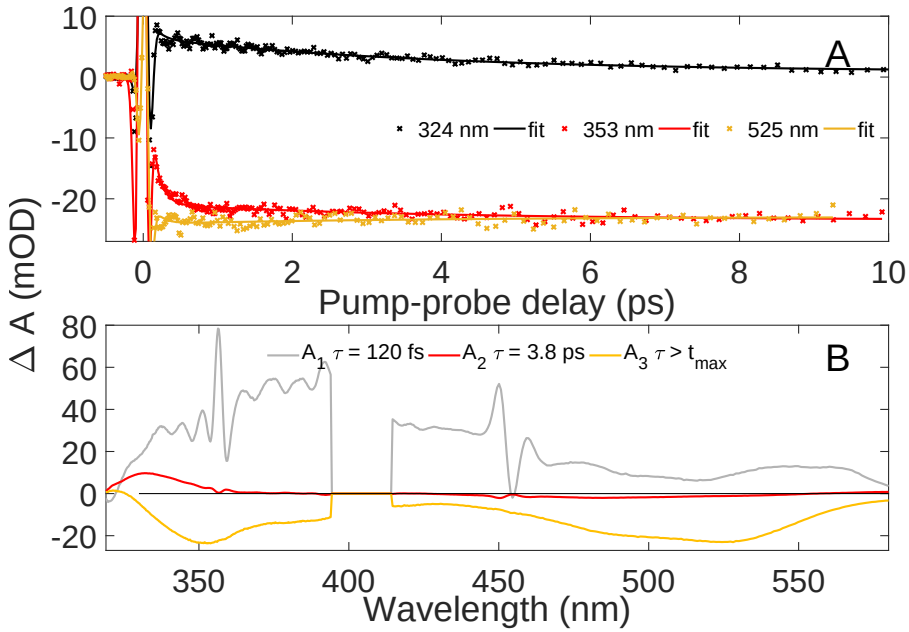

Figure 2.20: *Kinetic traces(**A**) and DAS (**B**) of the ultrafast TA measurement of Fe(bpy)$_3$ in ethanol. The global analysis program Glotaran was used to fit the data to a sequential model [63].*

some water was added. After mixing the bpy and the $FeCl_2$ a dark red colour occurred immediately. To crystallize the $[Fe^{II}(bpy)_3]^{2+}[(BF_4)_2]^{2-}$ the solution was cooled with ice and after a while without any success, more $NaBF_4$ was added to the solution. Together with the cooling crystallization took place. The crystals were collected using a filter and washed with cold water and cold ethanol. But not all $[Fe^{II}(bpy)_3]^{2+}[(BF_4)_2]^{2-}$ ($Fe(bpy)_3$) could be collected at once and after removing some solvent by evaporation (not completely), the rest of the complex crystallized and was collected.

For the ultrafast TA experiment the synthesized $Fe(bpy)_3$ is dissolved in ethanol. The concentration was around 8.2×10^{-3} mol/l. As cuvette the before mentioned 200 μm pathlength cuvette was used. The pump power was set to 3.2 μJ per pulse at 400 nm wavelength. The maximum pump-probe delay is 8 ps and the detected white light spans from 319 nm to 580 nm. 1000 spectra are averaged per time delay and the measurement was repeated 3 times. The minimum step size from -1 ps to 1 ps was set to 25 fs.
The resulting ultrafast TA data is plotted as contour plot in Figure 2.18. The two blue bands are GSB, which can seen be by comparing the peak positions with the ground

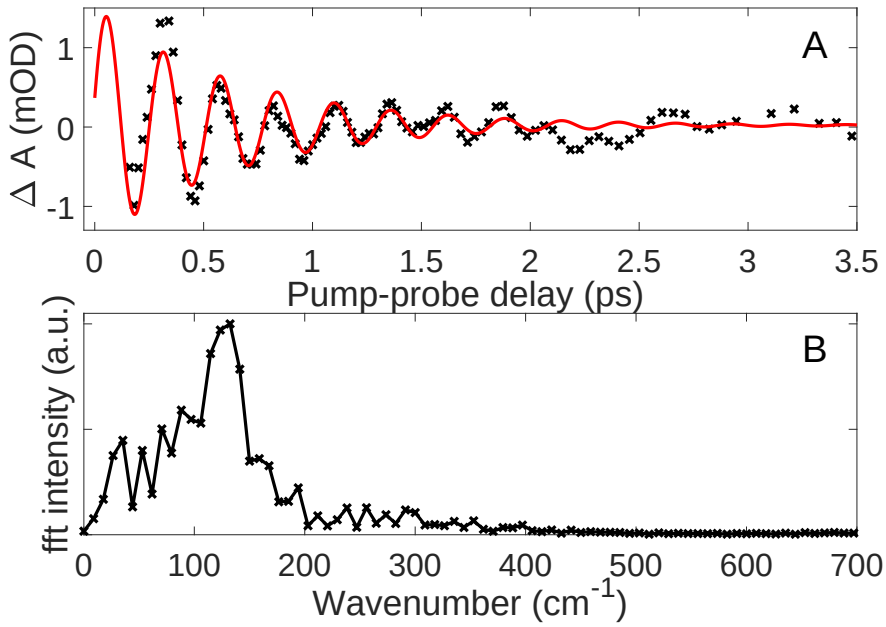

Figure 2.21: ***A*** *Ultrafast TA data of Fe(bpy)$_3$ dissolved in ethanol. The data was fitted using a global biexponential fit plus a constant offset. The residues of this fit from 320 nm to 330 nm are averaged and plotted together with a exponentially damped sine fit.* ***B*** *The Fourier transform intensity of the averaged residues is plotted against the energy in wavenumbers.*

state absorption spectra in Gawelda et al. [28]. In the UV part below 335 nm of the contour plot ESA in red is visible.

In the first picosecond after photoexcitation oscillatory modulations of the TA signal can been seen. This effect occurs due to excitation of a coherent vibrational wave packet. In general a coherent vibrational wave packet is formed by a coherent superposition of several vibrational excited states in an electronic state. For Fe(bpy)$_3$ it was found that no single vibrational mode is responsible for the oscillations and several vibrational modes need to be considered [30, 32, 65]. In Figure 2.21 the averaged residues between 320 nm and 330 nm of a global fit is plotted together with a damped cosine fit in panel **A**. The cosine fit give a energy of 128 $\pm$ 2 cm^{-1} and a damping time of 660 $\pm$ 160 fs. In literature a damping time of 400-780 fs depending on the wavelength was found [30, 32]. In **B** the Fourier transform spectrum of the shown trace in **A** is plotted. The Fourier spectrum is a bit noisy, but one peak is clearly visible at around 128 cm^{-1}. This fits perfectly to the literature where a energy of 130 cm^{-1} was found [32]. There is a further shoulder at around 160 cm^{-1} which would also fit to the literature where 158 cm^{-1} [30] was found. Also lower frequency modes with the same intensity as the

158 cm^{-1} shoulder can be seen in Figure 2.21 **B** but are not known in literature for $Fe(bpy)_3$ in solution. For single crystals two low lying modes in the Fourier transform spectrum were found in Field et al. [65]. In conclusion, the 128 cm^{-1} is a perfect match with literature while all the other peaks and shoulders are in the noise level.
The kinetic traces of the $Fe(bpy)_3$ after photoexcitation are plotted in Figure 2.20 **A**. The traces are fitted by a global sequential tri-exponential fit according to Equation 2.2 using the software package Glotaran [63]. The shortest decay constant found is $\tau_1 = 120 \pm 50$ fs and therefore faster than the cross correlation time of around 160± 20 fs. Nevertheless it is a very good agreement with literature where 116 fs [32] and 130 fs [64] were found. This time constant is assigned as multiple ISC from the excited ^{1}LMCT to the Fe centred $^5T_2$ state. It was shown that the process is with < 50 fs even faster [30]. The second time constant $\tau_2 = 3.8 \pm 0.3$ ps is assigned to vibrational cooling in the $^5T_2$ state. The second time constant is in good agreement with literature as well where 1.1 ps and 3.4 ps for the cooling were found [30,64]. The third time constant which was found is several nanoseconds long. On a 10 ps time scale this is equal to an offset. In literature the longest time constant which was determined for $Fe(bpy)_3$ in solution is 665 ps [28]. Since this is also far out of range of the used maximum pump-probe delay, the conclusion is that τ_3 is in good agreement with literature.
Overall the ultrafast TA measurement of the $Fe(bpy)_3$ dissolved ethanol fits very well to the literature. The kinetics are in very good agreement as far as the time resolution of the experiment is taken into account. The vibrational wave packet is detected in a wavelength range which is not easy to measure with a 800 nm pumped CaF_2 white light continuum. The found frequency of the oscillations and the dephasing time are in good agreement with literature as well.

2.9.4 Ultrafast magnetic circular dichroism measurements on a Nickel film

This test measurement on a thin nickel film was performed in order to show that the ultrafast magneto-optics setup shows reasonable results and to compare the found results with the literature, especially with Beaurepaire et al. [66]. This paper was the first who showed that the magnetization of a material can be manipulated on a ultrafast time scale using fs laser pulses. The thin nickel film was produced by Luke Hedley in

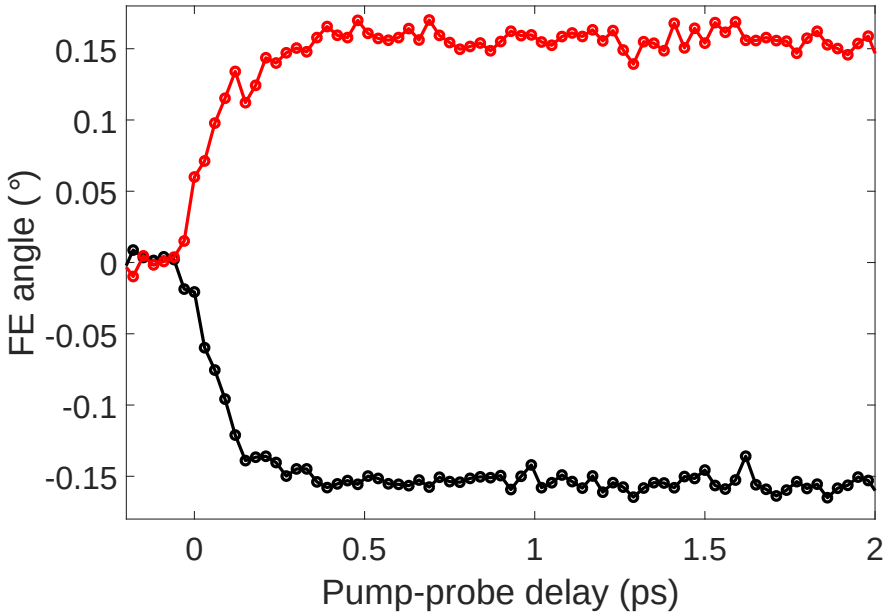

Figure 2.22: *Pump-probe FE of a thin Ni film on glass substrate in the cryostat at r.t.. The pump was the 400 nm SHG of the laser fundamental and the pump fluence was 2.6 mJ/cm^2. The pump polarization was circular. The central probe wavelength was 488± 2 nm (FWHM = 10 nm). The electromagnet was kept at constant 375 mT (or 5 A) for one field direction. Black and red symbolize opposite field direction.*

our group using electron beam evaporation. The film is around 10 nm thick. The Ni film was exposed to air for some time, so a nickel-oxide layer should have formed on the surface. The Ni film for the experiments of Beaurepaire et al. [66] was 22 nm thick and covered with a 100 nm thick MgF_2 layer to protect it from oxidation. Beaurepaire et al. [66] measured the magneto optical Kerr effect (MOKE) of the Ni film. MOKE spectroscopy is performed in reflection and the applied external magnetic field is perpendicular to the normal vector of the film surface, but parallel to the large in-plane magnetization of the Ni film. The experiment described here uses transmission trough the Ni film to measure the FE of the sample. So the applied external magnetic field is parallel to the normal vector of the film surface and perpendicular to the in-plane magnetization. Nevertheless a magnetic signal is observed in Figure 2.22 where the FE signal is plotted against the pump probe delay. The settings for the ultrafast FE measurement were the following: The pump wavelength was 400 nm and the pump diameter was 205 μm and therefore a pump fluence of 2.6 mJ/cm^2 was calculated. The polarization was set to circular using a $\lambda/4$ wave plate. The probe pulse was the white light continuum and after the sample a band pass filter at 488± 2 nm (FWHM = 10

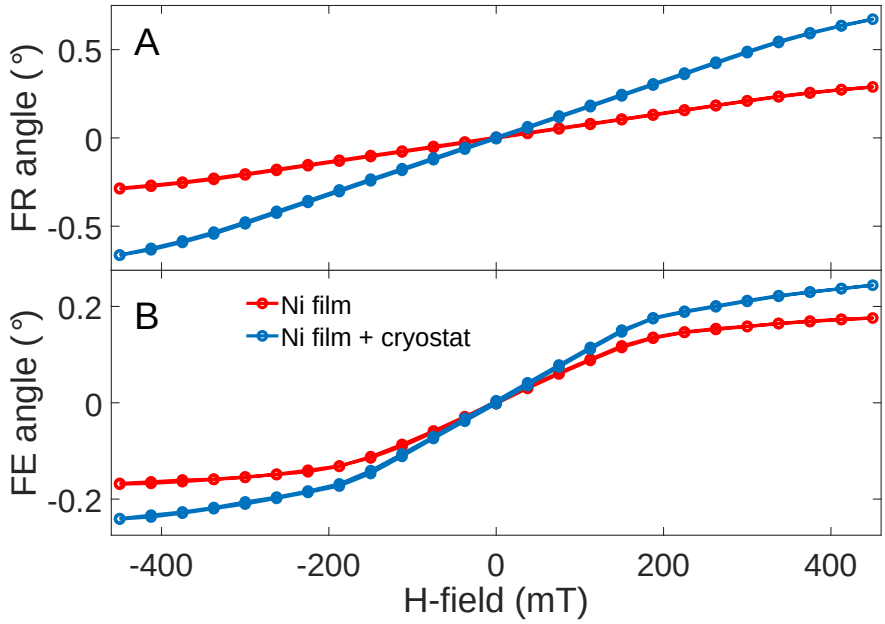

Figure 2.23: *Static FR (**A**) and FE (**B**) of a thin Ni film on a glass substrate in and outside the cryostat at r.t. using a 450 nm diode laser.*

nm) from Thorlabs was placed to just detect that small wavelength range with the balanced photodiodes. The probe polarization was linear and the polarization axis was set with a broadband wire grid polarizer (Thorlabs WP25M-VIS) to be parallel to the laser table surface. The Ni film was mounted in the cryostat but was kept at r.t. The electromagnet was set to a current of 5 A which is equal to a magnetic field of 0.375 T. The detection used was described earlier in this chapter.

Figure 2.22 shows the FE after photoexcitation for both (parallel and anti-parallel to the beam direction) field directions plotted against the pump-probe delay. A fast demagnetization in less then 250 fs is observed, which is good agreement with Beaurepaire et al. [66]. No further dynamics up to 2 ps are observed, which is not in agreement with literature, where Beaurepaire et al. [66] found a fast partially recovery of the magnetization. This different result to literature can be explained by the different measured observable and by the different thickness of the sample. Further to mention here is that the dynamics after photoexciation are wavelength and pump fluence dependent which was shown by Bierbrauer et al. [67] and that for high pump fluences no partial recovery of the magnetization is observed. Beaurepaire et al. [66] used 7 mJ/cm^2 at a wavelength of 620 nm while the measurement here was performed with 2.6 mJ/cm^2 at a wavelength of 400 nm. The combination of different sample thickness, partially

oxidation, different measurement observable, pump wavelength and pump fluence dependent dynamics is an explanation why a different result as in Beaurepaire et al. [66] is observed.

Static Faraday rotation and magnetic circular dichroism of the thin nickel film

In Figure 2.23 **A** the static FR and in **B** FE are plotted. In red the FR/FE of the Ni film and in blue the the FR/FE of the Ni film in the cryostat is plotted. The nickel film has a FR of -0.25° at -0.375 T. The Ni film in the cryostat shows a FR of -0.58° at -0.375 T. The difference is assigned to the contribution of the cryostat windows and the substrate. In 2.23 **B** the static FE signal is plotted for the Ni film and the Ni film in the cryostat, using the same color scheme as in **A**. For the Ni film a saturation effect is observed from 0.175 T on. The FE angle still increases from 0.15° at 0.175 T to around 0.18° at 0.45 T which can be assigned as the substrate and cryostat window contribution. The Ni film in the cryostat shows the same behaviour as the Ni film on itself. Just the linear part after the saturation is steeper. No hysteresis is visible for the Ni film which would be expected. This is explained by assuming in-plane magnetization, while the FR/FE experiment is sensitive for the out-of-plane component. Further the Ni film is most likely partially oxidized which also impacts the magnetic behaviour.

Chapter 3

Vibrational coherences in manganese single molecule magnets

In this chapter, the results of the static UV/Vis spectroscopy, Raman spectroscopy and ultrafast TA measurements on two manganese SMMs and the monomer model system Mn(acac)$_3$ are shown. The two Mn SMMs are a $[Mn(III)_3O(Et-sao)_3(\beta-pic)_3(ClO_4)]$ [68] or Mn$_3$ and a $[Mn(III)_6O_2(Et-sao)_6(O_2CPh(Me)_2)_2(EtOH)_6]$ [69] or Mn$_6$ complex with the highest blocking temperature of 4.5 K for a Mn SMM (Et-sao $\equiv$ ethyl-salycilaldoxime; β-pic $\equiv$ 2-picolylamine). The Mn(acac)$_3$ was used without further purification from Sigma-Aldrich. Mn$_3$ and Mn$_6$ were synthesized in the group of Euan Brechin from the University of Edinburgh. The Mn(acac)$_3$ complex contains just one Mn(III) ion with three anionic acetylacetonate ligands. The spectroscopic results are compared with high level quantum mechanical calculations, performed by our collaborators Julien Eng and Thomas J. Penfold from Newcastle University. Since quantum mechanical calculations on molecules with several highly correlated metal centres with several unpaired electrons are extremely expensive and complicated, our collaborators performed calculations on Mn(acac)$_3$ and Mn$_3$, but not on Mn$_6$. This is the reason why the focus is on the Mn(acac)$_3$ and Mn$_3$ samples. Nevertheless are the Mn$_6$ spectroscopic results impressive and are shown at the end of this chapter.

The study of the initial dynamics after photoexcitation of SMMs is based on the de-

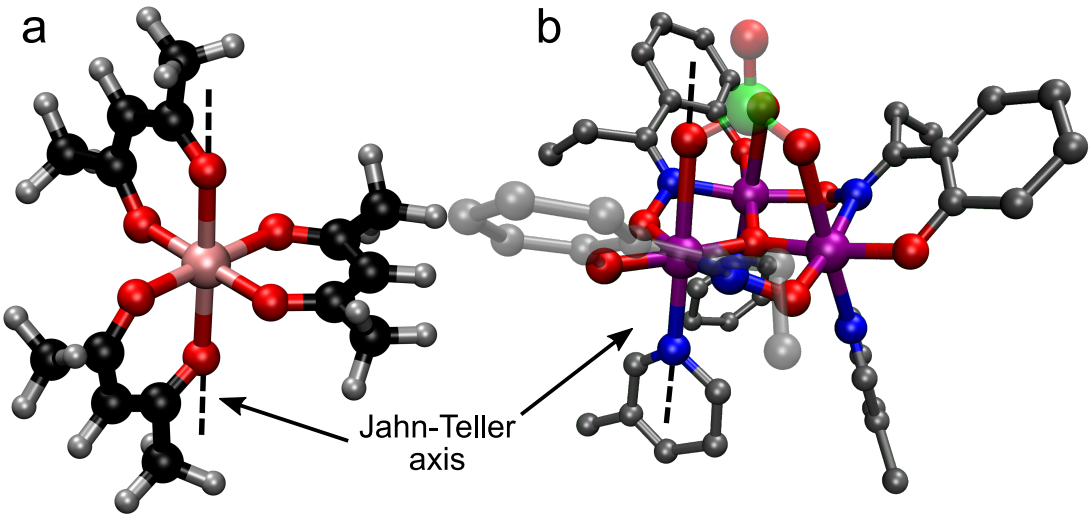

Figure 3.1: *Chemical structures of Jahn-Teller distorted Mn(III) complexes, showing the axial JT distortion along the z-axis (perpendicular to the triangle in Mn_3). The structures are based on the x-ray crystal structure and following geometry optimization.* ***a*** *$Mn(acac)_3$;* ***b*** *Mn_3. The hydrogen atoms in Mn_3 were removed for clarity. The figures were made by Julien Eng from Newcastle University. Colour code: Manganese ≡ purple (b), pink (a); oxygen ≡ red; nitrogen ≡ blue; carbon ≡ grey; hydrogen ≡ grey; chlorine ≡ green.*

mand for smaller magnetic particles for data storage applications and faster ways to manipulate them. Femtosecond laser pulses have the properties to switch the magnetization direction in magnetic materials (e.g. metals, magnetic perovskites) via absorption of a photon, on a ps time scale [20, 21]. For molecule-based magnets and SMMs a control over the magnetization was not shown yet and limited studies are available on that topic. Well studied examples are Prussian blue analogues (PBA), which are coordination polymers containing metal ions linked by cyanide bridges. Studies of PBAs involved ISC [70], ultrafast charge-transfer dynamics [71] and phase transitions [72]. Using the JT distortion to control magnetization was shown on the Mn_{12}(acetate) complex, where high external pressure changes the crystal structure and forces the reorientation of the JT distortion [73]. Also light can be used to reorient the JT distortion and therefore switch the magnetic properties. This was shown on a copper-nitroxide-based molecular chain magnet [74, 75].

All aforementioned examples of molecule-based magnets are large systems and the understanding of detailed photophysics is generally easier with smaller molecules. The magnetic properties of a group of Mn(III) based trinuclear SMM with oxime-based

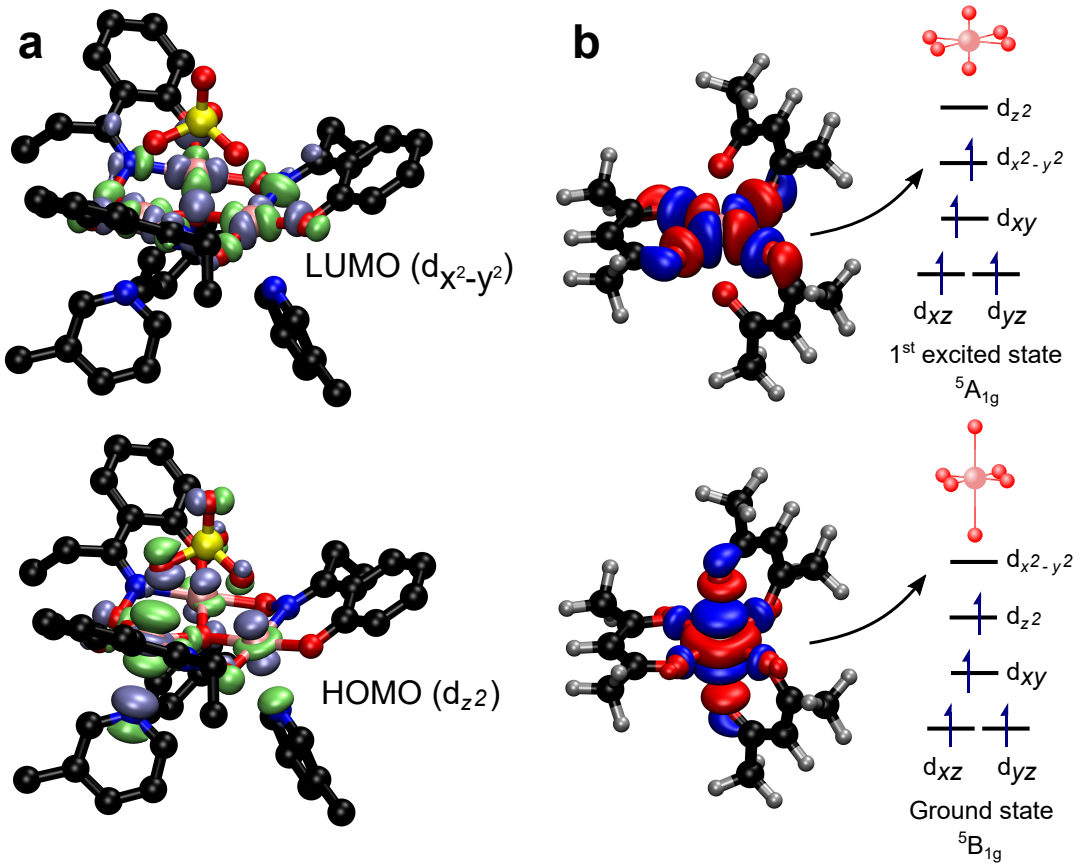

Figure 3.2: ***a*** *Molecular orbitals (MOs) of Mn_3 obtained using density functional theory (DFT) at the Def2-SVP level. The HOMO orbital, and other MOs at the same energy, are made up from superpositions of atomic d_{z^2} orbitals, which lead to a JT distortion along the axis perpendicular to the triangle due to the anti-bonding nature of the d_{z^2} orbital. The LUMO orbital, is comprised of atomic $d_{x^2-y^2}$ orbitals. The hydrogens have been removed from the structure for clarity.* ***b*** *The $Mn(acac)_3$ HOMO and LUMO orbitals. The HOMO orbital is constructed of the d_{z^2} orbital of the Mn and ligand orbitals, while the LUMO is constructed of the $d_{x^2-y^2}$ orbital on the Mn. The Figure was taken from Liedy et al. [76].*

ligands, including the presented Mn_3 complex, were studied extensively [68, 77].

The SMM properties in the mentioned Mn_3 and Mn_6 complexes result from a large total spin momentum and negative zero-field splitting (ZFS) caused by the magnetic anisotropy of individual Mn(III) ions. The magnetic anisotropy in both complexes is based on axial JT distortion, which reduces the symmetry on each Mn ion and lowers the total energy of the system. JT distortion is typical for complexes of the high spin Mn(III) ion, due to the four unpaired electrons in five d-orbitals. This anisotropy of the coordination environment leads in combination with SOC and ZFS to a situation where the M_S states are split in a way where the maximum M_S states are minima. This means there are two degenerate magnetic ground states in a zero-field environment and the resulting magnetic moment is orientated either parallel or anti-parallel to the magnetic easy axis.

The chemical structure of Mn_3 is more complicated than $Mn(acac)_3$. It is shown together with the $Mn(acac)_3$ complex in Figure 3.1. The μ_3-oxo bridge, connecting all three Mn ions, makes this system highly correlated. The angle formed by the plane of the three Mn ions and the μ_3-oxygen as well as the μ-oxime groups (Et-sao ligands) plays an important role for the super-exchange interactions [68]. The μ_3-oxo and Et-sao ligands form the equatorial ligands. The axial ligand on one side is a ClO_4^- ligand, which coordinates all three Mn ions. On the other side are three β-pic ligands, which coordinate the Mn with the aromatic nitrogen donor. Both, the β-pic and the ClO_4^- ligands are weak ligands. Since the JT distortion is axial as well, the weak ligand stretches the bond length even further, which leads to an increased anisotropy. All three Mn ions in Mn_3 are high spin and show ferromagnetic super-exchange coupling at low temperatures. In Figure 3.2 the HOMO and LUMO orbitals from quantum mechanical calculations are shown and they show clear similarities between Mn_3 and $Mn(acac)_3$. In Figure 3.2 **a** the Mn_3 HOMO orbital shows that it is a superposition of metal d_{z^2} orbitals and p-orbitals on the ligands. The orbital lobes on the Mn and the ligands are of opposite phase, meaning an anti-bonding nature of the HOMO orbital. Since the d_{z^2} orbital has most of the electron density along the z-axis, the stretch of the bond length along this axis is clear. The LUMO orbital of Mn_3 is a superposition of $d_{x^2-y^2}$ orbitals on the Mn ions and p-orbitals on the ligand. The electron density of the $d_{x^2-y^2}$ orbital is along the equatorial axis, pointing towards the ligands. Populating

this orbital would mean an expansion of the bond lengths in the equatorial plane.
The $Mn(acac)_3$ complex has three deprotonated, bi-dentate acetylacetonate ligands. The coordination geometry is, as for the Mn_3 complex, a distorted octahedron. The calculated HOMO orbital is shown together with the d-orbital splitting in Figure 3.2 **b**. The HOMO orbital, which is comprised of an atomic d_{z^2} orbital, is anti-bonding as can be seen by the opposite phases of the orbital lobes on the metal and the ligand. Also the LUMO is equivalent to the Mn_3 complex. The d-orbital splitting on the right shows the difference in d-orbital splitting between ground and first excited state. The difference is just the exchange in energy position of the d_{z^2} and $d_{x^2-y^2}$ orbital.

3.1 Results

The UV/Vis absorbance spectra of $Mn(acac)_3$ and Mn_3 dissolved in ethanol are shown in Figure 3.3 **a**. The spectrum of $Mn(acac)_3$ in the inset of Figure 3.3 **a** shows at least three weak and broad transitions in the visible at 800 nm, 600 nm and 405 nm. In the UV, one peak at 283 nm and shoulders at 308 nm and 326 nm are detectable. The line spectrum in panel **a** shows the calculated positions of electronic transitions in the $Mn(acac)_3$ complex. The bar height represents the type of transition. The shortest bars stand for spin forbidden transitions. The intermediate bars represent spin allowed metal centred dd-transitions and the long bars are spin allowed intra ligand transitions. As expected for a JT distorted octahedral ligand field with four d-electrons in a high-spin configuration, there are four spin allowed dd-transitions. All atomic d-orbitals on the Mn are non-degenerate. Three dd-transitions are close in energy at 435, 455 and 495 nm and belong to transitions from the d_{xz}, d_{yz} and d_{xy} to the empty $d_{x^2-y^2}$ orbital. The low energy transition at 900 nm belongs to the d_{z^2} to $d_{x^2-y^2}$ transition. The change in electron density for the four dd-transitions can be seen Figure 3.3 **b** to **d**. By comparing the calculated electronic transitions with the measured spectrum it is clear that they are in good agreement. Due to the low extinction coefficient, the low energy band is not well resolved. The 400 nm shoulder is due to the high extinction coefficient most likely not purely a dd-transition and has some ligand to ligand charge transfer (LLCT) character. The transition is shown in Figure 3.3 **e**. The found literature spectra [78, 79] are in good agreement with the shown spectrum and also assign

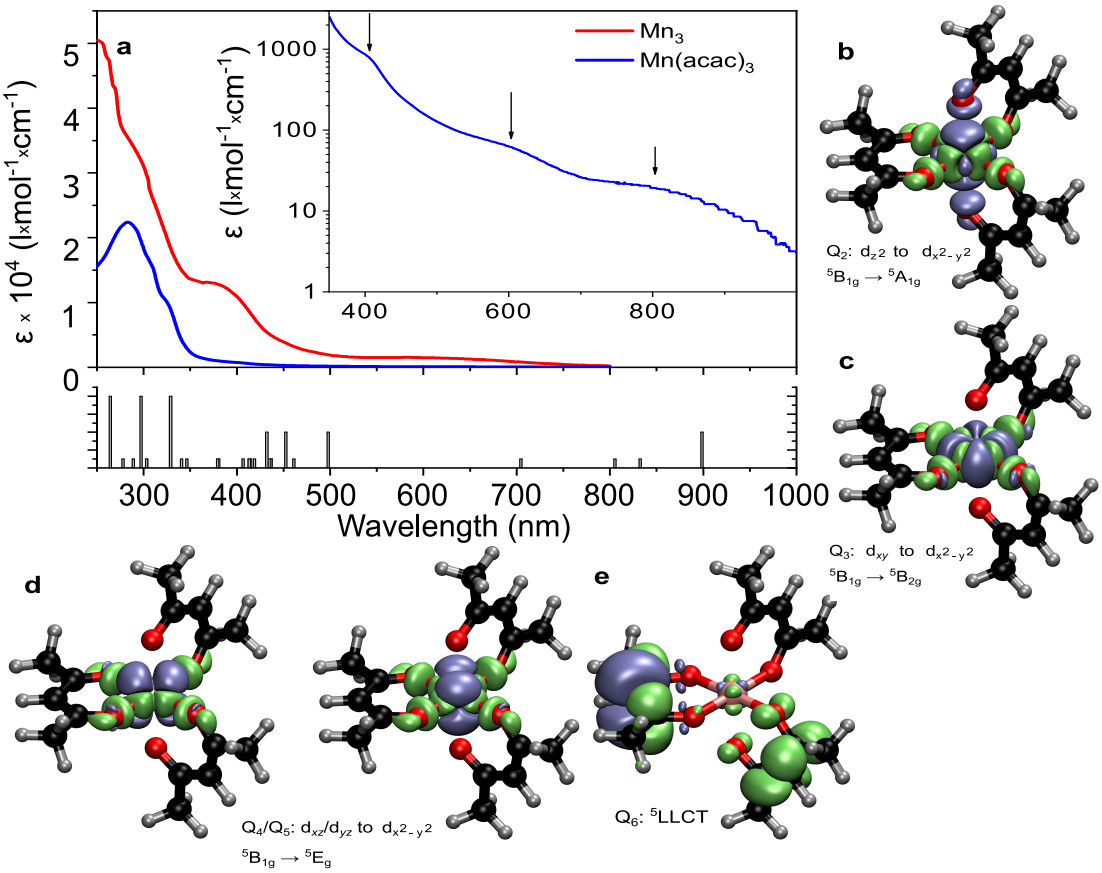

Figure 3.3: ***a*** *UV/Vis absorption spectra of $Mn(acac)_3$ and Mn_3 in ethanol at room temperature. The inset has a logarithmic scale for the extinction coefficients to underline the dd-transitions at 800 nm ($^5B_{1g}$ to $^5A_{1g}$; Q_2), 600 nm ($^5B_{1g}$ to $^5B_{2g}$; Q_3) and 400 nm ($^5B_{1g}$ to ^5E_g; $Q_{4,5}$). The onset of the ligand-to-ligand charge-transfer state (^5LLCT; Q_6) can be seen below 400 nm. The bar diagram shows the wavelengths of the calculated transitions (see Appendix 7.7), where the bar height is scaled as 1:4:8 for transitions that are spin-forbidden, spin-allowed metal-centred (^5MC), and spin-allowed LLCT, respectively. Difference of electronic density between each excited state and the ground state for the five lowest quintet transitions calculated at the CASSCF//NEVPT2 level (see Appendix) are shown in* ***b*** *for $^5B_{1g}$ to $^5A_{1g}$ (Q_2),* ***c*** *for $^5B_{1g}$ to $^5B_{2g}$ (Q_3),* ***d*** *$^5B_{1g}$ to ^5E_g ($Q_{4,5}$), and* ***e*** *for ^5LLCT (Q_6). Colour-code: grey: decrease of electronic density. green: increase. The Mn – O bond along the z-axis is removed for clarity. The Figure was taken from Liedy et al. [76].*

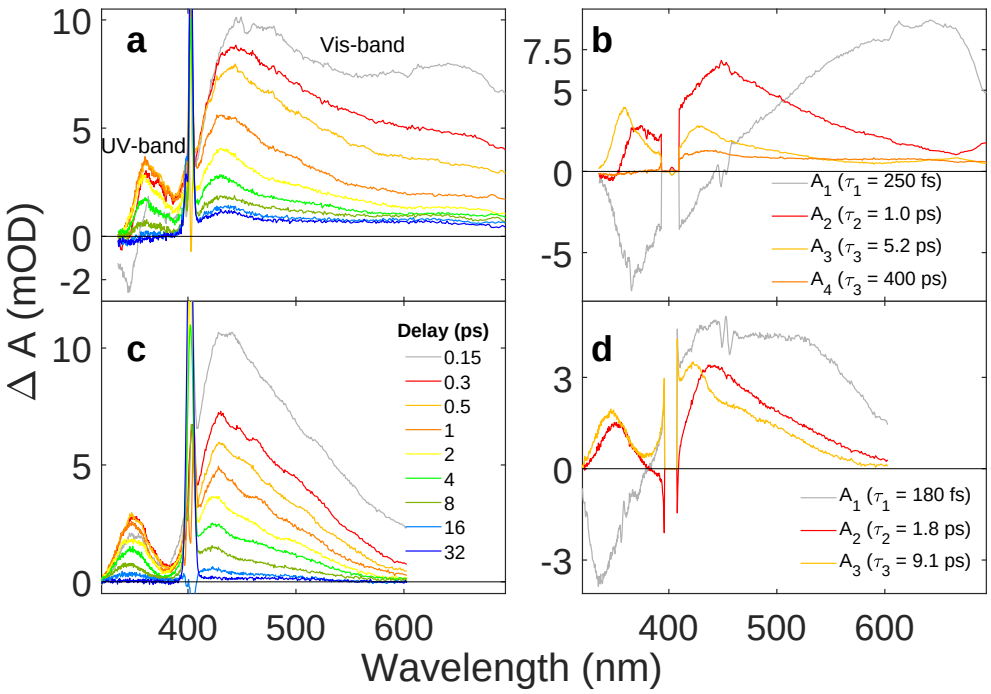

Figure 3.4: *Ultrafast TA results of $Mn(acac)_3$ and Mn_3.* ***a*** *Difference spectra for $Mn(acac)_3$ in ethanol for selected pump-probe delays from the TA data (λ_{pump} = 400 nm). The sharp spikes around 400 nm are due to scattered pump light.* ***b*** *DAS from a global analysis using a sequential exponential fit model for $Mn(acac)_3$. The DAS plot the pre-exponential factors A_x against the wavelength. The corresponding decay constants are shown in the legend. The difference spectra and DAS for Mn_3 are plotted in panel* ***c*** *and* ***d****, respectively. The Figure was taken from Liedy et al. [76].*

the three broad bands in the visible to dd-transitions.

The spectrum of Mn_3 shows the same bands and shoulders in the visible as the $Mn(acac)_3$ complex, but with much larger extinction coefficients. Below 300 nm the spectrum of Mn_3 shows a further increase of extinction, in opposite to $Mn(acac)_3$. The shoulder around 400 nm has a large extinction coefficient of approximately 14,000 $l \times mol^{-1} \times cm^{-1}$. This indicates a strong contribution of a ligand or LMCT transition. But for such highly correlated systems as Mn_3, CT via the μ_3-oxo bridge is involved for any transition. This can be seen in Chapter 4 and in Liedy et al. [80], where the calculations on the Fe_3 complex show that the μ_3-oxo bridge is strongly involved in all electronic transitions.

Ultrafast TA experiments were performed using a solution of the Mn_3 (1.88 mmol/l) and $Mn(acac)_3$ (14.8 mmol/l) complexes in ethanol solution. During the measurement the in Chapter 2 described Starna flow cuvette with 0.2 mm pathlength and a flow

rate of 8 μl/min was used. The ultrafast TA measurements were done using the set-up described in Chapter 2. The pump wavelength was set to the SHG of the laser fundamental $\lambda_{pump} = 400$ nm and the fluence was 3.3 mJ/cm^2.

The results, in form of difference spectra, are plotted in Figure 3.4 **a** for the $Mn(acac)_3$ complex and in **c** for the Mn_3 SMM. The difference spectra are plotted for selected pump-probe delays from 0.15 ps after excitation up to 32 ps. The 400 nm pump light causes the sharp signals (pump scatter) which can be seen in difference spectra for all pump-probe delays.

3.1.1 $Mn(acac)_3$ ultrafast TA results

The difference spectra in Figure 3.4 **a** show two ESA bands. One broad ESA band covering the whole visible spectrum (Vis-band) and another ESA band is in the UV (UV-band). The Vis-band decays fast, especially in the red part of the spectrum. This manifests in the difference spectra as narrowing of the ESA band. The peak position of 450 nm at 0.15 ps shifts to 430 nm at 4 ps, which is a energy shift of 1034 cm^{-1}. This, together with the narrowing of the ESA band, indicates cooling by energy distribution into several vibrational modes via IVR and transfer to the environment/solvent [81]. The UV-band is initially negative, implying a decaying GSB signal and is growing up to a pump-probe delay of 0.5 ps with a peak at 361 nm. For this peak, no shift for longer pump-probe delays are visible. At a pump-probe delay of 32 ps, the difference spectrum shows still the Vis-band, but no dynamics are observed up to the maximum pump-probe delay of 200 ps. The UV-band at a pump-probe delay of 32 ps already decayed to zero absorbance change. The ultrafast TA data was analysed using a sequential global fit with a sum of four exponential decay functions according to Equation 2.2. The Glotaran program package [63] was used for this. The DAS, showing the amplitudes of the exponential functions, are plotted in Figure 3.4 **b**. The DAS A_1 for the decay constant $\tau_1 = 250 \pm 30$ fs shows the initial dynamics of the fast decay of the Vis-band and the growth of the UV-band. The fast decay of the GSB signal in the UV with τ_1, to form a ESA band, implies a change of electronic state. The DAS A_2 and A_3 for the decay constants $\tau_2 = 1.0 \pm 0.2$ ps and $\tau_3 = 5.2 \pm 0.5$ ps show a similar shape, but with the UV- and Vis-band maxima shifted to lower wavelengths in the A_3 spectrum. This indicates vibrational cooling. The DAS A_4 for the decay constant $\tau_4 = 400$ ps was

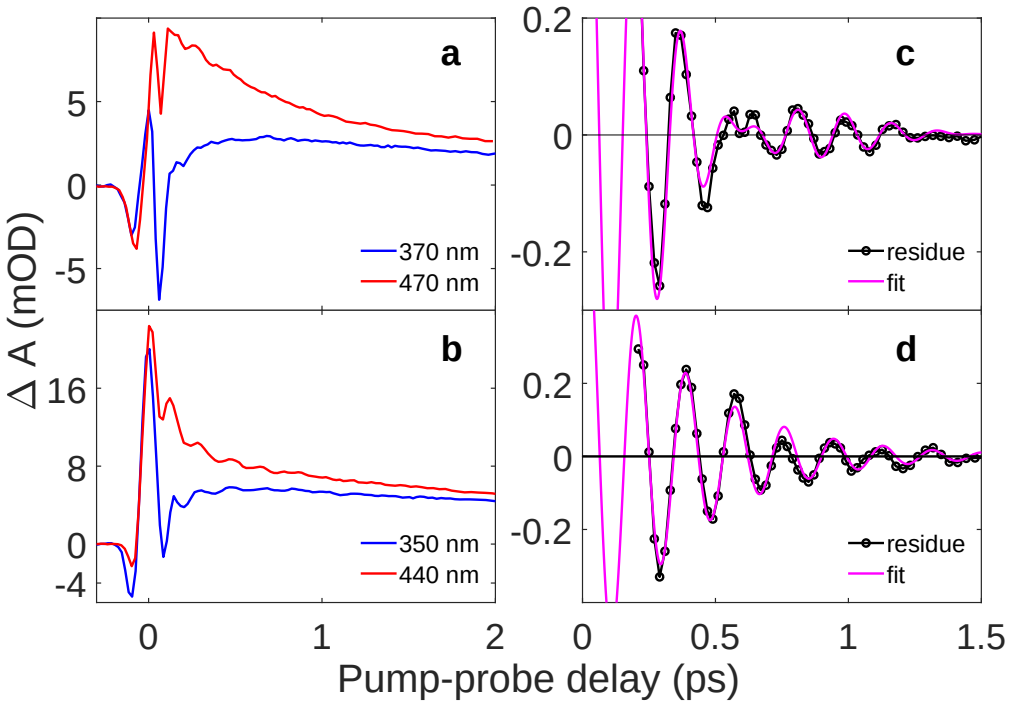

Figure 3.5: *Kinetic traces for the UV- and Vis-band for $Mn(acac)_3$ in* ***a*** *and Mn_3 in* ***b****. The XPM signal of the ethanol is observed around zero pump-probe delay. An average of the fit residues of the global analysis using a sum of exponentials from the kinetic trace data in* ***a*** *and* ***b*** *are shown in* ***c*** *from 426 nm to 492 nm for the $Mn(acac)_3$ and in* ***d*** *for the Mn_3 from 435 nm to 460 nm. Two frequencies at 170 ± 5 cm^{-1} and 208 ± 6 cm^{-1} and a exponential damping constant of 325 ± 11 fs were fitted for the $Mn(acac)_3$ data. Only one frequency at 181 ± 3 cm^{-1} with a exponential damping constant of 360 ± 15 fs was used for the Mn_3 data. The Figure was taken from Liedy et al. [76].*

included in the fit to simulate a residual long living state, which decays much slower than the maximum pump-probe delay of 200 ps.

Kinetic traces, showing the absorbance change plotted against pump-probe delay, are visualized in Figure 3.5 **a**. The traces at 370 nm and 440 nm show oscillations superimposed on the exponential decay. To further analyse this feature, an average across the Vis-band (426 nm to 492 nm) of the fit residues from the global analysis was taken and fitted with a sum of two damped cosine functions. The general equation is:

$$\Delta A(t) = e^{\frac{-t}{\tau_{damp}}} \times \sum_{i}^{N} A_i cos(2\pi(t - t_{0,i})/\omega_i). \tag{3.1}$$

The equation shows that all cosine components decay with the same dephasing time τ_{damp}. The phase constant $t_{0,i}$ and the period ω_i are free fit parameters. For the aver-

aged residue of $Mn(acac)_3$ in Figure 3.5 **c** two cosine functions were used with frequencies of 170 ± 5 cm^{-1} and 208 ± 6 cm^{-1}. The phase constant for both frequencies was found to be close to zero. The dephasing constant was found to be $\tau_{damp} = 325 \pm 11$ fs. A fast Fourier transform of the averaged residues was performed and the result is plotted in Figure 3.6 **a**. Two peaks can be seen at 167 cm^{-1} and 215 cm^{-1}.

Beside the Fourier transform spectrum also the measured Raman spectrum of a crystal grain of $Mn(acac)_3$ is plotted. Raman spectroscopy was performed to get the low frequency vibrational modes of the Mn samples in order to compare it with the found frequencies in the Fourier transform spectrum and the calculated Raman spectrum. Finding the vibrational normal mode of the wave packet is important to understand the reaction coordinate of the wave packet. Raman spectroscopy measures the vibrational modes of the ground state, but serves here as a good starting point for the analysis. The Raman spectra were measured using the method described in Chapter 2 using a 785 nm laser. As seen from the absorbance spectrum in Figure 3.3, this wavelength resonates with the lowest absorbance band of $Mn(acac)_3$. The Raman spectrum shows the low energy vibrational modes of the $Mn(acac)_3$ in the range of 100 cm^{-1} to 710 cm^{-1}. There are several bands in the spectrum. A broad band centred around 150 cm^{-1}, obviously consisting of several vibrational modes almost coincides in energy with the band in the Fourier spectrum and also shows the same shape. To assign the involved modes, the calculated Raman spectrum, obtained using DFT at the Def2-SVP level, is also plotted [76]. The spectrum was simulated by using Gaussian functions to fit the found peak positions of the calculated normal modes. The spectral positions of the bands fit well with the measured Raman spectrum.

Anisotropy measurements were also carried out by measuring the ultrafast TA with pump-probe polarization angles parallel $I_{\parallel}$ and perpendicular $I_{\perp}$ in relation to each other. The anisotropy parameter r is defined as:

$$r = \frac{I_{\parallel} - I_{\perp}}{I_{\parallel} + 2I_{\perp}}. \tag{3.2}$$

The r values for $Mn(acac)_3$ are plotted in Figure 3.8 **A** for the UV- and the Vis-band. The Vis-band shows an anisotropy signal around r = 0.08 for up to 2 ps. After that the r value decreases to around r = 0.05. From 8 ps on the ESA signal of the UV-band

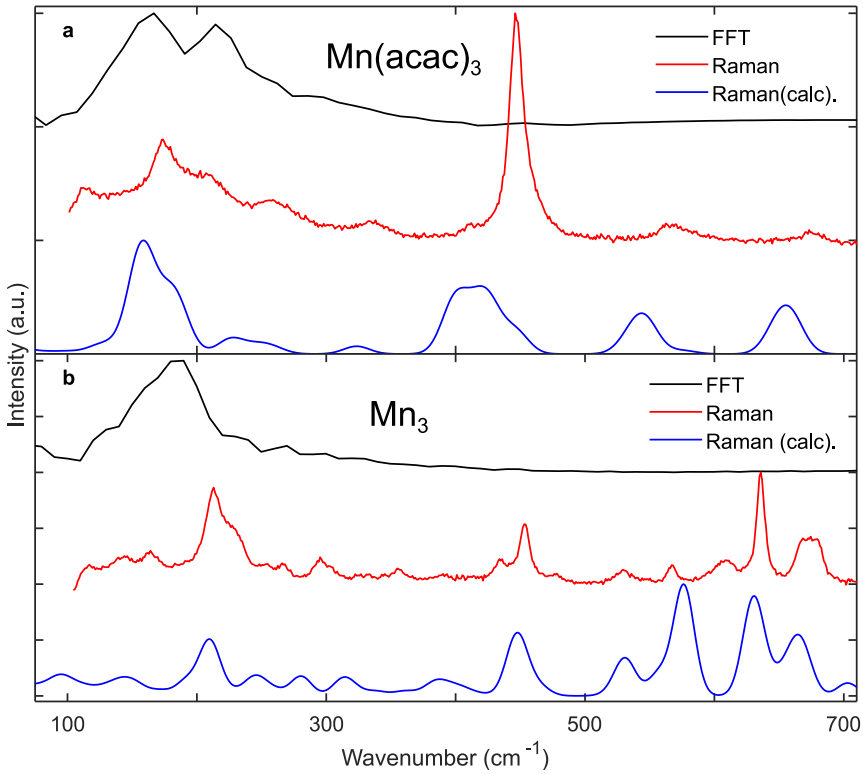

Figure 3.6: ***a*** *Fast Fourier transformation spectrum of the averaged residues of the multi-exponential fit for the Mn(acac)$_3$ data from Figure 3.5* ***c****. Two strong peaks at 167 cm^{-1} and 215 cm^{-1} were found. Also in panel* ***a****: Raman spectrum for Mn(acac)$_3$ crystal grains excited at 785 nm and the calculated Raman spectrum (Def2-SVP level). Several calculated modes overlap with the Fourier spectrum. The modes at 156 cm^{-1}, 159 cm^{-1} and 187 cm^{-1} are complicated modes including symmetric stretch motion along all axes but also ligand torsional scissor modes. See Figure 3.9 for details. The related spectra for Mn$_3$ are plotted in* ***b****. One peak is found at 185 cm^{-1} in the Fourier spectrum. The Raman spectrum shows no peak at 185 cm^{-1}, but a strong peak at 213 cm^{-1} which fits to the calculations which have been obtained at the same level as for the Mn(acac)$_3$ complex. The Figure was taken from Liedy et al. [76].*

is getting to low and no reasonable r value can be extracted. The UV-band shows negative anisotropy of r = -0.3 at 200 fs pump-probe delay which increases quickly to r = -0.1 at 2 ps. From 6 ps on the signal-to-noise level is to low so that no reasonable r value can be extracted.

3.1.2 Mn$_3$ ultrafast TA results

The ultrafast TA results in form of difference spectra of Mn$_3$ are presented in Figure 3.4 **c**. As for the Mn(acac)$_3$, two ESA bands were measured but the peak positions are shifted to smaller wavelengths. The Vis-band shows at 0.15 ps pump-probe delay a

peak at 440 nm and the peak position shifts to 425 nm at 4 ps delay. This is a shift of 802 cm^{-1}. The UV-band is growing up to 0.5 ps pump-probe delay and the peak position at that pump-probe delay is at around 350 nm. At 4 ps pump-probe delay the peak maximum is shifted to 348 nm and subsequently shifts to 346 nm at 8 ps delay. The same conclusion from this observation is drawn as for the $Mn(acac)_3$ complex, connecting the peak shift to lower wavelength with IVR and energy transfer to the solvent. In opposite to $Mn(acac)_3$, no long living state is observed and at 32 ps pump-probe delay, the absorbance change reached nearly zero over the whole spectral range. The same fitting procedure as for $Mn(acac)_3$ was used as well for Mn_3 and three decay constants were extracted. The DAS, showing the pre-exponential factors of the exponential decay functions are shown in Figure 3.4 **d**. The A_1 spectrum of the decay constant $\tau_1 = 180 \pm 10$ fs has a similar shape as the A_1 spectrum of $Mn(acac)_3$. It is just shifted towards the UV and so the same conclusion, a change in electronic state, is drawn. The A_2 and A_3 spectra both show the UV- and Vis-band. The difference between them is a peak shift to smaller wavelengths for the A_3 spectrum. So the $\tau_2 = 1.8 \pm 0.2$ ps decay constant is interpreted as vibrational cooling process. There is no longer time constant than $\tau_3 = 9 \pm 1$ ps. This is assigned as decay of the intermediate electronic state, back to the ground state.

In Figure 3.5 **b** the kinetic traces for the peak maxima of UV- and Vis-band at 350 nm and 440 nm are plotted, respectively. Beside the XPM signal, they show the multi-exponential decay and an oscillatory signal, which is seen easily in the raw data presented here. After subtracting the multi-exponential fit from the raw data, an average over the residues of the Vis-band (435 nm to 460 nm) was fitted by a single damped cosine fit according to equation 3.1. The frequency found was 181 ± 3 cm^{-1} and a damping constant of $\tau_{damp} = 360 \pm 15$ fs was extracted. The experimental Raman spectrum of the ground state in Figure 3.6 **b** was performed according to the description in Chapter 2. Beside several other peaks, one prominent peak at 213 cm^{-1} is visible, which is close to the peak in the Fourier spectrum ($\Delta E = 22$ cm^{-1}). The calculated Raman spectrum was calculated at the same level of theory as the $Mn(acac)_3$ spectrum and shows a good agreement with the measured Raman spectrum.

Beside the ultrafast TA experiments using $\lambda_{pump} = 400$ nm, also measurements with $\lambda_{pump} = 535$ nm were performed. This was for the reason to exclude any intra-ligand

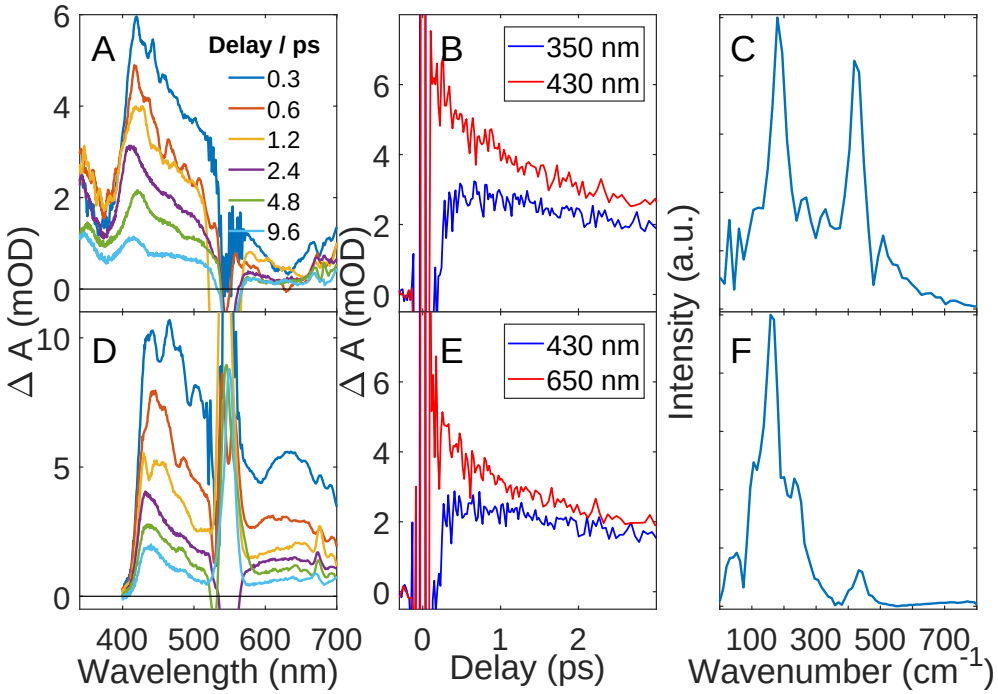

Figure 3.7: ***A*** *Difference spectra from the ultrafast TA measurement of the Mn_3 complex dissolved in ethanol ($c = 9.873 \times 10^{-4} mol/l$). $\lambda_{pump} = 535$ nm and 2.9 mJ/cm^2. Magic angle between pump and probe polarization planes.* ***B*** *Kinetic traces at selected wavelengths for the measurement in* ***A****.* ***C*** *Fourier transform spectrum of the fit residue from a global tri-exponential fit of the kinetic traces in* ***B****.* ***D-F*** *Difference spectra, kinetic traces and Fourier transform of the fit residue for $Mn(acac)_3$ ($c = 0.115$ mol/l). $\lambda_{pump} = 535$ nm and 1.5 mJ/cm^2. A difference in the measurement of Mn_3 and $Mn(acac)_3$ is that the step size of the pump-probe delay is 10 fs for the Mn_3 measurement and 20 fs for the $Mn(acac)_3$ data. This leads to the difference in the intensity ratio of the peaks at lower and higher wavenumbers in the Fourier spectrum.*

CT transitions, which were found in the calculations close to the excitation at 400 nm. The results in form of difference spectra are shown in Figure 3.7 **A** and **D**. The UV part below 400 nm is not shown in **D** for the $Mn(acac)_3$, because a high concentration of c = 0.115 mol/l was necessary to reach a satisfying absorbance level at 535 nm. The difference spectra for Mn_3 in **A** show the same two bands as for the TA measurement with $\lambda_{pump} = 400$ nm. The kinetics are difficult to extract from the ultrafast TA data shown in Figure 3.7 **B** and **E**, because the exponential decay is overlapped with the previously shown oscillatory behaviour. The damped oscillations were analysed in the same way as the $\lambda_{pump} = 400$ nm data and the Fourier transform spectra for both complexes are plotted in Figure 3.7 **C** and **F**. For the Mn_3 clearly two peaks at 180 cm^{-1} and 427 cm^{-1} are visible. The 180 cm^{-1} peak is a perfect fit to the measurement with

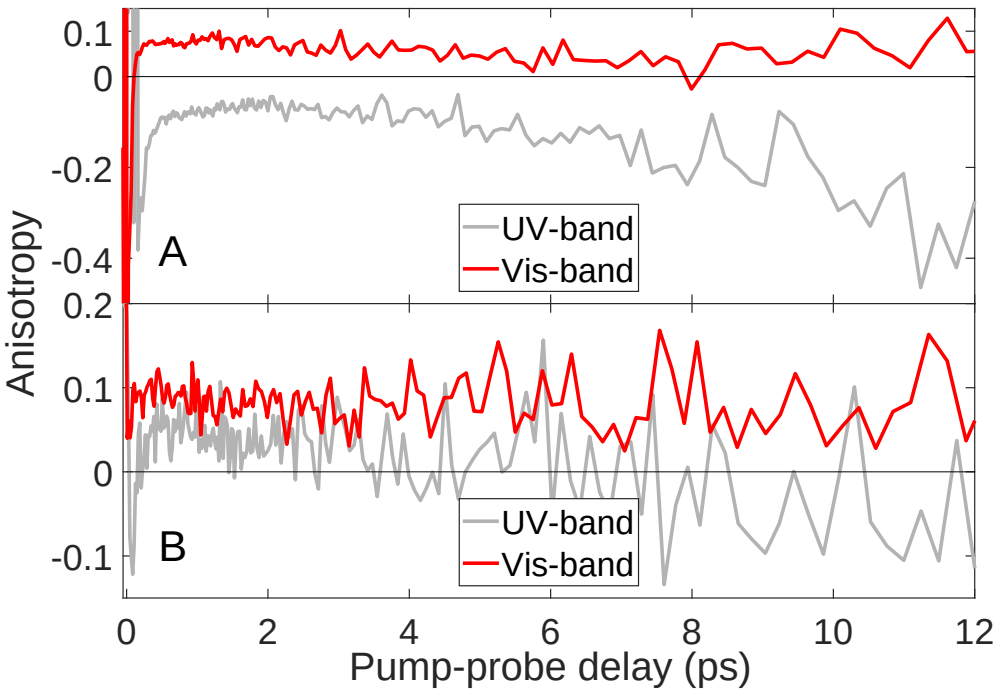

Figure 3.8: ***A*** *The averaged anisotropy data are plotted for Mn(acac)$_3$ (average from 353 nm to 363 nm (UV) / average from 478 nm to 506 nm (Vis)) and* ***B*** *for Mn$_3$ (average from 346 nm to 364 nm (UV) / average from 426 nm to 444 nm (Vis)) for the UV and Vis band as seen in Figure 3.4.*

λ_{pump} = 400 nm. The peak at 427 cm^{-1} is assigned to a ethanol peak known from literature [54–56] and from the ultrafast TA measurement performed in pure ethanol shown in Chapter 2. The Fourier transform spectrum of Mn(acac)$_3$ in Figure 3.7 **F** also shows the ethanol peak. The peaks assigned to modes of Mn(acac)$_3$ at 163 cm^{-1} and 232 cm^{-1} are in good agreement with the earlier described results.

Anisotropy measurements were also performed for Mn$_3$. The results are presented in Figure 3.8 **B**, where the r values are plotted against the pump-probe delay for the UV- and Vis-band. The signal for the UV-band seems to be positive for up to 2 ps, but since the signal-to-noise level is not good, no further observations can be made. The anisotropy r values for the Vis-band are around r = 0.1 up to the pump-probe delay where the noise level is to high to extract any further values.

3.2 Discussion

The assignment of the bands in the UV/Vis spectrum of $Mn(acac)_3$ is easily possible due to the literature [78, 79] and the CASSCF multi-configurational calculations performed by our collaborators [76] (see Appendix Figures 7.4 to 7.7). Three bands in the visible are assigned to dd-transitions. The $^5B_{1g}$ to $^5A_{1g}$ transition at > 800 nm, which can be explained in terms of atomic orbitals as d_{z^2} to $d_{x^2-y^2}$ transition on the Mn ion. One transition at 600 nm is assigned as $^5B_{1g}$ to $^5B_{2g}$ transition which translates in atomic orbital terms as d_{xy} to $d_{x^2-y^2}$ transition. The wavelength area at around 400 nm, which was used as pump wavelength for the ultrafast TA experiment, is assigned as $^5B_{1g}$ to ^5E_g or d_{xz} to $d_{x^2-y^2}$ and d_{yz} to $d_{x^2-y^2}$ transition overlapping with a ^{5}LLCT transition. For the ultrafast TA experiment using $\lambda_{pump} = 535$ nm a ligand centred or CT transition can be excluded because $\epsilon(535\text{ nm}) = 93\ l \times mol^{-1} \times cm^{-1}$ and it is unlikely that a CT or ligand centred transition has such a low extinction coefficient.

The analysis of the ultrafast TA data allowed us to extract four decay constants and their DAS in a sequential decay model. The fastest decay constant of $\tau_1 = 250 \pm 30$ fs is assigned as decay of the initially excited state, because of the fast spectral change in the UV and visible. The initially excited state is the ^5E_g state and it is assumed out of two reasons that the lowest metal centred (MC) excited state ($^5A_{1g}$) is populated via IC. The first reason is the long living state (>200 ps) that seems to be populated with τ_1. The second reason is that the ultrafast TA experiment with $\lambda_{pump} = 535$ nm shows the same spectra as the $\lambda_{pump} = 400$ nm after the initial 200-300 fs. Both indicates a population of the lowest MC excited state. This was also found in literature for $Cr(acac)_3$ [81] and $Fe(acac)_3$ [82]. The difference between the Cr, Fe and Mn version of the tris-acac complex is the JT distortion in the Mn version. Together with the d^4 electron configuration, this leads to the low energy spin allowed transition. The Cr(d^3) and Fe(d^5) analogues on the other hand show no JT distortion and the lowest excited MC state is a spin forbidden transition. So the fast process for $Mn(acac)_3$ is IC instead of ISC.

As mentioned earlier, the population of the ^5E_g state means that the $d_{x^2-y^2}$ is populated. The sudden shift of electron density from the d_{xz} or d_{yz} to the $d_{x^2-y^2}$ orbital means that the ligands will adjust to the new electronic structure of the Mn. The

logical way to react for the ligands is an elongation of the equatorial bond lengths, due to the higher electron density along the Mn-ligand bonds. The decay of this state is assigned to the fastest time constant of $\tau_1 = 250 \pm 30$ fs. With the decay of the ^5E_g state via IC into the $^5A_{1g}$ state, the MC d_{z^2} orbital is empty and a shortening of the axial bonds should be observed. So during the IC process, the d_{z^2} and the $d_{x^2-y^2}$ orbitals change their order and the bond lengths change accordingly. This leads the molecule into an equatorial JT distorted state.

In the $^5A_{1g}$ state IVR and energy transfer to the solvent with $\tau_2 = 1 \pm 0.2$ ps and $\tau_3 = 5.2 \pm 0.5$ ps take place. This is according to the blue shift of the peak and the spectral narrowing which was explained earlier in this chapter and can be observed in Figure 3.4 **a**. Vibrational cooling is not necessarily a sequential process, so an exponential fit does not express the actual cooling rate accurately. Highly excited vibrational states, tend to show a faster cooling rate, due to a higher density of vibrational states, than vibrational states already closer to the potential energy surface minimum [81].

Through the comparison of the Fourier transform spectrum of the residuals with the experimental and calculated Raman spectra it is possible to identify the vibrational modes which are involved in the coherent superposition (wave packet). As it can be seen in Figure 3.6 **a**, several wave packets are launched in the excited state, which can be tentatively assigned with the help of the calculated Raman spectrum (of the ground state) to normal modes around 200 cm^{-1}. Beside the strong peaks at 167 cm^{-1} and 215 cm^{-1} in the fft spectrum also weaker modes at higher energy are visible. The vibrational normal modes in the range of 159 cm^{-1} to 323 cm^{-1} are shown in Figure 3.9 and it is visible that, due to the flexible ligands, several normal modes are involved in the wave packet. The modes can be best described as symmetric stretch motions along all axes. But also ligand torsional scissor modes are observed. Most modes also show a large bending motion of the acetylacetonate backbone.

This is also known in literature where e.g. the $Fe(II)(bpy)_3^{2+}$ [32] and the $Cr(acac)_3$ [83] complexes also show wave packets composed of several vibrational modes. The frequencies found for the $Fe(II)(bpy)_3^{2+}$ complex are 127 cm^{-1}, 157 cm^{-1} and 225 cm^{-1} [30]. The frequencies found are in the similar range as for the $Mn(acac)_3$ complex. Auböck and Chergui assigned the 127 cm^{-1} and 157 cm^{-1} modes tentatively as non-totally symmetric Fe-N bending and stretching modes and the mode at 225 cm^{-1} as Fe-N

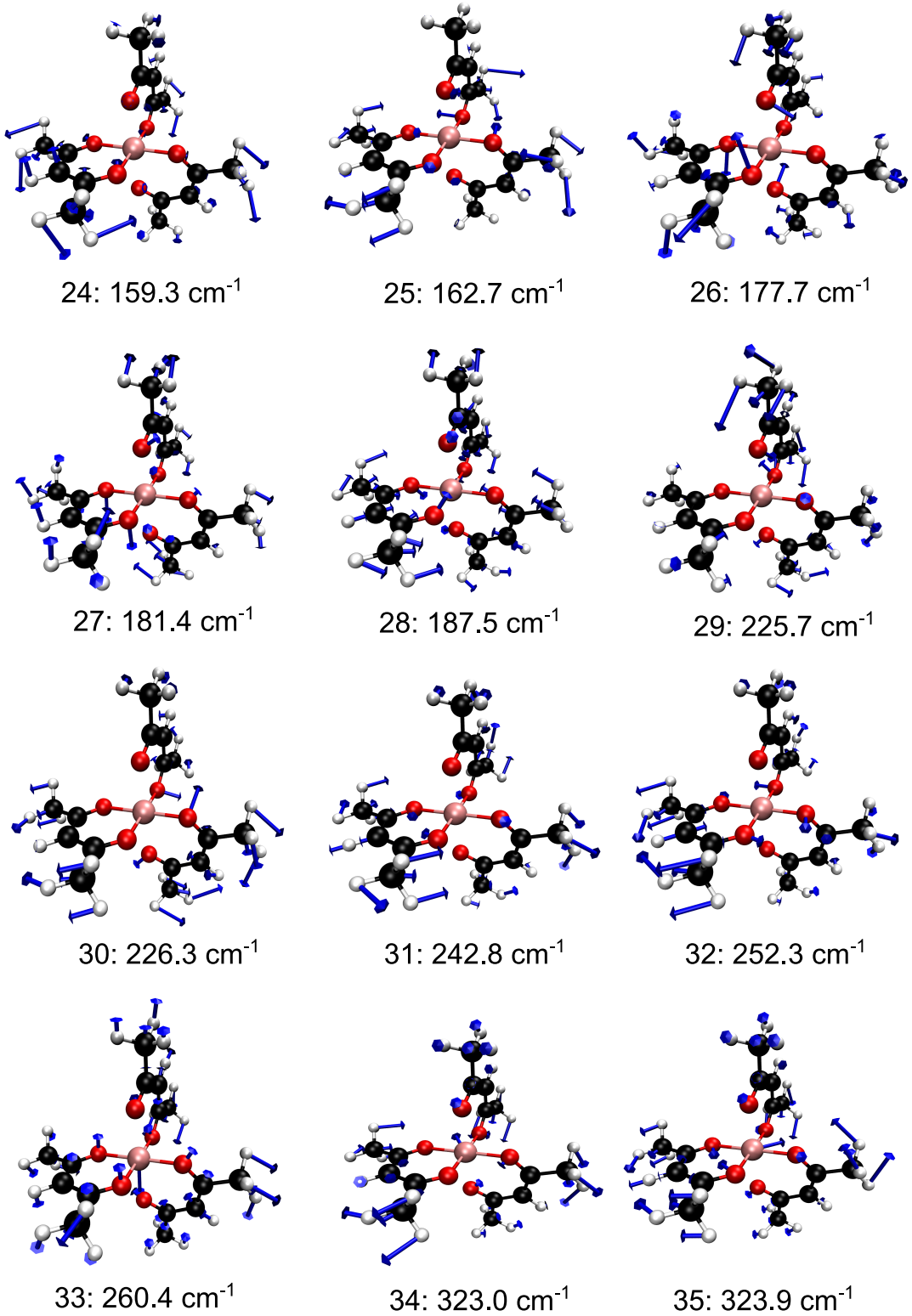

Figure 3.9: *Vibrational normal modes 24 to 35, calculated at the Def2-SVP level. The calculations were performed by our collaborator Julien Eng from Newcastle University. The normal modes show that there is not just one reaction coordinate for the transition from axial to equatorial JT distortion of the $Mn(acac)_3$.*

stretching mode in the HS state [30]. These modes are similar to the assigned modes for the $Mn(acac)_3$ complex. Also the formation process of the wave packet in the $Fe(II)(bpy)_3^{2+}$, an impulsive Fe-N bond length change due to ISC into a quintet state, is similar in $Mn(acac)_3$, where the impulsive bond length change is induced by the change of the JT distortion.

The $Cr(acac)_3$ complex showed mainly one vibrational mode at around 164 ± 20 cm^{-1}. The accuracy has to do with the extremely short lifetime of the wave packet of $\tau_{damp} = 70$ fs, where as a result just one oscillation is observed [83]. The authors of the paper assigned the mode tentatively as symmetric breathing mode or torsional scissor mode [83]. The energy of the vibrational mode and the assigned mode type are close to what is observed for the $Mn(acac)_3$. This is not surprising, since the ligands are equal and the Raman spectra are close. The excitation method of the wave packet is assigned by Schrauben et al. [83] as direct excitation through the pump pulse and the following retention of coherence during the ISC. This is different to $Mn(acac)_3$ and $Fe(II)(bpy)_3^{2+}$ where impulsive geometric changes after photoexcitation were assigned as excitation mechanism. Overall low energy vibrational modes play an important role for the photophysical process / reaction coordinate of the 3d metal complexes with bidentate ligands, be it for ISC as for $Cr(acac)_3$ and $Fe(II)(bpy)_3^{2+}$ or IC for $Mn(acac)_3$.

Taking into account the dephasing time of the wave packet for $Mn(acac)_3$ ($\tau_{damp} = 325 \pm 11$ fs) and compare it to τ_1 ($\tau_1 = 250 \pm 30$ fs) it is obvious, that the wave packet survives the IC process and dephases in the $^5A_{1g}$ state through IVR and cooling via the solvent. This interpretation is also supported by the $\lambda_{pump} = 535$ nm measurement, where the same frequencies were found in the Fourier spectrum. The long life time of the $^5A_{1g}$ equatorial JT distorted state is assigned to the flexible acac ligand. Even though they are bidentate ligands, they still allow a great flexibility to adjust to the new electron density on the Mn ion.

The summarized photocycle for the $Mn(acac)_3$ is shown in Figure 3.10 **a**. An assignment of the UV- and Vis-band in the difference spectra (Figure 3.4 **a**) is difficult, because of the complex electronic structure of the $Mn(acac)_3$ molecule. In the Appendix Figure 7.7, electronic transitions from the $^5A_{1g}$ state (now ground state) are shown. The calculations on the CASSCF/NEVPT2 level reveal three ^{5}MC states at 478 nm, 515 nm and 543 nm. These fit to the observed Vis-band and would explain the

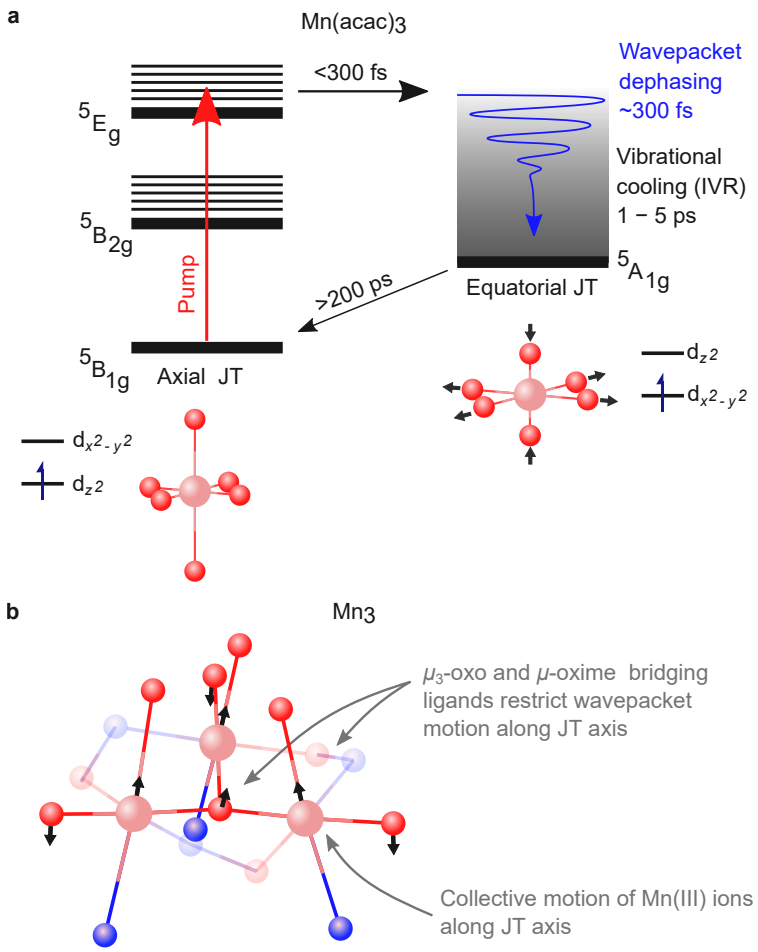

Figure 3.10: ***a*** *Model of the $Mn(acac)_3$ states involved in the dynamics after photoexcitation. Excitation (λ_{pump} = 400 nm) into the ^5E_g state in $Mn(acac)_3$ followed by a fast decay via IC into the $^5A_{1g}$ state. The population of the ^5E_g state leads to a switch from axial to equatorial JT distortion via the IC. A wave packet is launched in this displacive process. The wave packet dephases with 325 fs due to IC, IVR and vibrational cooling. The IVR and vibrational cooling take place on a 1-5 ps time scale. The lifetime of the $^5A_{1g}$ state in $Mn(acac)_3$ was found to be > 200 ps.* ***b*** *Scheme of the Mn_3 vibrational mode at 213 cm^{-1}. The movement can be described as a collective in-phase oscillation of all three Mn ions along the JT-axis, where the equatorial ligands bond lengths adjust according to the centre of mass. The Figure was taken from Liedy et al. [76] where also a video of the mode can be found in the supporting information.*

relatively weak absorbance change signal. At around 313 nm to 339 nm two quintet ligand centred transitions might contribute to the UV-band. Shifted MLCT to lower energies can not be excluded either. Also no LMCT transitions were observed in the calculations, even if that seems to be a feasible transition. So the ESA bands are not so clear to assign by comparison with the calculations. The most important point for the $Mn(acac)_3$ complex is the change of the axial to equatorial JT distortion.

The Mn_3 complex data are interpreted with the background of the $Mn(acac)_3$ results, knowing how close the ground state UV/Vis absorbance spectrum and the difference spectra from the ultrafast TA experiments are. The bands of Mn_3 in the visible are assigned as transitions between bands, formed by the atomic d-orbitals on the three Mn ions. The shoulder at 400 nm is assigned as overlap of d-band and ligand transitions. Except of different ligands, the main difference between $Mn(acac)_3$ and Mn_3 is the bridging via the μ_3-oxo and μ-oxime ligands. This bridging leads to a highly exchange correlated electronic structure and leads to a large number of spin states.

The results of the ultrafast TA experiments on Mn_3 are close to $Mn(acac)_3$ with the main difference of no observation of a long living state. Overall the first three decay constants are smaller for the Mn_3 than for the $Mn(acac)_3$. As for the $Mn(acac)_3$, $\tau_1 = 180 \pm 10$ fs is assigned as decay of the initial excited state into the equatorial JT distorted state with now occupied $d_{x^2-y^2}$ band. If this process is IC or ISC can not be determined. The intermediate decay constant of $\tau_2 = 1.8 \pm 0.2$ ps is assigned as vibrational cooling. $\tau_3 = 9 \pm 1$ ps is assigned as decay of the occupied $d_{x^2-y^2}$ band back to the ground state. This is the main difference to $Mn(acac)_3$, where τ_3 is assigned as vibrational cooling.

Also for the Mn_3 complex oscillations of a wave packet were found in the ultrafast TA data and were analysed as a single frequency of 181 ± 3 cm^{-1}. The Raman spectrum shows a strong peak at 213 cm^{-1} and it can be assigned according to the calculations as a collective in-phase asymmetric stretch-mode along the JT axis for all three Mn ions. The mode is shown in Figure 3.10 **b**. The axial Mn-O bond is getting shorter, while the axial Mn-N bond is elongated. The axial ligand-Mn bonds all get shorter and a flattening of the angle between the Mn-μ_3-oxo bonds in relation to the plane of all three Mn ions is observed. To prevent confusion about the shortening in the equatorial ligand plane in expectation of expansion due to population of the $d_{x^2-y^2}$ band, it is to

say that the movement also goes into the other direction and the calculated structure is not the turning point of the oscillation. So the expansion of the equatorial ligand-Mn bonds are included in this vibrational mode. The reason behind the longer dephasing time and the one involved normal mode in the wave packet is assumed to be the in-plane bridge bonding between the Mn ions. This restricts the space for expansion in the equatorial plane and allows for the delocalization of the excited state. The restriction in equatorial bond expansion also limits the lifetime of the excited state of the Mn_3 to $\tau_3 = 9 \pm 1$ ps. The $Mn(acac)_3$ on the other hand shows a lifetime of τ_4 longer than 200 ps.

The shift in the frequency of the found strong Raman peak at 213 cm^{-1} in relation to the peak in the Fourier transform spectrum at 181 ± 3 cm^{-1} is explained by assigning the wave packet to be formed in the electronic excited state. The reasons why the wave packet is assigned to the excited state are: The cosine-like nature of the oscillations implies that the wave packet is generated in a displacive way. This is a hint towards the excited state. Furthermore is the wave packet observed in the Vis-band. Since no GSB character of the ultrafast TA signal is expected in the Vis-band, this further strengthens the assumption of the wave packet being formed in the excited state.

Anisotropy measurements (see Figure 3.8) were also performed in order to gather more information about the change in JT distortion. Interpretation is difficult since MC transitions show generally little anisotropic signal. The nature of the pump transition needs to be considered in order to interpret the anisotropy data. The 400 nm excitation is assigned as MC d_{xz}/d_{yz} to $d_{x^2-y^2}$ transition (Q_4 and Q_5 in Figure 3.3 **d**). For a doubly degenerate electronic state (Q_4 and Q_5) an anisotropy value r = 0.7 for zero pump-probe delay and a decay to r = 0.1 as the two states dephase is expected [84–86]. The r values for $Mn(acac)_3$ are between 0.08 and 0.05 which indicates an already dephased degenerate state.

3.3 Mn_6 SMM results

Beside the Mn_3 SMM and the $Mn(acac)_3$ complex, ultrafast TA measurements, Raman and UV/Vis spectroscopy were also performed on a Mn_6 SMM. As mentioned earlier in this chapter the focus lies on the other two complexes, where the results can be

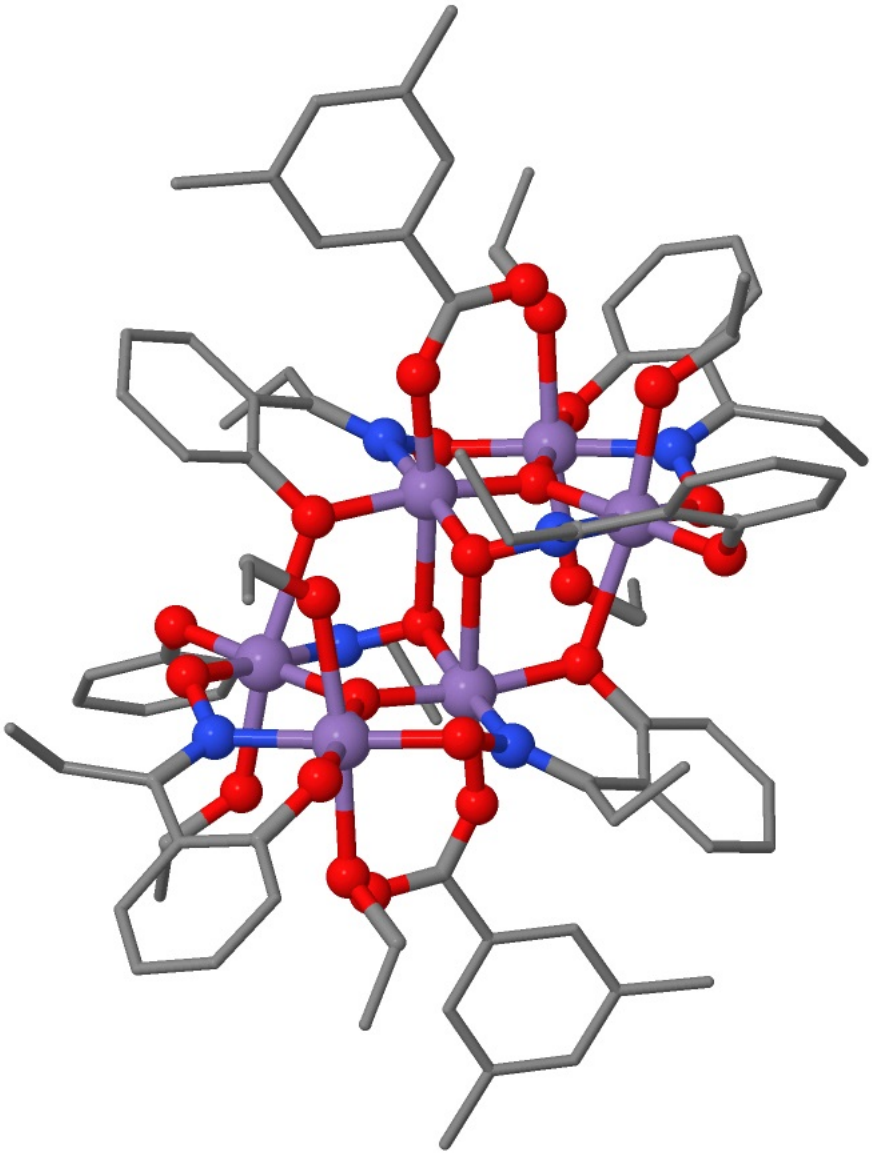

Figure 3.11: *Chemical structure of the Mn_6 complex ($[Mn(III)_6O_2(Et{-}sao)_6(O_2CPh(Me)_2)_2(EtOH)_6]$). The structure shows the close relationship with the Mn_3 complex. The Mn_6 complex looks like a two stacked Mn_3 complexes. The hydrogen atoms are neglected for clarity. Colour code: Manganese≡purple; oxygen≡red; nitrogen≡blue; carbon≡grey; hydrogen are omitted for clarity. The figure is based on the crystal structure data from Milios et al. [69].*

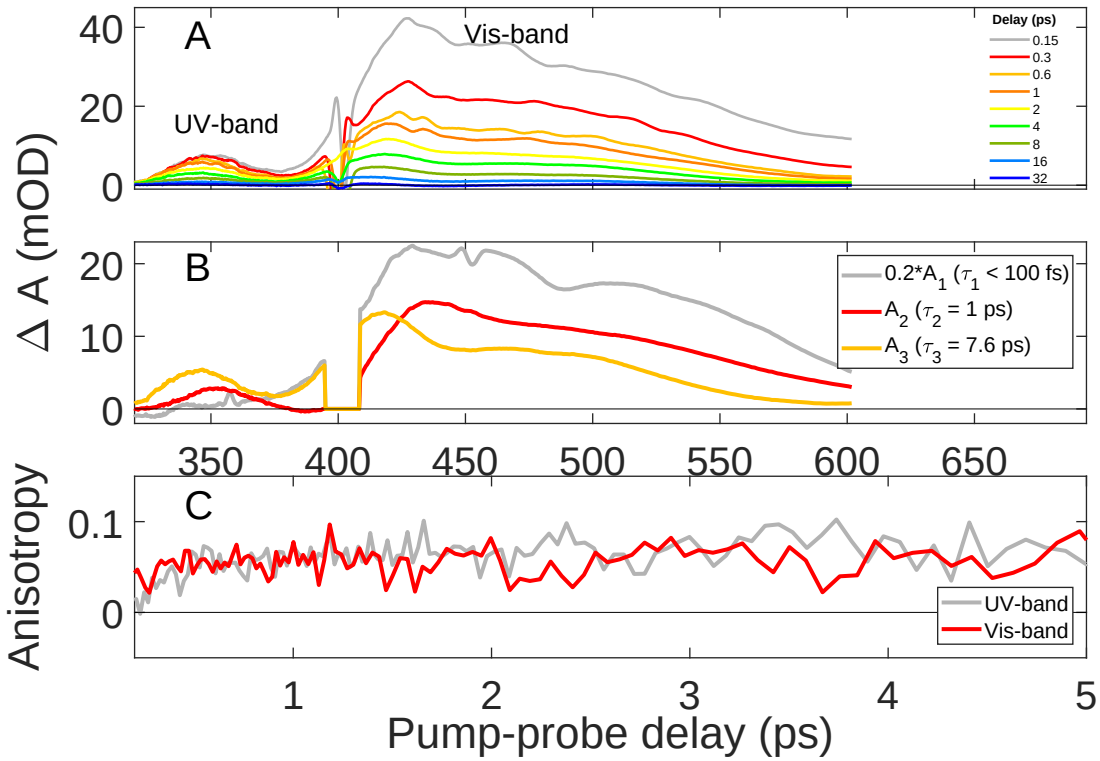

Figure 3.12: ***A*** *Difference spectra from the ultrafast TA measurement of the Mn_6 complex dissolved in ethanol ($c = 1.798 \times -3 mol/l$). $\lambda_{pump} = 400$ nm and a pump fluence of 3.3 mJ/cm^2.* ***B*** *DAS of a global tri-exponetial fit using the software package Glotaran [63]. Anisotropy traces according to Equation 3.2 from the ultrafast TA measurements using perpendicular and parallel polarization angles between pump and probe pulse.*

explained by and compared with the theoretical calculations of our collaborators. For Mn_6 this is not possible due to the high complexity. Nonetheless, the measurements show a good signal to noise ratio and are similar to the Mn_3 results. Figure 3.11 shows the chemical structure of the Mn_6 complex. The Mn_6 complex is constructed of two Mn_3 units interconnected via two out of the three oxime groups. As a result of the structural similarities, the UV/Vis absorbance spectrum in Figure 7.1 looks similar to the Mn_3 spectrum, but shows higher extinction coefficients. The absorbance bands can be assigned according to the interpretation for Mn_3.

Ultrafast TA experiments were performed according to the description in Chapter 2 using a solution of Mn_6 (c = 1.8 mmol/l). The results of the ultrafast TA experiments are shown in Figures 3.12, 3.13, 3.14, 7.2 and 7.3. In Figure 3.12 **A**, the difference spectra for selected pump-probe delays are plotted. As for the difference spectra of

Mn_3 and $Mn(acac)_3$, a UV- and a Vis-band were found. The absorbance change is around four times larger at 0.15 ps pump-probe delay than for the Mn_3 complex. The ultrafast TA data were analysed using the same global fit routine as for the other two Mn complexes. Three decay constants $\tau_1 < 100$ fs, $\tau_2 = 1 \pm 0.3$ ps and $\tau_{32} = 7.6 \pm 1$ ps were found. In comparison to the Mn_3 results, all decay constants are faster. The underlying physical processes are assigned the same as for Mn_3. The reason for the increased decay rates (shorter decay constants) can be explained by the size of the Mn_6 molecule and the large density of states. This should accelerate processes like IC or IVR. Anisotropy measurements were performed and analysed according to Equation 3.2. The anisotropy traces for the UV- and Vis-band are shown in Figure 3.12 **C**. An increase in anisotropy from almost zero to r = 0.05 at 0.5 ps is observed. It is assumed that the anisotropy is already dephased at this pump-probe delay.

For the Mn_6 complex also oscillations were found and are shown in Figure 3.13 **E** and **F**. In Figure 3.13 **E** the kinetic traces are shown and in **F** the residuals, averaged over the Vis-band are plotted together with a damped cosine fit according to Equation 3.1. A sum of two cosine functions were used to fit the residues. The frequencies found are 187 ± 3 cm^{-1} and 85 ± 4 cm^{-1}. The damping constant found is 370 ± 20 fs. The Fourier transform spectrum together with the measured ground state Raman spectrum are plotted in Figure 3.14. Two major peaks at 100 cm^{-1} and 182 cm^{-1} are found together with some smaller peaks. The 187 cm^{-1} peak fits to a strong Raman peak. The 100 cm^{-1} peak cannot be observed in the Raman spectrum because of technical limitations, but fit well to the frequency found in the cosine fit. The 182 cm^{-1} mode is around the same energy that was found in Mn_3 (181 ± 3 cm^{-1}). Thus, it might be assigned to the same kind of mode, where all Mn ions oscillate in phase. The 100 cm^{-1} mode cannot be assigned due to the difficulties performing adequate calculations. Due to size of the Mn_6 and the low frequency of the mode, implying movement of heavy parts, this mode might be explained as mode involving the movement of both Mn triangles. As for the Mn_3 complex and with the same argumentation, the wave packet is assigned to the excited state.

3.4 Conclusions

There are several conclusions that were made using the results of the ultrafast TA, the Raman spectroscopy and the multiconfigurational calculations. For the $Mn(acac)_3$, the calculations show that the first excited state is a shift from axial JT distortion to equatorial. This result is used together with the ultrafast TA results to assign the long living state in $Mn(acac)_3$ to the equatorial JT distorted state. The found wave packet, extracted from oscillations in the TA signal, is attributed to the excited state and is interpreted as result of the changed electronic structure and the following structural adjustment into the equatorial JT distorted state. For the Mn_3 it was found that the strong equatorial bonding is blocking the relaxation channel into a equatorial JT distorted state. This, together with the delocalization of the excited state, leads to the single mode wave packet and the longer dephasing time. The change of JT distortion after photoexcitation was previously found in literature in a perovskite manganite [87]. The found vibrational coherences in the Mn_3 SMM are opening ways for new ideas towards control and function-enhancement in complex chemical systems. The field of ultrafast coherences is currently a developing area [88]. The field of (ultrafast) photophysics of transition metal complexes showed recently a couple of interesting observation of coherences. E.g. the vibrational wave packet survives ISC (retaining the phase relation between several excited vibrational states) in $Cr(acac)_3$ [83], di-Pt(II) complexes showing coherent Pt-Pt stretch vibrations over several ps [47,89] and Cu(II) complexes show a "flattening" after excitation where JT distortion plays a significant role [13]. The results shown here are a contribution to the field in showing that JT distortion can be controlled on an ultrafast time scale and that vibrational coherences can be achieved even in metal complexes with up to six Mn ions. The Mn_{12}Ac SMM also shows a strong Raman peak at 209 cm^{-1} [90] and it was shown that continuous light can induce magnetization changes [91]. These two studies, together with the results shown here indicate, that the control of the JT distortion can be achieved for a larger group of Mn based SMMs.

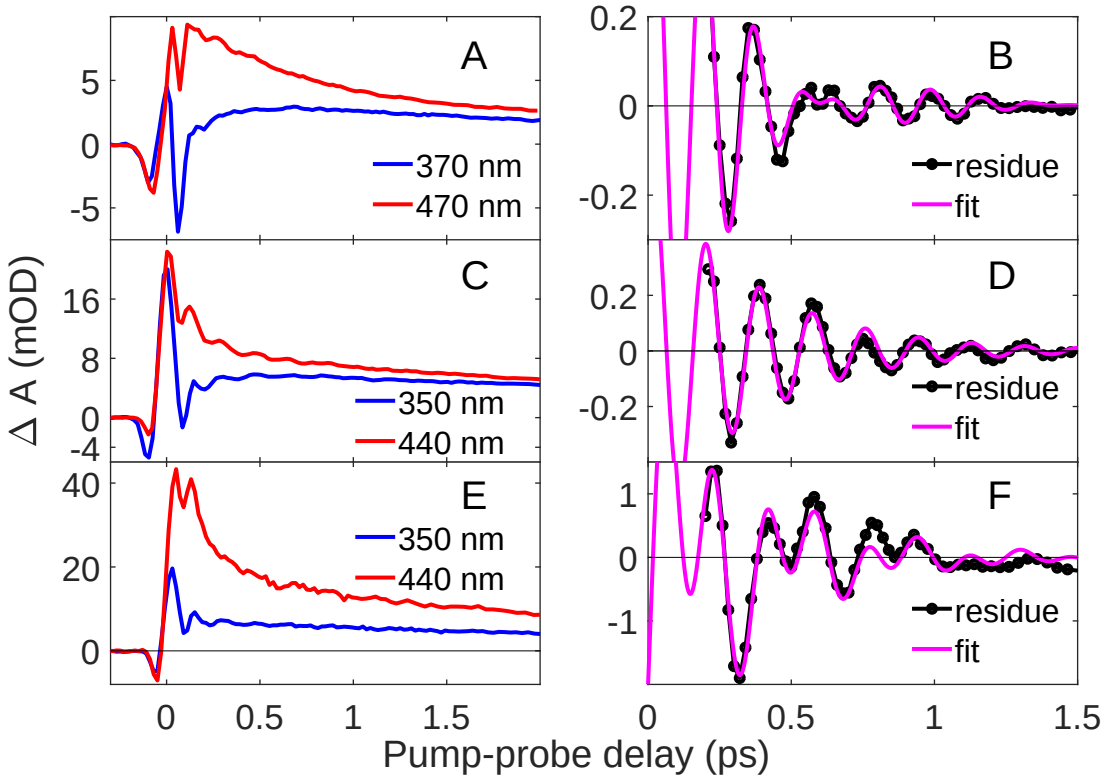

Figure 3.13: ***A-B*** *Kinetic traces from the ultrafast TA measurement of the* $Mn(acac)_3$ *complex dissolved in ethanol and the fit residues from a global tri-exponential fit, fitted with a sum of two damped cosine functions. The found periods are 160 ± 5 fs and 196 ± 6 fs and the dephasing time is 325 ± 11 fs.* ***C-D*** *Kinetic traces from the ultrafast TA measurement of the* Mn_3 *complex dissolved in ethanol and the fit residues from a global tri-exponential fit, fitted with a damped cosine function. The found period is 184 ± 3 fs and the dephasing time is 360 ± 15 fs.* ***E-F*** *Kinetic traces from the ultrafast TA measurement of the* Mn_6 *complex dissolved in ethanol and the fit residues from a global tri-exponential fit, fitted with a sum of two damped cosine functions. The found periods are 178 ± 3 fs and 390 ± 20 fs and the dephasing time is 370 ± 20 fs. For all shown measurements:* λ_{pump} *= 400 nm and a pump fluence of 3.3 mJ/cm*^{2}*. Magic angle between pump and probe polarization planes.*

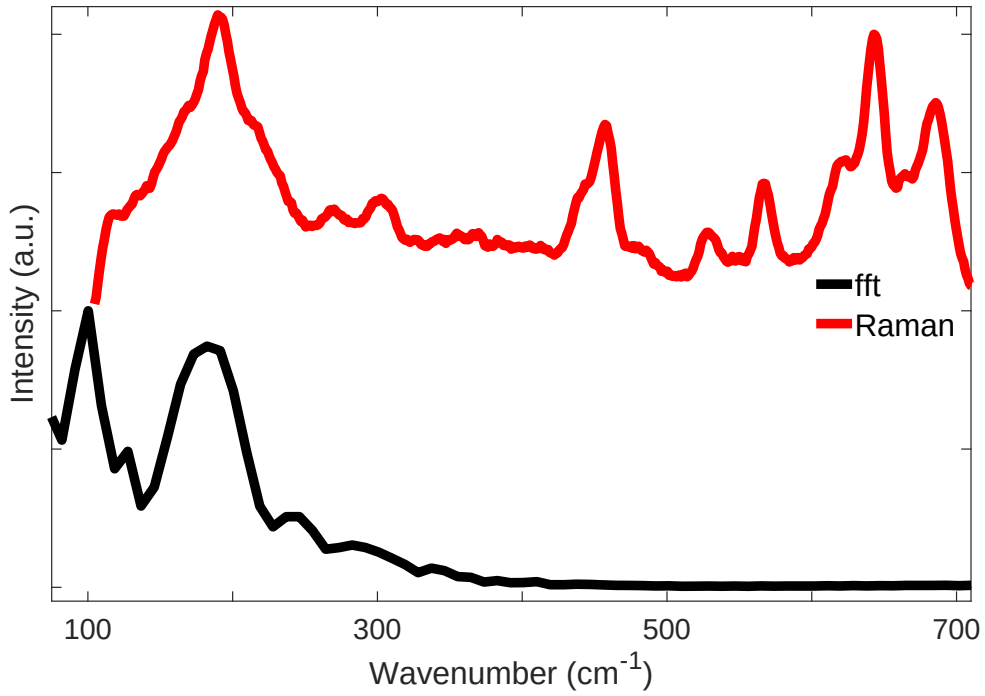

Figure 3.14: *Raman spectrum of a crystal grain of the Mn_6 complex (red spectrum) using a 785 nm laser. Fourier transform of the in Figure 3.13* ***F*** *shown fit residues. The peaks at 100 cm^{-1} and 182 cm^{-1} fit well to the converted periods (187 cm^{-1}) and 86 cm^{-1}) from the double cosine fit.*

Chapter 4

Photoinduced dynamics in an exchange-coupled trinuclear iron cluster

In this chapter, photophysics of $Fe_2^{III}Fe^{II}O(CH_3CO_2)_6(H_2O)_3$ (Fe_3) are presented. Techniques such as static UV/Vis spectroscopy, vibrational spectroscopy, static magnetic circular dichroism (MCD) spectroscopy, ultrafast TA measurements and theoretical calculations (from a group in the physics department at the University of Kaiserslautern) are presented. The Fe_3 complex is a highly correlated system with three coupled spin centres. Since many magnetic molecular systems are highly correlated systems, this complex is of great interest. The electron, spin and vibrational coupling between the iron centres and their influence on the ultrafast excited state dynamics is therefore of general interest in this field.

The neutral Fe_3 complex (see Figure 4.1) is a well studied coordination complex [93–95]. The Fe_3 complex was synthesized in the group of Euan Brechin at the University of Edinburgh according to the instructions in Blake et al. [96]. The three Fe ions are coordinated by six carboxylate ligands, three water molecules and one μ_3-oxo ligand. The coordination geometry is distorted octahedral for all three Fe ions, while the overall symmetry of the molecule is assumed as D_3. Two Fe ions are formally in oxidation state +III and one Fe is in oxidation state +II; all three Fe ions are high spin [97]. The μ_3-oxo ligand coordinates to all three Fe ions and the bond lengths are

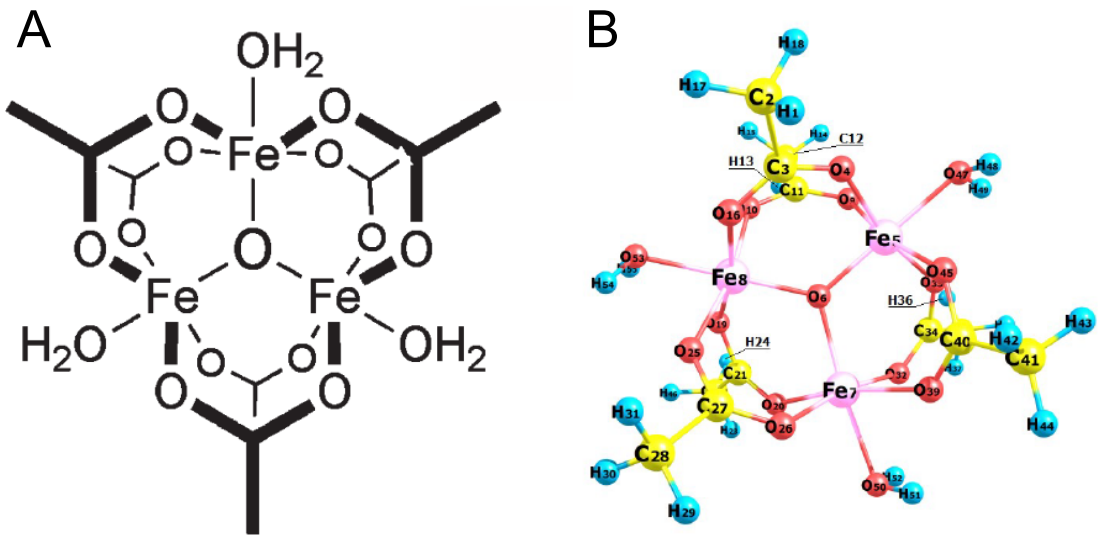

Figure 4.1: ***A*** *Chemical structure of the $Fe_2^{III}Fe^{II}O(CH_3CO_2)_6(H_2O)_3$ complex. The figure was taken from Li et al. [92].* ***B*** *Optimized structure of the triplet ground state of the $Fe_2^{III}Fe^{II}O(CH_3CO_2)_6(H_2O)_3$ complex at the Hartree-Fock level of theory (3-21G basis set). The structure is dominated by the triangular shape of the three Fe ions, which are linked by a μ_3-oxo bridge, connecting all three Fe centres. Together with the carboxylate ligands, this structure provides a pathway for exchange interactions. The figure was taken from Liedy et al. [80]. Colour code: oxygen≡red; iron≡pink; carbon≡yellow; hydrogen≡blue.*

almost equal [98]. Together with the carboxylates, the μ_3-oxo bridge opens up possible pathways for exchange interactions. The exchange energy was determined to be around $J = -50$ to -10 cm^{-1} based on the $-2J$ formalism [99, 100]. The complex is a mixed valence compound where one electron is at r.t. delocalized via the μ_3-oxo bridge over all three Fe ions. The electron-hopping time from one ion to the other was determined to be 2.5 ns [99]. This means for the later shown ultrafast measurements, that the excess electron can be seen as localized on one Fe side. Furthermore this complex shows a phenomenon called spin frustration, where it is impossible to have all the spins anti-ferromagnetically coupled [101]. This is also the reason why the Fe-oxo bond lengths are not equal and that the effective spin state of the Fe_3 complex was determined by calculations to be S = 1 at 0 K, meaning a spin multiplicity of 2S+1 = 3. For higher temperatures, a change of the effective spin towards the high temperature limit of S = 2 is expected [101].

Figure 4.2 shows the UV/Vis/NIR absorbance spectrum of the Fe_3 complex dissolved in double-distilled water. The black curve shows the spectrum from 1100 nm to 250 nm.

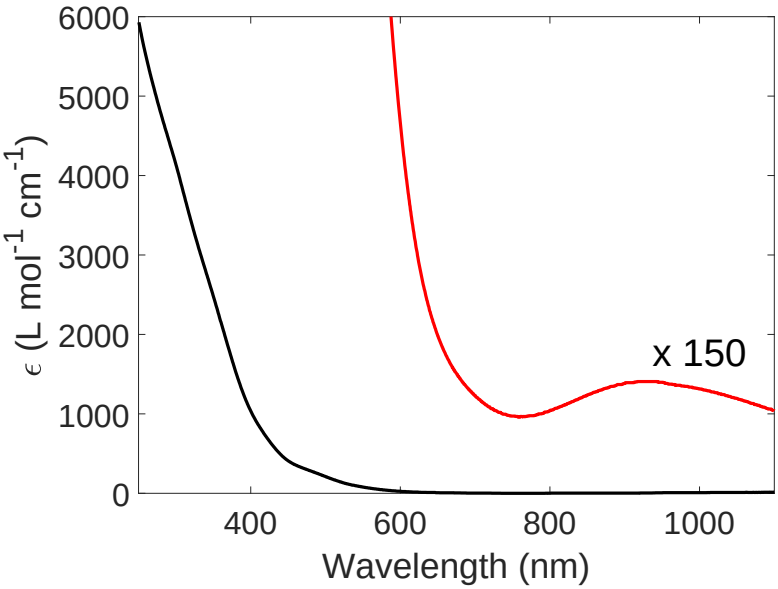

Figure 4.2: *Absorption spectrum from the UV to the NIR of the Fe_3 complex in water. The NIR part is zoomed in to see the lowest-energy transition at 930 nm.*

A shoulder at 480 nm is clearly visible. Otherwise, the spectrum shows a growth of the extinction coefficient towards shorter wavelengths. A weak low-energy band with a maximum at around 930 nm is visible (Figure 4.2, red curve). It is known that water shows a vibrational hot band at 950 nm. Accordingly, a cuvette with water was used as reference so that no bands of the solvent are visible in the shown spectrum. The whole spectrum is in good agreement with literature [99]. In the UV region strong ligand-field and CT transitions overlap and their tail reaches into the visible and gives this complex its red-brown colour [102]. The shoulder at 480 nm was also found in the literature for a Fe^{III}–O–Fe^{III} ($Fe_2^{III}O(OAc)_2(Me_3tacn)_2$) complex and was assigned as a mixture of d-d and oxo $\rightarrow Fe^{3+}$ CT transitions [103–105]. This is possible due to the covalent nature of the μ-oxo bridge connecting the Fe sides. The low energy transition was observed earlier in Fe(III) dimers [99] and was assigned as ${}^6A_1 \rightarrow {}^4T_{1,2}$ spin-forbidden transition [103–105]. It shows an increased oscillator strength in relation to monomeric Fe(III) complexes due to coupling of the ${}^4T_{1,2}$ excited state to the ${}^6A_1$ ground state of the neighbouring Fe ion [105].

Quantum mechanical calculations at the Hartree-Fock and CCSD (Coupled Cluster with single and double excitations) level of theory (3 - 21G basis set) were performed by Rui Shi, Georgios Lefkidis and Wolfgang Hübner at the University of Kaiserslautern.

State	Multiplicity	Energy (eV)
26	1	6.309
25	3	6.284
24	3	6.247
23	1	5.927
22	3	5.571
21	1	5.382
20	3	5.368
19	3	4.628
18	1	4.348
17	1	3.961
16	3	3.881
15	1	3.455
14	3	3.420
13	3	3.353
12	3	3.264
11	1	3.145
10	3	2.80
9	1	2.760
8	3	2.505
7	3	1.969
6	1	1.423
5	3	1.362
4	1	1.345
3	1	0.435
2	3	0.329
1	3	0.000

Table 4.1: *EOM-CCSD (EOM ≡ equation of motion) and CCSD energies and multiplicities of the lowest 26 many-body electronic excited states. These results use the Hartree-Fock level of theory for the triplet ground state and the 3-21G basis set. The calculations were performed by Rui Shi, Georgios Lefkidis and Wolfgang Hübner at the University of Kaiserslautern. The table was taken from [80].*

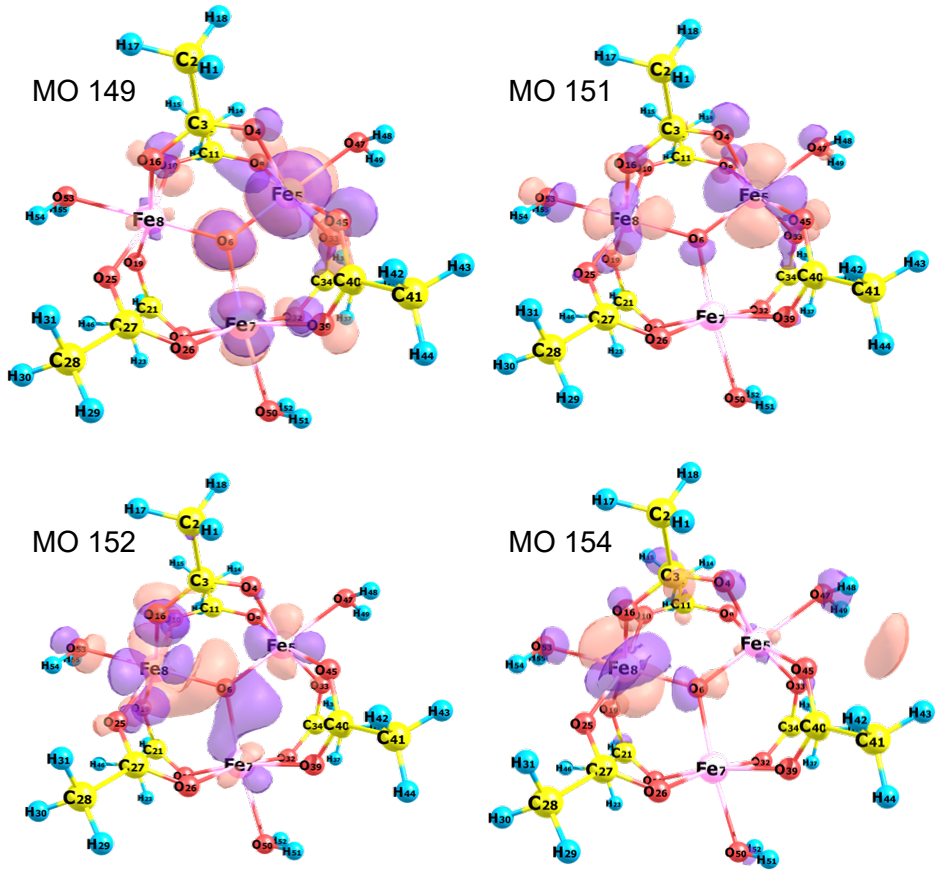

Figure 4.3: *Molecular orbitals involved in the main virtual transitions* 149 → 152, 149 → 154, 151 → 152, *and* 151 → 154 *of the correlated CCSD many-body function (first excited state, which is also the reference state), with transition amplitudes 0.231, 0.115, 0.234, and 0.189, respectively. In order to enhance visibility of the orbitals, the structure is rotated with respect to Figure 4.1. The figure was taken from Liedy et al. [80]. Colour code: oxygen≡red; iron≡pink; carbon≡yellow; hydrogen≡blue.*

They calculated the energy of the 25 lowest singlet and triplet electronic states above the triplet ground state. The energies and the multiplicities are shown in Table 4.1. The energy levels 2 and 3 in Table 4.1 are in the IR at similar energies to the OH stretch vibration of the water molecules, which makes analysis difficult. The calculated states 4 and 5 are in good agreement with the peak at around 930 nm in the absorbance spectrum in Figure 4.2. State 7 coincides with the rise in the extinction coefficient at around 630 nm and state 8 coincides with the shoulder at 480 nm. Figure 4.3 shows the one electron molecular orbitals, which are involved in the main virtual transitions 149 → 152, 149 → 154, 151 → 152, and 151 → 154 of the correlated CCSD many-body function for the first excited state (0.329 eV). But they also contribute to all d-character

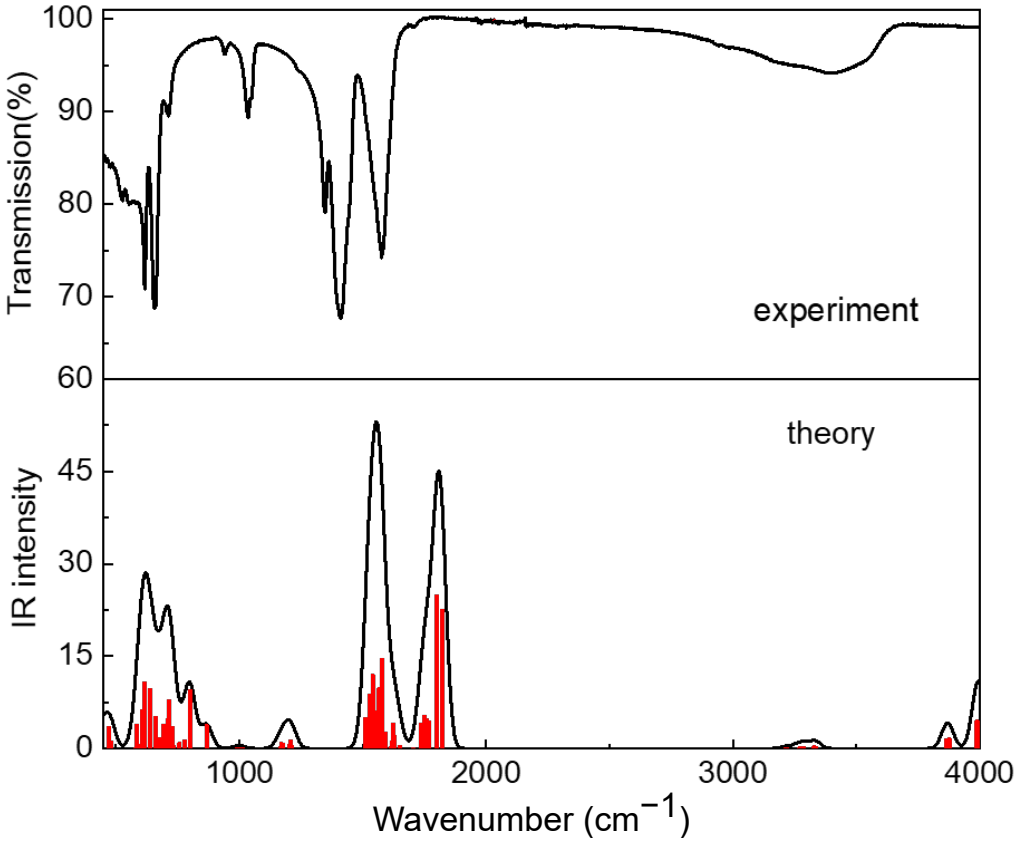

Figure 4.4: *Experimental FT-IR ATR vibrational spectrum obtained on a powder sample of Fe_3 (upper panel). Theoretical (lower panel) bands of the Fe_3 vibrational modes at the Hartree-Fock level (for triplet ground state)(red lines) fitted with Gaussian curves to simulate the experimental spectrum. The Gaussian curves used, were set to a FWHM of 54 cm^{-1}. The figure was taken from Liedy et al. [80].*

transitions up to 2 eV [80]. The shape of the orbitals on the Fe centres show that these states are formed partially by d-orbitals of the Fe ions. In all four orbitals, electron density can be found on at least two Fe ions and on the central μ_3-oxo bridge. This shows the electron delocalization via the μ_3 oxygen and explains the increased oscillator strength in relation to mono-nuclear iron complexes. The electron density shifts on at least two Fe centres and on the ligands for a d-d transition which always introduces some (LM)CT character.

4.1 Vibrational spectrum

An FT-IR spectrum for the Fe_3 complex in the solid state was performed by using the ATR mode of an FT-IR spectrometer. This is shown in the upper spectrum of

Figure 4.4 and it fits well to the spectrum found in the literature [99]. The peak with a maximum at 3400 cm^{-1} and two shoulders at 3550 cm^{-1} and 3190 cm^{-1} are assigned to the OH stretch vibration. The shoulder at 3550 cm^{-1} and the peak at 3400 cm^{-1} are assigned to the water in the crystal structure. The shoulder at 3190 cm $^{-1}$ is assigned to the coordinated water, because of the large shift in relation to the free water OH stretch energy.

At lower energies two weak peaks at 2982 cm $^{-1}$ and 2940 cm^{-1} are overlapping with the very broad OH stretch band. The energetic position fits to aliphatic CH stretch-modes. By looking at the molecular structure of the complex (see Figure 4.1), it is clear that there should be just one mode, since all six carboxylate groups are chemically equivalent. So the two peaks are assigned to the CH stretch-mode of the carboxylate groups, which are split by intermolecular interactions in the crystal structure.

The strong peak at 1580 cm^{-1} is assigned as H-O-H bend mode, which is shifted to lower energies due to the coordination. The two peaks at 1411 cm^{-1} and 1348 cm^{-1} are tentatively assigned as C=O stretch mode where the oxygen is coordinated to the Fe.

Besides shifting ligand modes to lower energies, transition metal coordination complexes also have vibrational modes of the metal with the ligand donor groups as well as skeletal vibrations, which are unique for the respective coordination complex. Due to the high mass of the transition metals, the direct metal-ligand (e.g. M-O, M-N,...) vibrational modes are at low energies. The same is true for the skeletal modes, where large parts of the metal complex are moving.

In the finger print region stretch vibrations of the Fe with ligands as well as scissor and bending modes of the ligands can be found. The mode at around 500 cm^{-1} is assigned as asymmetric Fe_3O stretch vibration of the Fe_3 complex [99, 106–109]. The symmetric Fe_3O stretch vibration and other Fe-O modes are at lower energy and some are only Raman but not IR active [106]. Other Fe complexes show Fe-ligand modes also at low energies. The $Fe(acac)_3$ complex shows a O-Fe-O stretch mode at 226 cm^{-1} [110].

In Figure 4.4, the lower spectrum shows the calculated line spectrum (red lines) and the simulated spectrum. It is based on the line positions and the intensity, fitted with a Gaussian curve (FWHM to 54 cm^{-1}). The vibrational spectrum was calculated by our collaborators in the following way:

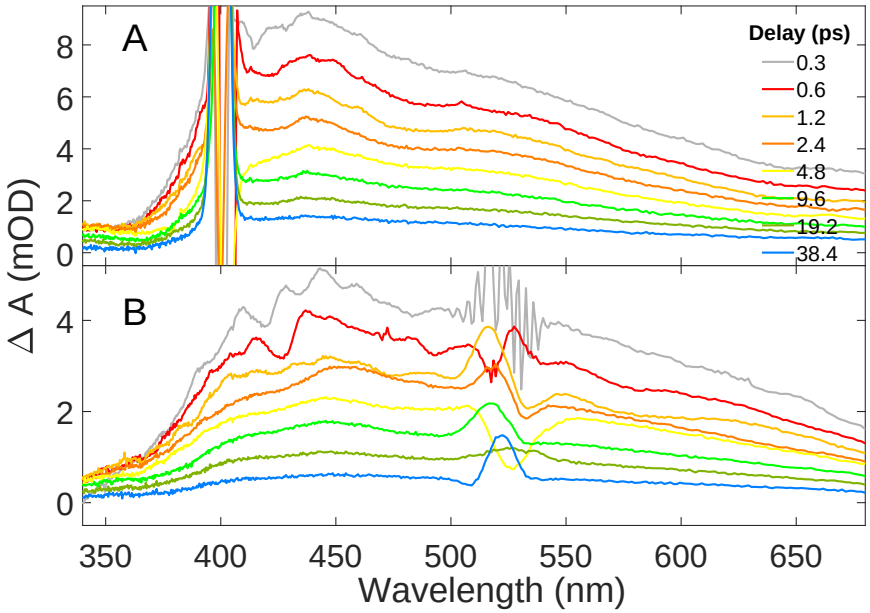

Figure 4.5: *Femtosecond TA difference spectra of the Fe_3 complex in water for selected time delays. In* ***A*** $\lambda_{pump} = 400$ *nm and in* ***B*** $\lambda_{pump} = 520$ *nm. The noise around the pump wavelengths in* ***A*** *and* ***B*** *is due to scattered pump light.*

First the calculations were performed at the Hartree-Fock level of theory (both for a triplet and a singlet ground state). The force matrix was determined and normal modes and their respective vibrational frequencies were extracted. For selected normal modes, an energy snapshot at the EOM-CCSD (EOM = equation of motion) level for eleven (in some cases thirteen) points along the normal mode were calculated and the total-energy curve was fitted to a quadratic and a cubic polynomial [111]. A scaling factor of 0.943 was used [112].

Aside from the modes at 3800 cm $^{-1}$, which again overlap with electronic transitions, the simulated spectrum fits well to that obtained experimentally.

4.2 Ultrafast transient absorption

Ultrafast TA measurements of the Fe_3 complex in water were performed using the set-up described in chapter 2. The aim was to study the initial dynamics after photo-excitaion of such a highly correlated system.

For the ultrafast TA experiments, solutions of Fe_3 in water were prepared with concentrations of 6.53 and 12.0 mM. The less concentrated sample was used for the ex-

periment using the $\lambda_{pump} = 400$ nm SHG of the fundamental laser wavelength and the more concentrated solution was used for the $\lambda_{pump} = 520$ nm excitation from the two stage NOPA (TOPAS light conversion). The laser fluence was 4.07 mJ/cm^2 for $\lambda_{pump} = 400$ nm and 1.48 mJ/cm^2 for $\lambda_{pump} = 520$ nm. For each time delay, an average over 1000 spectra was taken and for $\lambda_{pump} = 400$ nm, the measurement was repeated four times and for $\lambda_{pump} = 520$ nm 16 times. So in total for the $\lambda_{pump} = 400$ nm measurement 4000 spectra per time delay are averaged and for the $\lambda_{pump} = 520$ nm measurement 16,000 spectra.

The results of the ultrafast TA measurements in water solution are shown in Figure 4.5. In part **A**, difference spectra for several pump-probe delays for the excitation with $\lambda_{pump} = 400$ nm and in **B**, the difference spectra for the excitation with $\lambda_{pump} = 520$ nm are shown. In both sets of difference spectra, scattered pump light is clearly visible at the pump wavelength. By excitation with $\lambda_{pump} = 400$ nm in panel **A**, a broad ESA over the whole visible range can be seen. There are clearly two broad and unresolved bands at 440 nm and 530 nm visible. Below the pump wavelength of 400 nm, a drop in absorbance change is observed. This is most likely the overlap of ESA with the GSB. When exciting at $\lambda_{pump} = 520$ nm the drop as well as the the band at 440 nm are also visible in the spectra. One additional band at 405 nm, which is overlapping with the $\lambda_{pump} = 400$ nm measurements pump scatter, was found. For the $\lambda_{pump} = 520$ nm measurement, the band at 530 nm can not be seen due to overlap with the scattered pump light. The described spectral structure can be seen up to a pump-probe delay of 38.4 ps. In the literature, the $[Fe_3(\mu_3{-}O)(O_2CPh)_6(C_5H_5N)_3]ClO_4$ complex from Hanna et al. [113] also showed a broad ESA over the whole visible range. In the $[Fe_3(\mu_3{-}O)(O_2CPh)_6(C_5H_5N)_3]ClO_4$ complex all three iron ions are in oxidation state +3 and the ligands are changed in relation to the Fe_3 complex presented in this chapter. Hanna et al. [113] observed the ESA band at 530 nm. However, due to the bandwidth limitations of their white light probe, the bands at 405 nm and 440 nm were not found.

To extract the kinetic information from the ultrafast TA measurements, the resulting data was fitted with a global tri-exponential fit according to Equation 2.2 using the Glotaran program package [63]. The fits for the 440 nm kinetic trace is shown in Figure 4.6 for both pump wavelengths: $\lambda_{pump} = 400$ nm in **A** and $\lambda_{pump} = 520$ nm in **B**. The fits (black solid line) obviously are a good match with the measured data (red circles).

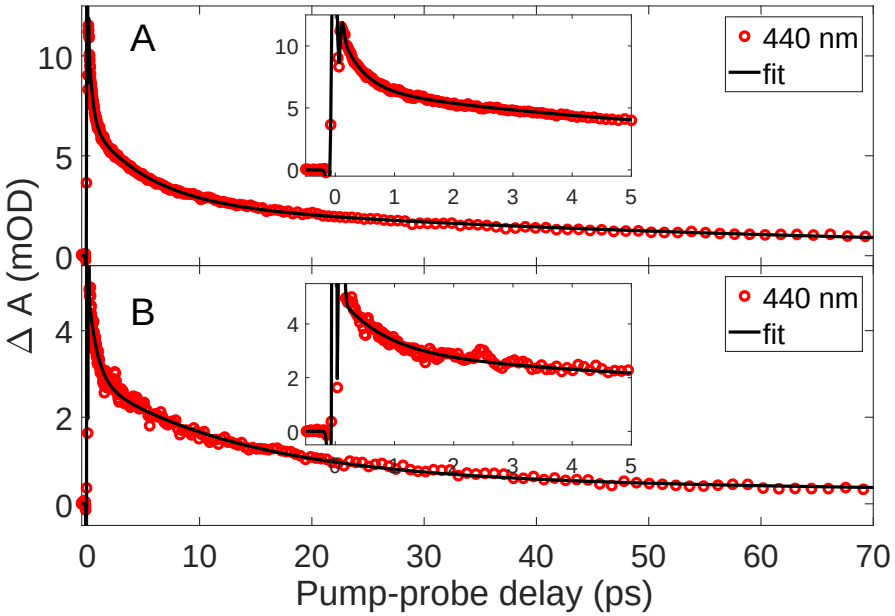

Figure 4.6: *Kinetic traces at a probe wavelength of λ = 440 nm from the ultrafast TA measurement of Fe_3 in water. In* ***A*** *using a pump wavelength of λ_{pump} = 400 nm and* ***B*** *λ_{pump} = 520 nm. The insets show the dynamics for pump-probe delays up to 5 ps. Red dots correspond to experimental data points, while the black lines are tri-exponential fits from the global analysis using Glotaran [63].*

The decay constants from the fits can be found in Table 4.2. By comparing the time constants of the λ_{pump} = 400 nm measurement with the λ_{pump} = 520 nm measurement, it can be seen that longer wavelength excitation shows slower kinetics. For at least the first two decay constants τ_1 and τ_2. Due to the maximum pump-probe delay of 80 ps, the uncertainty for τ_3 is assumed to be larger than is shown in Table 4.2. This was tested with another measurement up to 500 ps using λ_{pump} = 400 nm as pump wavelength (see Figure 7.8 and 7.9 in the Appendix 7). This measurement showed that τ_3 = 31 $\pm$0.4 ps (see Table 4.2) and that there is a even longer decay constant which is on the scale of $>$ 1 ns. This means that a long-lived state is populated, which is the key observation in analysis of the kinetics. This is also in agreement with Hanna et al. [113], where a 250 ps decay constant was found.

The DAS, showing the amplitudes for the three decay constants from the exponential fit according to Equation 2.2 are plotted in Figure 4.7. For the DAS of the λ_{pump} = 400 nm measurement in Figure 4.7 **A**, the decay kinetics are dominated by the short time constant τ_1 (amplitudes A_1 are plotted as grey solid line). In the visible part of the spectrum, A_1 shows the largest amplitude in relation to A_2 and A_3. The A_1

	τ_1(fs)	τ_2(ps)	τ_3(ps)
400 nm (80 ps)	360 ± 30	5.3 ± 0.6	65 ± 5
400 nm (500 ps)	340 ± 50	3.9 ± 0.4	31 ± 4
520 nm (80 ps)	460 ± 40	8.9 ± 2	88 ± 12

Table 4.2: *Decay constants τ_i from the global analysis (Glotaran program package [63]). For the maximum delay 80 ps (400 nm (80 ps) and 520 nm (80 ps) rows) measurements, a tri-exponential fit was used. For the 500 ps (400 nm (500 ps) row) maximum delay, a fourth decay constant of more then 1 ns was added to fit the long-lived component. The corresponding amplitudes for all wavelengths are shown in the DAS in Figure 4.7 and in the Appendix Figure 7.8.*

spectrum replicates the broad ESA bands at 440 nm and 530 nm from the difference spectra in Figure 4.5 **A**. The A_1 spectrum indicates that the 530 nm band reaches from 500 nm up to 675 nm. The A_2 spectrum also includes the ESA bands at 440 nm and 530 nm. In the UV, the A_2 spectrum is positive. The A_3 spectrum has a similar shape to A_2 with just minor differences. The DAS for the λ_{pump} = 520 nm measurement (panel **B**) show the similar features as the DAS for the λ_{pump} = 400 nm measurement. The data is more noisy, so that the ESA band structure is hidden in the A_1 spectrum. The A_2 and the A_3 spectra are less noisy and show the aforementioned ESA bands at 405 nm and 440 nm.

To investigate the influence of higher-lying exchange-coupled states - which are populated at higher temperatures - on the dynamics, further TA measurements were performed at reduced temperature. To facilitate this, the Fe_3 sample was dispersed in a PMMA matrix and mounted in the cryostat previously described in Chapter 2. As the exchange interactions observed are on the order of of J = -50 cm^{-1}, which corresponds to ca. 70 K, these measurements were performed from 77 K (the boiling point of liquid nitrogen) to 280 K.

The difference spectra for the liquid nitrogen TA measurements are shown in Figure 4.10 **A**, where those for 1 ps and 20 ps pump-probe delay are plotted for all the measured temperatures, indicated by the colour code. The two ESA bands at 440 nm and 530 nm are at the same wavelength positions, previously found in the TA measurements in solution. Also no temperature-dependence on the difference spectra can be observed. In panel **B** and **C** of Figure 4.10, the kinetic traces for 440 nm and 510 nm are plotted. The kinetic traces are normalized in order to compare them. No change in kinetics with

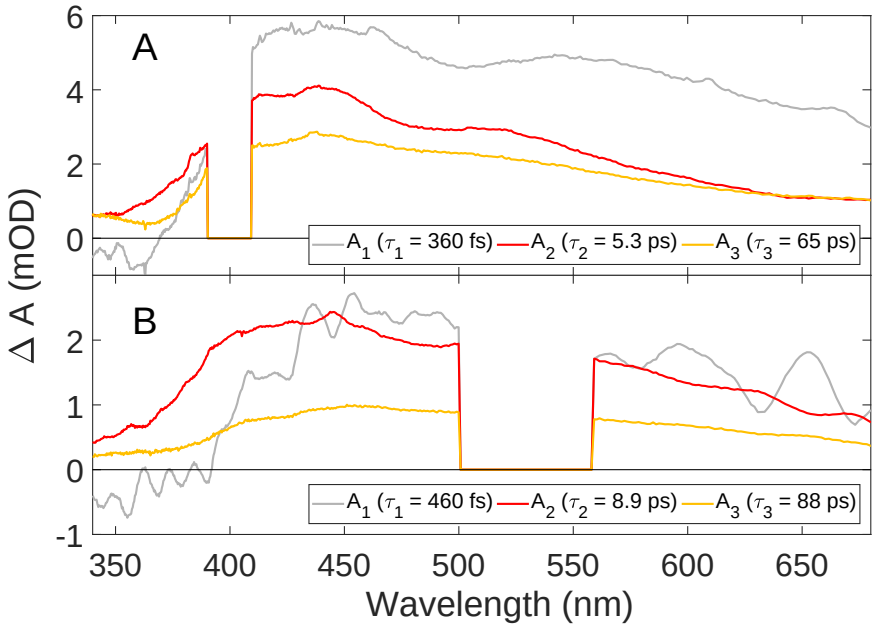

Figure 4.7: *DAS from the tri-exponential fit using a global analysis. In* ***A****, the DAS for* $\lambda_{pump} = 400$ *nm are shown and in* ***B*** *the DAS for* $\lambda_{pump} = 520$ *nm . The spectral region around* λ_{pump} *was excluded from the fit.*

increasing temperature is observed. The ultrafast TA data for all temperatures were fitted with a global tri-exponential fit (Equation 2.2) plus a constant offset using the Glotaran program package. The decay constants were so close to each other that here just the average decay constants found over the temperature range $77 \leq T \leq 280$ K are shown. The plotted decay constants can be found in Figure 4.11. The average decay constants are $\tau_{1,avg} = 232 \pm 12$ fs, $\tau_{2,avg} = 5.0 \pm 0.4$ ps, and $\tau_{3,avg} = 67 \pm 3$ ps. The found decay constant $\tau_{1,avg}$ is smaller than determined from the measurement in water at r.t., while the other two decay constants are close to their counterparts from the measurement in water.

The low-temperature TA measurements were then extended down to 4.5 K using liquid He. Further to this, application of an external magnetic field was employed to see if any change in the dynamics due to Zeeman splitting could be observed. Zeeman splitting is the splitting of the m_J sub-levels due to a static external magnetic field. The data is shown in Figures 4.8 and 4.9). Figure 4.8 shows the difference spectra for selected time delays. It is obvious that the spectra look similar to the ones in water solution. No evidence for any influence of the magnetic field on the dynamics and spectral properties was found in Figure 4.9, where difference spectra and kinetic traces from field on and

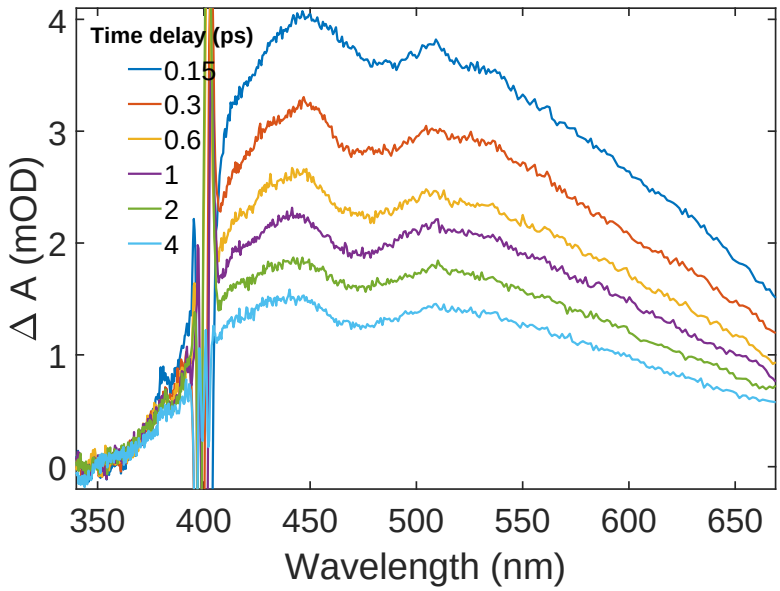

Figure 4.8: *Difference spectra from the ultrafast TA measurement of the $Fe_3O(CH_3CO_2)_6(H_2O)_3$ complex dispersed in a PMMA matrix. The sample was cooled to 4.5 K. λ_{pump} = 400 nm and a pump fluence of 0.95 mJ/cm^2. Magic angle between pump and probe polarization planes.*

field off measurements are compared.

In order to study the influence of the solvent, ultrafast TA measurements were also performed in dimethylformamide (DMF) and 2-propanol (IPA). The results are shown in chapter 7, for DMF in Figure 7.11 and for IPA in Figure 7.12. The conclusion drawn from these experiments is that it can not be guaranteed that there is no ligand exchange reaction between the Fe_3 water ligand and the DMF and IPA solvent molecules. Therefore it was decided that the ultrafast TA measurements in DMF and IPA can not be compared with the ones in water.

Overall several conclusions can be drawn from the ultrafast TA measurements shown above. First, the change of excitation wavelength has little effect on the shape and kinetics of the experiment. This, coupled together with the observation that the shape of the difference spectra does not change from around 200 fs up to 500 ps, leads to the conclusion that there is no change in electronic state after the initial excitation [81] and that the first process after excitation has to be on sub-100 fs scale. This is not measurable with our experimental set-up. Secondly, this rapidly populated state has a lifetime that far exceeds 500 ps. For this to occur, the coupling to the ground state has

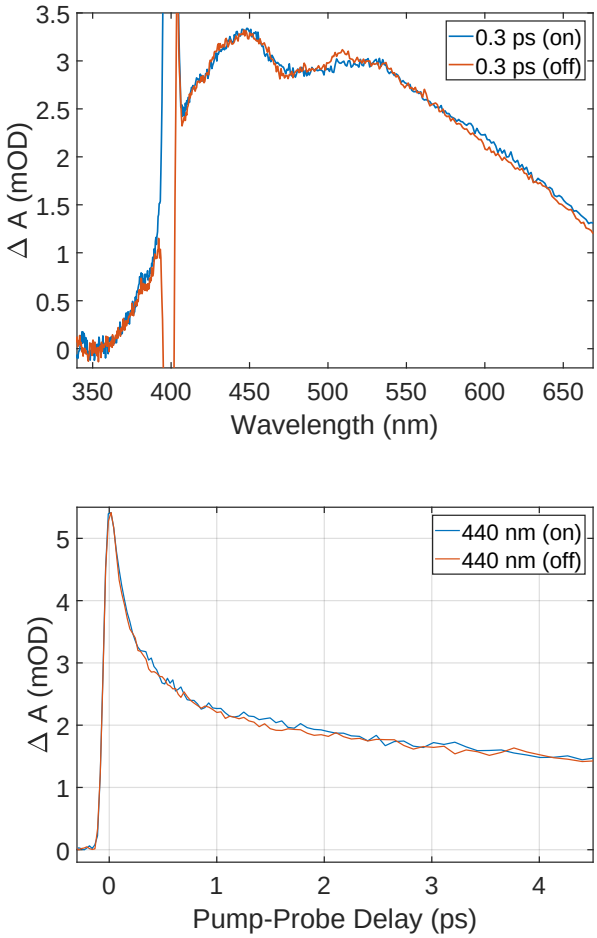

Figure 4.9: *Comparison of difference spectra and kinetic traces from the ultrafast TA measurements of the $Fe_3O(CH_3CO_2)_6(H_2O)_3$ complex dispersed in a PMMA matrix with (on) and without (off) external magnetic field. The sample was cooled to 4.5 K. λ_{pump} = 400 nm and 0.95 mJ/cm^2. Magic angle between pump and probe polarization planes. The magnetic field strength was set to 0.375 T.*

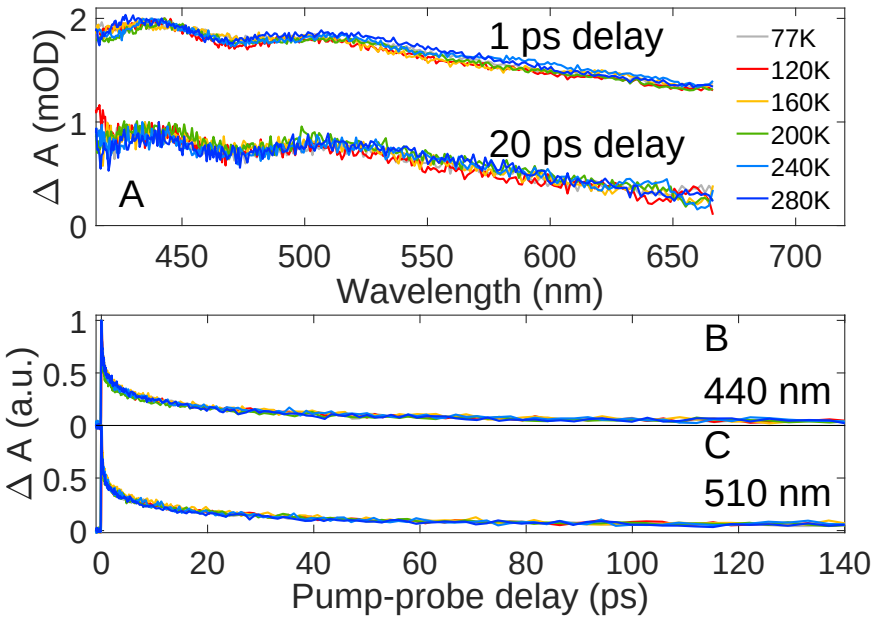

Figure 4.10: *Femtosecond TA measurements were performed on the Fe_3 complex dispersed in a PMMA film for various temperatures from 77 K to 280 K. Difference spectra for 1 ps and 20 ps pump-probe delay for temperatures from 77 K to 280 K are shown in* ***A****. In* ***B*** *and* ***C*** *kinetic traces at 440 nm and 510 nm probe wavelength for all the different temperatures are shown.*

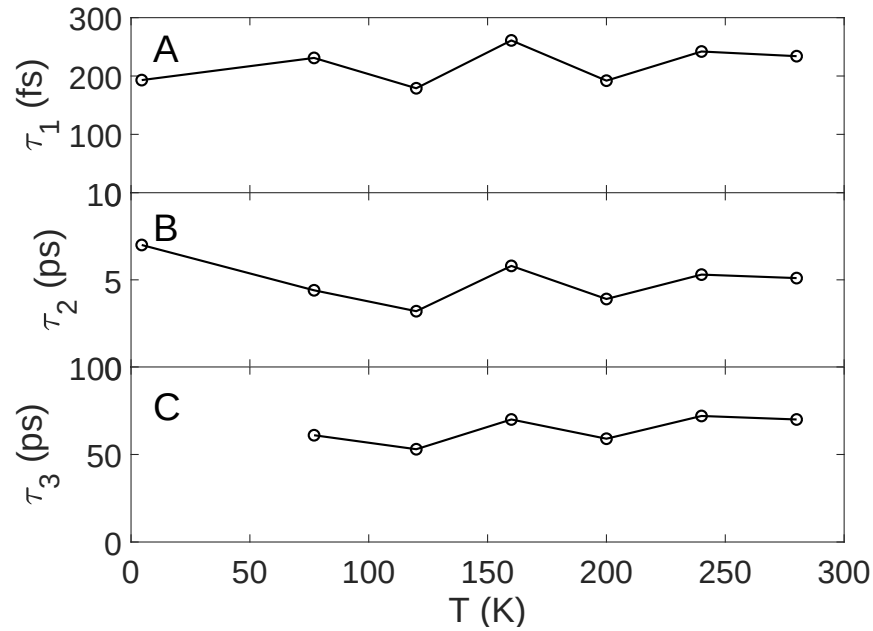

Figure 4.11: *Comparison of the decay constants from the temperature dependent measurements fitted by a global tri- (77 K to 280 K) or bi-exponential (4.5 K) fit using the software package Glotaran [63].*

State	Energy (eV)	Fe5	Fe7	Fe8
19	3.355	0.343	0.343	0.413
18	3.354	0.041	0.042	0.051
17	3.353	-0.384	-0.386	-0.463
16	2.100	0.304	0.055	0.360
15	2.098	0.824	0.145	0.979
14	2.097	-1.129	-0.196	-1.334
13	1.595	0.005	-0.010	0.001
12	1.536	0.416	0.044	0.136
11	1.535	-0.395	-0.042	-0.130
10	1.507	-0.023	0.008	-0.007
9	1.465	-0.001	0.002	-0.000
8	0.537	-0.003	-0.001	-0.000
7	0.495	0.039	-0.008	0.009
6	0.445	0.037	0.013	0.021
5	0.443	-0.056	-0.022	-0.030
4	0.201	-0.009	0.009	0.006
3	0.132	0.003	-0.000	-0.001
2	0.130	-0.004	-0.001	-0.000
1	0.000	-0.007	0.007	-0.004

Table 4.3: *EOM-CCSD energies and localised spin densities of the lowest 19 many-body electronic states after the inclusion of SOC and an external magnetic field $B = 10^{-5}$ a.u. For the numbering of the iron atoms, see Figure 4.1. These results use the HF level for the triplet ground state and the 3-21G basis set as starting point. This table is extracted from Liedy et al. [80].*

to be limited. This can be afforded by a change of geometry (bond lengths and angles) in the excited state that creates a large enough energy barrier to inhibit transition back to the ground state. Furthermore, the energy gap to the ground state has to be sufficiently large to disfavour IC. Also, no emission was found (see Figure 7.10) as was the case for the $[Fe^{III}(btz)_3]^{3+}$complex from Chabera et al. [114], who found a 100 ps lifetime for a CT state with almost no coupling to metal centred states. Another recent class of Fe(II) complexes (Fe(phenanthridin-4-yl)(quinolin-8-yl)amido$_2$) were developed by Braun et al. [115]. These complexes showed a CT lifetime of several nanoseconds. Therefore, it can be concluded that the that population of the lowest triplet d-d/CT state (around 1.3 eV above the ground state; state 5 in Table 4.1) for the Fe_3 molecule occurs very quickly after photoexcitation. The very broad ESA together with the calculated orbitals (see Figure 4.3) show that this state is at least partially delocalized.

In contrast to spin-crossover in single ion Fe(II) complexes, it is difficult to identify ISC

in the Fe_3 complex, because of the large spin angular momenta on the ions, and difficult to see in the TA experiments due to time resolution limitations. The $Fe(bpy)_3^{2+}$ complex shows a ISC time of less than 50 fs [30] and in the Methods 2 part, the whole SCO process is fitted with a time constant of 120 fs. Any process faster than this is impossible to resolve. Another factor which might play a role is the absorbance change which should follow a change of spin state on the Fe(II) ion in the Fe_3 complex. It could be that due to the strong coupling, the new localized spin state on the Fe(II) is delocalized very quick and the resulting change in bond length and the resulting change in absorbance is small and difficult to detect in the visible spectral range. Another iron complex with Fe(III) as central metal ion is the $Fe(acac)_3$ complex. A ultrafast transient IR spectroscopy study could not resolve the fast initial process which the authors assigned as ISC [82]. For this complex no long living state was found and it decays back to the ground state with a time constant of less than 20 ps [82].

The coupled-cluster calculations performed by our collaborators at the University of Kaiserslautern allow for a more detailed picture. SOC is included in the calculation of the one-electron SOC-integrals. Also the effective core potentials for the contributions of the two-electron integrals include SOC [116, 117]. The combination of one-electron SOC-integrals and the use of effective core potentials for the contributions of the two-electron integrals showed good results in the literature for the first-row transition elements [118]. Table 4.3 displays the energies after the inclusion of SOC and a static external magnetic field of magnitude $B = 10^{-5}$ a.u.. The magnetic field is introduced to split spin up and spin down states (Zeeman splitting). A range of different spin densities is observed in the energy range of the lowest excited dd band (states 9 - 11) in Table 4.3, showing that the spin state of this band can not be determined.

4.3 Static Magnetic Circular Dichroism

In this section, the static magnetic circular dichroism (MCD) spectrum for the Fe_3 complex dispersed in a PMMA matrix is shown (see Figure 4.13).

In MCD spectroscopy the difference in absorbance of RCP and LCP light in a magnet-

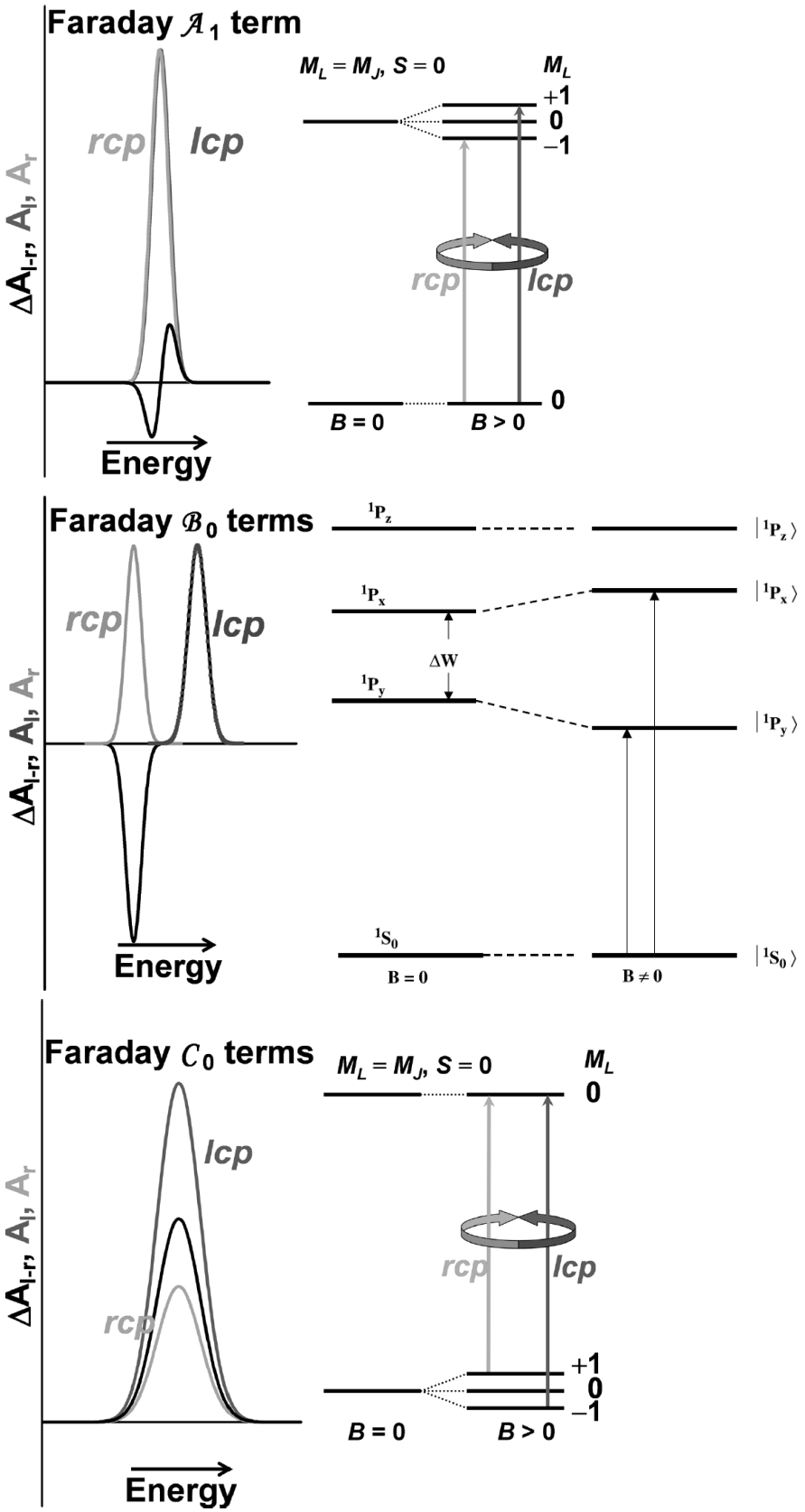

Figure 4.12: *Schematics for the selection rules and band shapes of Faraday A_1, B_0 and C_0 terms. Extracted from "Circular Dichroism and Magnetic Circular Dichroism Spectroscopy for Organic Chemists" [119] and "A Practical Guide to Magnetic Circular Dichroism Spectroscopy" [120].*

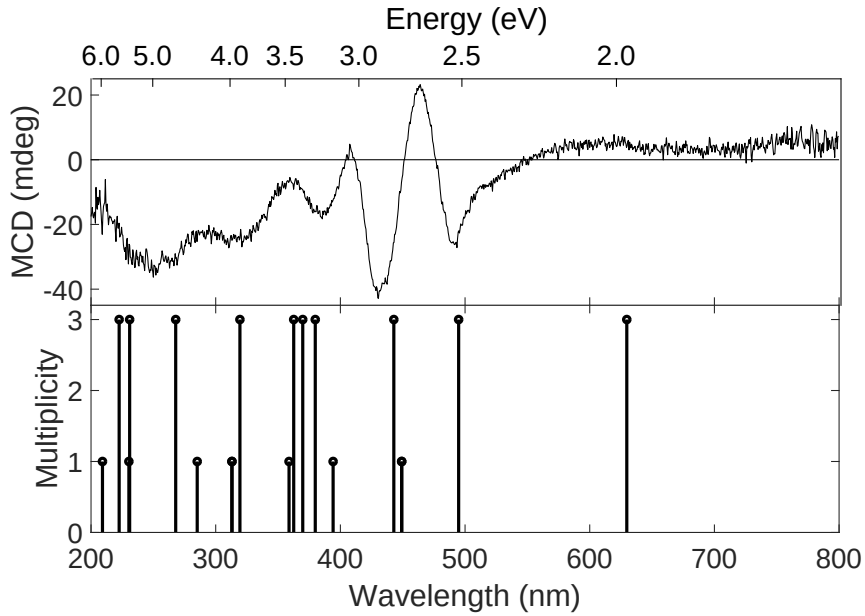

Figure 4.13: ***A*** *MCD spectra in the UV/Vis range of the Fe_3 complex dispersed in a PMMA matrix. The temperature was 1.47 K (0.13 meV or 10.5 cm^{-1}) and the external magentic field was 7 T. The spectrum was measured by Stergios Piligkos at the University of Copenhagen.* ***B*** *Calculated singlet and triplet energy levels are plotted. The multiplicity of the states is indicated by the height level (from Table 4.1).*

ized sample is measured. The MCD signal ΔA is defined as

$$\Delta A = \frac{A_{LCP} - A_{RCP}}{A_{LCP} + A_{RCP}}. \tag{4.1}$$

MCD signals can be generally divided in three terms called Faraday A_1, B_0 and C_0 term. They have their origin in different effects of the applied magnetic field onto the electronic structure of the sample. The origins of the three terms is graphically explained in terms of atomic energy levels in Figure 4.12. A_1 terms arise from Zeeman splitting of a degenerate excited state. In Figure 4.12 the Zeeman splitting is shown on hand of a ^{1}P term which splits into three M_J states. Due to the selection rule for absorption of RCP and LCP light, the applied magnetic field produces two absorption bands. The energy splitting is small in relation to the bandwidth of the transitions and the ΔA signal has the typical derivative like A_1 term shape. C_0 terms arise due to the opposite splitting scheme than A_1 terms. For C_0 terms the ground state is degenerate and split by an applied external field. In Figure 4.12 this is shown on a ^{1}P term again. As for the A_1 term selection rules apply and LCP light can just be absorbed by the

$M_J = -1$ state while RCP light is absorbed by the $M_J = +1$ state. Assuming an equal population of the $M_J = \pm 1$ states due to thermal population, a similar shape to an A_1 term would be observed. At cryogenic temperatures, where kT $<$ ΔE, the intensity of the LCP absorption band would be much larger than the RCP absorption band and the RCP band almost vanishes. B_0 terms arise due to magnetic field induced coupling between excited states close in energy. In Figure 4.12 this is shown on hand of am example where the atomic P terms are split due to an anisotropic ligand field. Assuming a mixing between ^1P_x and ^1P_y, the same band pattern as for the A_1 term is produced. Just that the splitting is generally larger, so that separated negative and positive bands are the result.

The MCD spectrum was measured by Stergios Piligkos at the University of Copenhagen. The spectrometer is a commercial Jasco J-1700 Circular Dichroism (CD) spectrometer used alongside a cryostat and a superconducting magnet. As expected for a paramagnetic sample, a high magnetic field of 7 T and a low temperature of 1.47 K (0.13 meV or 10.5 cm^{-1}) needed to be applied to see sufficient MCD signal. In Figure 4.13 **A**, the MCD spectrum of the Fe_3 complex shows several positive and negative bands which all overlap. This makes it very difficult to determine the kind of transition as Faraday A_1, B_0 and C_0 terms. In addition to the spectral overlap, the Fe_3 complex has three iron centres which strongly couple.

Five negative bands at 250 nm, 315 nm, 385 nm, 430 nm and 490 nm are visible. At 407 nm and 464 nm two sharp positive bands and above 580 nm at least two broad positive bands can be seen. Negative signals can indicate B_0 terms, but at low temperatures A_1 and C_0 terms should dominate [119]. The negative band at 490 nm is close to the position, where a shoulder was found in the absorbance spectrum, which was assigned to a mixture of metal-centred and CT transition.

In panel **B** of Figure 4.13, the calculated singlet and triplet energy levels are plotted. These levels fit well to the bands found in the MCD spectrum. The calculated triplet state at 630 nm fits well to a broad MCD band and to the steep increase of absorbance in the static ground state absorbance spectrum in Figure 4.2.

The MCD spectrum is in relation to the UV/Vis absorbance spectrum much more structured and more bands are visible, which is helpful in validating the theoretical calculations.

4.4 Conclusions

In order to understand the excited state dynamics after photoexcitation, static UV/Vis, FT-IR, static MCD and femtosecond TA spectroscopy of the mixed valence $Fe_2^{III}Fe^{II}O(CH_3CO_2)_6(H_2O)_3$ complex were performed and compared to quantum chemical calculations from our collaborators. The UV/Vis absorbance shows the ${}^6A_1 \rightarrow {}^4T_{1,2}$ transition at 930 nm known from literature. The shoulder at 480 nm is assigned as d-d and oxo $\rightarrow Fe^{3+}$ CT transitions. Calculations showed, that the extra electron of the Fe(II) is fully delocalized. A comparison of the calculated IR spectrum shows good agreement with the measured spectrum, which itself is a good match to literature. Low energy modes around 500 cm^{-1} were assigend as asymmetric Fe_3O stretch vibrations. In the ultrafast TA experiments in solution, it was found that the lowest charge-transfer/metal centred excited state at 930 nm (1.3 eV) was populated in approximately < 120 fs, which is faster than the experimental time resolution. This state is assigned to a delocalised state with ligand-field excitation at several iron sites and delocalised over the μ_3-oxo bridge. Excitation at 400 nm was assigned as a mixture of d-d and oxo $\rightarrow Fe^{3+}$ CT transition. The initial kinetics after photoexcitation can be described with a multi-exponential decay, but a remaining population lives for more than 500 ps. The low temperature TA experiments showed no significant change in dynamics to r.t. measurements in solution. Liquid helium temperature TA measurements with applied magnetic field also showed no significant effect of the magnetic field on the measured spectra and dynamics. The shown MCD study showed a reasonable good agreement with the calculations of the electronic excited states of the Fe_3 complex. Strong peakes were assigned as transitions into triplet states.

Chapter 5

Luminescence in a Terbium Single-Molecule Magnet

In this chapter, the results of the static UV/Vis spectroscopy, luminescence spectroscopy, ultrafast TA measurements and ultrafast MCD measurements on a single ion terbium complex are shown. This Tb complex is a so-called sandwich complex where two porphyrin type ligands, called phtalocyanines (Pc), coordinate the metal ion in the middle ($Tb(Pc)_2$) (see Figure 5.1). The sample was synthesized and characterized by Luke Burt in the group of Prof Neil McKeown at the University of Edinburgh. The sandwich structure is universal and all lanthanides as well as other TM ions with the right size and charge can take the place in the middle between the Pc ligands. The electronic structure of the lanthanide ions has little influence on the properties of the Pc ligands, but the size of the lanthanide ions plays an important role, since it mediates the distance between the Pc ligands and therefore how strong they are coupled [123]. For this chapter here, this means that it is possible to compare spectra and dynamics of other lanthanide ions in $Ln(Pc)_2$ with the results of $Tb(Pc)_2$. For example, the ground state UV/Vis spectra for the terbium (see Figure 5.1) and the lutetium version (see De Cian et al. [124]) show the same absorption bands at exactly the same wavelength positions. This is helpful since the lutetium version is the most studied $Ln(Pc)_2$ complex. The Tb^{+3} ion in $Tb(Pc)_2$ is eightfold coordinated by nitrogen donor atoms (see Figure 5.1 B), where the two Pc ligands are rotated by 45° in relation to each other. Further the ligands are bent and not planar. The Pc ligands in their neutral form have two

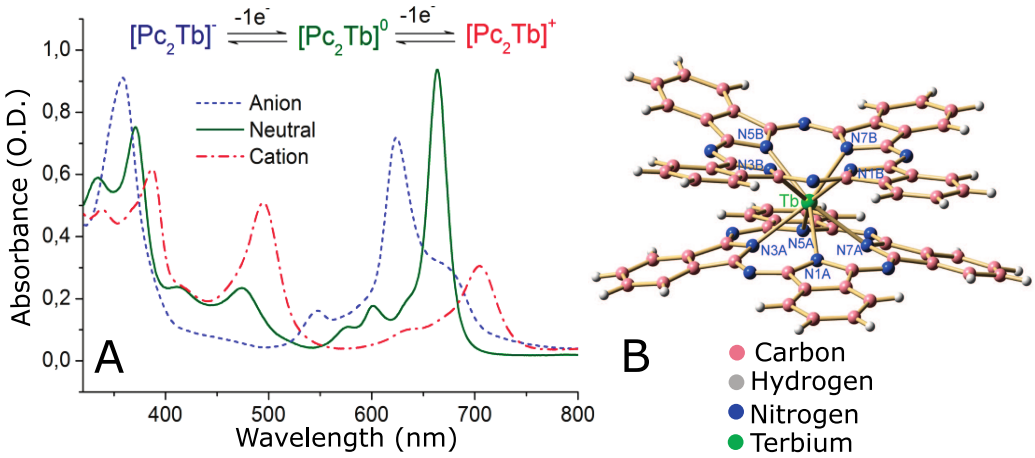

Figure 5.1: ***A*** *Absorbance spectra of the $Tb(Pc)_2$ complex in dichloromethane as positively, neutral and negatively charged. The Figure was taken from Gonidec et al. [121].* ***B*** *Molecular structure from x-ray crystallography of the anionic $Tb(Pc)_2$ complex from Branzoli et al. [122].*

acidic protons on two opposite nitrogen sites. So when they are deprotonated, the charge is -2. To form the neutral $Tb(Pc)_2$ complex with the Tb^{3+}, one electron needs to be added. This is the reason why the neutral complex is a mixed valence system with a formal oxidation state of the Pc ligands of -1.5 each [124]. This means that the complex is a radical, where the electron hole is in the highest occupied π-orbital which is delocalized over both Pc ligands [123, 125–128]. Beside the neutral form also stable salts of the positively charged and negatively charged version of this complex exist [121]. Their ground state spectra are well distinguishable as can be seen in Figure 5.1.

Besides being a interesting complex due to the mixed valence character and the semiconductor properties, this complex also works as a SMM and shows a remarkably high barrier for magnetization reversal for of 230 cm^{-1} [129]. Malavolti et al. [130] showed that the temperature under which hysteresis can be observed for the $Tb(Pc)_2$ in the magnetization versus magnetic field plots, depends on the dilution factor. So a definitive blocking temperature was not found.

Because of the remarkable high energy barrier, which was the highest of any SMM at the time of publication in 2003 from Ishikawa et al. [129], a lot of work was done trying to increase the energy barrier of lanthanide based SMMs. By modifying the Pc ligands, the energy barrier of the $Tb(Pc)_2$ was further increased [131]). This ef-

fort finally led to a energy barrier which was high enough so that magnetic hysteresis was observed as high as 80 K in a linear coordinated dysprosium metallocene [16]. Several techniques were used in literature to determine the magnetic properties of the $Tb(Pc)_2$(e.g. [122, 132, 133]).

Except of magnetic measurements also optical spectroscopy was performed on $Tb(Pc)_2$. The MCD spectra of $Tb(Pc)_2$ were measured by Gonidec et al. [121]. Also ultrafast spectroscopy was performed to measure electronic properties and especially the coupling between the Pc ligands using 2D electronic spectroscopy and ultrafast TA [134–136]. The ultrafast TA were done on the Lutetium analogue of the $Tb(Pc)_2$ complex. It was shown that the charge state, not just has a large influence on the ground state absorption spectrum, but also on the excited state and the excited state dynamics.

The aim for this study presented in this chapter is to perform an ultrafast TA experiment, luminescence spectroscopy and static UV/Vis/NIR absorption spectroscopy of the $Tb(Pc)_2$ complex in solution. It was aimed to combine the results from the three experiments and develop a consistent model of the photocycle of this interesting metal complex. Further a ultrafast Faraday ellipticity experiment is shown and the reasons behind the negative result is discussed.

Terbium and phthalocyanine luminescence background

Before starting to discuss the results, a brief background of what is known in literature about luminescence of lanthanide complexes in general and of $LnPc_2$ complexes in particular is given. The focus is on terbium luminescence and the Tb^{3+} ion is used as example for the general rules for the so called antenna effect.

The Tb^{3+} ion ([Xe] $4f^8$ $6s^0$) is known for luminescence originating from transitions in the f-shell of the ion. Direct excitation of f-f transitions are Laport and/or spin forbidden electronic transitions. Laport allowed transitions are f-d transitions into the 5d orbitals. These transitions are normally deep in the UV, but since the 5d orbitals are effected by ligands, the transitions can be shifted into the visible by choosing appropriate ligands [137]. This was found especially in Ce [138] and Eu [139] complexes and doped crystals. The with Eu and Ce doped crystals even show luminescence from the 5d orbitals and can be used in emissive devices [140].

For using the luminescence from the f-orbitals, ligands coordinating the e.g. Tb^{3+} ion are essential in avoiding the transition rule, so that emission from the Tb^{3+} ion can take place. Lanthanides in general have very different properties than transition metals because of the shielding of the f-electrons by other electrons in the s-, p- and d-shells. In opposite to transition metals, the splitting of the f-levels is very weakly influenced by the electric field of the ligands and dominated by electron repulsion and SOC (see Figure 5.2). The bonding between lanthanide and ligand is mainly electrostatic. Therefore the lanthanide-ligand systems energy levels can be separated in ligand and lanthanide levels. For the electronic levels of the lanthanide ions in lanthanide complexes it is common to use the nomenclature for atoms. The splitting scheme for lanthanides and the f-levels of the Tb^{3+} ion are shown in Figure 5.2. When the Tb^{3+} ion is excited, emission arises from the $^5D_4$-level into the six ^6F levels.

Ligands in general show strong absorption bands in the UV and visible range. This can be utilized to transfer energy to the Tb^{3+} ion. Energy transfer to the lanthanide ion is achieved via donor states (e.g. triplet states of the ligand). Important for an effective energy transfer from the excited ligand and a high quantum yield, is the energetic position and lifetime of the donor excited ligand state in relation to the emitting state, which is the $^5D_4$-level on the Tb ion. The route for energy transfer with the highest efficiency for most lanthanide-ligand systems was found is the route via the ligand triplet state [143]. The energy transfer process from the ligand triplet state to the lanthanide can be either a Dexter or a Förster mechanism. Both transfer schemes are shown in Figure 5.3. Figure 5.3 **A** shows the Dexter process, which is a exchange mechanism. After photoexcitation of the ligand singlet state, ISC to the triplet state occurs. The electron in the triplet state can now transfer into a f-level of the lanthanide ion, while one lectron of the ground state f-level will move into the ground state of the ligand. The resulting state leaves an electronically excited lanthanide ion. The Förster process in Figure 5.3 **B** is a dipole-dipole interaction between the triplet state of the ligand and the lanthanide f-states. The resulting state is equal to the Dexter process. Beside the triplet state also other states, e.g. singlet states, LMCT states and intra-ligand CT states can be donor states [137]. The process of energy transfer is called antenna effect [144].

The Pc ligands have no triplet states since the system is a radical and so the ground

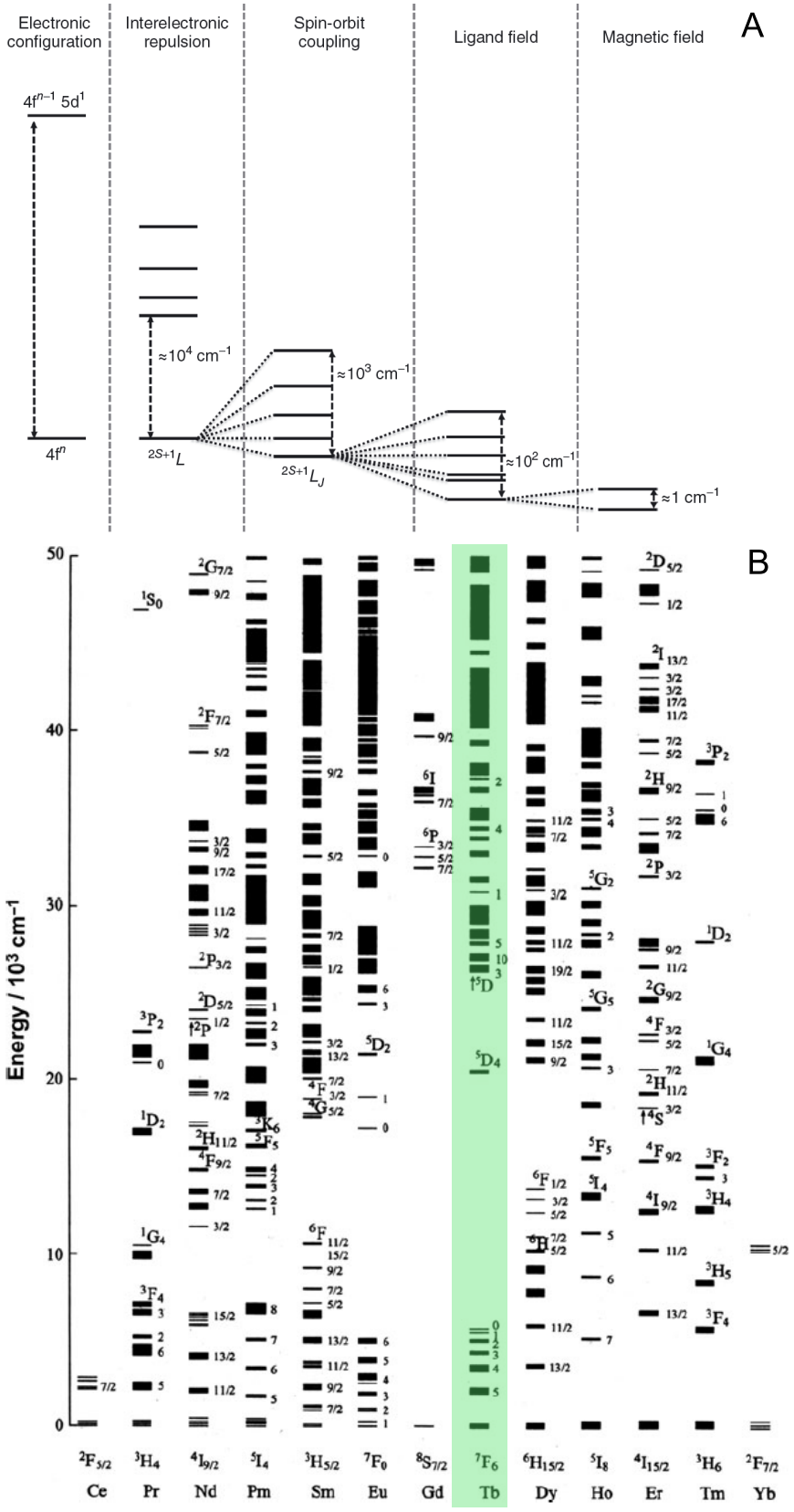

Figure 5.2: ***A*** *Electronic level splitting scheme for lanthanides taken from Sorace and Gatteschi [141].* ***B*** *Diagram for the splitting of the f-levels of lanthanide ions (all 3+) doped into a low symmetry crystal (LaF_3) field. The graphic was taken from Buenzli and Eliseeva [142]. The Tb^{3+} ion is marked with a green box.*

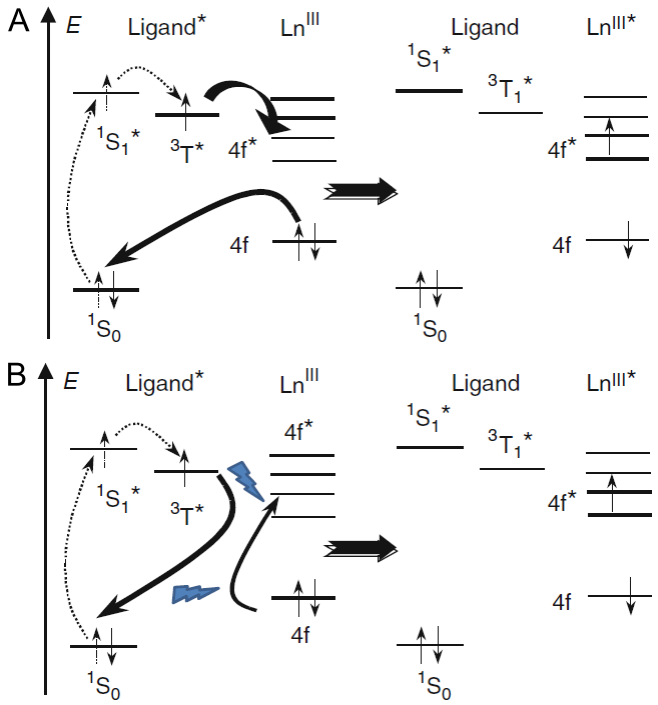

Figure 5.3: *Energy transfer mechanisms for lanthanide complexes with closed shell ligands, so ligands having a singlet ground state. Energy transfer is typically via a long living triplet state using either the Dexter* ***A*** *or Förster* ***B*** *mechanism. The Figure was taken from Bünzli and Eliseeva [142].*

state is a doublet. The luminescence of the $Eu(Pc)_2$ complex, with iso-electronic ligand sphere, was measured by Sun et al. [145]. They found that by exciting in a high enough state of the Pc ligands, emission from the Eu^{+3} is observed. They further found ligand emission at 410 nm, 525 nm and at 700 nm. The intensities of the ligand emission bands change with the excitation wavelength. Phtalocyanine ligands are well known for the Q- ($S_0 \rightarrow S_1$) and B-band ($S_0 \rightarrow S_2$) transitions which are transitions of $\pi \rightarrow \pi^\star$ character [146]. So Sun et al. [145] assigned the emission at 410 nm to the B-band and the emission at 700 nm to the Q-band. This is in accordance with emission found in several Pc coordination compounds [147, 148]. The emission at 525 nm is assigned to an excited state, which includes the singly occupied molecular orbital (SOMO). Kaneko et al. [147] found emission lifetimes for the 410 nm B-band emission of metal Pc compounds of several ns depending on the metal and the solvent (e.g. $CuPc(SO_3-)_4$ in acetonitrile-water mixture: 3 ns; $ZnPc(OCH_2CMe_3)_4$ in chloroform: 12.5 ns). It is remarkable, that there is emission from the B-band at all. Since it is not expectable because normally in organic compounds non-radiative decay of a high lying electronic

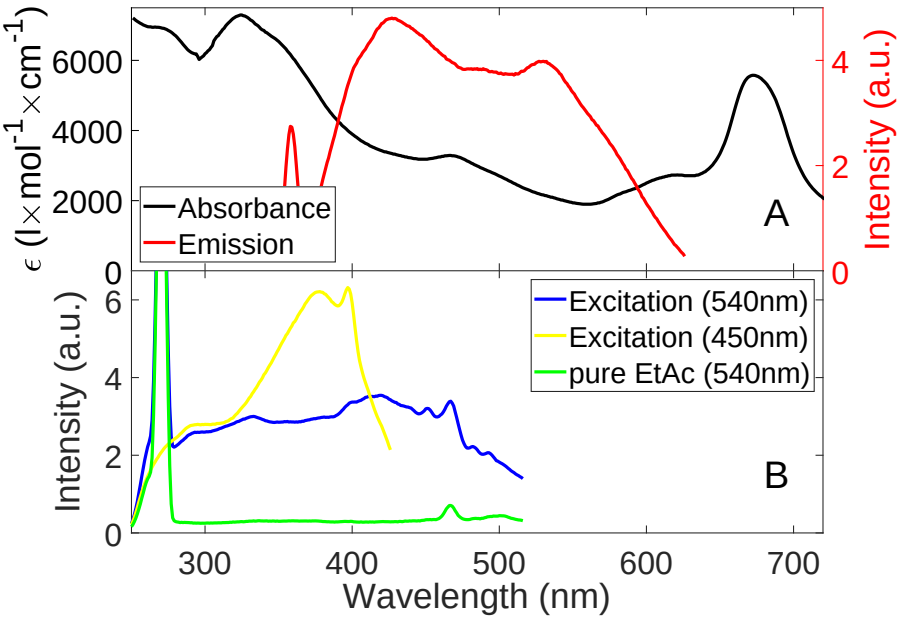

Figure 5.4: ***A*** *Absorbance spectrum of the Tb(Pc)$_2$ complex in ethanol plotted together with the emission spectrum (λ_{ex} = 325 nm) in ethyl acetate. The slit widths for both excitation and emission were set to 5 nm. The scan speed was set to medium and 5 spectra were averaged.* ***B*** *Excitation spectra of Tb(Pc)$_2$ in ethyl acetate for fixed emission wavelengths of 450 nm and 540 nm.*

state is much faster then the radiative decay (Kasha rule). For Pc this seems to be not the case.

In summary, this means for Tb(Pc)$_2$ that emission from the ligand is expected. When exciting the B-band and if the lifetime of this state is long enough also energy transfer to the Tb^{+3} ion seems possible.

5.1 Static UV/Vis absorbance and luminescence

In this section the results of the UV/Vis absorbance and the luminescence spectroscopic measurements are shown and explained. The spectrometers used for the UV/Vis absorbance and luminescence measurements were described earlier in chapter 2. For the luminescence measurements a slit width of 5 nm for excitation and emission slit was used. The scan speed was set to medium and 5 spectra were averaged for both the emission and excitation spectra.

In Figure 5.4 **A** the absorbance spectrum of the Tb complex dissolved in ethanol is plotted together with the luminescence spectrum (λ_{ex} = 325 nm) in ethyl acetate.

Ethyl acetate was used because the spectroscopy grade ethanol showed some emission overlapping with the sample emission. The absorbance spectrum shows a good match with the shown literature spectrum of the neutral species in Figure 5.1 A. The peaks around 470 nm and 914 nm (see Figure 5.10 A) are specific for the neutral/radical species, because they are transitions where the SOMO state is involved. The band at 470 nm is assigned as transition from a lower lying state (HOMO-X) into the SOMO state [123, 149]. Orti et al. [123] assigned the 914 nm transition as SOMO to LUMO (lowest unoccupied molecular orbital) transition. This is not in agreement to an earlier paper from Markovitsi et al. [149], who assigned the transition as a transition from a lower lying state into the SOMO level. The lowest electronic transition is assigned as transition from the one energy level below the SOMO (HOMO-1) to the SOMO level. This transition lies in the NIR around 1500 nm [149] and could not be measured due to limitations of the equipment. No peaks from the other two species are observed which implies only the neutral species is present. Also there is little effect of the solvent visible in the absorption spectra. In the shown literature spectrum in Figure 5.1 the solvent is dichloromethane. There are no shifts in peak position with the change of solvent to ethanol. Only the peaks seem to be more broad in ethanol, which is probably due to hydrogen bridge bonding.

It is interesting to see if there is energy transfer to the Tb^{3+} ion and, if so, which electronic states are involved. As visible in panel **A** of Figure 5.4, the emission spectrum shows several peaks and shoulders. The excitation wavelength was set to 325 nm or 30,770 cm^{-1}, in order to excite somewhere in the Q-band. This is a chance to populate the $^5D_4$ state of the Tb^{3+} at around 20,000 cm^{-1} either directly from the B-band or from a lower lying ligand quartet state via ISC. The emission peaks visible at around 500 nm ($^5D_4 \rightarrow {}^6F_6$) and 540 nm ($^5D_4 \rightarrow {}^6F_5$) as well as a shoulder around 580 nm ($^5D_4 \rightarrow {}^6F_4$) are assigned to the three strongest Tb^{3+} emission bands [150]. The overall emission intensity is very weak when compared to the Raman peak of the solvent. The peak at 427 nm is assigned as emission from the phthalocyanine ligands, which is in good agreement with the $Eu(Pc)_2$ equivalent from Sun et al. [145].

In Figure 5.4 B the excitation spectra of the $Tb(Pc)_2$ in ethanol are shown for two emission wavelengths of 450 nm and 540 nm. The excitation spectrum monitoring the emission at 450 nm shows mainly one peak at 378 nm which is in the area of the

Wavelength (nm)	Energy (cm^{-1})	Type of transition
292	34,247	ligand
332	30,120	ligand
356	28,090	ligand?
380	26,316	Tb
400	25,000	Tb?
412	24,272	ligand
420	23,809	?
439	22,779	?
452	22,124	?
482	20,746	Tb?
493	20,284	Tb

Table 5.1: *Peak positions of the excitation spectrum (emission at 540 nm) of Tb(Pc)$_2$ in ethyl acetate from Figure 5.4.*

B-bands. So together with the emission peak position this can be clearly assigned as emission from the ligand. Most likely emission from the B-band, which was shown earlier, has a fairly long emission lifetime of several ns [147]. The peak at 398 nm is due to the solvent Raman excitation. The shape of the excitation spectrum monitoring 540 nm shows numerous peaks. To distinguish between the solvent peak and the real signal of the sample, the excitation spectrum of the pure solvent is plotted as well and two peaks can be seen at around 270 nm and 467 nm which should both belong to Raman excitations. All the other peaks originate from the Tb(Pc)$_2$ sample. The peaks are listed in Table 5.1. The assignment of the peaks is quite difficult due to the overlap of ligand bands and Tb^{3+} bands. The 380 nm band can be clearly assigned as excitation of the Tb^{3+} $^6F_6 \rightarrow {}^5D_3$ transition [143, 151, 152]. The bands at lower energy fit to the $^6F_6 \rightarrow {}^5D_4$ transition. The effect of seeing the absorbance bands of ff-transitions in excitation spectra is well known and also occurs in solution e.g. for a Eu^{3+} complex in Woodward et al. [153] and for several other lanthanide ions in Nagaishi et al. [154].
So by exciting at 325 nm into the B-band of the Pc ligand, luminescence of the ligand is observed as well as energy transfer to the terbium and subsequent emission. By measuring the excitation spectra monitoring the ligand emission as well as the terbium emission it can be shown that the terbium emission is really originating from the lanthanide ion.

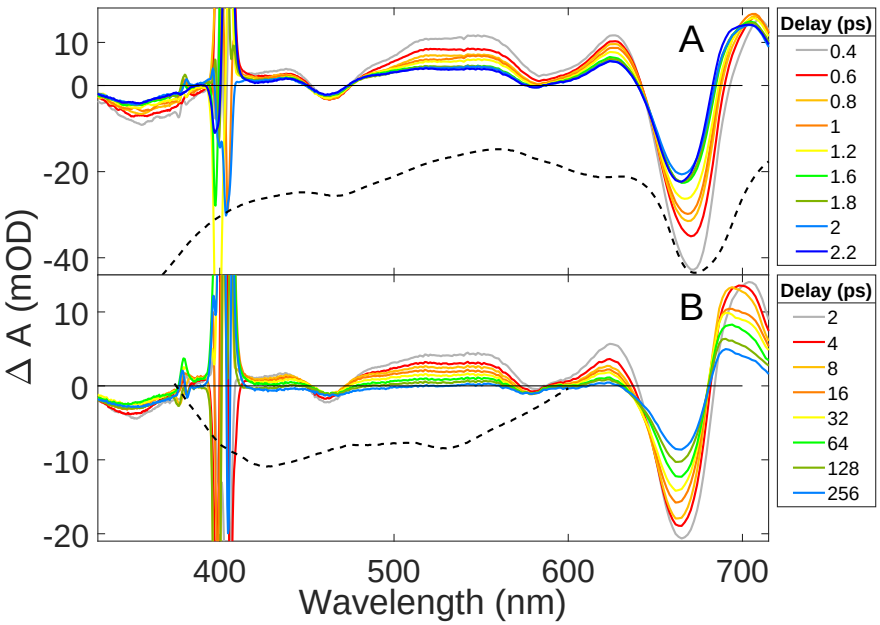

Figure 5.5: ***A*** *Difference spectra from the ultrafast TA experiments of the Tb(Pc)$_2$ complex in ethanol for several time delays between 0.4 ps and 2.2 ps. Overlaid is the absorbance spectrum which is multiplied by minus one to show the GSB contributions.* ***B*** *Difference spectra for later time delays between 2 ps and 256 ps overlaid with the emission spectrum multiplied by minus one. The large signals around 400 nm and the small spike around 380 nm are due to scattered pump light.*

5.2 Ultrafast transient absorption of the Tb(Pc)$_2$ complex in ethanol solution

The ultrafast TA experiment of the Tb(Pc)$_2$ complex was performed in order to study the initial dynamics after photoexcitation at 400 nm into the overlap region of the low energy edge of the Q-band and the HOMO-X to SOMO transition at 470 nm. The measurement was performed in solution and the concentration of the dissolved Tb(Pc)$_2$ complex in ethanol was $c_0 = 4.505 \times 10^{-4}$ mol/l. The cuvette used was a 1 mm pathlength quartz cuvette with 1 mm thick windows. The absorbance at 400 nm was therefore 0.18 OD. The pump laser fluence was set to 1.8 mJ/cm^2. The maximum pump-probe delay was 300 ps and the step size was 25 fs for time delays up to 1 ps. For every time delay 1000 spectra were averaged and the experiment was repeated 5 times. So in total 5000 spectra per time delay are averaged. Figure 5.5 shows the results of the ultrafast TA experiment as difference spectra. Panel **A** shows difference spectra for early pump-probe delays from 0.4 ps to 2.2 ps. Panel **B** shows spectra for

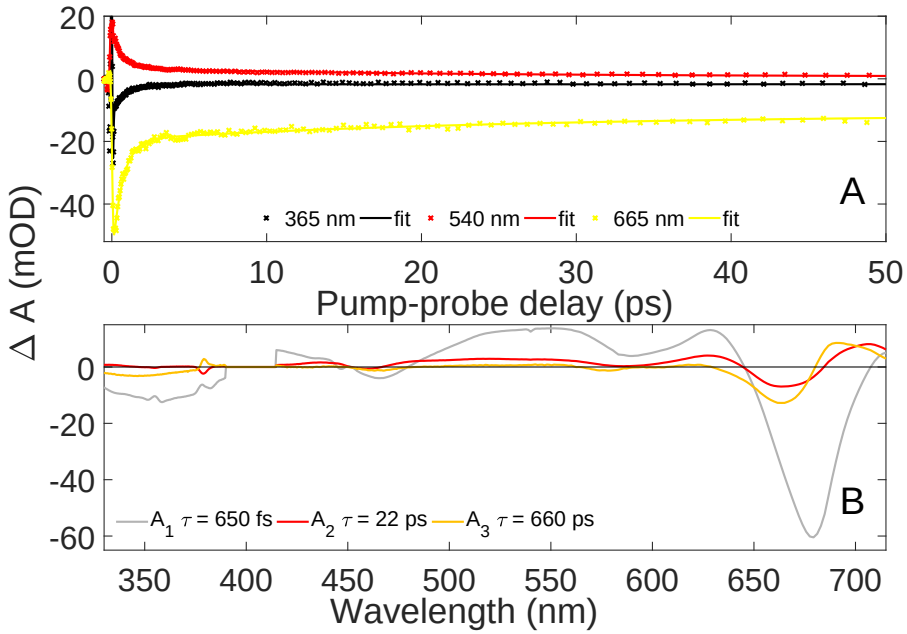

Figure 5.6: ***A*** *Kinetic traces of the ultrafast TA experiments of the $Tb(Pc)_2$ complex in ethanol for several wavelengths. The shown fits were performed using the Glotaran software package. A tri-exponential global fit was used to fit the data.* ***B*** *The DAS of the global analysis with the three decay components are shown.*

longer time delays from 2 ps to 256 ps. Further to the difference spectra, panel **A** also includes the static absorbance spectrum and panel **B** includes the emission spectrum. Both plotted as black dashed lines.

Overall the difference spectra show several ESA and GSB bands. Starting with the GSB bands in comparison with the ground state spectrum, it is visible that the GSB signals of the Q-band at 672 nm, the HOMO-X to SOMO transition at 463 nm and the low energy edge of the B-band at around 350 nm in the 0.4 ps pump-probe delay spectrum fit well to the peak positions in the ground state absorbance spectrum. Beside the GSB bands in the 0.4 ps spectrum, ESA with peaks at 710 nm, 625 nm, 550 nm, 518 nm and 440 nm are visible. The ESA is overlapped with GSB. The dips in the ESA signal at 603 nm and 585 nm fit well to the absorbance bands of the ground state. For pump-probe delays up to 1.6 ps the peak maximum of the GSB signal at 672 nm shifts to lower wavelengths. No change in the GSB position is observed for longer time delays. The GSB signatures at 603 nm and 585 nm are first positive, due to overlap with the strong ESA signal, but change sign for time delays longer than 2 ps. The GSB signals at 463 nm and 350 nm are negative already from the start, loosing intensity over time and

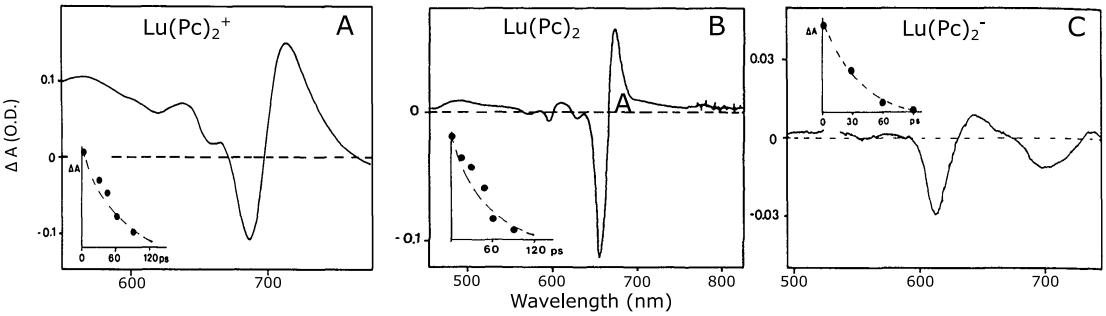

Figure 5.7: ***A*** *Difference spectrum directly after excitation of the* $Lu(Pc)_2^+$ *complex dissolved in dichloromethane with a 20 ps laser pulse at 354 nm.* ***B*** *Difference spectrum directly after excitation of the neutral* $Lu(Pc)_2$ *complex dissolved in dichloromethane with a 20 ps laser pulse at 354 nm.* ***C*** *Difference spectrum directly after excitation of the* $Lu(Pc)_2^-$ *complex dissolved in dichloromethane with a 20 ps laser pulse at 532 nm. All spectra were taken from A. Germain and T. W. Ebbesen [157].*

are still recognizable as bands at 256 ps delay. By comparing the emission spectrum with the difference spectra it is obvious that no or very weak stimulated emission (SE) is visible. For the maximum shown pump-probe delay of 256 ps a negative signal at around 430 nm is observed, but it can not be distinguished between GSB and SE. The excited state lives clearly much longer then the 300 ps maximum pump-probe delay in this experiment, since dynamics up to the maximum pump-probe delay are observed. In literature the luminescence decay for the B-band is on the ns scale [147] and for Tb emission typically on the scale of μs [155] or even longer [156].

The ultrafast TA data was then fitted with a global tri-exponential fit according to Equation 2.2 using a sequential model by the analysis software Glotaran [63]. The results are plotted in Figure 5.6, where in **A** kinetic traces including their fits for three different wavelengths are plotted. In **B** the DAS are plotted. The found time constants are $\tau_1 = 650 \pm 150$ fs, $\tau_2 = 22 \pm 2$ ps and $\tau_3 = 660 \pm 150$ ps. It is to mention that τ_3 is way longer then the maximum pump-probe delay of 300 ps and therefore, the accuracy is small. The A_1 spectrum shows the shape of the early time delay difference spectra and therefore shows all GSB bands mentioned earlier. In comparison to A_2 and A_3, which show almost similar spectra, the A_1 spectrum looks different. First it almost shows no ESA above around 690 nm while A_2 and A_3 show strong ESA bands. Further all GSB bands are red shifted in relation to A_2 and A_3.

In the literature only a few ultrafast TA experiments performed on lanthanide phtalocyanine double-decker complexes are known. One TA experiment was performed

on the Eu analogue of the $Tb(Pc)_2$ complex by Bian et al. [158]. After excitation with a 150 fs laser pulse at 400 nm, a long living state (>>1 ns) was observed, which is also observed in the experiments on the Tb analogue shown here. A. Germain and T. W. Ebbesen [157] performed TA spectroscopy on the $Lu(Pc)_2^{+.0.-}$ complex in three oxidation states and found large differences in the dynamics and in the TA spectra (see Figure 5.7). The difference spectrum directly after excitation with a 20 ps laser pulse look similar to the difference spectra for longer delays of the $Tb(Pc)_2$ complex in Figure 5.5 **B**.

Prall et al. [134, 135] and Bixner et al. [136] performed 2D electronic spectroscopy, ultrafast TA spectroscopy and theoretical work on the $Lu(Pc)_2^-$ complex in order to investigate the dynamics and the coupling of the two Pc^{2-} ligands. Bixner et al. [136] also investigated the neutral $Lu(Pc)_2$ complex in comparison to the negatively charged version to see how the energetic position of the CT-band (just in the $Lu(Pc)_2^-$ complex; CT between the Pc ligands) influences the electronic properties and the relaxation dynamics after photoexcitation. As mentioned earlier, the influence of the extra charge carrier is large. Bixner et al. [136] also showed in the theoretical calculations, that the counter ion is located close to one PC ligand which stabilizes CT states. Therefore the counter ion has great influence on the UV/Vis absorbance and the relaxation dynamics.

Prall et al. [135] found in their ultrafast TA studies of $Lu(Pc)_2^-$ a vibrational wavepacket which they tentatively assigned to the electronic ground state of the molecule, but could not exclude that the wavepacket is on the excited state potential surface. The energy of the wavepacket is 159 cm^{-1} and fits well to the Raman spectrum in ethanol solution in the same publication. Further the energy is also in agreement with the ground state resonance Raman spectrum of the neutral $Lu(Pc)_2$ complex [160] and to the calculated energy from Bixner et al. [136]. In the ultrafast TA study of $Tb(Pc)_2$ which is presented in this chapter, a vibrational wavepacket could not be proven unambiguously.

Quantum mechanical calculations on the B3LYP/LANL2DZ level on the yttrium $Y(Pc)_2$ and the lanthanum $La(Pc)_2$ were performed by Zhang et al. [159]. Yttrium is known for the chemically close behaviour to the lanthanide group, has an oxidation state of +3 and has an effective ion radius of 90 pm, very close to the Tb^{+3} radius of 92.3 pm (both radii from R. D. Shannon [161]). For the $Y(Pc)_2$ complex it was found that the

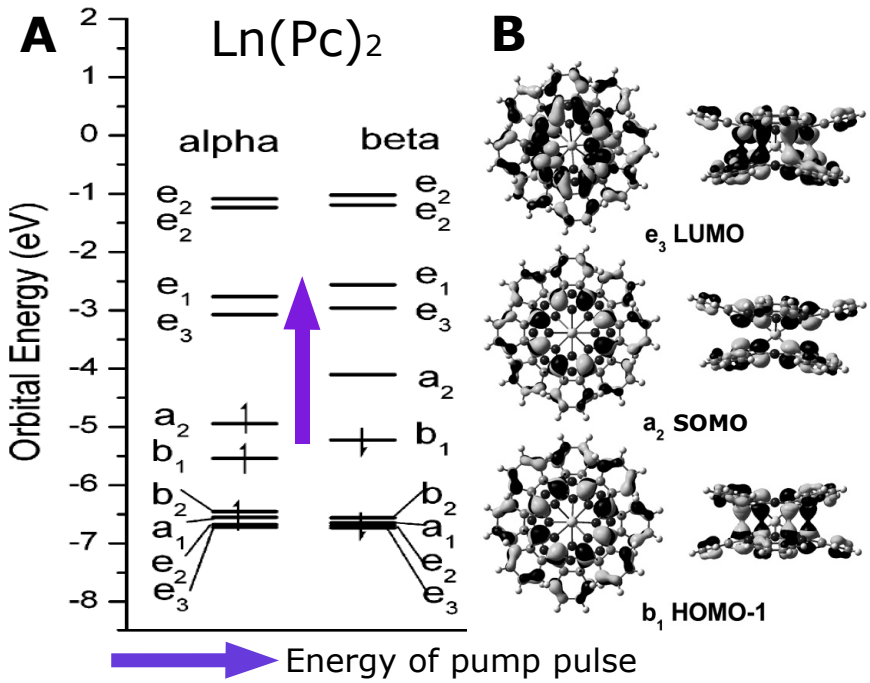

Figure 5.8: *Energylevel diagram (**A**) for the $Y(Pc)_2$ complex from DFT calculations (B3LYP/LANL2DZ). Alpha and Beta represent spin up and spin down ,respectively. Orbital map of the HOMO-1, the SOMO and the LUMO orbitals (**B**). The diagram and the orbital pictures were taken from Zhang et al. [159].*

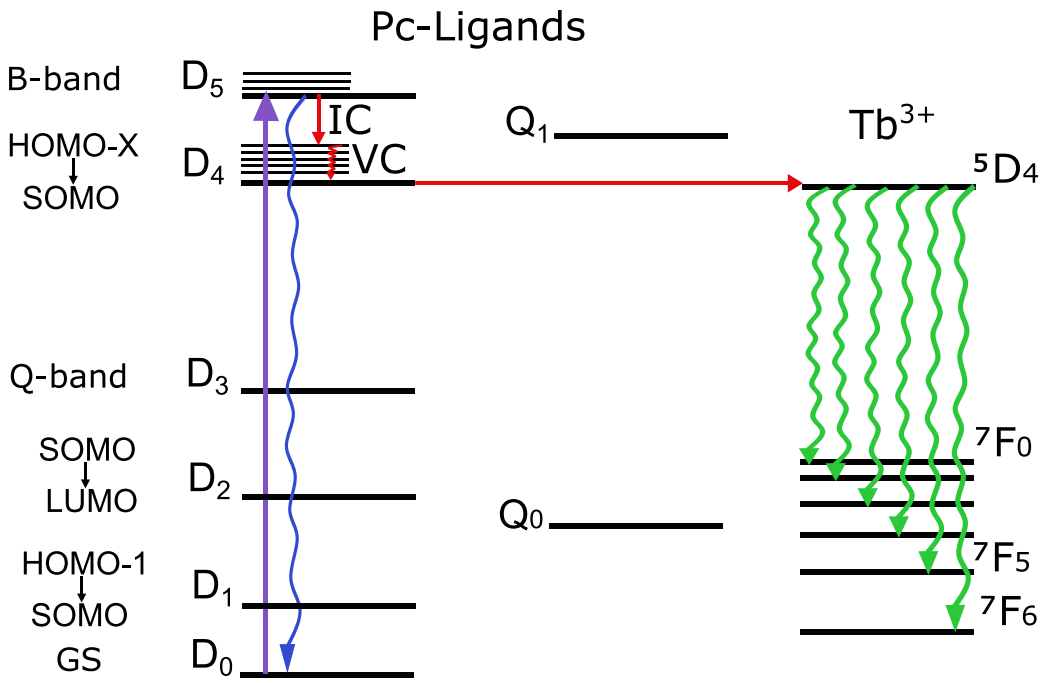

Figure 5.9: *Proposed photocycle after 400 nm excitation in the low vibrational excess energy part of the B-band. Electronic levels are indicated by thick, black horizontal lines while vibrational levels are indicated by shorter and thinner black lines. GS = ground state; IC = internal conversion; VC = vibrational cooling; D = doublet states; Q = quartet states. All doublet transitions are* $\Pi \rightarrow \Pi^{\star}$ *transitions. The column on the left side gives the type of transition. In the* Q_1 *and* Q_4 *states the SOMO is directly involved.*

α a_2 orbital ($\alpha \equiv$ spin up) is the SOMO and it has antibonding character. This can be seen in Figure 5.8, where in **A** the orbital energy is plotted and in **B** the orbital lobes for the HOMO-1, the SOMO and the LUMO are presented. It is clearly visible in Figure 5.8 **B**, that the SOMO has no σ-bonding between the rings. While the HOMO-1 and LUMO have σ-bonding character. The SOMO is lower in energy than the LUMO because it shows π-bonding between the Pc rings. The purple arrow indicates the 400 nm (3.1 eV) pump energy and shows that it is possible to excite several states from the SOMO to higher lying LUMOs and from lower lying states to the LUMO.

To identify the pathway of the energy from the Pc ligands to the Tb^{+3}, the information from the static UV/Vis and emission/excitation spectra and ultrafast TA spectroscopy have to be combined with the literature. From the UV/Vis absorbance spectrum it is clear that with 400 nm excitation the Tb(Pc)$_2$ complex is excited in the low vibrational excess energy B-band. Maybe also partially in the high vibrational excess energy HOMO-X to SOMO transition at 470 nm. From the ultrafast TA measurement it can

be extracted, that the initially excited state decays with a time constant of 650 fs. The low vibrational excess energy (1300 cm^{-1} difference between the Q-band at 380 nm and 400 nm pump) in the Q-band prevents that vibrational cooling in the B-band is visible in the TA spectra. In addition to that, the DAS A_1 from Figure 5.6 shows a different shape than the other two DAS spectra A_2 and A_3. This indicates a change of electronic state. A possible ISC to a quartet state seems unlikely since the HOMO-X to SOMO state is also a doublet state, it is close in energy to the B-band and IC should be more efficient than ISC. Therefore the 650 fs time constant is assigned as IC from the B-band into the HOMO-X to SOMO state. One point here is not fully in line with this explanation. There is emission from the B-band at 427 nm. For visible fluorescence from the B-band, its lifetime has to be substantial. This emission-process has a low probability when the B-band decays with the 650 fs. On the other hand the intensity is very low and a lifetime of 650 fs might be enough for emission from the B-band.
Here is a limit for ultrafast TA. When the kinetics are not consecutive, several processes run parallel and if bands overlap in the TA spectra, it is impossible to extract the exact kinetic model. Since the fluorescence intensity of the B-band is very low and the 650 fs lifetime might be long enough for weak emission, the splitting of the process is recognized. The fluorescent decay of the B-band ends in any case in the ground state. Since it is more interesting to follow the process for sensitizing the Tb^{3+} ion, the following steps in the kinetics are treated as consecutive.
Figure 5.9 shows the proposed energy transfer to the Tb^{+3} and beside the doublet states (D_0 to D_4) on the very left, quartet states (Q_0,Q_1) are drawn in the centre. On the very right the Tb^{+3} states are shown. After IC from the D_4 state to a hot D_3 state, most likely vibrational cooling takes place. This is assigned as the second time constant of 22 ps which is linked to the DAS A_2. Vibrational cooling can be seen in ultrafast TA by a blue shift of ESA bands. This is what is visible for the ESA band around 700 nm. This is also visible in the DAS where the A_3 spectrum shows the ESA peak around 680 nm while the A_2 spectrum's ESA peaks at around 700 nm. Another observation is that the two DAS A_2 and A_3 look fairly similar which indicates that they represent the same electronic state. The longest time constant of 660 ps is afflicted with a large error since the maximum measured pump-probe delay is 300 ps. In Figure 5.9 the horizontal red arrow represents the energy transfer from the ligand into the $^5D_4$ level of the Tb^{+3}.

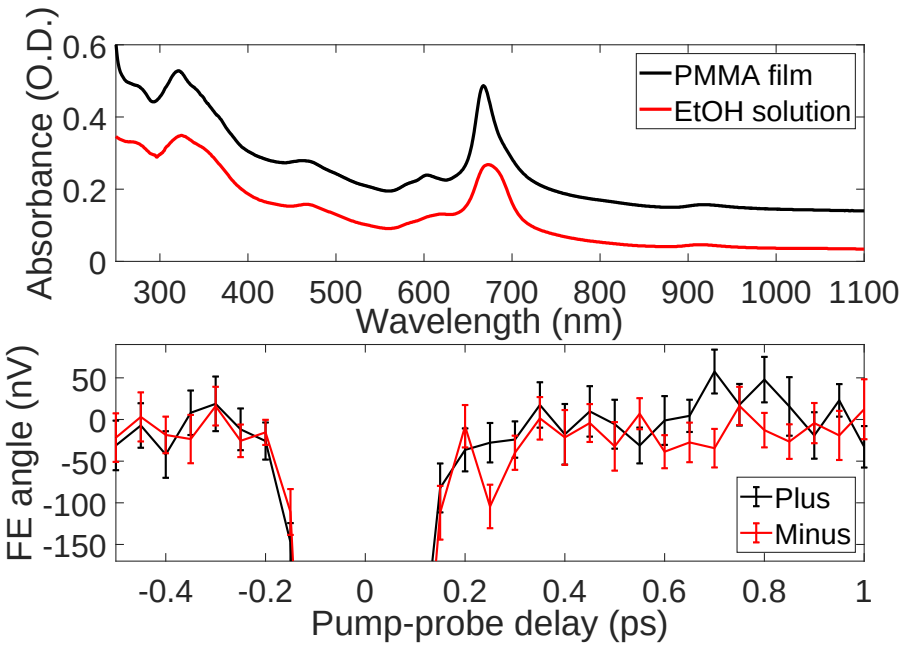

Figure 5.10: ***A*** *UV/Vis absorbance spectra of the Tb(Pc)$_2$ dispersed in a PMMA film and in ethanol solution. The PMMA film was produced according to the procedure described in chapter 2.* ***B*** *The ultrafast FE signal is plotted against the pump-probe delay. The large signal around time zero is due to the optical Kerr effect. The pump was the 400 nm SHG and was set to magic angle polarization in relation to the probe beam. The probe wavelength was set to 670 nm using a color filter after the sample. Pump fluence was set to 0.95 mJ/cm^2.*

Steps in between can not be excluded but are not in the scope of the measurements here. It is assumed, that the signature of the D_4 state in the difference spectra is the one which is seen for the maximum pump-probe delay.

5.3 Ultrafast Faraday ellipticity spectroscopy

The aim of this section should have been to show the magnetic response of the Tb(Pc)$_2$ complex after photoexcitation using the technique of FE spectroscopy as described in chapter 2. First of all it can be stated that the measurement was no success and most likely the ultrafast FE signal was hidden in the noise level. Since to my knowledge no ultrafast MCD measurement on a SMM is published at the time I write this thesis, it is potentially helpful and worth discussing how the measurement was done and how it can be improved.

As mentioned earlier in this chapter the Tb(Pc)$_2$ complex works as SMM at cryogenic temperatures [121, 129]. The $[Pc_2Tb]^-\cdot TBA^+$ SMM which was used by Ishikawa [129]

was in a retrospective view not the optimal choice. This was shown by Gonidec et al. [121], who performed MCD measurements on the three oxidation states and showed that the neutral version shows the largest coercive field of 0.16 T at 1.5 K and 664 nm. The negative and positive charged versions of the complex show quantum tunneling at a low magnetic field of 0.09 T due to a resonance between J_z levels introduced by Zeeman splitting [121]. In the MCD spectrum for the neutral $Tb(Pc)_2$ complex large MCD signals of over one degree are visible in the Q-band region [121]. Therefore this wavelength region was chosen here for the ultrafast MCD measurements.

To be able to cool the $Tb(Pc)_2$ sample down to liquid helium temperatures, the sample has to be in the solid state. In general there are at least four ways how this can be realized. The first way is, that the sample has to be crystalline (e.g. single-crystals). For MOKE experiments, which are performed in reflection of the sample, a single-crystal is a good sample. The FE signal is measured in transmission and a too thick crystal in combination with a high extinction coefficient will not allow any measurable amount of probe light to pass the sample. The second method is to produce thin films on a substrate. This method works well for metals and samples who can be spin coated on to a substrate. A limitation for this method is that the samples need a high extinction coefficient. The third method for a solid state sample is a frozen solution. This is a common method (e.g. used by Gonidec et al. [121]) to prepare samples to be used in a cryostat. The method has some disadvantages, because the sample has to be kept at low temperatures.

The method of choice here was to embed the $Tb(Pc)_2$ complex in a polymer host matrix of PMMA. The procedure how to produce thin films of $Tb(Pc)_2$ complex in PMMA is described in chapter 2. The polymer film can be cooled down to liquid helium temperatures and heated up back to room temperature without cracking. The polymer film has a high optical quality, which can be seen in Figure 5.10 **A**, where the UV/Vis absorption spectra of the PMMA film and the $Tb(Pc)_2$ sample in solution are plotted. The PMMA film spectrum is offset to the spectrum in solution because no background spectrum with a pure PMMA film was measured. Otherwise all the absorbance bands of the $Tb(Pc)_2$ are at the same position as for the sample in solution.

For the ultrafast MCD measurement the PMMA film was transferred into the cryostat (Oxford Microstat HE2 Rectangular tail) and cooled down to 6 K using liquid helium.

The measurement was then performed according to the description in chapter 2. The pump-probe polarization was set to 45°. The Lock-In amplifier waiting time was set to three seconds and the measurement was repeated 20 times for each magnetic field direction. After 10 measurements for one field direction the sample spot was changed to avoid degradation. The 400 nm pump was set to 200 nJ/pulse and the magnetic field was set to 375 mT, the highest possible constant magnetic field. The probe wavelength was set to 670 nm, which should show the strongest MCD signal [121]. The results of this measurement are shown in Figure 5.10. The two curves in red and black represent the two opposite magnetic field directions. The signal at zero pump-probe delay is the optical Kerr effect (OKE). Each data point is plotted with the standard error (SE) over the 20 measurements. There is no obvious MCD signal visible. By having a closer look, it is visible that from 0.25 ps onwards, 13 out of 16 minus field data points are around 25 to 35 nV below the plus field data points. The SE is on the same scale of around 20-30 nV.

To estimate what FE angle of the 25-35 nV signal, the static value (380 μV) of the FE measurement was used in Equation 2.1. The estimated FE angle found is around 3.5 mdeg. This rotation angle can be compared with the maximum static FE angle that can be expected with the settings of the experiment. By comparing the measurement variables like optical density of the sample and magnetic field with the MCD measurement from Gonidec et al. [121], an estimated maximum static FE angle of around 19 mdeg is estimated. A 3.5 mdeg transient change after photoexcitation seems reasonable. So the problem really is related to the signal to noise ratio.

What are the problems with this measurement and what could be improved for future experiments? Several things with this measurement are problematic and can be improved. First, the sample preparation could be improved. The orientation of the uniaxial anisotropy axis of the $Tb(Pc)_2$ molecules is randomly orientated in space since the PMMA film is made from solution. The largest FE signal can be reached when all the molecules are ordered and the magnetic field vector is perpendicular to the propagation direction of the probe laser beam. The $Tb(Pc)_2$ molecules are paramagnetic at room

temperature and it might be possible to influence the spatial orientation by applying a strong magnetic field to the PMMA film while drying [162,163]. This should orient the molecules along the magnetic field. Another improvement of the PMMA film would be to increase the concentration of the $Tb(Pc)_2$ sample. This would increase the absorbance, which is positive at the pump wavelength but critical at the probe wavelength. This leads to the next point of the experiment which can be improved.

For the detection of the FE signal a colour filter is used to filter out a small wavelength range which will be monitored for changes in the FE signal. A large amount of the probe light is lost in that way, even if the colour filter has a good transmission at the specified wavelength. The usage of the colour filter could be avoided if the probe light would be already monochromatic. The TOPAS white light conversion unit, described in chapter 2, could be used for that purpose. This would need changes in the set-up, because with the current configuration, the TOPAS can be just used as pump laser source. The changes in the beam path will also effect the temporal overlap of pump and probe pulse in the sample.

Other improvements which can be made are connected to the set-up. The PMMA film degrades over time and has to be moved manually in certain time intervals. A mechanical motorized stage could be applied to move the PMMA film continiously to avoid degradation. One improvement would be to get a liquid helium cryostat who can cool down to sub liquid helium temperatures. This can be achieved by using the thermal energy of the sample for evaporation of liquid helium. The last improvement concerns the electromagnet. The maximum current of 5 A produces a magnetic field of about 0.375 T at the current pole distance. To improve the magnetic field strength either the poles should be moved closer together, the current has to be increased or the number of windings of the coils has to be increased. The poles can not be moved closer together, because the head of the cryostat has to fit between them. The current also can not be increased with the actual electromagnet in order to avoid overheating. The only option to improve the magnetic field would be a new superconducting electromagnet with larger coils and more windings.

5.4 Conclusions

The overall conclusion for the static UV/Vis, luminescence and ultrafast TA studies is that there is energy transfer to the Tb^{3+} ion and subsequent luminescence and that the sensitization process by excitation at 400 nm is tentatively assigned via the D_3 state (HOMO-X to SOMO transition). The UV/Vis spectrum shows that the low energy B-band of the $Tb(Pc)_2$ molecule is excited when exciting with 400 nm in the ultrafast TA experiment. It also shows that the molecule is the neutral radical $Tb(Pc)_2$, due to the specific bands at 470 nm and 914 nm. The luminescence spectrum shows luminescence from the B-band as well as from the lanthanide levels. This shows that the B-band is involved in the energy transfer to the Tb and it shows that energy is transferred to the Tb ion. The ultrafast TA showed dynamics on three time scales. The fastest time constant of $\tau_1 = 650 \pm 150$ fs is assigned as IC from the B-band to the D_3 state. In the D_3 state state subsequent vibrational cooling is observed with the second time constant of $\tau_2 = 22 \pm 2$ ps. The longest time constant of $\tau_3 = 660 \pm 150$ ps is assigned as decay process from the D_3 state state to the $^5D_4$ level of the Tb^{+3}. The GSB features in the difference spectra show a good overlap with the ground state absorption. No stimulated emission signal of the lanthanide can be seen, which is explained by the long time which is needed to populate these states in relation to the maximum pump-probe delay.
Conclusions for the ultrafast MO studies are that no ultrafast FE signal after excitation with 400 nm and probe with 670 nm is observed. The reasons why no signal is observed are explained and ways to improve the experiment are exemplified. The most easy way to improve the signal should be to improve the sample and to automate the movement of the sample while performing the measurement.

Chapter 6

Summary and Outlook

In this thesis the description of an ultrafast TA set-up, that was build and tested during the PhD project, is shown. Three experimental chapters are presented, using the ultrafast TA set-up to measure the TA signal of three classes of metal coordination complexes. Beside the description of the set-up, also test measurements of well studied samples are presented and it is concluded that the ultrafast TA set-up works according to expectations.

For the TA set-up it was shown that it effectively can reproduce data known from literature. As examples, ultrafast TA experiments of the DCM laser dye and the $Fe(bpy)_3^{2+}$ in solution are shown and compared with literature. An ultrafast TA experiment of pure ethanol showed the ability to measure even small oscillations accurately with the correct phase. Improvements on the TA set-up could be done by avoiding scattered pump light. This could be either done by using a pin hole after the sample cuvette where the probe light passes through the hole while the pump light is blocked. Since the detection is sensitive, it is very difficult to avoid all scattered pump light. Another possible improvement is to project a larger part of the white light spectrum simultaneously on to the CCD cameras. Because of the dispersion, TA measurements at 320 nm and below will lead to a cut-off wavelength around 550 nm to 580 nm. By changing the spectrometer beam path and using a shorter focal length concave mirror all of the UV and the visible part of the white light could be detected. The loss of spectral resolution, especially in the red part of the white light spectrum, would be the down part of this change.

The conclusions from the chapter "Vibrational coherences in single-molecule magnets"

are that the kind of bottom-up approach for multi metal complexes is a good starting point to understand the photophysics of metal complexes with more than one metal centre. Since calculations are difficult for open shell multi-metal complexes, the comparison of the Mn_3 results with the $Mn(acac)_3$ results was helpful. There are three main results from this chapter. First is the found vibrational wave packet in Mn_3 with the main reaction coordinate along the axial JT distortion. Second, the change from axial elongated to axial compressed JT distortion after photoexcitation. Third, it was shown that the fast initial process after photoexcitation is IC for Mn(III) complexes, which is different to e.g. Cr(III) or Fe(II) complexes, where ultrafast ISC is the fastest process. Wave packets were also found for $Mn(acac)_3$ and Mn_6. There reaction coordinate could not be well defined due to involvement of multiple vibrational modes. The Mn_6 is one of the largest metal complex where a vibrational wave packet was found. The TA results on $Mn(acac)_3$ were so far missing in the 3d metal row, where acetylacetonate complexes of Cr, Fe and Co complexes are well studied.

The finding of vibrational wave packets in SMMs opens up new design ways for the synthesis of molecules and experiments exploiting the coherences that can be observed for more than 1 ps. To study how the environment has influence on the wave packet evolution, ultrafast TA studies in solid state, be it in crystalline form or dispersed in a matrix host, could be performed. Studies of the ultrafast magnetic response after photoexcitation would bring further insights in the magnetic response after photoexcitation and in how the wave packet could be exploited. One experiment to fully explain the JT distortion change in the excited state would be to measure the structure of the complex using ultrafast x-ray diffraction or absorption.

The conclusions from the chapter "Photoinduced dynamics in an exchange-coupled trinuclear iron cluster" are a long living state that was found in the TA experiments and the good agreement between the measurements and the coupled cluster calculations. Another finding is the population of the lowest excited state on a sub 120 fs time scale. This leaves room for time resolved measurements with better time resolution, to capture the dynamics and the spectral signature of the initially excited state. The cryogenic temperatures showed no effect on the dynamics and on the TA spectra. Further studies at cryogenic temperatures would be interesting. For example static UV/Vis spectra which have a much better spectral resolution and a more stable light source.

The MCD spectra showed a good agreement with the calculations and further MCD studies in combination with higher level calculations would clearly help to assign the electronic structure of the Fe_3 complex. Ultrafast magneto-optical studies could also help to resolve the excited state dynamics. This kind of measurements are challenging, since the sample had to be cooled to sub liquid helium temperatures and a reasonable strong magnetic field had to be applied. Further, the detection system had to be sensitive enough. To follow the structural changes and spin dynamics, ultrafast x-ray absorption or fluorescence would help to distinguish the spin states of the Fe centres.
The conclusions from the chapter " Luminescence in a terbium single-molecule magnet" are the found luminescence and the proposed energy transfer path that leads to the sensitization of the Tb ion. It was shown that the coupling between the two phthalocyanine ligands is important for the energy transfer to the Tb ion. The emission found could be clearly assigned to ligand emission and Tb emission. The ultrafast TA experiments showed the initial dynamics after photoexcitation, but could not totally follow the whole path towards the sensitization of the Tb(III), due to limitations of the maximum pump-probe delay. This is a measurement which would be beneficial for further studies of the $Tb(Pc)_2$ complex. Ultrafast TA measurements using excitation wavelengths into the low energy excited states should give insights into the excited states dynamics and help to assign all involved states in the photocycle. The further outlook for this study is that there is more to know about the energy transfer path and more detailed luminescence measurements could help to identify the involved states. Especially cryogenic temperature measurements should help to increase the luminescence signal and therefore help to assign all bands. Modifications of the Pc ligands is another way to learn more about the energy transfer in the $Ln(Pc)_2$ complex family. Shifting the B-band and the radical specific band at at 470 nm to higher energies, should help to increase the luminescent yield.
The ultrafast MO studies were not successful, but the conclusions drawn should help for future studies. The main result here is that an improvement of the set-up is necessary to measure small signals.

Chapter 7

Appendix

This is the supporting information section. In the following, Figures that are of minor relevance to the main text are shown here and will be referenced in the main text if applicable.

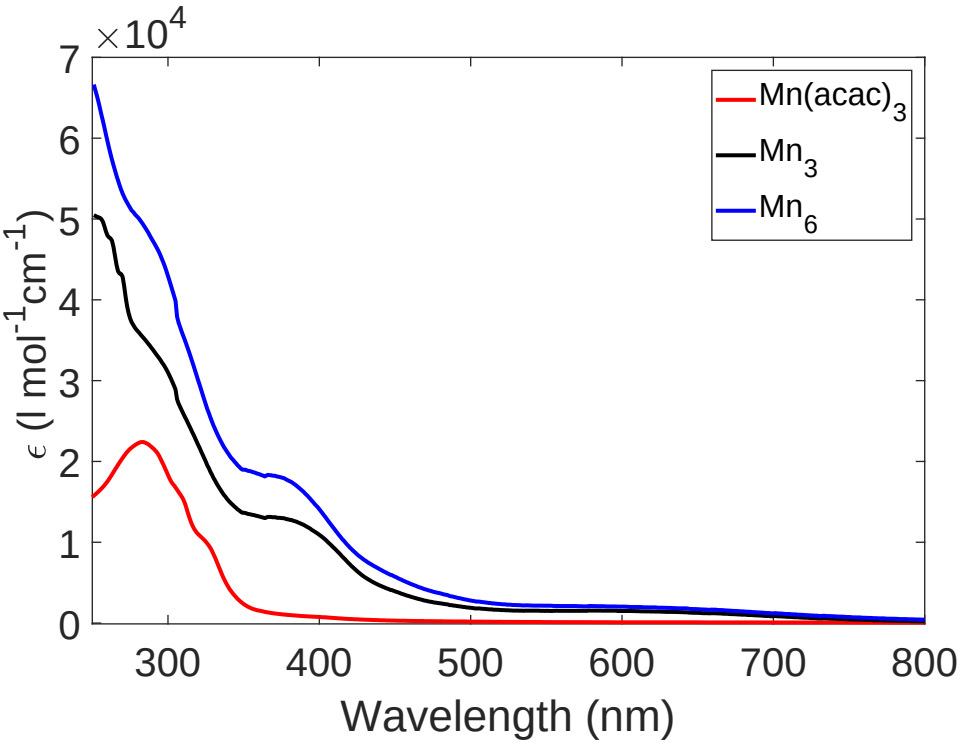

Figure 7.1: *UV/Vis absorbance spectra of the Mn_6, Mn_3 and $Mn(acac)_3$ complexes in ethanol solution.*

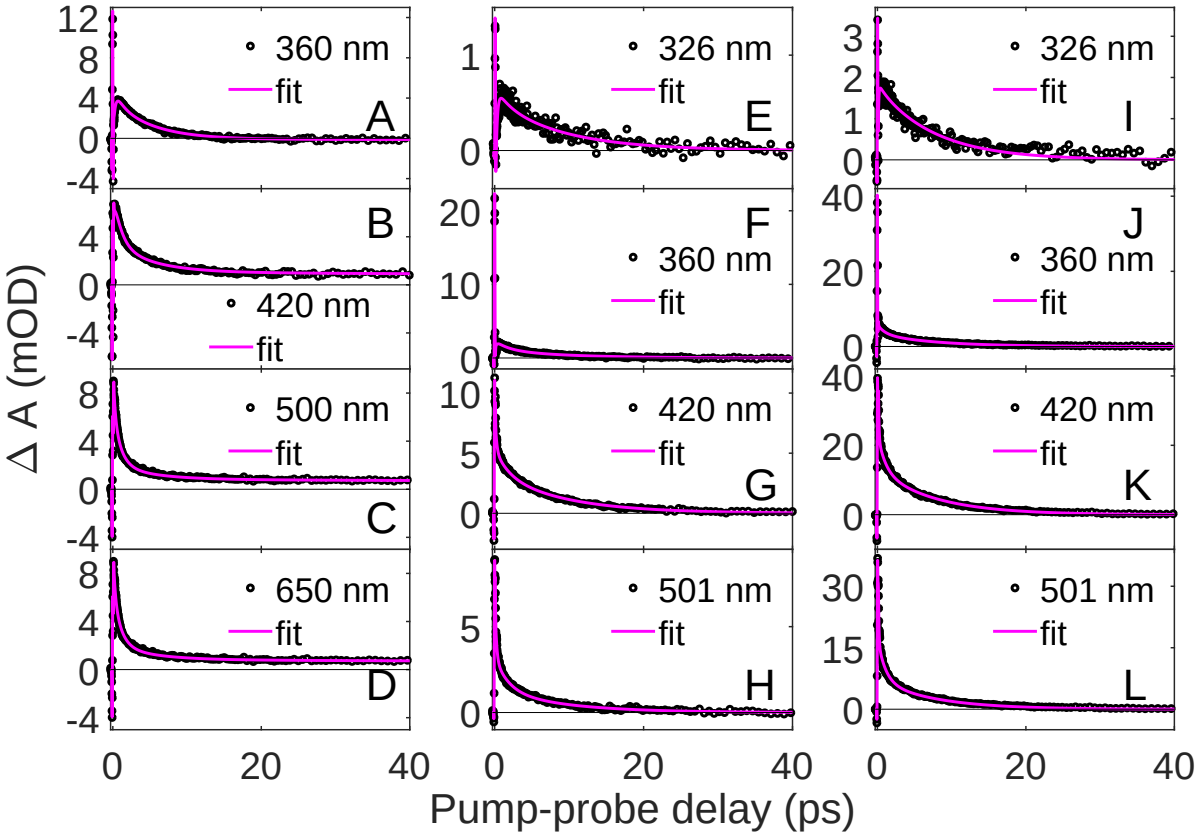

Figure 7.2: ***A-D*** *Kinetic traces for selected wavelengths from the ultrafast TA measurement of the Mn(acac)$_3$ complex dissolved in ethanol.* ***E-H*** *Kinetic traces for selected wavelengths from the ultrafast TA measurement of the Mn$_3$ complex dissolved in ethanol.* ***I-L*** *Kinetic traces for selected wavelengths from the ultrafast TA measurement of the Mn$_6$ complex dissolved in ethanol. λ_{pump} = 400 nm and 3.3 mJ/cm^2. Magic angle between pump and probe polarization planes.*

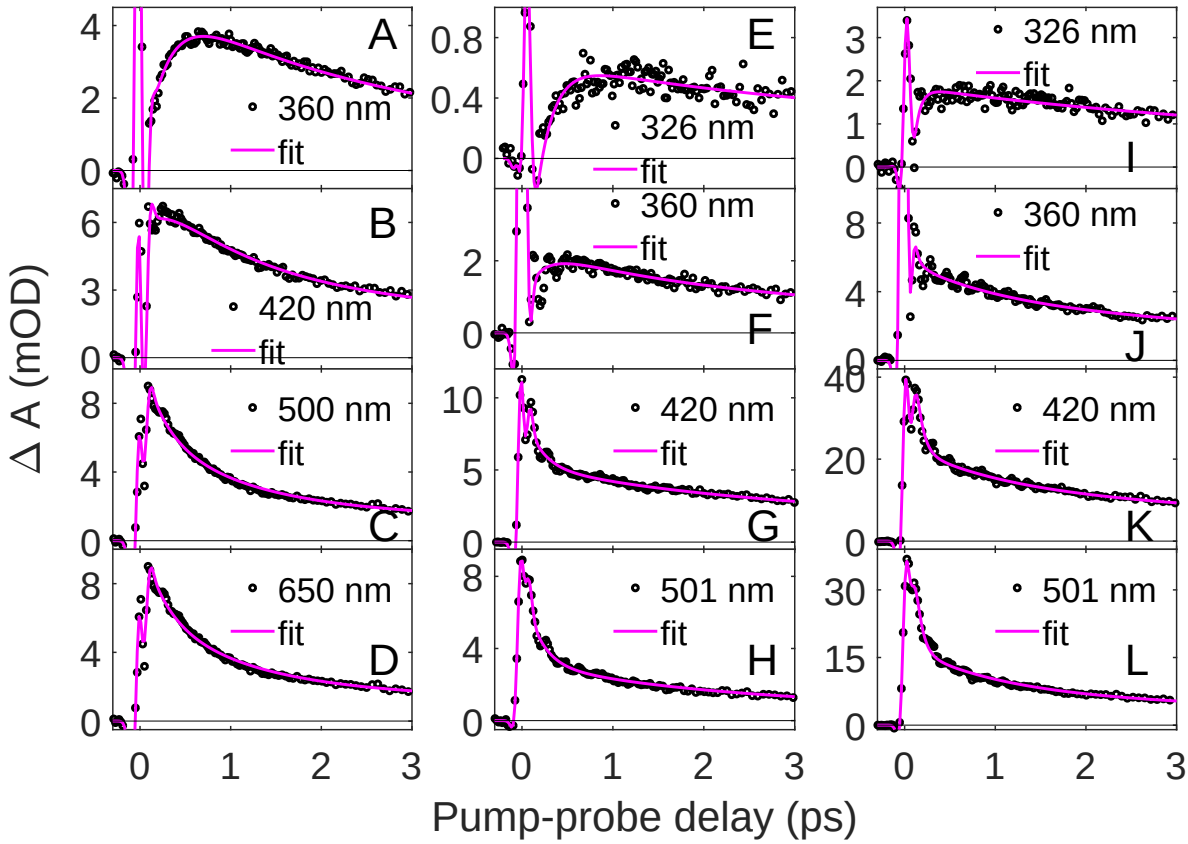

Figure 7.3: ***A-D*** *Kinetic traces for selected wavelengths from the ultrafast TA measurement of the $Mn(acac)_3$ complex dissolved in ethanol.* ***E-H*** *Kinetic traces for selected wavelengths from the ultrafast TA measurement of the Mn_3 complex dissolved in ethanol.* ***I-L*** *Kinetic traces for selected wavelengths from the ultrafast TA measurement of the Mn_6 complex dissolved in ethanol. The figure shows the same data as Figure 7.2, but just showing data up to 3 ps pump-probe delay. λ_{pump} = 400 nm and 3.3 mJ/cm^2. Magic angle between pump and probe polarization planes.*

2. $Mn(acac)_3$ geometry

The optimised structures using both the def2-SVP basis set and def2-TZVP are in good agreement with the experiment (**Table 1**). $Mn(acac)_3$ exhibits Jahn-Teller distortion along the z axis (**Figure 1**).

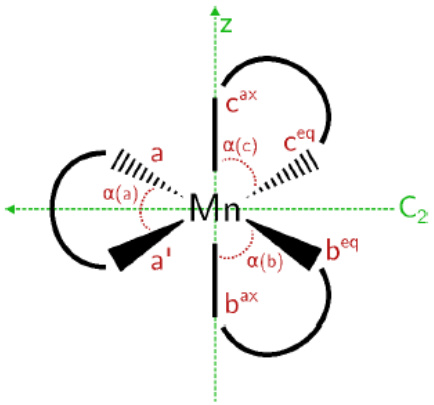

Figure 1: Definition of the structural parameters of the $Mn(acac)_3$ complex.

	Q_0		Q_1
	Expt.	Def2-TZVP/PBE (SVP)	Def2-TZVP/PBE (SVP)
a / Å	1.946 (1.932)	1.943 (1.947)	2.07 (2.06)
a' / Å	1.946 (1.932)	1.942 (1.948)	2.06 (2.06)
b^{ax} / Å	2.157 (2.110)	2.185 (2.175)	1.91 (1.91)
b^{eq} / Å	1.932 (1.937)	1.926 (1.934)	2.06 (2.07)
c^{ax} / Å	2.157 (2.110)	2.184 (2.169)	1.91 (1.91)
c^{eq} / Å	1.932 (1.937)	1.926 (1.934)	2.07 (2.06)
α(a) / °	91.4 (90.9)	90.8 (90.3)	86.4 (86.22)
α(b) / °	88.9 (88.4)	88.1 (87.9)	90.0 (89.69)
α(c) / °	88.9 (88.4)	88.1 (87.9)	90.1 (89.56)

Figure 7.4: *Structural parameters of the Mn(acac)3 complex. Experimental values are taken from reference [164].Figure was taken from Liedy et al. [80]*

3. $Mn(acac)_3$ Electronic structure

The electronic structure reported in this section has been obtained at the CASSCF//NEVPT2 level with an active space including 10 electrons in 11 orbitals. The 11 orbitals considered are three doubly occupied π orbitals localized on each acac ligand, 4 singly occupied and 1 empty d orbitals of the Mn atom and 3 empty π orbitals localized on the acac ligands. The first one is localized on the equatorial ligand while the two remaining ones are delocalized on the two other acac ligands. The orbitals of the active space are shown in **Figure 2**. 10 quintet, 10 triplet and 10 singlet states were including in the state-average casscf calculation. The electronic ground state is a quintet and the four lowest excited quintet states are metal centered transitions (^{5}MC). Higher lying quintet states are either ligand-to-ligand charge transfer (^{5}LLCT) or intra-ligand excitation (^{5}IL). The nature of the triplet and singlet states dramatically change depending on the basis set. While all lowest 10 triplet and singlet states are MC states with def2-SVP, using a more diffuse basis set (def2-TZVP) lowers the energy of the singlet and triplet CT contributions. Therefore, they mix with the low-lying MC states. All computed triplet and singlet states are MC states (**Table 3**). In total, 45 ^{3}MC and 50 ^{1}MC states are expected. Triplet and singlet CT states are expected to be above in energy. The energy of the lowest ^{5}MC states match the experimental values (**Table 2**). We however do not observe ^{5}LMCT states.

Relaxation in the first excited quintet state Q_2 involves a compression of the Mn-O along the z axis and an elongation of the equatorial bonds. This effect is such that Q_2 of configuration $d_{xz}^1,d_{yz}^1,d_{xy}^1,d_{x^2-y^2}^1$ becomes the ground state at this geometry. It lies 0.06eV above the optimized ground state geometry.

Expt.		Def2-SVP [Def2-TZVP]	
Label	Wavenumber / cm^{-1}	Label	Wavenumber / cm^{-1}
GS	0	Q_1	0 [0]
$^5A_{1g}$	9 520	Q_2	10 307 [11 119]
$^5B_{2g}$	17 900	Q_3	19 442 [20 060]
^5E_g	21 500	Q_4 (Q_5)	21 477 (22 462) [22 113 (23 157)]

Table 2: Comparison between metal centered transitions obtained experimentally (taken from reference [12]) and from CASSCF/NEVPT2(10,11) calculation taking into account the 10 lowest quintet, triplet and singlet states.

Figure 7.5: *Figure was taken from Liedy et al. [80]*

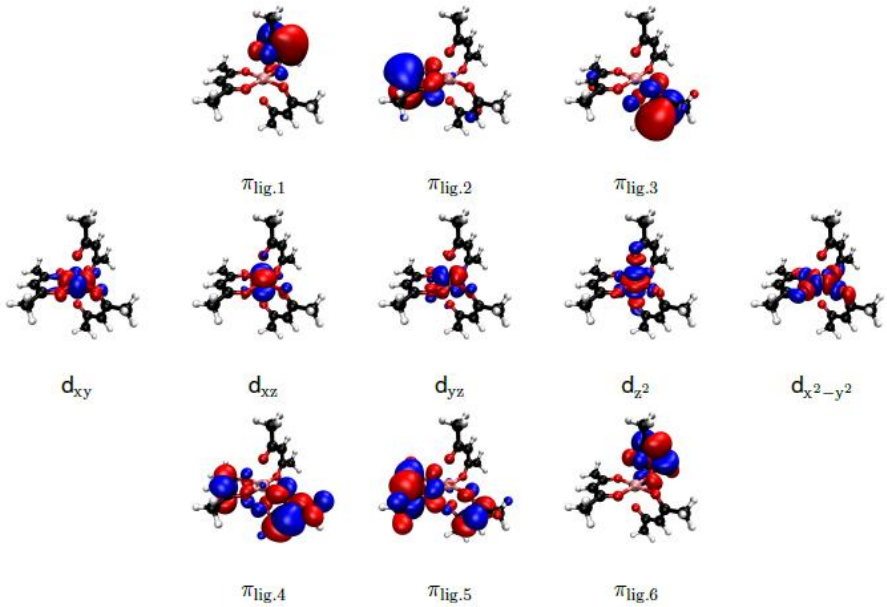

Figure S3: 10,11 active space used for the CASSCF/NEVPT2 calculations.

S2 Larger active space

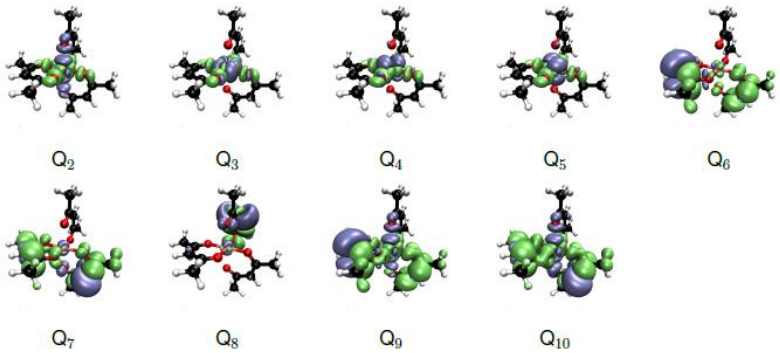

Figure S4: Difference of electronic density between each excited and the ground states for $Q_{1\rightarrow10}$. In gray: decrease of electronic density. In green: increase.

Figure 7.6: *Figure was taken from Liedy et al. [80]*

Minimum of Q_1				Minimum of Q_2			
State	Character	Δ E / eV	Wavenumber / cm^{-1}	State	Character	Δ E / eV	Wavenumber / cm^{-1}
Q_1	^{5}GS	0.00		Q_1	^{5}GS	0.06	
Q_2	^{5}MC	1.28	10 307	Q_2	^{5}MC	0.93	7 003
T_1	^{3}MC	1.63	13 150	T_1	^{3}LMCT/^{3}MC	1.46	11 319
T_2	^{3}MC	1.66	13 355	T_2	^{3}LMCT/^{3}MC	1.60	12 421
T_3	^{3}MC	1.88	15 141	T_3	^{3}LMCT/^{3}MC	1.66	12 913
Q_3	^{5}MC	2.41	19 442	Q_3	^{5}MC	2.34	18 409
Q_4	^{5}MC	2.66	21 478	Q_4	^{5}MC	2.47	19 403
Q_5	^{5}MC	2.79	22 462	Q_5	^{5}MC	2.65	20 918
T_4	^{3}MC	2.91	23 468	S_1	^{1}LMCT/^{1}MC	2.90	22 927
T_5	^{3}MC	2.95	23 819	S_2	^{1}LMCT/^{1}MC	2.96	23 386
S_1	^{1}MC	3.06	24 673	T_4	^{3}LMCT/^{3}MC	2.96	23 394
S_2	^{1}MC	3.07	24 736	T_5	^{3}LMCT/^{3}MC	3.00	23 737
T_6	^{3}MC	3.11	25 83	T_6	^{3}LMCT/^{3}MC	3.07	24 236
T_7	^{3}MC	3.12	25 146	S_3	^{1}LMCT/^{1}MC	3.08	24 385
S_3	^{1}MC	3.15	25 435	S_4	^{1}LMCT/^{1}MC	3.10	24 504
T_8	^{3}MC	3.22	25 932	T_7	^{3}LMCT/^{3}MC	3.14	24 877
S_4	^{1}MC	3.28	26 467	T_8	^{3}LMCT/^{3}MC	3.25	25 758
T_9	^{3}MC	3.36	27 95	S_5	^{1}LMCT/^{1}MC	3.38	26 774
S_5	^{1}MC	3.55	28 609	T_9	^{3}LMCT/^{3}MC	3.46	27 395
T_{10}	^{3}MC	3.62	29 154	T_{10}	^{3}LMCT/^{3}MC	3.48	27 574
Q_6	^{5}LLCT/^{5}IL	3.66	29 478	S_6	^{1}LMCT/^{1}MC	3.66	28 998
S_6	^{1}MC	3.72	29 995	Q_6	^{5}IL/^{5}LLCT	3.72	29 490
Q_7	^{5}LLCT/^{5}IL	4.19	33 775	Q_7	^{5}IL/^{5}LLCT	4.02	31 894
S_7	^{1}MC	4.32	34 824	S_7	^{1}LMCT/^{1}MC	4.27	33 918
S_8	^{1}MC	4.33	34 912	S_8	^{1}LMCT/^{1}MC	4.48	35 644
S_9	^{1}MC	4.58	36 927	Q_8	^{5}IL/^{5}MLCT	4.53	36 025
S_{10}	^{1}MC	4.66	37 589	S_9	^{1}LMCT/^{1}MC	4.56	36 310
Q_8	^{5}LLCT/^{5}IL	4.8	38 690	S_{10}	^{1}LMCT/^{1}MC	4.56	36 319
Q_9	^{5}IL	4.93	39 784	Q_9	^{5}IL/^{5}MLCT	4.83	38 469
Q_{10}	^{5}LLCT/^{5}IL	5.54	44 647	Q_{10}	^{5}IL	4.94	39 341

Table 3: 10 lowest quintet, triplet and singlet states of Mn(acac)3 using CASSCF//NEVPT2(10,11). MC, IL, LLCT, MLCT and LMCT refers to Metal centered, Intra-ligand, Ligand to ligand, Metal to ligand and Ligand to metal charge transfer, respectively.

Figure 7.7: *Figure was taken from Liedy et al. [80]*

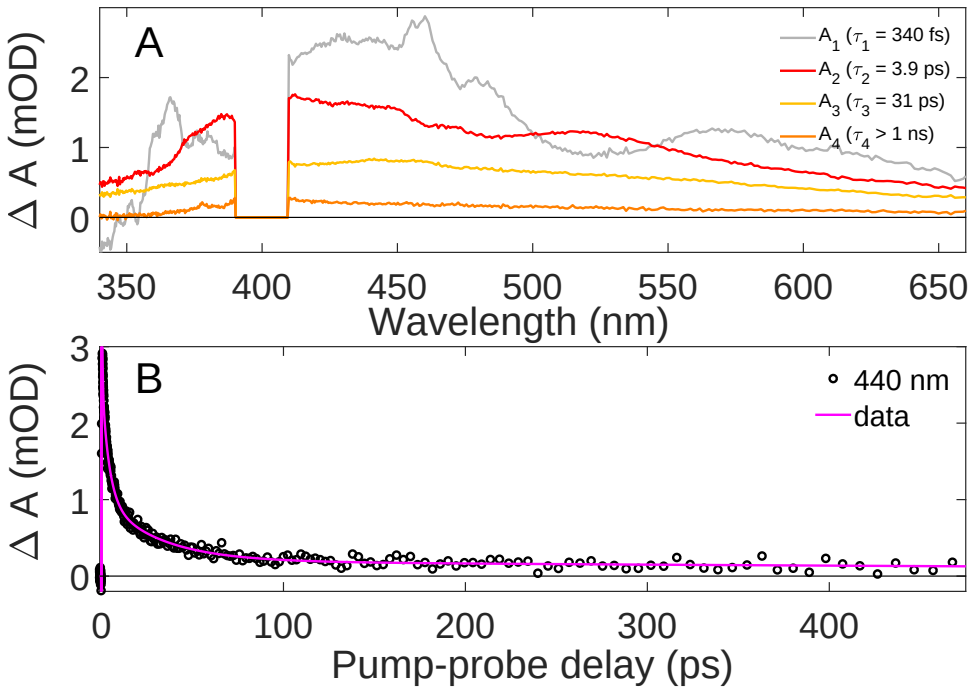

Figure 7.8: *Kinetic traces from the ultrafast TA measurement of the $Fe_3O(CH_3CO_2)_6(H_2O)_3$ complex dissolved in water. λ_{pump} = 400 nm and 1200 nJ/pulse. Magic angle between pump and probe polarization planes.*

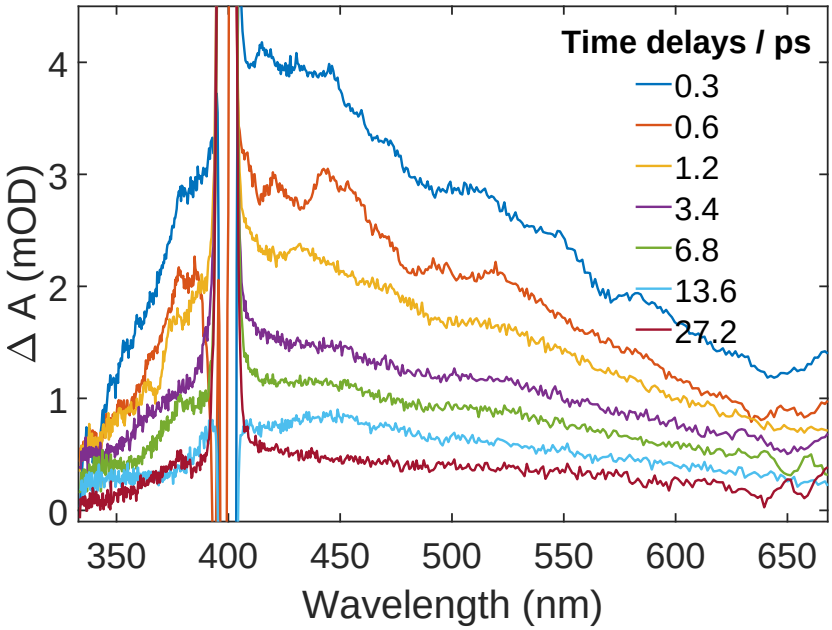

Figure 7.9: *Difference spectra from the ultrafast TA measurement of the $Fe_3O(CH_3CO_2)_6(H_2O)_3$ complex dissolved in water. λ_{pump} = 400 nm and 1200 nJ/pulse. Magic angle between pump and probe polarization planes.*

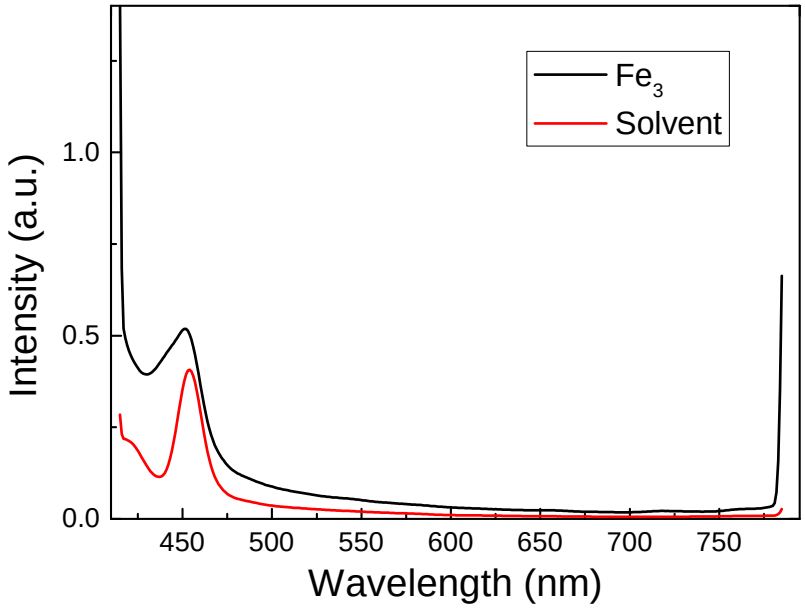

Figure 7.10: *Luminescence emission spectrum of the Fe_3 complex dissolved in isopropanol. The excitation wavelength was 400 nm. $c = 2.15 \times 10^{-5} mol/l$. This means an absorption of around 0.08 OD at 400 nm and 0.12 OD at 375 nm.*

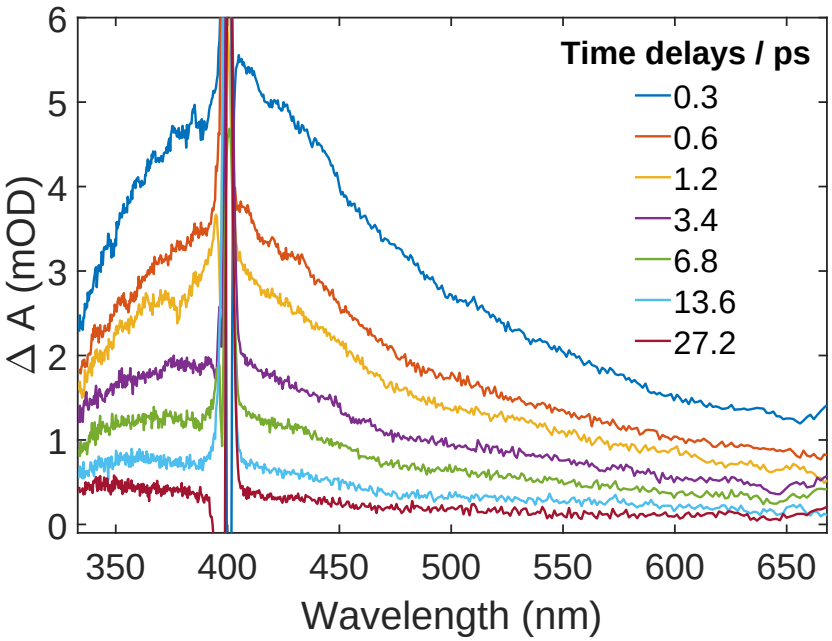

Figure 7.11: *Difference spectra from the ultrafast TA measurement of the $Fe_3O(CH_3CO_2)_6(H_2O)_3$ complex dissolved in dimethylformamide. $\lambda_{pump} = 400$ nm and 1200 nJ/pulse. Magic angle between pump and probe polarization planes.*

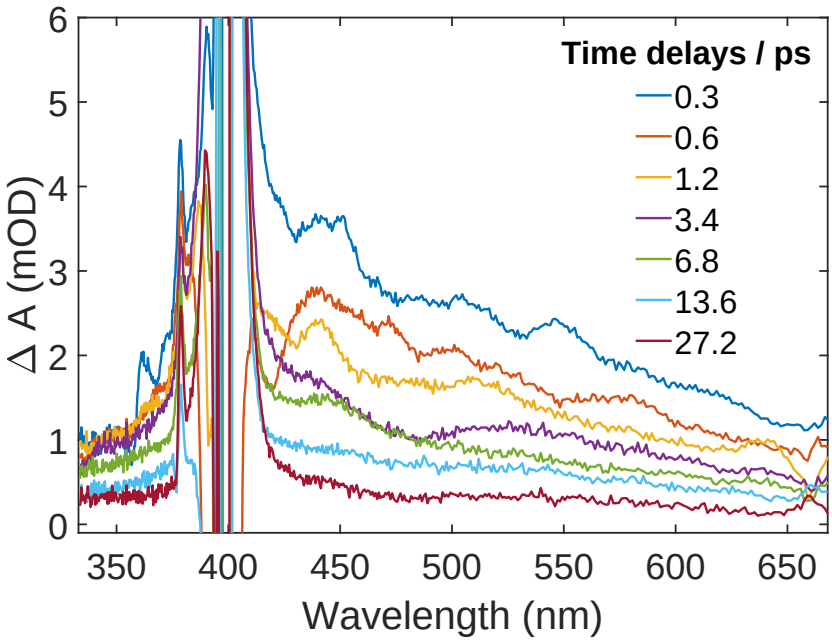

Figure 7.12: *Difference spectra from the ultrafast TA measurement of the $Fe_3O(CH_3CO_2)_6(H_2O)_3$ complex dissolved in iso-propanol. λ_{pump} = 400 nm and 1200 nJ/pulse. Magic angle between pump and probe polarization planes.*

Bibliography

[1] Oliver J. Stacey and Simon J. A. Pope. New avenues in the design and potential application of metal complexes for photodynamic therapy. *RSC Adv.*, 3:25550–25564, 2013.

[2] Kuangda Lu, Chunbai He, and Wenbin Lin. Nanoscale metal–organic framework for highly effective photodynamic therapy of resistant head and neck cancer. *J. Am. Chem. Soc.*, 136(48):16712–16715, 2014.

[3] Luke K. McKenzie, Igor V. Sazanovich, Elizabeth Baggaley, Mickaële Bonneau, Véronique Guerchais, J. A. Gareth Williams, Julia A. Weinstein, and Helen E. Bryant. Metal complexes for two-photon photodynamic therapy: A cyclometallated iridium complex induces two-photon photosensitization of cancer cells under Near-IR light. *Chem. Eur. J.*, 23(2):234–238, 2017.

[4] Stuart A. Archer, Ahtasham Raza, Fabian Dröge, Craig Robertson, Alexander J. Auty, Dimitri Chekulaev, Julia A. Weinstein, Theo Keane, Anthony J. H. M. Meijer, John W. Haycock, Sheila MacNeil, and James A. Thomas. A dinuclear ruthenium(II) phototherapeutic that targets duplex and quadruplex DNA. *Chem. Sci.*, 10:3502–3513, 2019.

[5] Kai Li, Glenna So Ming Tong, Qingyun Wan, Gang Cheng, Wai-Yip Tong, Wai-Hung Ang, Wai-Lun Kwong, and Chi-Ming Che. Highly phosphorescent platinum(II) emitters: photophysics, materials and biological applications. *Chem. Sci.*, 7:1653–1673, 2016.

[6] Chin-Yiu Chan, Lin-Song Cui, Jong Uk Kim, Hajime Nakanotani, and Chihaya Adachi. Rational molecular design for deep-blue thermally activated delayed fluorescence emitters. *Adv. Funct. Mater.*, 28(11):1706023, 2018.

[7] Ling-Yang Hsu, Qiumin Liang, Zhiheng Wang, Hsin-Hung Kuo, Wun-Shan Tai, Shi-Jian Su, Xiuwen Zhou, Yi Yuan, and Yun Chi. Bis-tridentate Ir(III) phosphors bearing two fused five-six-membered metallacycles: A strategy to improved photostability of blue emitters. *Chem. Eur. J.*, 25(67):15375–15386, 2019.

[8] Rasha Hamze, Jesse L. Peltier, Daniel Sylvinson, Moonchul Jung, Jose Cardenas, Ralf Haiges, Michele Soleilhavoup, Rodolphe Jazzar, Peter I Djurovich, Guy Bertrand, et al. Eliminating nonradiative decay in Cu(I) emitters:> 99% quantum efficiency and microsecond lifetime. *Science*, 363(6427):601–606, 2019.

[9] Alexander S. Romanov, Saul T. E. Jones, Qinying Gu, Patrick J. Conaghan, Bluebell H. Drummond, Jiale Feng, Florian Chotard, Leonardo Buizza, Morgan Foley, Mikko Linnolahti, Dan Credgington, and Manfred Bochmann. Carbene metal amide photoemitters: tailoring conformationally flexible amides for full color range emissions including white-emitting OLED. *Chem. Sci.*, 11:435–446, 2020.

[10] Munetaka Iwamura, Satoshi Takeuchi, and Tahei Tahara. Real-time observation of the photoinduced structural change of Bis(2,9-dimethyl-1,10-phenanthroline)copper(I) by femtosecond fluorescence spectroscopy: A realistic potential curve of the Jahn-Teller distortion. *J. Am. Chem. Soc.*, 129(16):5248–5256, 2007.

[11] Munetaka Iwamura, Hidekazu Watanabe, Kunihiko Ishii, Satoshi Takeuchi, and Tahei Tahara. Coherent nuclear dynamics in ultrafast photoinduced structural change of Bis(diimine)copper(I) complex. *J. Am. Chem. Soc.*, 133(20):7728–7736, 2011.

[12] Linqiang Hua, Munetaka Iwamura, Satoshi Takeuchi, and Tahei Tahara. The substituent effect on the mlct excited state dynamics of Cu(I) complexes studied by femtosecond time-resolved absorption and observation of coherent nuclear wavepacket motion. *Phys. Chem. Chem. Phys.*, 17:2067–2077, 2015.

[13] Munetaka Iwamura, Satoshi Takeuchi, and Tahei Tahara. Ultrafast excited-state dynamics of copper(i) complexes. *Acc. Chem. Res.*, 48(3):782–791, 2015.

[14] Philipp Gütlich, Andreas Hauser, and Hartmut Spiering. Thermal and optical switching of iron(II) complexes. *Angew. Chem. Int. Ed.*, 33(20):2024–2054, 1994.

[15] Daniel N Woodruff, Richard EP Winpenny, and Richard A Layfield. Lanthanide single-molecule magnets. *Chem Rev*, 113(7):5110–5148, 2013.

[16] Fu-Sheng Guo, Benjamin M Day, Yan-Cong Chen, Ming-Liang Tong, Akseli Mansikkamäki, and Richard A Layfield. Magnetic hysteresis up to 80 Kelvin in a dysprosium metallocene single-molecule magnet. *Science*, 362(6421):1400–1403, 2018.

[17] C. D. Stanciu, F. Hansteen, A. V. Kimel, A. Kirilyuk, A. Tsukamoto, A. Itoh, and Th Rasing. All-optical magnetic recording with circularly polarized light. *Phys. Rev. Lett.*, 99(4):047601, 2007.

[18] Stéphane Mangin, M Gottwald, C.H. Lambert, D Steil, V Uhlíř, L Pang, Michel Hehn, S Alebrand, M Cinchetti, Grégory Malinowski, et al. Engineered materials for all-optical helicity-dependent magnetic switching. *Nat Mater*, 13(3):286–292, 2014.

[19] C-H. Lambert, S. Mangin, B. S. D. Ch. S. Varaprasad, Y. K. Takahashi, M. Hehn, M. Cinchetti, G. Malinowski, K. Hono, Y. Fainman, M. Aeschlimann, and E. E. Fullerton. All-optical control of ferromagnetic thin films and nanostructures. *Science*, 345(6202):1337–1340, 2014.

[20] A. Stupakiewicz, K. Szerenos, D. Afanasiev, A. Kirilyuk, and A. V. Kimel. Ultrafast nonthermal photo-magnetic recording in a transparent medium. *Nature*, 542(7639):71–74, 2017.

[21] A Stupakiewicz, K Szerenos, MD Davydova, KA Zvezdin, AK Zvezdin, A Kirilyuk, and AV Kimel. Selection rules for all-optical magnetic recording in iron garnet. *Nat Commun*, 10(1):612, 2019.

[22] Isaac Bersuker. *The Jahn-Teller Effect*. Cambridge University Press, 2006.

[23] Kenji Ohmori, Hiroyuki Katsuki, Hisashi Chiba, Masahiro Honda, Yusuke Hagihara, Katsutoshi Fujiwara, Yukinori Sato, and Kiyoshi Ueda. Real-time obser-

vation of phase-controlled molecular wave-packet interference. *Phys. Rev. Lett.*, 96:093002, 2006.

[24] Barry M. Garraway and Kalle-Antti Suominen. Wave packet dynamics in molecules. *Contemp. Phys.*, 43(2):97–114, 2002.

[25] M. Gruebele and A. H. Zewail. Femtosecond wave packet spectroscopy: Coherences, the potential, and structural determination. *J. Chem. Phys.*, 98(2):883–902, 1993.

[26] Ch. Meier and V. Engel. Electron kinetic energy distributions from multiphoton ionization of na2 with femtosecond laser pulses. *Chem. Phys. Lett.*, 212(6):691–696, 1993.

[27] Monica C Carey, Sara L Adelman, and James K McCusker. Insights into the excited state dynamics of Fe(II) polypyridyl complexes from variable-temperature ultrafast spectroscopy. *Chem. Sci.*, 10(1):134–144, 2019.

[28] Wojciech Gawelda, Andrea Cannizzo, Van-Thai Pham, Frank van Mourik, Christian Bressler, and Majed Chergui. Ultrafast nonadiabatic dynamics of $[Fe(II)(bpy)_3]^{2+}$ in solution. *J. Am. Chem. Soc.*, 129(26):8199–8206, 2007.

[29] James K. McCusker, Kevin N. Walda, Robert C. Dunn, John D. Simon, Douglas Magde, and David N. Hendrickson. Subpicosecond ^{1}MLCT $\rightarrow$ $^5T_2$ intersystem crossing of low-spin polypyridyl ferrous complexes. *J. Am. Chem. Soc.*, 115(1):298–307, 1993.

[30] G. Auböck and M. Chergui. Sub-50-fs photoinduced spin crossover in $[Fe(bpy)_3]^{2+}$. *Nat Chem*, 7(8):629–633, 2015.

[31] Ch Bressler, C Milne, V-T Pham, Amal El-Nahhas, Renske M. van der Veen, Wojciech Gawelda, S. Johnson, Paul Beaud, Daniel Grolimund, Maik Kaiser, et al. Femtosecond xanes study of the light-induced spin crossover dynamics in an iron(II) complex. *Science*, 323(5913):489–492, 2009.

[32] Cristina Consani, Mirabelle Prémont-Schwarz, Amal ElNahhas, Christian Bressler, Frank van Mourik, Andrea Cannizzo, and Majed Chergui. Vibrational

coherences and relaxation in the high-spin state of aqueous $[Fe^{II}(bpy)_3]^{2+}$. *Angew. Chem. Int. Ed.*, 48(39):7184–7187, 2009.

[33] J. E. Monat and J. K. McCusker. Femtosecond excited-state dynamics of an iron(II) polypyridyl solar cell sensitizer model. *J. Am. Chem. Soc.*, 122(17):4092–4097, 2000.

[34] Niels H. Damrauer, Giulio Cerullo, Alvin Yeh, Thomas R. Boussie, Charles V. Shank, and James K. McCusker. Femtosecond dynamics of excited-state evolution in $[Ru(bpy)_3]^{2+}$. *Science*, 275(5296):54–57, 1997.

[35] Andrea Cannizzo, Frank van Mourik, Wojciech Gawelda, Goran Zgrablic, Christian Bressler, and Majed Chergui. Broadband femtosecond fluorescence spectroscopy of $[Ru(bpy)_3]^{2+}$. *Angew. Chem. Int. Ed.*, 45(19):3174–3176, 2006.

[36] Henrik T. Lemke, Kasper S. Kjær, Robert Hartsock, Tim B. van Driel, Matthieu Chollet, James M. Glownia, Sanghoon Song, Diling Zhu, Elisabetta Pace, Samir F. Matar, Martin M. Nielsen, Maurizio Benfatto, Kelly J. Gaffney, Eric Collet, and Marco Cammarata. Coherent structural trapping through wave packet dispersion during photoinduced spin state switching. *Nat. Commun.*, 8(1):15342, 2017.

[37] Jon R. Kirchhoff, Roland E. Gamache, Marcus W. Blaskie, Alan A. Del Paggio, Russell K. Lengel, and David R. McMillin. Temperature dependence of luminescence from $Cu(NN)^{2+}$ systems in fluid solution. evidence for the participation of two excited states. *Inorg. Chem.*, 22(17):2380–2384, 1983.

[38] Kazuteru Shinozaki and Youkoh Kaizu. Structure and state-energy relationship of photo-excited Cu(I) complex. *Bull. Chem. Soc. Jpn.*, 67(9):2435–2439, 1994.

[39] Corey T. Cunningham, Jeffrey J. Moore, Kurstan L. H. Cunningham, Phillip E. Fanwick, and David R. McMillin. Structural and photophysical studies of $Cu(NN)^{2+}$ systems in the solid state. emission at last from complexes with simple 1,10-phenanthroline ligands. *Inorg. Chem.*, 39(16):3638–3644, 2000.

[40] Tetsuo Katayama, Thomas Northey, Wojciech Gawelda, Christopher J Milne, György Vankó, Frederico A Lima, Zoltán Németh, Shunsuke Nozawa, Tokushi

Sato, Dmitry Khakhulin, et al. Tracking multiple components of a nuclear wavepacket in photoexcited Cu(I)-phenanthroline complex using ultrafast X-ray spectroscopy. *Nat Commun*, 10(1):1–8, 2019.

[41] Jonas Börgel, Michael G. Campbell, and Tobias Ritter. Transition metal d-orbital splitting diagrams: An updated educational resource for square planar transition metal complexes. *J. Chem. Educ.*, 93(1):118–121, 2016.

[42] Andreas F. Rausch, Herbert H. H. Homeier, and Hartmut Yersin. *Organometallic Pt(II) and Ir(III) Triplet Emitters for OLED Applications and the Role of Spin–Orbit Coupling: A Study Based on High-Resolution Optical Spectroscopy*, pages 193–235. Springer Berlin Heidelberg, 2010.

[43] Hartmut Yersin, Andreas F. Rausch, Rafał Czerwieniec, Thomas Hofbeck, and Tobias Fischer. The triplet state of organo-transition metal compounds. triplet harvesting and singlet harvesting for efficient oleds. *Coord. Chem. Rev.*, 255(21):2622 – 2652, 2011.

[44] Samantha E. Brown-Xu, Matthew S. J. Kelley, Kelly A. Fransted, Arnab Chakraborty, George C. Schatz, Felix N. Castellano, and Lin X. Chen. Tunable excited-state properties and dynamics as a function of pt–pt distance in pyrazolate-bridged pt(ii) dimers. *J. Phys. Chem. A*, 120(4):543–550, 2016.

[45] Renske M. van der Veen, Chris J. Milne, Amal El Nahhas, Frederico A. Lima, Van-Thai Pham, Jonathan Best, Julia A. Weinstein, Camelia N. Borca, Rafael Abela, Christian Bressler, and Majed Chergui. Structural determination of a photochemically active diplatinum molecule by time-resolved exafs spectroscopy. *Angew. Chem. Int. Ed.*, 48(15):2711–2714, 2009.

[46] D. Max Roundhill, Harry B. Gray, and Chi Ming Che. Pyrophosphito-bridged diplatinum chemistry. *Acc. Chem. Res.*, 22(2):55–61, 1989.

[47] Renske M. van der Veen, Andrea Cannizzo, Frank van Mourik, Antonín Vlček, and Majed Chergui. Vibrational relaxation and intersystem crossing of binuclear metal complexes in solution. *J. Am. Chem. Soc.*, 133(2):305–315, 2011.

[48] W. A. Fordyce, J. G. Brummer, and G. A. Crosby. Electronic spectroscopy of a diplatinum(ii) octaphosphite complex. *J. Am. Chem. Soc.*, 103(24):7061–7064, 1981.

[49] Steven F. Rice and Harry B. Gray. Electronic absorption and emission spectra of binuclear platinum(ii) complexes. characterization of the lowest singlet and triplet excited states of tetrakis(diphosphonato)diplatinate(4-) anion ($Pt_2(H_2P_2O_5)_4^{4-}$). *J. Am. Chem. Soc.*, 105(14):4571–4575, 1983.

[50] Donna Strickland and Gerard Mourou. Compression of amplified chirped optical pulses. *Opt. Commun.*, 55(6):447–449, 1985.

[51] M. Bradler and E. Riedle. Temporal and spectral correlations in bulk continua and improved use in transient spectroscopy. *J. Opt. Soc. Am. B*, 31(7):1465–1475, 2014.

[52] U. Megerle, I. Pugliesi, C. Schriever, C. F. Sailer, and E. Riedle. Sub-50 fs broadband absorption spectroscopy with tunable excitation: Putting the analysis of ultrafast molecular dynamics on solid ground. *Appl. Phys. B*, 96(2):215–231, 2009.

[53] S. A. Kovalenko, A. L. Dobryakov, J. Ruthmann, and N. P. Ernsting. Femtosecond spectroscopy of condensed phases with chirped supercontinuum probing. *Phys. Rev. A*, 59:2369–2384, 1999.

[54] J. F. Mammone, S. K. Sharma, and M. Nicol. Raman spectra of methanol and ethanol at pressures up to 100 kbar. *J. Phys. Chem.*, 84(23):3130–3134, 1980.

[55] Leornardo S. Mendes, Flavia C.C. Oliveira, Paulo A.Z. Suarez, and Joel C. Rubim. Determination of ethanol in fuel ethanol and beverages by Fourier transform (FT)-near infrared and FT-Raman spectrometries. *Anal. Chim. Acta*, 493(2):219 – 231, 2003.

[56] Güneş Açikgöz, Berna Hamamci, and Abdulkadir Yildiz. Determination of ethanol in blood samples using partial least square regression applied to surface enhanced Raman spectroscopy. *Toxicol. Res.*, 34(2):127, 2018.

[57] A. Maciejewski, R. Naskrecki, M. Lorenc, M. Ziolek, J. Karolczak, J. Kubicki, M. Matysiak, and M. Szymanski. Transient absorption experimental set-up with femtosecond time resolution. Femto- and picosecond study of the DCM molecule in cyclohexane and methanol solution. *J. Mol. Struct.*, 555(3):1–13, 2000.

[58] S. L. Bondarev, V. N. Knyukshto, V. I. Stepuro, A. P. Stupak, and A. A. Turban. Fluorescence and electronic structure of the laser dye DCM in solutions and in polymethylmethacrylate. *J. Appl. Spectrosc.*, 71(2):194–201, 2004.

[59] Zhang Hsing-Kang, Ma Ren-Lan, Niu Er-pin, and Guo Chu. Behaviour of the laser dye 4-dicyanomethylene-2-methyl-6-dimethylaminostryryl-4h-pyran in the excited singlet state. *J. Photochem.*, 29(3):397 – 404, 1985.

[60] T. Gustavsson, G. Baldacchino, J.-C. Mialocq, and S. Pommeret. A femtosecond fluorescence up-conversion study of the dynamic stokes shift of the DCM dye molecule in polar and non-polar solvents. *Chem. Phys. Lett.*, 236(6):587–594, 1995.

[61] S.A. Kovalenko, N.P. Ernsting, and J. Ruthmann. Femtosecond hole-burning spectroscopy of the dye DCM in solution: The transition from the locally excited to a charge-transfer state. *Chemical Physics Letters*, 258(3):445 – 454, 1996.

[62] Stanislas Pommeret, Thomas Gustavsson, Ryszard Naskrecki, Gérard Baldacchino, and Jean-Claude Mialocq. Femtosecond absorption and emission spectroscopy of the DCM laser dye. *J. Mol. Liq.*, 64(1):101–112, 1995. Ultrafast Phenomena in Liquids and Glasses.

[63] Joris J. Snellenburg, Sergey Laptenok, Ralf Seger, Katharine M. Mullen, and Ivo H.M. Van Stokkum. Glotaran: A Java-based graphical user interface for the R package TIMP. *J. Stat. Softw.*, 49(3):1–22, 2012.

[64] A. Cannizzo, C.J. Milne, C. Consani, W. Gawelda, Ch. Bressler, F. van Mourik, and M. Chergui. Light-induced spin crossover in Fe(II)-based complexes: The full photocycle unraveled by ultrafast optical and x-ray spectroscopies. *Coord. Chem. Rev.*, 254(21):2677 – 2686, 2010.

[65] Ryan Field, Lai Chung Liu, Wojciech Gawelda, Cheng Lu, and R. J. Dwayne Miller. Spectral signatures of ultrafast spin crossover in single crystal $[Fe^{II}(bpy)_3](PF_6)_2$. *Chem. Eur. J.*, 22(15):5118–5122, 2016.

[66] E. Beaurepaire, J.-C. Merle, A. Daunois, and J.-Y. Bigot. Ultrafast spin dynamics in ferromagnetic nickel. *Phys. Rev. Lett.*, 76:4250–4253, 1996.

[67] Ute Bierbrauer, Sebastian T Weber, David Schummer, Moritz Barkowski, Anna-Katharina Mahro, Stefan Mathias, Hans Christian Schneider, Benjamin Stadtmüller, Martin Aeschlimann, and Baerbel Rethfeld. Ultrafast magnetization dynamics in nickel: impact of pump photon energy. *J. Phys.: Condens. Matter*, 29(24):244002, 2017.

[68] R. Inglis, S. M. Taylor, L. F. Jones, G. S. Papaefstathiou, S. P. Perlepes, S. Datta, S. Hill, W. Wernsdorfer, and E. K. Brechin. Twisting, bending, stretching: strategies for making ferromagnetic $[Mn(III)_3]$ triangles. *Dalton Trans.*, (42):9157–9168, 2009.

[69] C. J. Milios, A. Vinslava, W. Wernsdorfer, S. Moggach, S. Parsons, S. P. Perlepes, G. Christou, and E. K. Brechin. A record anisotropy barrier for a single-molecule magnet. *Journal of the American Chemical Society*, 129(10):2754–2755, 2007.

[70] J. O. Johansson, J. W. Kim, E. Allwright, D. M. Rogers, N. Robertson, and J. Y. Bigot. Directly probing spin dynamics in a molecular magnet with femtosecond time-resolution. *Chem. Sci.*, 2016.

[71] H. Kamioka, Y. Moritomo, W. Kosaka, and S. Ohkoshi. Dynamics of charge-transfer pairs in the cyano-bridged $Co^{2+}-Fe^{3+}$ transition-metal compound. *Phys. Rev. B*, 77:180301, 2008.

[72] Akifumi Asahara, Makoto Nakajima, Ryo Fukaya, Hiroko Tokoro, Shin-ichi Ohkoshi, and Tohru Suemoto. Ultrafast dynamics of reversible photoinduced phase transitions in rubidium manganese hexacyanoferrate investigated by midinfrared CN vibration spectroscopy. *Phys. Rev. B*, 86(19):195138, 2012.

[73] Pascal Parois, Stephen A. Moggach, Javier Sanchez-Benitez, Konstantin V. Kamenev, Alistair R. Lennie, John E. Warren, Euan K. Brechin, Simon Parsons,

and Mark Murrie. Pressure-induced Jahn-Teller switching in a Mn_{12} nanomagnet. *Chem. Commun.*, 46:1881–1883, 2010.

[74] W. Kaszub, A. Marino, M. Lorenc, E. Collet, E. G. Bagryanskaya, E. V. Tretyakov, V. I. Ovcharenko, and M. V. Fedin. Ultrafast photoswitching in a copper-nitroxide-based molecular magnet. *Angew. Chem. Int. Ed.*, 53(40):10636–10640, 2014.

[75] Xu Dong, Maciej Lorenc, Evgeny V. Tretyakov, Victor I. Ovcharenko, and Matvey V. Fedin. Light-induced spin state switching in copper(ii)-nitroxide-based molecular magnet at room temperature. *J. Phys. Chem. Lett.*, 8(22):5587–5592, 2017.

[76] Florian Liedy, Julien Eng, Robbie McNab, Ross Inglis, Thomas J. Penfold, Euan K. Brechin, and J. Olof Johansson. Vibrational coherences in manganese single-molecule magnets after ultrafast photoexcitation. *Nat. Chem.*, 12(5):452–458, 2020.

[77] J. M. Bradley, A. J. Thomson, R. Inglis, C. J. Milios, E. K. Brechin, and S. Piligkos. MCD spectroscopy of hexanuclear Mn(III) salicylaldoxime single-molecule magnets. *Dalton Trans.*, 39:9904–9911, 2010.

[78] John P. Fackler, T. S. Davis, and I. D. Chawla. Hydrogen bonding to manganese(III) β-ketoenolates: Influence on the low energy electronic band. *Inorg. Chem.*, 4(1):130–132, 1965.

[79] J. Krzystek, Gregory J. Yeagle, Ju-Hyun Park, R. David Britt, Mark W. Meisel, Louis-Claude Brunel, and Joshua Telser. High-frequency and -field EPR spectroscopy of Tris-(2,4-pentanedionato)manganese(III): Investigation of solid-state versus solution Jahn-Teller effects. *Inorg. Chem.*, 42(15):4610–4618, 2003.

[80] Florian Liedy, Rui Shi, Marco Coletta, Julia Vallejo, Euan K. Brechin, Georgios Lefkidis, Wolfgang Hübner, and J. Olof Johansson. Photoinduced dynamics in an exchange-coupled trinuclear iron cluster. *J. Magn. Magn. Mater.*, 501:166476, 2020.

[81] Eric A. Juban and James K. McCusker. Ultrafast dynamics of 2E state formation in $Cr(acac)_3$. *J. Am. Chem. Soc.*, 127(18):6857–6865, 2005.

[82] Ermelinda MS Maçôas, Robertas Kananavicius, Pasi Myllyperkiö, Mika Pettersson, and Henrik Kunttu. Ultrafast electronic and vibrational energy relaxation of $Fe(acetylacetonate)_3$ in solution. *J. Phys. Chem. A*, 111(11):2054–2061, 2007.

[83] Joel N. Schrauben, Kevin L. Dillman, Warren F. Beck, and James K. McCusker. Vibrational coherence in the excited state dynamics of $Cr(acac)_3$: Probing the reaction coordinate for ultrafast intersystem crossing. *Chem. Sci.*, 1(3):405–410, 2010.

[84] Klaas Wynne and R.M. Hochstrasser. Coherence effects in the anisotropy of optical experiments. *Chem. Phys.*, 171(1):179–188, 1993.

[85] Alvin T. Yeh, Charles V. Shank, and James K. McCusker. Ultrafast electron localization dynamics following photo-induced charge transfer. *Science*, 289(5481):935–938, 2000.

[86] Staffan Wallin, Jan Davidsson, Judit Modin, and Leif Hammarström. Femtosecond transient absorption anisotropy study on $[Ru(bpy)_3]^{2+}$ and $[Ru(bpy)(py)_4]^{2+}$. Ultrafast interligand randomization of the MLCT state. *J. Phys. Chem. A*, 109(21):4697–4704, 2005.

[87] P. Beaud, S.L. Johnson, E. Vorobeva, U. Staub, R.A. De Souza, C.J. Milne, Q.X. Jia, and G. Ingold. Ultrafast structural phase transition driven by photoinduced melting of charge and orbital order. *Phys. Rev. Lett.*, 103(15):155702, 2009.

[88] Gregory D. Scholes, Graham R. Fleming, Lin X. Chen, Alán Aspuru-Guzik, Andreas Buchleitner, David F. Coker, Gregory S. Engel, Rienk Van Grondelle, Akihito Ishizaki, David M Jonas, et al. Using coherence to enhance function in chemical and biophysical systems. *Nature*, 543(7647):647–656, 2017.

[89] Sung Cho, Michael W. Mara, Xianghuai Wang, Jenny V. Lockard, Aaron A. Rachford, Felix N. Castellano, and Lin X. Chen. Coherence in metal-metal-to-ligand-charge-transfer excited states of a dimetallic complex investigated by

ultrafast transient absorption anisotropy. *J. Phys. Chem. A*, 115(16):3990–3996, 2011.

[90] J.M North, L.J van de Burgt, and N.S Dalal. A Raman study of the single molecule magnet Mn_{12}-acetate and analogs. *Solid State Commun.*, 123(1):75 – 79, 2002.

[91] Eric Rivière, Bertrand Donnio, Emilie Voirin, Guillaume Rogez, Jean-Paul Kappler, and Jean-Louis Gallani. Magneto-optical control of a Mn_{12} nano-magnet. *J. Mater. Chem.*, 20:7165–7168, 2010.

[92] Yang Li, Justin J. Wilson, Loi H. Do, Ulf-Peter Apfel, and Stephen J. Lippard. A C2-symmetric, basic Fe(III) carboxylate complex derived from a novel triptycene-based chelating carboxylate ligand. *Dalton Trans.*, 41(31):9272–9275, 2012.

[93] Kenjiro Kambe. On the paramagnetic susceptibilities of some polynuclear complex salts. *J. Phys. Soc. Jpn.*, 5(1):48–51, 1950.

[94] R. J. P. Williams. The absorption spectra of some complex ions of analytical importance. *Journal of the Chemical Society (Resumed)*, (0):137, 1955.

[95] D. Lupu, D. Barb, G. Filoti, M. Morariu, and D. Tarină. Mössbauer spectra and thermal electron transfer in mixed valence iron compounds. *J. Inorg. Nucl. Chem.*, 34(9):2803 – 2810, 1972.

[96] Antony B. Blake, Ahmad Yavari, William E. Hatfield, and C.N. Sethulekshmi. Magnetic and spectroscopic properties of some heterotrinuclear basic acetates of chromium(III), iron(III), and divalent metal ions. *Dalton Trans.*, (12):2509–2520, 1985.

[97] Michio. Sorai, Kazutoshi. Kaji, David N. Hendrickson, and Seung M. Oh. Heat capacity and phase transitions of the mixed-valence compound $[Fe_3O(O_2CCH_3)_6(py)_3](py)$. *J. Am. Chem. Soc.*, 108(4):702–708, 1986.

[98] Takuma Sato, Fumitoshi Ambe, Kazutoyo Endo, Motomi Katada, Haruka Maeda, Tadahiro Nakamoto, and Hirotoshi Sano. Mixed-valence states of

$[Fe_3O(CH_2XCO_2)_6(H_2O)_3]\cdot nH_2O$ (x = H, Cl, and Br) characterized by x-ray crystallography and ^{57}Fe-Mössbauer spectroscopy. *J. Am. Chem. Soc.*, 118(14):3450–3458, 1996.

[99] Chester T. Dziobkowski, James T. Wrobleski, and David B. Brown. Magnetic and spectroscopic properties of $Fe^{II}Fe_2^{III}(CH_3CO_2)_6L_3$, L = water or pyridine. Direct observation of the thermal barrier to electron transfer in a mixed-valance complex. *Inorg. Chem.*, 20(3):679–684, 1981.

[100] Roderick D. Cannon and Ross P. White. Chemical and physical properties of triangular bridged metal complexes. *Prog. Inorg. Chem.*, 36:196 – 298, 1988.

[101] G. Filoti, J. Bartolome, D.P.E. Dickson, C. Rillo, I. Prisecaru, T. Jovmir, V. Kuncser, and C. Turta. Intermediate frustration in $[Fe_3O(CH_3COO)_6(H_2O)_3]NO_{3\cdot 4}(H_2O)$ trinuclear cluster. *J. Magn. Magn. Mater.*, 196-197:561–563, 1999.

[102] Paul J. McCarthy and Hans U. Güdel. Optical spectroscopy of exchange-coupled transition metal complexes. *Coord. Chem. Rev.*, 88:69–131, 1988.

[103] Edward I. Solomon, Felix Tuczek, David E. Root, and Carl A. Brown. Spectroscopy of binuclear dioxygen complexes. *Chem. Rev.*, 94(3):827–856, 1994.

[104] Carl A. Brown, Glenn J. Remar, Ronald L. Musselman, and Edward I. Solomon. Spectroscopic and electronic structure studies of met-hemerythrin model complexes: A description of the ferric-oxo dimer bond. *Inorg. Chem.*, 34(3):688–717, 1995.

[105] Felix Tuczek and Edward I. Solomon. Excited electronic states of transition-metal dimers and the VBCI model: an overview. *Coord. Chem. Rev.*, 219–221:1075–1112, 2001.

[106] W. P. Griffith. Tri- and tetra-nuclear oxy-complexes. *J. Chem. Soc. A*, (0):2270–2273, 1969.

[107] Gary J. Long, William T. Robinson, Wilbur P. Tappmeyer, and Douglas L. Bridges. The magnetic, electronic, and moessbauer spectral properties of several trinuclear iron(III) carboxylate complexes. *Dalton Trans.*, (6):573–579, 1973.

[108] L. Meesuk, U. A. Jayasooriya, and R. D. Cannon. Vibrational spectra of carboxylate complexes. vii. partial valence trapping in a trinuclear mixed-valence iron(III,III,II) cluster: vibrational spectra of $[Fe_3O(OOCCH_3)_6L_3]$ and related mixed-metal complexes. *J. Am. Chem. Soc.*, 109(7):2009–2016, 1987.

[109] Tadahiro Nakamoto, Motomi Katada, and Hirotoshi Sano. Mixed-valence states of iron long-chain carboxylate complexes. *Inorg. Chim. Acta*, 291(1):127–135, 1999.

[110] Irina Diaz-Acosta, Jon Baker, Wallace Cordes, and Peter Pulay. Calculated and experimental geometries and infrared spectra of metal tris-acetylacetonates: Vibrational spectroscopy as a probe of molecular structure for ionic complexes. Part I. *J. Phys. Chem. A*, 105(1):238–244, 2001.

[111] D. Dutta, M. Becherer, D. Bellaire, F. Dietrich, M. Gerhards, G. Lefkidis, and W. Hübner. Characterization of the isolated $[Co_3Ni(EtOH)]^+$ cluster by IR spectroscopy and spin-dynamics calculations. *Phys. Rev. B*, 97:224404, 2018.

[112] R. D. Johnson III. NIST Computational Chemistry Comparison and Benchmark Database, NIST Standard Reference Database Number 101, 2019.

[113] Lauren Hanna, Pavel Kucheryavy, Cunming Liu, Xiaoyi Zhang, and Jenny V. Lockard. Long-lived photoinduced charge separation in a trinuclear iron-μ^3-oxo-based metal–organic framework. *J. Phys. Chem. C*, 121(25):13570–13576, 2017.

[114] Pavel Chábera, Yizhu Liu, Om Prakash, Erling Thyrhaug, Amal El Nahhas, Alireza Honarfar, Sofia Essén, Lisa A Fredin, Tobias CB Harlang, Kasper S Kjær, et al. A low-spin Fe(III) complex with 100-ps ligand-to-metal charge transfer photoluminescence. *Nature*, 543(7647):695, 2017.

[115] Jason D. Braun, Issiah B. Lozada, Charles Kolodziej, Clemens Burda, Kelly M. E. Newman, Johan van Lierop, Rebecca L. Davis, and David E. Herbert. Iron(II) coordination complexes with panchromatic absorption and nanosecond charge-transfer excited state lifetimes. *Nat Chem*, 11(12):1144–1150, 2019.

[116] Willard R. Wadt and P. Jeffrey Hay. Ab initio effective core potentials for molecular calculations. potentials for main group elements Na to Bi. *J. Chem. Phys.*, 82(1):284–298, 1985.

[117] P. Jeffrey Hay and Willard R. Wadt. Ab initio effective core potentials for molecular calculations. Potentials for K to Au including the outermost core orbitals. *J. Chem. Phys.*, 82(1):299–310, 1985.

[118] G. Lefkidis and W. Hübner. Ab initio treatment of optical second harmonic generation in NiO. *Phys. Rev. Lett.*, 95:077401, 2005.

[119] Nagao Kobayashi and Atsuya Muranaka. *Circular dichroism and magnetic circular dichroism spectroscopy for organic chemists.* The Royal Society of Chemistry, 2012.

[120] W. Roy Mason. *A practical guide to magnetic circular dichroism spectroscopy.* Wiley & Sons, 2006.

[121] Mathieu Gonidec, E. Stephen Davies, Jonathan McMaster, David B. Amabilino, and Jaume Veciana. Probing the magnetic properties of three interconvertible redox states of a single-molecule magnet with magnetic circular dichroism spectroscopy. *J. Am. Chem. Soc.*, 132(6):1756–1757, 2010.

[122] Francesca Branzoli, Pietro Carretta, Marta Filibian, Giorgio Zoppellaro, Michael J. Graf, Jose R. Galan-Mascaros, Olaf Fuhr, Susan Brink, and Mario Ruben. Spin dynamics in the negatively charged terbium(III) bis-phthalocyaninato complex. *J. Am. Chem. Soc.*, 131(12):4387–4396, 2009.

[123] E. Ortí, J. L. Brédas, and C. Clarisse. Electronic structure of phthalocyanines: Theoretical investigation of the optical properties of phthalocyanine monomers, dimers, and crystals. *J. Chem. Phys.*, 92(2):1228–1235, 1990.

[124] Andre De Cian, Mehdi Moussavi, Jean Fischer, and Raymond Weiss. Synthesis, structure, and spectroscopic and magnetic properties of lutetium(III) phthalocyanine derivatives: $LuPc_2{\cdot}CH_2Cl_2$ and $[LuPc(OAc)(H_2O)_2]{\cdot}H_2O{\cdot}2CH_3OH$. *Inorg. Chem.*, 24(20):3162–3167, 1985.

[125] Naoto Ishikawa, Osamu Ohno, and Youkoh Kaizu. Hole delocalization in naphthalocyaninatophthalocyaninatolutetium(III). *Chem. Phys. Lett.*, 180(1):51–56, 1991.

[126] Naoto Ishikawa, Osamu Ohno, Youkoh Kaizu, and Hiroshi Kobayashi. Localized orbital study on the electronic structure of phthalocyanine dimers. *J. Phys. Chem.*, 96(22):8832–8839, 1992.

[127] Thomas C. VanCott, Zbigniew Gasyna, Paul N. Schatz, and Michael E. Boyle. Magnetic circular dichroism and absorption spectra of lutetium bis(phthalocyanine) isolated in an argon matrix. *The Journal of Physical Chemistry*, 99(13):4820–4830, 1995.

[128] N. Ishikawa. Electronic structures and spectral properties of double- and triple-decker phthalocyanine complexes in a localized molecular orbital view. *J. Porphyrins Phthalocyanines*, 5(1):87–101, 2001.

[129] N. Ishikawa, M. Sugita, T. Ishikawa, S. Koshihara, and Y. Kaizu. Lanthanide double-decker complexes functioning as magnets at the single-molecular level. *J. Am. Chem. Soc.*, 125(29):8694–8695, 2003.

[130] Luigi Malavolti, Matteo Mannini, Pierre-Emmanuel Car, Giulio Campo, Francesco Pineider, and Roberta Sessoli. Erratic magnetic hysteresis of $TbPc_2$ molecular nanomagnets. *J. Mater. Chem. C*, 1:2935–2942, 2013.

[131] Satoshi Takamatsu, Tadahiko Ishikawa, Shin-ya Koshihara, and Naoto Ishikawa. Significant increase of the barrier energy for magnetization reversal of a single-4f-ionic single-molecule magnet by a longitudinal contraction of the coordination space. *Inorg. Chem.*, 46(18):7250–7252, 2007.

[132] F. Branzoli, P. Carretta, M. Filibian, M. J. Graf, S. Klyatskaya, M. Ruben, F. Coneri, and P. Dhakal. Spin and charge dynamics in $[TbPc_2]^0$ and $[DyPc_2]^0$ single-molecule magnets. *Phys. Rev. B*, 82:134401, 2010.

[133] M. Urdampilleta, S. Klyatskaya, J. P. Cleuziou, M. Ruben, and W. Wernsdorfer. Supramolecular spin valves. *Nat. Mater.*, 10(7):502–506, 2011.

[134] Bradley S. Prall, Dilworth Y. Parkinson, Graham R. Fleming, Mino Yang, and Naoto Ishikawa. Two-dimensional optical spectroscopy: Two-color photon echoes of electronically coupled phthalocyanine dimers. *J. Chem. Phys.*, 120(6):2537–2540, 2004.

[135] Bradley S. Prall, Dilworth Y. Parkinson, Naoto Ishikawa, and Graham R. Fleming. Anti-correlated spectral motion in bisphthalocyanines: Evidence for vibrational modulation of electronic mixing. *J. Phys. Chem. A*, 109(48):10870–10879, 2005.

[136] Oliver Bixner, Vladimír Lukeš, Tomáš Mančal, Jürgen Hauer, Franz Milota, Michael Fischer, Igor Pugliesi, Maximilian Bradler, Walther Schmid, Eberhard Riedle, Harald F. Kauffmann, and Niklas Christensson. Ultrafast photo-induced charge transfer unveiled by two-dimensional electronic spectroscopy. *J. Chem. Phys.*, 136(20):204503, 2012.

[137] Jean-Claude G. Bünzli. On the design of highly luminescent lanthanide complexes. *Coord. Chem. Rev.*, 293-294:19–47, 2015.

[138] Youkoh Kaizu, Koji Miyakawa, Keiko Okada, Hiroshi Kobayashi, Minoru Sumitani, and Keitaro Yoshihara. Aqualigand dissociation of $[Ce(OH)_9]^{3+}$ in the 5d $\longleftarrow$ 4f excited state. *J. Am. Chem. Soc.*, 107(9):2622–2626, 1985.

[139] P Dorenbos. Anomalous luminescence of Eu^{2+} and Yb^{2+} in inorganic compounds. *J. Phys.: Condens. Matter*, 15(17):2645–2665, 2003.

[140] Philippe F. Smet, Iwan Moreels, Zeger Hens, and Dirk Poelman. Luminescence in sulfides: A rich history and a bright future. *Materials*, 3(PMC5445864):2834–2883, 2010.

[141] Lorenzo Sorace and Dante Gatteschi. *Electronic structure and magnetic properties of lanthanide molecular complexes*, pages 1–26. John Wiley & Sons, Ltd, 2015.

[142] Jean-Claude G. Bünzli and Svetlana V. Eliseeva. *Basics of lanthanide photophysics*, pages 1–45. Springer Berlin Heidelberg, Berlin, Heidelberg, 2011.

[143] Manju Bala, Satish Kumar, Rekha Devi, Avni Khatkar, V. B. Taxak, Priti Boora, and S. P. Khatkar. Synthesis, photoluminescence behavior of green light emitting

Tb(III) complexes and mechanistic investigation of energy transfer process. *J. Fluoresc.*, 28(3):775–784, 2018.

[144] Svetlana V. Eliseeva and Jean-Claude G. Bünzli. Lanthanide luminescence for functional materials and bio-sciences. *Chem. Soc. Rev.*, 39:189–227, 2010.

[145] Xuan Sun, Changqin Ma, and Jianzhuang Jiang. Luminescence and photophysics of sandwich-type bis(phthalocyaninato) europium compound. *Synth. Met.*, 139(2):497–500, 2003.

[146] Martin Gouterman. Study of the effects of substitution on the absorption spectra of porphin. *J. Chem. Phys.*, 30(5):1139–1161, 1959.

[147] Yuji Kaneko, Yoshinobu Nishimura, Nobuaki Takane, Tatsuo Arai, Hirochika Sakuragi, Nagao Kobayashi, Daisaku Matsunaga, Chyongjin Pac, and Katsumi Tokumaru. Violet emission observed from phthalocyanines. *J. Photochem. Photobiol., A*, 106(1):177 – 183, 1997.

[148] Quan Gan, Shayu Li, Fabrice Morlet-Savary, Shuangqing Wang, Shuyin Shen, Huijun Xu, and Guoqiang Yang. Photophysical properties and optical limiting property of a soluble chloroaluminum-phthalocyanine. *Opt. Express*, 13(14):5424–5433, 2005.

[149] Dimitra Markovitsi, Thu-Hoa Tran-Thi, Raymond Even, and Jacques Simon. Near infrared absorption spectra of lanthanide bis-phthalocyanines. *Chem. Phys. Lett.*, 137(2):107 – 112, 1987.

[150] Jérôme Long, Yannick Guari, Rute A.S. Ferreira, Luis D. Carlos, and Joulia Larionova. Recent advances in luminescent lanthanide based single-molecule magnets. *Coord. Chem. Rev.*, 363:57–70, 2018.

[151] Fengming Zhang, Pengfei Yan, Hongfeng Li, Xiaoyan Zou, Guangfeng Hou, and Guangming Li. Towards full-color-tunable emission of two component Eu(III)-doped Gd(III) coordination frameworks by the variation of excitation light. *Dalton Trans.*, 43:12574–12581, 2014.

[152] E. Bartolomé, J. Bartolomé, A. Arauzo, J. Luzón, R. Cases, S. Fuertes, V. Sicilia, A. I. Sánchez-Cano, J. Aporta, S. Melnic, D. Prodius, and S. Shova. Heteronuc-

lear [Tb_xEu_{1-x}] furoate 1D polymers presenting luminescent properties and SMM behavior. *J. Mater. Chem. C*, 6:5286–5299, 2018.

[153] Adam W. Woodward, Andrew Frazer, Alma R. Morales, Jin Yu, Anthony F. Moore, Andres D. Campiglia, Evgheni V. Jucov, Tatiana V. Timofeeva, and Kevin D. Belfield. Two-photon sensitized visible and near-IR luminescence of lanthanide complexes using a fluorene-based donor–π-acceptor diketonate. *Dalton Trans.*, 43:16626–16639, 2014.

[154] Ryuji Nagaishi, Takaumi Kimura, and Shyama P. Sinha. Luminescence properties of lanthanide(III) ions in concentrated carbonate solution. *Mol. Phys.*, 101(7):1007–1014, 2003.

[155] H. Lemmetyinen, E. Vuorimaa, A. Jutila, Veli-Matti Mukkala, Harri Takalo, and Jouko Kankare. A time-resolved study of the mechanism of the energy transfer from a ligand to the lanthanide(III) ion in solutions and solid films. *Luminescence*, 15(6):341–350, 2000.

[156] Andrew Beeby, Stephen Faulkner, David Parker, and J. A. Gareth Williams. Sensitised luminescence from phenanthridine appended lanthanide complexes: analysis of triplet mediated energy transfer processes in terbium, europium and neodymium complexes. *J. Chem. Soc.*, pages 1268–1273, 2001.

[157] Arnaud Germain and Thomas W. Ebbesen. Picosecond photphysics of lutetium bis-phthalocyanines. *Chem. Phys. Lett.*, 199(6):585 – 589, 1992.

[158] Yongzhong Bian, Xinghai Chen, Dongying Wang, Chi-Fung Choi, Yang Zhou, Peihua Zhu, Dennis K. P. Ng, Jianzhuang Jiang, Yuxiang Weng, and Xiyou Li. Porphyrin-appended europium(III) bis(phthalocyaninato) complexes: Synthesis, characterization, and photophysical properties. *Chem. Eur. J.*, 13(15):4169–4177, 2007.

[159] Yuexing Zhang, Xue Cai, Yang Zhou, Xianxi Zhang, Hui Xu, Zhongqiang Liu, Xiyou Li, and Jianzhuang Jiang. Structures and spectroscopic properties of bis(phthalocyaninato) yttrium and lanthanum complexes: Theoretical study based on density functional theory calculations. *J. Phys. Chem. A*, 111(2):392–400, 2007.

[160] G. Ostendorp and H. Homborg. Darstellung und spektroskopische Eigenschaften der gemischtvalenten Di(phthalocyaninato)lanthanide(III). *Z. Anorg. Allg. Chem.*, 622(7):1222–1230, 1996.

[161] R. D. Shannon. Revised effective ionic radii and systematic studies of interatomic distances in halides and chalcogenides. *Acta Crystallogr. A*, 32(5):751–767, 1976.

[162] Janine Nunes, Kevin P. Herlihy, Lamar Mair, Richard Superfine, and Joseph M. DeSimone. Multifunctional shape and size specific magneto-polymer composite particles. *Nano Lett.*, 10(4):1113–1119, 2010.

[163] Karam Nashwan Al-Milaji, Ravi L. Hadimani, Shalabh Gupta, Vitalij K. Pecharsky, and Hong Zhao. Inkjet printing of magnetic particles toward anisotropic magnetic properties. *Sci. Rep.*, 9(1):16261, November 2019.

[164] Raphael J. F. Berger, Georgiy V. Girichev, Nina I. Giricheva, Angelika A. Petrova, and Natalya V. Tverdova. The structure of $Mn(acac)_3$—experimental evidence of a static Jahn–Teller effect in the gas phase. *Angew. Chem. Int. Ed.*, 56(49):15751–15754, 2017.